Mineralogical and geochemical constraints on the origin, alteration history and metallogenic significance of the Manganore iron-formation, Northern Cape Province, South Africa

A thesis submitted in fulfillment of the requirements for the degree of

MASTER OF SCIENCE

of RHODES UNIVERSITY

by

VLASSIS PAPADOPOULOS

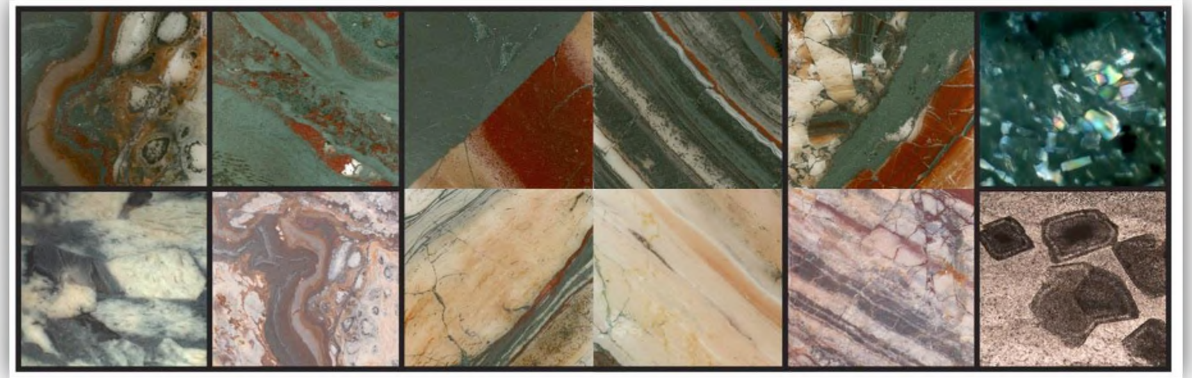

Supervisor: Prof Harilaos "Hari" Tsikos

Co-supervisor: Dr. Bertus Smith

FEBRUARY 2016, SOUTH AFRICA

Abstract

The Manganore iron-formation (MIF) of the Transvaal Supergroup is host to the most important high-grade iron ore bodies in South Africa. Prevailing models for ore genesis invoke supergene processes performing during a long period of erosion, oxidation and weathering under tropical lateritic conditions while the role of potential hydrothermal processes is not addressed. Lack of detailed petrographical and geochemical data necessitated reexamination of the MIF through new and existing drill core exploration material.

Thorough petrographical investigation revealed a multi-event complex alteration history involving hydrothermal activity. Iron and silica mobility during alteration is demonstrated by a series of replacement, overprinting, crosscutting textures, extensive silicification and hematitization. Metasomatized textures such as pseudomorphs of primary magnetite, carbonate minerals and chert pods/lenses point to an alteration occurring in layer-controlled fronts and link stratigraphically the MIF to Kuruman and Griquatown iron-formations. Whole-rock geochemical data verify textural observations suggesting strong enrichment of iron or silica in meter-scale horizons, expressed by different generations of quartz and hematite. High-grade iron ore is highly enriched in TiO_2 and Al_2O_3 compared to the protolith while both BIF and iron ore display highly increased concentrations of trace elements (transition metals and HFSE). Oxygen isotopes from different quartz textures reveal little to none isotopic exchangement during alteration whereas O isotopes from hematite are in concert to values from literature and suggest two different generations of hematite.

A total of 20 minerals apart from quartz and hematite were documented. An earlier alkali/HFSE alteration event that is believed to have affected the overlying Gamagara shales is recorded in the BIF by the presence of muscovite, apatite, rutile, zircon and xenotime. A later and possibly ongoing event of succeeding hydrothermal pulses involves mainly sulphates (gypsum, baryte, celestine), pyrite, carbonates (siderite, calcite) and silicates (berthierine and tourmaline). Alkali-bearing brines persistently exploit the BIF mainly through karstification-related secondary porosity, are evidently carrying iron and are proposed to participate in or control the iron enrichment by facilitating removal of silica. The source of metals, sulfur and carbon is attributed to the underlying Campbellrand dolomites and especially to the upper Gamogaan Formation. The unconformable contact between BIF and the overlying shales is suggested as a suitable fluid conduit for the development of the observed BIF and shale-derived high-grade hematite iron ore.

Declaration

I declare that this thesis is my own work, and information from other publications is adequately referenced. It is being submitted in fulfillment for the Master of Sciences degree in the Department of Geology, Rhodes University.

VLASSIS PAPADOPOULOS

Vlassis Papadopoulos

…………………………………

Contents

Acknowledgements

The current thesis is the result of desires and ambitions, coincidences and endeavors, hard work and encouragement, an association of feelings, ideas and great exertions occurring from several people and not just the author. A person who decides to undertake the rewarding path of scientific research can largely benefit from the teachers, fellow researchers and students, staff, friends and any life experiences during the time of research, inside and outside of academia. So at the end, a thesis gains so much more because of these interactions and that expands to science itself which as history has shown is in fact meaningful for the world only through several kinds of interaction. In that sense, a number of names not mentioned here might have also helped in the improvement of this work in their own way.

Implementation of almost every idea today requires financial support and for that I am indebted to Kumba Iron Ore Limited which gave me the financial opportunity to undertake research at Rhodes and partly at UCT, participate in the Goldschmidt conference in Europe while having an adequate and enjoyable standard of living in the serene and occasionally turbulent Grahamstown. The geologists Stuart McGregor, Deon Nel and Lauren Gericke are particularly thanked for their insights, help with transportation, hospitality and eagerness to share knowledge. Their aid during logging is much appreciated as well as the braais provided.

Endless gratitude is expressed towards my supervisor, Professor Hari Tsikos and his warm family who made my stay in South Africa the best experience it could have been. Hari is one of these remarkable and charismatic persons who you can dress with myriads of positive adjectives. Allow me an indirect try. Imagine that you are assigned with the task to present your work in front of others and thus you have to make extra preparations, in other words imagine you have a meeting in an almost weekly basis. The difference between meetings, which I tend to believe are usually mundane if not stressful for most people and a PRIMOR (research group) meeting, is the coordinator, Hari. He makes science breathe, encourages critical thinking, always provides useful insights, subversive ideas and priceless jokes (and occasionally beer) and maintains perfectly the balance between a great teacher and a good friend. Hari, thank you for allowing me the chance to be your student for two years and for everything you’ve done for me.

Special thanks go also to my co-supervisor, Bertus Smith, whose help especially with thin section preparation and micro-drilling for oxygen isotopes was direct and exceptional. Professor Goonie Marsh is kindly thanked for his help with the XRF analyses and his

invaluable advices on the analytical data. Furthermore, I would like to thank John Hepple and his assistances Chris and Thulani for the effort they put in thin section preparation. John has been particularly helpful with any need I might have had in the labs and I can sincerely say that he is one of the most willing, patient and unique persons I've ever met (and a true hard worker). Professor Chris Harris form the University of Cape Town is thanked for oxygen isotope determinations and Christel Tinguely for her valuable assistance with the EPMA analyses. Lastly, I'd like to thank all professors and staff member of the Geology department at Rhodes for being convenient to me and for the talks they shared at the tea room.

The members of PRIMOR are of course not to be forgotten. David Cousins, William Moloto, Xolane Mhlanga, Sihle Rafuza and Paul Oonk, all contemporaries, made my stay in the country much pleasant, memorable and greatly helped me fight any longing for things I couldn't have at that time of my life. The field trips in the alluring Northern Cape are for me an overstuffed chest of memories. Parties, beers, laughs, trips and conversations we shared fill the valuable keepsake I hold from South Africa very close to my heart.

Last but not least I would like to thank my beloved parents who as I grow older, I consciously realize their importance in my life, the sacrifices they've made for me and their own way of unconditional love. My sister is genuinely thanked for her love, support and her exceptional way of gratifying me every time I am in need.

The invisible presence not only behind the composition of these pages but also behind any creative process I've ever engaged with, was, is and will be my partner in life, Danae Apeiranthiti. She managed to provide so much in this thesis, in a way that nobody else could have done and that is by just being her. It would be inaccurate to name her only as my muse because as weird as it may sound many times she is the creations themselves, at least through my eyes and a significant part of me as well. Thank you for hearing my musical volley and visiting me in the other end of the world during Christmas of 2014.

I shall not forget my good friend Stratis who for almost once every week and for two consecutive years was trying his best to keep me company, sitting in front of his monitor in Athens. As much as I hate communicating through screens I must admit your humor stays top notch even when cables are involved.

List of abbreviations

Ap	Apatite
APS	Alumino-phosphate-sulphate minerals
bdl	below detection limit
BID	BIF-derived iron ore
Brt	Baryte
Bth	Berthierine
Cal	Calcite
Clt	Celestine
Gp	Gypsum
Hem	Hematite
Ilm	Ilmenite
MIF	Manganore iron-formation
Mnz	Monazite
Ms	Muscovite
Mt	Martite
n.a.	not available
PPT	Plane-polarized transmitted
Py	Pyrite
Qtz	Quartz
Rt	Rutile
Sd	Siderite
SID	Shale-derived iron ore
Tur	Tourmaline
XPR	Cross-polarized reflected
XPT	Cross-polarized transmitted
Xtm	Xenotime
Zrn	Zircon

Introduction and regional geology

Chapter 1

1.1 Introduction

Iron (Fe) is the fourth most abundant element in the crust and is present in iron-bearing minerals in nearly all sedimentary rocks. Average shale has about 4.8 percent of iron whereas in average sandstones and limestones iron is found in much lower concentrations (Blatt, 1982). Sedimentary rocks that contain more than about 15 percent iron, corresponding to 21.3 percent Fe_2O_3 or 19.4 percent FeO, are considered to be iron rich (Boggs, 2009). True iron-rich rocks though are very unevenly distributed by age in the geologic record and at the same display wide global distribution (Klein, 2005). Iron was massively deposited during three major time periods: the Precambrian, the early Palaeozoic and the Jurassic and cretaceous. This deposition led to the formation of the unusual, enigmatic chemical marine sediments broadly known as iron-formations and ironstones. Understanding of their origin has grown into one of the most fruitful ways of studying the environmental and geochemical evolution of Earth. Precambrian banded iron-formations (BIF) are primarily located in the shield areas of the continental masses and despite making up only < 1 percent of the sedimentary rocks their economic significance is enormous. Each of the main appearances of Precambrian BIF in the world is associated with a major deposit. The current study is a research on such a Precambrian BIF and its associated iron ore deposit.

Banded iron-formations (BIF) can be defined as: chemical sediments distinctively banded by thin alternating beds or laminae (mm- to cm-scale) composed primarily of chert and iron oxides and exhibiting an anomalously high content of iron (James, 1954, Gross, 1980). The lower quantitative limit of Fe content has been arbitrarily defined as 15 wt. % by James (1954) but generally it ranges from about 20 to 40 wt. % while the SiO_2 content is even greater, ranging from 34 to 56 wt. % (Klein, 2005). Their mineralogy is mainly dominated by oxides, carbonates and silicates, all hosting Fe in various amounts.

Furthermore, the altered iron formation and associated iron ore bodies being subject of this study (Manganore iron-formation) have been classified as altered Lake Superior-type BIF, meaning that they generally lack deformation, display high degree of lateral continuity and are associated with successions such as platform carbonates, carbonaceous shales and quartz arenites, typical of near- shore continental-shelf of a cratonic margin (Beukes and Gutzmer, 2008).

Iron formations are not Fe-rich enough to be considered as ore deposits under today's standards and therefore to be mined. However, the high initial accumulated iron makes them the best candidates for iron-enrichment or upgrading that will lead to ore formation if the required processes are present. There are still areas of controversy though on many aspects concerning the exact processes responsible for the transformation of BIF to high-grade iron ore (Hagemann et al., 2007) and in many cases ore formation is the result of multiple superimposed processes affecting the original BIF. It is these processes that the current thesis is trying to elucidate to the point that this is permissible. The next section presents briefly the current knowledge, models and ideas on the genesis of BIF-associated high-grade iron ores and the coeval alteration of the host iron-formations.

1.2 Altered BIF and associated high-grade iron ores

The majority of high-grade iron ore (>60 wt. % Fe) mined today is BIF-hosted and derives mainly from large deposits in Australia (Hamersley district), Brazil (Carájas, Quadriláterro Ferrífero and Urucum districts), India and South Africa. Mineralogically these deposits consist of hematite and/or martite-textured hematite ± magnetite ± goethite, the latter mostly in hydrated, supergene-modified surficial ores (Gutzmer et al., 2008, Mukhopadhyay et al., 2008). Additionally, traces of apatite and quartz occur as the main gangue minerals. Most of the aforementioned orebodies are found in sharp contact with oxidized BIF which have been categorized as altered only where they have been laterally traced into unaltered rock (Thorne et al., 2004). A number of models have been proposed for these deposits invoking field (Taylor et al., 2001), petrographic (Barley et al., 1999), isotope geochemical (Powel et al., 1999) and geochronological (Rasmussen et al., 2007) evidence which support that the enrichment is taking place: i) through hydrothermal activity, ii) in a supergene environment or ii) through the combination of both hydrothermal and supergene processes. Beukes et al. (2003) following the available literature of the time classified the major high-grade hematite ore deposits into three genetic groups namely: ancient supergene, hydrothermal and supergene-modified hydrothermal. To this day though, the controversy between a hydrothermal and supergene origin is still subject of debate and it expands in all kinds of aspects around the origin of the BIF and the enrichment processes which transform them into ore.

Conventional wisdom until the mid-1990s was that high-grade iron ores were formed by the supergene upgrading of BIF to iron ore (Morris, 1980, 1985). The BIF-hosted deposits in the Northern Cape Province in South Africa have long been considered as a prime example of ancient supergene deposit (Beukes et al., 2003), i.e. they are believed to be lithified ore from previous saprolitic soft ores that developed in the ancient supergene environment. Other major characteristics of the supergene deposits as suggested by the previous authors are: i) the presence of a regional (modern day or ancient) unconformity bounding them and ii) decrease of the grade of the ore body downwards from this unconformity and grading into partly mineralized or unaltered BIF host rock. Urucum in Brazil is one of the best examples of modern deposits of such type associated with Neoproterozoic IF.

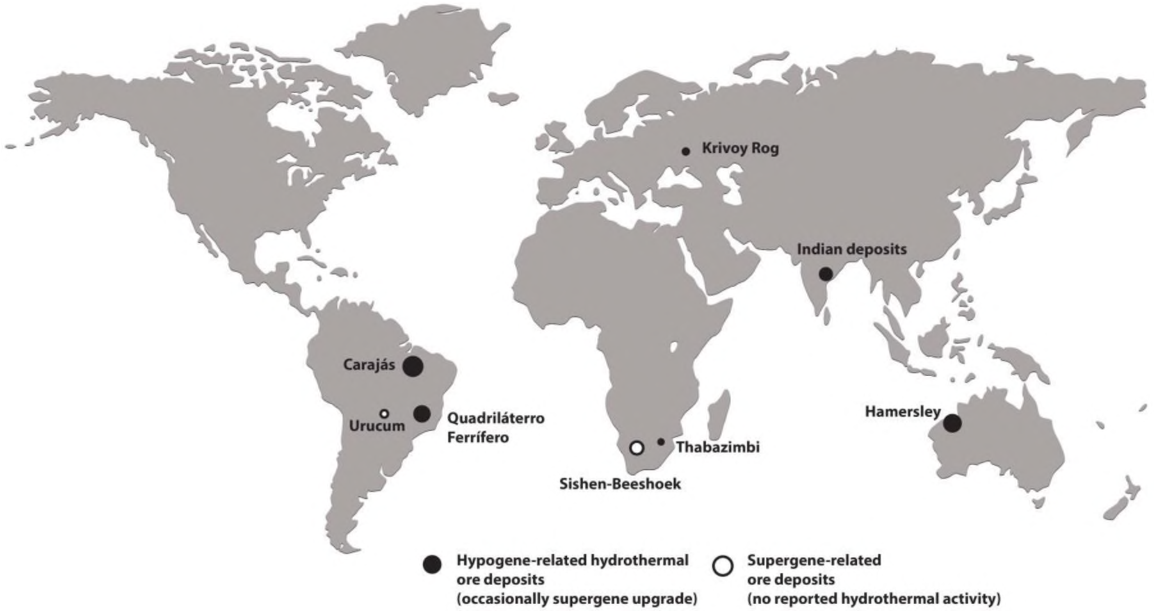

Figure 1.1. World map illustrating the distribution of the most important high-grade iron ore deposits districts mined at present. Relative resource of the different deposits is depicted by differences in the diameter of the circles marking their location. In all districts shown, ore formation has been partly or entirely attributed to hypogene alteration even if supergene enrichment is essential. The only BIF-hosted large deposit in which hydrothermal activity has not been recognized is that of Sishen-Beeshoek. Urucum is associated with Neoproterozoic IF. Modified after Beukes et al. (2003) and Dalstra and Guedes (2004).

Features which seemed inconsistent with supergene models such as dissolution of silica with meteoric waters, bottom-up development of the ore bodies and large vertical extent of some ores led to the proposition of hypogene models as alternatives with Gruner (1930) being one of the pioneers on this matter. Hypogene models including hard facts on hydrothermal fluid-flow and abundant analytical evidence came only in the late 90s. Powel et al. (1999) used geological mapping, basin analysis and stable isotope data to propose a largely hydrothermal origin for Mount Whaleback in the Hamersley district, involving heated meteoric waters. Detailed microthermometry, oxygen and hydrogen isotopes on different species and ion-chromatography were applied from Hagemann et al. (1999) to suggest basinal brines for the upgrade of BIF to high-grade iron ore in the same district. Taylor et al. (2001) published the so far most comprehensive genetic model for ore bodies from Australia by supporting the hypogene fluids through integrated structural study, hydrothermal alteration and fluid chemistry. Dalstra (2006) and Rosière et al. (2005) emphasized the structural control on hydrothermally-induced iron ore formation. Studies from different authors added data or redefined hydrothermal models for various iron ore bodies from different districts (Web et al., 2003, Thorne et al., 2004, Brown et al., 2004, Lobato et al., 2004, Figueiredo e Silva, 2007b).

It has been demonstrated that the host rock can account for all the iron required for the formation of high-grade ore and there is no necessity for processes requiring significant iron addition (Taylor et al., 2001). Although remobilization of iron during the ore-forming process is a plausible and elegant explanation it does not necessarily exclude the possibility of iron introduction in some cases. Nevertheless, the formation of a high-grade iron ore requires enrichment of iron at the expense of silica which is believed to happen either with transformation of all iron-bearing minerals of the BIF into oxides and/or hydroxides or with their dissolution and removal from the system and lastly but most important with leaching or replacement of the remaining silica being in the form of quartz. Some scientists (e.g. Morris, 1985) consider the possibility of quartz being dissolved almost completely from BIF by meteoric water given a reasonable time while others find it difficult to accept the former scenario of silica-supersaturated fluids moving down-temperature being able to remove such large volume of quartz (Evans et al., 2013). Instead, they propose mildly alkaline hydrothermal fluids flowing up-temperature which would enhance effectively the silica transport and oxidizing enough to render ferric oxide immobile (Barnes, 1997, Lobato et al., 2008). In ore districts such as Carájas in Brazil, hot magmatic fluids interacting with a colder exhumed rock sequence have been suggested to account for silica removal (Figueiredo e Silva et al., 2008) whereas in the Hamersley Province, removal of SiO_2 has been proposed to occur by basinal brines before the final supergene enrichment (Thorne et al., 2004). Indirect leaching of SiO_2 involving leaching of hydrothermal carbonate that replaced SiO_2 during hydrothermal alteration has been suggested to occur in districts where secondary carbonates have been found (Lobato et al., 2008).

Removal of SiO_2 from the BIF precursor would be paired by distinct increase in porosity which might lead to volume loss of the precursor BIF by 40-50% as it has been suggested for example by Blockley (1969) and Harmsworth et al. (1990) or even 60-70 % if the average chemistry of BIF from Klein (2005) is accounted for. This massive volume loss could be accommodated by a combination of porosity increase, collapse brecciation, bedding parallel compaction and introduction of additional iron from a hydrothermal fluid (Lobato et al., 2008). The enrichment of the host rock takes places under different environments and through different processes but what also controls ore formation is the host rock itself and its immediate and distant surroundings which differ in each major deposit. The distribution of ore bodies can be controlled for example by the presence of shale units or igneous rocks which may record prominently the effects of hydrothermal alteration in contrast to the BIF (Taylor et al., 2001, Lobato et al., 2005b). Dalstra and Guedes (2004) pointed out that mafic dikes and sills that intruded BIF prior to hydrothermal ore formation display marked hydration expressed by Mg chlorite and talc. Another major control on the location of ore deposits is structure since it forms a pathway allowing access for supergene or hypogene fluids from the source area to the site of ore formation and provides a mechanism for preservation of mineralized systems by protecting them from erosion (Dalstra and Rosière, 2008).

In many studies on hydrothermal ore deposits, alteration zones have been defined where secondary carbonates, oxides, silicates and sulphides change from proximal to distal zone (Lobato et al., 2008). Especially hydrothermal carbonates can be crucial to ore formation since carbonate-rich protores can facilitate the final upgrading to iron ore by supergene processes, long after the precursors were formed (Dalstra and Guedes, 2004). Collectively, some important evidence indicating hypogene origin of an iron ore could be the following: i) evidence for fluid conduits or wall rock alteration below hematite ore bodies, ii) bottom to top iron grade increase, iii) great depth of some ore bodies (>400 m) with perfect textural preservation of BIF, iv) ascending basinal brines in contrary to descending shallow meteoric water and v) slightly elevated temperatures (>100°C).

1.3 Regional Geology

1.3.1. Transvaal Supergroup

The Manganore iron-formation (MIF) which is the subject of this study is part of the Transvaal Supergroup. In Table 1.1., its stratigraphic position corresponds to the Asbestos Hills Subgroup to which is thought to be a lateral correlative. The Palaeoproterozoic strata of the Transvaal Supergroup are preserved within the limits of the Archean tectonic unit known as the Kaapvaal Craton, an area of approximately 1.200.00 km^2 representing ancient pristine crust. The up to 12 km thick volcano-sedimentary succession that was initially deposited in a single sedimentary basin is now been split into two separate structural basins, the Transvaal basin which circumscribes the Bushveld Complex in the east and the Griqualand West basin which lies on western margin of the craton bordering the Proterozoic Kheis orogenic belt. The two basins are divided by an occurrence of basement rocks known as the Vryburg rise (Fig. 1.2) (Moore et al., 2001). All strata between the two areas are excellent correlated.

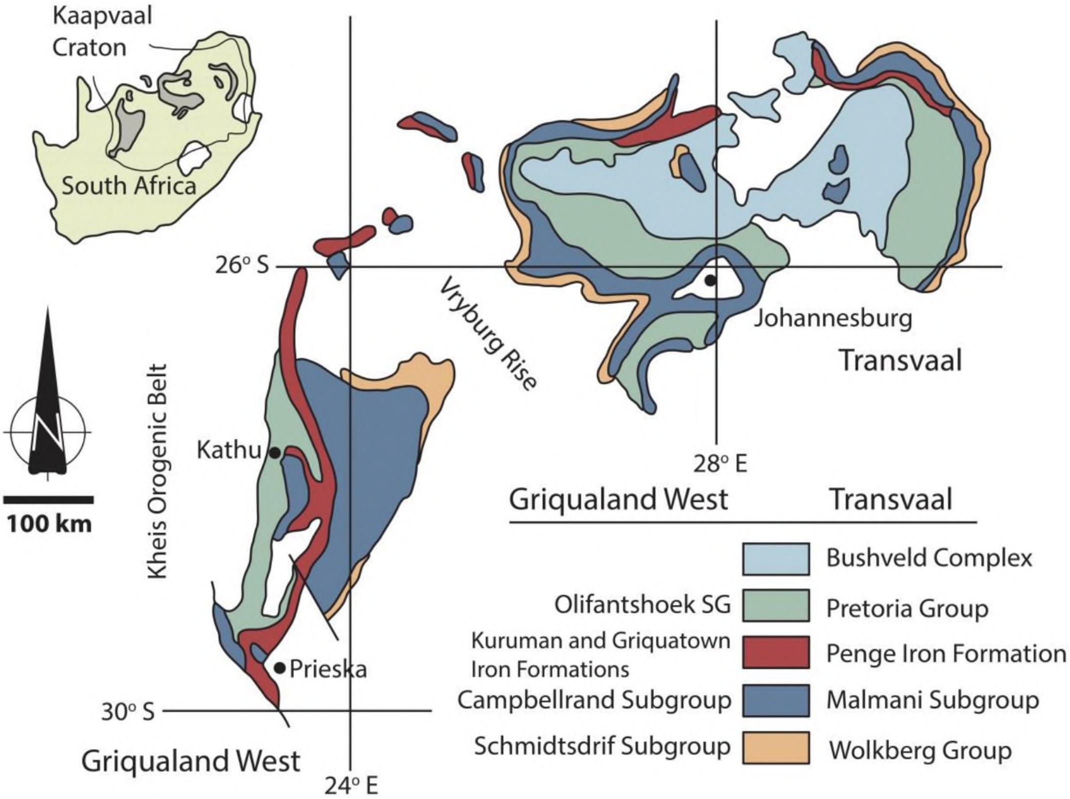

Figure 1.2. Transvaal Supergroup locality map illustrating the two lateral correlative basins of Transvaal and Griqualand West. Modified after Summer and Beukes (2006).

The Griqualand West basin consists of two Supergroups, the Transvaal and the overlying Olifantshoek. These two are thought to be divided by a major regional low-angle unconformity which marks a lengthy era of non-deposition and synchronous erosion (Grobbelaar et al., 1995). The area has undergone several extensive and compressional events comprising a complex tectonic evolution (Friese and Alchin, 2007). The most recent tectonic history affecting the Griqualand West basin after the deposition of the Ghaap and Postmasburg groups involves two major events. Kalahari orogeny (~2220-2100 Ma) induced east-directed crustal compression which led to large-scale folding, inversion of Postmasburg group rift structures, uplift and erosion (Alchin et al., 2008). The most conspicuous structural features associated with this event are the formation of the Maremane dome or anticline and the development of the regional unconformity through erosion of the folded and exposed strata and deposition of the sediments of Olifantshoek Supergroup. Subsequent Kheis orogeny (~1830-1730 Ma) was responsible for the deformation of the Kheis Belt along the western margin of the Kaapvaal Craton and the production of the Blackridge thrust which occasionally duplicates the strata of the Olifantshoek Supergroup (Grobbelaar et al., 1995). Metamorphism in the region never exceeded temperatures of ~170^{o}C and pressures of 2 kbar (Holland and Beukes, 1990). The stratigraphy of Transvaal is further discussed below through its occurrences in Kathu-Postmasburg region where Manganore iron-formation and the associated iron bodies also occur in the Maremane dome.

Supergroup	**Group**	**Subgroup**	**Formation**	**Predominant lithology**	**Approximate thickness (m)**
Transvaal	Postmasburg	Voëlwater	Mooidraai	Carbonate with minor chert	300
			Hotazel	BIF with Mn ore	250
			Ongeluk	Andesitic lava	900
			Makganyene	Diamictite	50-100
	Ghaap	Koegas		BIF, shales and wackes	240-600
		Asbestos Hills	Griquatown	Clastic textured BIF	200-300
			Kuruman	Microbanded BIF	150-750
		Campbellrand	Gamohaan	Carbonate, shale and chert	1500-1700
			Kogelbeen		
			Klippan		
			Papkuil		
			Klipfonteinheuwel		
			Fairfield		
			Reivilo		
			Monteville		
		Schmidtstdrif		Shale, quartzite, carbonate	10-250

Table 1.1. Simplified stratigraphy of the Transvaal Supergroup in Griqualand West basin. Modified after Beukes and Smit (1987) and Dorland (1999).

1.3.2. Stratigraphy of the Maremane dome and ore bodies distribution

The approximately 8-km-thick Transvaal Supergroup in the Northern Cape Province is host to all of the iron ore in the region and to the largest known resources of high-grade hematite ore in the Southern Africa continent (Carney and Mienie, 2003). The stratigraphy of Transvaal in the region consists of a lower chemically sedimentary unit known as the Ghaap Group which is unconformably overlain by the Postmasburg Group, a succession of andesitic lavas, clastic and chemical sediments (Table 1.1).

The pronounced structural feature accommodating the major orebodies is situated between Sishen and Postmasburg and is known as the Maremane dome (Fig. 1.4). This double plunging anticlinal structure dips gently at less than 10^{o} in a northerly, easterly and southeasterly direction and is defined by a core of carbonates of the Campbellrand Subgroup fringed by conformably overlying iron-formations of the Asbestos Hills Subgroup. Campbellrand Subgroup represents an extensive carbonate platform sequence of ~ 1.6 km thickness on average. It has been subdivided into eight laterally persistent formations which comprise chiefly stromatolitic dolomites with minor limestone chert and shales (Beukes, 1987).

Conformably overlying the carbonates is the Kuruman and Griquatown iron-formations of the Asbestos Hills Subgroup which can be up to ~ 1 km thick in total. Their deposition has been interpreted as a major transgression occurring with the shallowing of the carbonate platform. The two iron-formations differ in depositional setting and inherited textures. Kuruman iron-formation was deposited in an open shelf environment, comprises orthochemical sequences and exhibits microbanded textures whereas Griquatown iron-formation was deposited in a shallow-water storm-dominated epeiric sea, comprises orthochemical to allochemical sequences and thus it displays mostly clastic textures (Beukes, 1984). Geochemically and mineralogically the two iron-formations are very similar consisting mainly of quartz, magnetite, ankerite, siderite, greenalite, stilpnomelane, minnesotaite and riebeckite (Beukes and Klein, 1990). The unmineralized, unweathered BIF of the Asbestos Hills protrude as a range of hills that can be traced for ~400 km N-S in the wider region and exhibit conspicuous alternating magnetite-chert meso-bands and microbands.

The western half of the dome is covered by the younger Gamagara/Mapedi Formation the distribution of which is restricted to the Maremane dome. These siliciclastic sediments comprising conglomerates, shales and quartzites are thought to have been formed during an extended period of exposure and lateritic weathering mainly in ancient karstic sinkholes developed in the underlying dolomites of Campbellrand (Van Schalkwyk, 1984, Yamaguchi and Ohmoto, 2006). Other successions linked to the uplift and erosion, solution and karstification of the dolomites and associated development of the major unconformity are the Wolhaarkop Breccia and the Doorfontein conglomerate. Doorfontein is essentially the base of the Gamagara Formation, it was formed directly over the iron-formations and is characterized by hematite-rich matrix and variably enriched iron-formation pebbles. In places, it is considered as a low-grade iron ore and it is mined (Van Schalkwyk and Beukes, 1986). On the other hand, Wolhaarkop Breccia is developed locally between the basal dolomites and the overlying banded iron-formations, where the BIF has collapsed into sinkholes developed in the dolomites. Hence, it is believed to represent a residual manganese wad that is equivalent to the basinal contact of the Gamagara Formation to the underlying dolostones (Gutzmer and Beukes, 1996).

Further to the west of the Maremane dome, older strata of the Postmasburg Group have been thrust on top of the Gamagara beds along the Blackridge thrust. The latter is responsible for several thin thrust slices duplicating the stratigraphy of the Postmasburg Group and that of the underlying Koegas Subgroup. Koegas Subgroup consists of a series of intercalated iron-formations which in older times have been mined for iron and siliciclastic sediments, overall representing an upward-coarsening iron formation-siliciclastic sedimentary cycle (Beukes, 1983). The Makganyene Formation and the Ongeluk Formation forming the base of the Postmasburg Group represent a glacial diamictite and a 900 m thick succession of continental flood-type basaltic andesites respectively (Polteau et al., 2006).

As the geological cross-section illustrates (Fig. 1.3) the Manganore iron-formation (MIF) is preserved as large isolated blocks slumped into in palaeo-sinkhole structures in close vicinity to the dolomite units of the Campbellrand succession. Its original distribution is uncertain and more restricted than that of the Wolhaarkop Breccia as it is only preserved in pockets above the latter, pinching out before it towards the centre of the dome. The MIF-Wolhaarkop Breccia couplet dips below the Gamagara Formation along the southern and northern extremities of the Maremane dome whereas at its centre is defined by a broken arcuate belt of outliers extending for ~ 60 km. (Fig. 1.4) (Strauss, 1964, Van Schalkwyk and Beukes, 1986). It is important to note that the aforementioned couplet along with the basal Doorfontein conglomerate of the Gamagara might either be significantly reduced in thickness or in cases certain members might not be present.

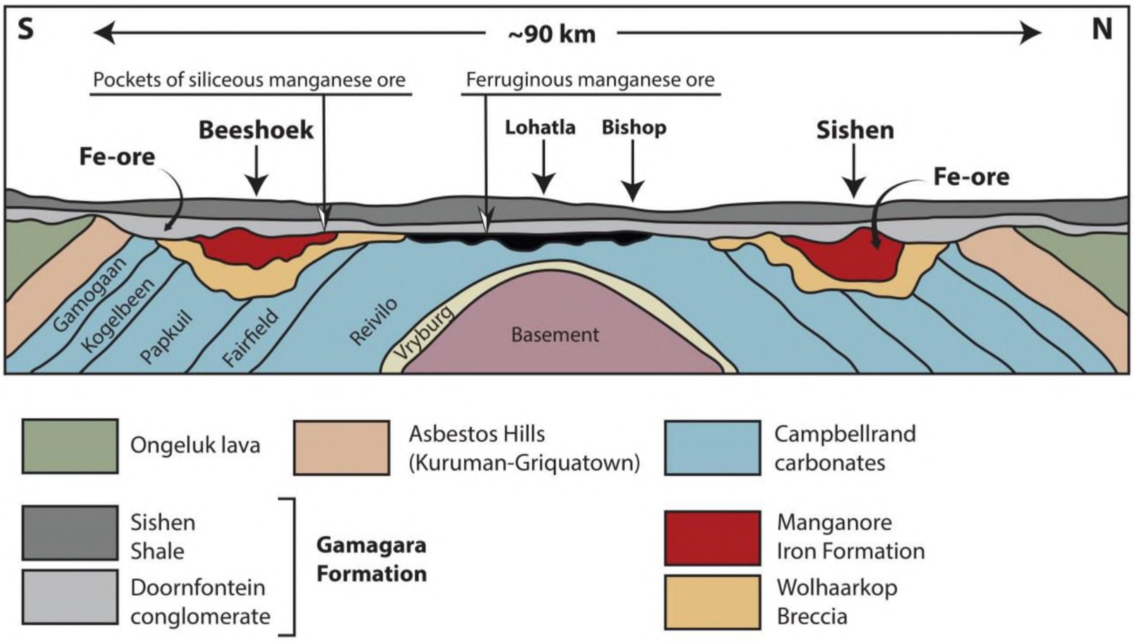

Figure 1.3. N-S schematic cross-section through the Maremane Dome. Fe-ore is hosted in the Manganore iron-formation and is preserved in ancient karstic collapse structures. Fe mineralization might also occur in the overlying Gamagara Formation (Doorfontein and/or shales). The regional unconformity is seen transecting different rock types owing to the deformed and tilted nature of the Transvaal Supergroup. Modified after Da Silva (2011).

Iron mineralization is pervasive throughout the region but it is especially prolific in the vicinity of the Maremane dome (Friese and Alchin, 2007). The primary source of high-grade iron ore is more specifically concentrated between the MIF and the Gamagara Formation as strata-bound bodies around the unconformity. It is from this stratigraphic horizon of locally mineralized BIF that all profitable extraction takes place. The ore generally preserves the meso and/or microbanding of the unmineralized BIF and thus it is characterized as laminated ore. The largest deposits are situated at the northern (Sishen and Khumani) and southern (Beeshoek and Sishen South) extremities of the anticline. In contrast to the thick, large, extensive and laterally continuous ore bodies at Sishen which constitute the largest accumulation of high-grade hematite ore in the country, the ore bodies in the other parts of the dome are in the form of numerous, small, isolated ore bodies spread over a large area (Carney and Mienie, 2003). Karstic structures that have caused the BIF to slump into large sinkholes are an important feature of preserving the iron ore (Beukes et al., 2003). Manganese ores also occur in the Maremane dome and their distribution is strictly controlled by the composition of the underlying dolomites. Ferruginous manganese ores occur where the unconformity cuts through manganese-rich members of the dolomites at the center of the dome such as Reivilo (Bishop, Lohatla) and insignificant pockets of manganese are found overlying manganese-poor dolomites (Fig. 1.3).

The MIF is notably brecciated in places and hematite forms massive, low-cluster clasts and fine-grained specularitic cement, vug and vein fillings. The hematite content usually increases upward through the BIF until the main horizon of the high-grade laminated to massive iron ore occurs (65-68% Fe) (Cairncross et al., 1997). Mineralization is also found within lithologies belonging to the overlying Gamagara Formation which can be enriched to ore grade (Fe > 60%) in places such as the Doorfontein conglomerate mentioned earlier and ferruginous shale horizons. According to mesoscopic textural attributes the ore bodies have been subdivided into different informal types such as laminated ore which exhibits conspicuous banding of alternating shiny and dull bands, massive ore which shows no lamination or is very poorly bedded and brecciated iron ore. The latter consists of angular to sub-angular hematite clasts set in a matrix or cement consisting mainly of hematite and can be found throughout the MIF but is usually immediately above the Wolhaarkop Breccia (locally known as Blinkklip Breccia) (Gutzmer and Beukes, 1996). It has been also proposed that the laminated and massive ores were folded into basinal and dome structures after their enrichment owing to being close to the western margin of the Kaapvaal craton where intensive structural deformation occurred (Carney and Mienie, 2003).

To date the most comprehensive and widely accepted model about the origin of the iron ore on the Maremane dome is the one established by Van Wyk and Beukes (1982) and Van Schalkwyk and Beukes (1986). According to this model the iron ore deposits have formed when BIF of the Asbestos Hills Subgroup slumped into karstic depressions formed in the vicinity of the dome within the Campbellrand dolomites during a long period of erosion, oxidation and weathering under tropical lateritic conditions. This process took place prior to the deposition of the Gamagara Formation as it is indicated by the iron ore pebbles found in the basal conglomerate of the latter mentioned while the sinkholes facilitated upgrading and preservation of breccia iron ores. The supergene origin of the ores is further supported by palaeomagnetic results indicating warm humid tropical environment during the believed time of ore formation (Evans et al., 2001) and by preservation of coated hematite pisolites in the

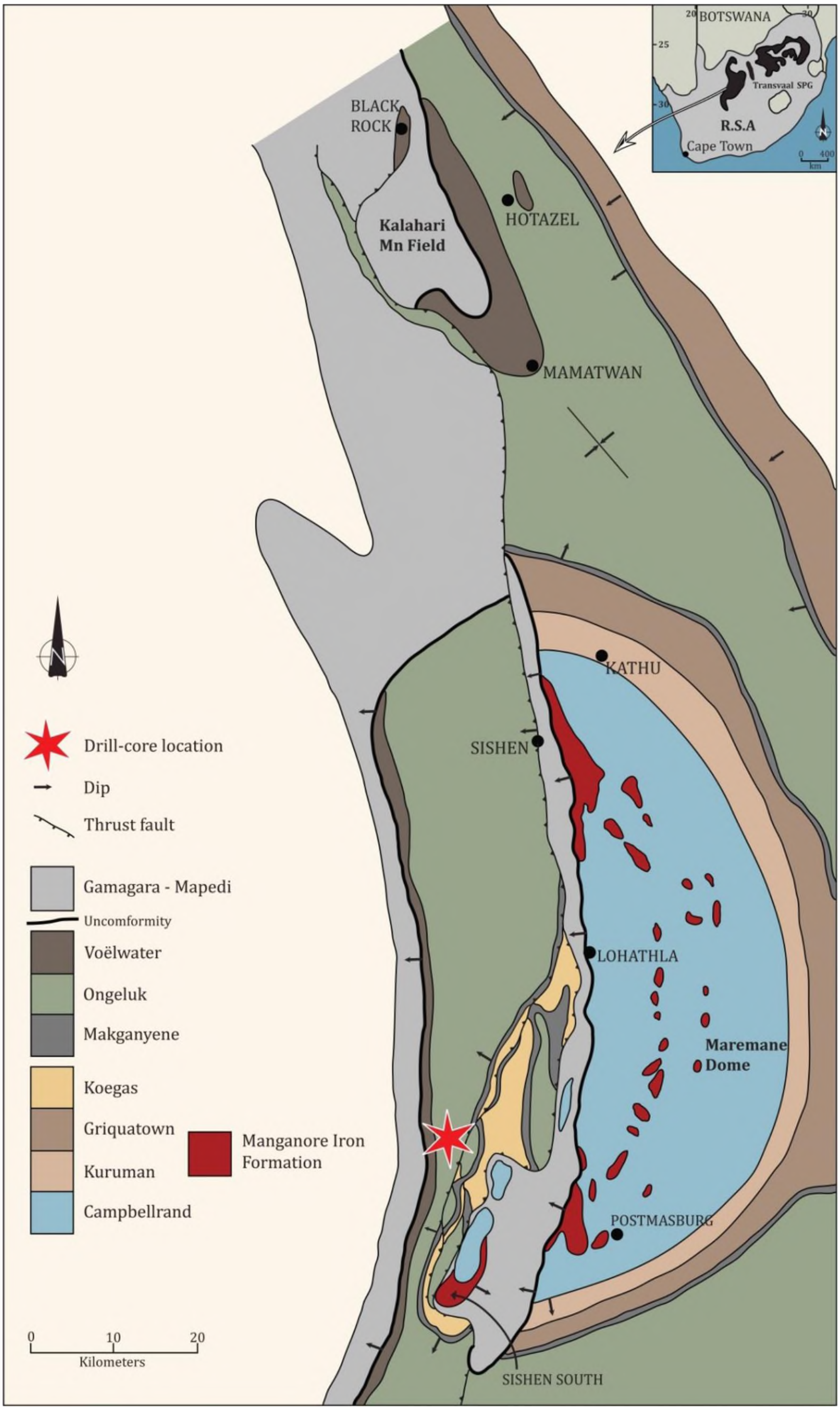

Figure 1.4. Detailed geological map displaying the development of Transvaal Supergroup in the Northern Cape Province, the Manganore iron-formation occurrence as well as the approximate localities of the studied drill cores (SLT207 and SLT284). Drill cores SA2491E and SA2072 come from Sishen. The current map is compiled from diamond core logging and field mapping. Modified after Moore et al. (2011).

lower beds of the Gamagara Formation (Gutzmer and Beukes, 1998). The only evidence supporting the involvement of hydrothermal fluids interacting with rocks and playing a pivotal role in the genesis of iron and manganese deposits in the wider region derive only from the Hotazel Formation of the Griqualand West basin which is further up to the north of the Maremane dome (Fig. 1.4.) (Tsikos et al., 2003).

1.4 Previous work on the Manganore iron-formation (MIF)

Manganore iron-formation is a term firstly introduced by Beukes (1978) to describe the iron-formation unit which overlies the Wolhaarkop Breccia on the Maremane dome. Its unconformable lower contact to the underlying Campbellrand dolomites in contrast to the conformable nature of the Asbestos Hills iron-formations contact to the same dolomites demanded further work to be done in order to prove its origin. Its correlation with the Asbestos Hills Subgroup was based on assumption rather than fact. Van Wyk (1980) and Van Schalkwyk (1984) later recognized that the lithostratigraphic sequence of the MIF corresponds very well with that of the Kuruman-Griquatown iron-formation sequence. However, the most complete work on the MIF to date was carried out by Van Schalkwyk and Beukes (1986) as part of their research on the local geologic and stratigraphic setting related to Sishen deposit.

The work of Van Schalkwyk and Beukes (1986) was conducted on cores drilled from the northern part of the dome where Sishen Mine occurs since MIF is developed within palaeo-sinkholes in the dolostones and any outcrop occurrences are largely masked by Tertiary clays, calcrete and sands of the Kalahari Formation. The total stratigraphic sequence of the MIF is not exposed in any one single borehole at the Sishen Mine because most holes are drilled to immediately below the ore bodies (Van Schalkwyk and Beukes, 1986) and furthermore extensive hematitization, brecciation due to karstification and folding and duplications produced by thrusting render any stratigraphic study difficult. For example the Asbestos Hills BIF can be found above the MIF due to thrusting or reverse folding. Using selected outcrops and cores the aforementioned authors constructed a composite stratigraphic profile of the MIF which correlates it well with the iron-formations of Kuruman and Griquatown. This profile consists of seven zones, the lowermost carbonaceous shale with chert and hematite nodules being equivalent to the Gamogaan Formation which is the base of the Campbellrand Subgroup and the uppermost peloidal and banded zone of the MIF corresponding to the upper part of the Griquatown iron-formation. Most zones correspond texturally and structurally well to the unaltered BIF apart from some uncertainties concerning a transition from one zone to another in approximately the middle of its stratigraphic profile.

Petrographically the MIF has been given very little attention because of its easily recognized dominant binary mineralogy of quartz and hematite and its very fine-grained nature in concert to most banded iron-formations. Pseudomorphic textures have also been largely neglected since as it was suggested by Van Schalkwyk and Beukes (1986) the recrystallized platy nature of hematite is inclined to obliterate original crystal textures. Therefore, for example martite has not been positively identified although it has been proposed that clusters of slightly coarser grains of hematite could represent martitized earlier magnetite crystals. Other textures such as hematite microbands possibly representing martitized magnetite microbands of the Kuruman iron-formation have been only vaguely described. Van Schalkwyk (1984) noted traces of greenalite and siderite detected by XRD within a zone correlative of the Riries Member of the Kuruman iron-formation. Since then, no author has conducted a study concerning the mineralogy of the MIF and the hosted ore bodies in attempt to add to the results of the previous authors. Other unpublished mineralogical data are scarce and derive from MSc theses where the main focus is given either on the iron ore or the Wolhaarkop Breccia (Schalkwyk, 2005, Van Deventer, 2009, Beyeme, 2009). Diaspore, pyrophyllite and muscovite deriving mainly from the brecciated ore have been suggested to represent a stage of low-grade metamorphism while cryptomelane and pyrolusite coming also from the ore are explained as supergene alteration products. Veins of baryte and calcite have been furthermore noted as well as specularite veins of secondary generation. Finally, traces of svanbergite intergrown with hematite have been recognized in the BIF (Van Deventer, 2009).

Summarizing, Manganore iron-formation is the footwall to the iron ore and host of the major iron orebodies in South Africa (80-90% of the ore of Sishen deposit is hosted by the MIF). However, no one has systematically worked on it during the last decades and after the work of the authors presented above. It is generally characterized as hematitized, oxidized but only weakly enriched hematite-chert banded iron-formation, partially enriched BIF, iron-enriched correlative of the Asbestos Hills or slumped Asbestos Hills Subgroup, all that in studies where it never constitutes the main focus.

1.5 Research aims and objectives

In light of the above, it is apparent that there is a lack of available data on different aspects concerning the Manganore iron-formation. Despite the existence of a macro- to mesoscopic stratigraphic correlation with Kuruman and Griquatown iron-formations there is a lack of detailed microscopic work. No attention has been given to the mineralogy of veins or breccias present in the BIF. The geochemical changes and degree of mineralization of the BIF have never been studied in detail since such procedure requires logging of its highly variable and brecciated stratigraphy and targeted sampling. Furthermore, current knowledge is based only on cores from Sishen while significant BIF-hosted iron ore discoveries have been made in recent years and exploration drill-core material has been made available also from other parts of the wider region. The possible role of involved hydrothermal activity of any fluid or brine has been given very little attention. One of the main questions addressed in the present study is if one can recognize indications or signs within the host rock capturing the alteration processes whatever their nature. This study does not intent to employ sophisticated methods but instead using relatively simple analytical tools combined with scrutinized investigation hopes to expand the available knowledge on the processes that formed the altered BIF and the related high-grade iron deposit. The main research aims are summarized in the following key points:

- Provide a detailed and thorough mineralogical characterization of the Manganore iron-formation (BIF and iron ore) with particular emphasis on the textures of its largely binary mineralogy, the potential remnant minerals from the precursor rock or any secondary minerals formed during alteration.
- Contribute new geochemical data of major and trace elements since at the moment there is no published record in literature for the altered BIF. Furthermore, link the obtained data to petrographic observations in attempt to identify and quantify patterns of enrichment/depletion in the two major components (silica and iron) and examine their relationship with textures.
- Emphasize any potential hydrothermal events involved mainly through the examination of veins, breccias and open space-filling material, define mineralogical parageneses and draw indirectly insights into the composition and nature of the fluid activity.
- Obtain isotopic signatures from quartz and hematite separates in attempt to further assess the alteration processes.

- Evaluate the collected data with view to shedding light on the alteration history of the BIF, defining alteration stages, linking it to its protolith and finally proposing new insights that will complement or even redefine current supergene models for the genesis of the iron ore. It is highlighted that the above will hopefully be achieved primarily though the examination of the footwall of the ore and additionally through the ore itself.

The main analytical procedures employed in this study are: i) standard mineralogical investigation through optical microscope and SEM, XRD and EPMA, ii) traditional whole-rock geochemical analysis (XRF) and iii) oxygen stable isotope geochemistry (GS-MS). Prior to the above, meticulous stratigraphic core logging is crucial for any subsequent sampling to be of value. In Figure 1.5 below, a simplified sketch illustrates the broad stratigraphic profile expected to be found in the studied area.

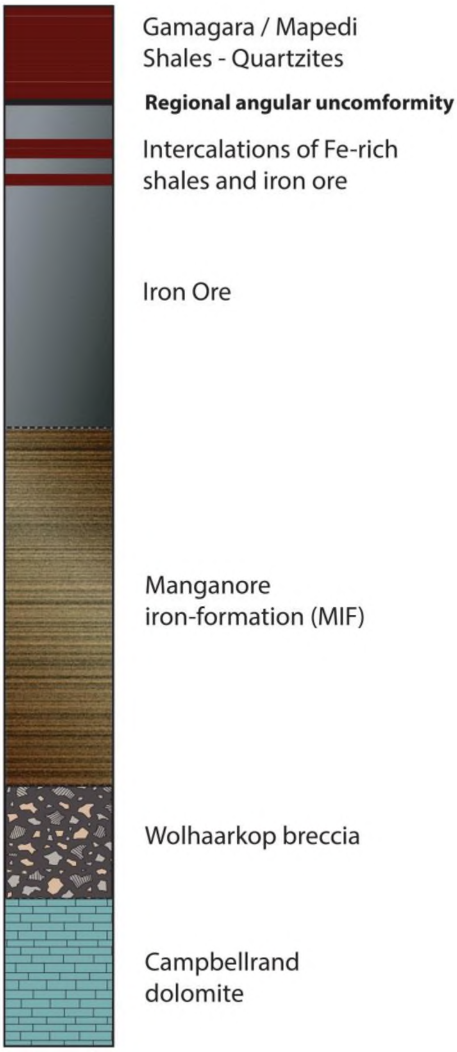

Figure 1.5. A simplified profile of the typical stratigraphy from the Maremane anticline. The Wolhaarkop Breccia at the base of the BIF shows localized distribution and thus might be missing from the stratigraphy. Regardless of the texture of the iron ore, intercalations of ferruginous shales and ore might be present at the top of the unit.

Lithostratigraphy and macroscopic observations

Chapter 2

2.1 Introductory remarks

Existing characterizations of the Manganore iron-formation (MIF) are scarce and when present in studies, only broad textural or descriptive terms are employed to characterize its attributes such as laminated, brecciated, oxidized, partially hematitized or mineralized BIF. Exception to this presents only the work of Van Schalkwyk and Beukes (1986) which requires from the reader to be familiar with the nomenclature on BIF of Beukes (1980) which can be a quite arduous task. These broad terms hold of little importance when a more detailed investigation is attempted since they consider the BIF as a uniform unit which has experienced the same alteration across its stratigraphy. For example the intensity, relative timing and scale of brecciation differ significantly across stratigraphy on core-scale of observation. Characteristics of lamination may vary from conspicuous thinner mm-scale dense microbands or thicker cm-scale mesobands to more irregular layering or it may be even absent. Furthermore, its colouration can be a distinctive feature for the enrichment in iron or silica as it will be shown later. While there is no doubt that mineralogy is dictated by quartz and hematite, their distribution in different textures might represent different generations and could reveal more on the MIF origin and alteration. For all these reasons, a crude classification of the altered BIF during logging is believed to be essential and will be further used for the presentation of the petrography and geochemistry of this study.

Criterions for borehole selection comprised: i) thick profile of the Manganore BIF and iron ore which also encompasses the shaley hanging-wall of mineralization ii) extensive and common appearances of brecciation, veins and infill-textures as well as other alteration attributes implying enrichments/depletions in the major constituents. Disclosure of the exact location of the drill cores is prevented by confidentiality reasons, therefore only their approximate location can be revealed (Figure 1.4). In establishing a detailed stratigraphy of the exposed sequence, high resolution core logging was undertaken.

It is widely recognized that studies carried on drill cores provide much clearer stratigraphic profiles along with other advantages but discourage thinking in different and particularly larger scales. That is being said because many peculiar textures observed macroscopically in the selected boreholes such as heavily undulating bands of vertical orientation being continuous for meters or sharp contacts between iron-enriched and unenriched portions render expanded visualization on a larger scale difficult and so their characterization is limited to core-scale of observation. This latter in conjunction with the absence of available altered BIF and iron ore outcrops in the wider region complicates any attempt of understanding the events related to mineralization and setting rigorous constraints on the timing of these events. Preserved structural controls which proved to be very helpful tools in other large deposits worldwide are not at least directly accessible for the orebodies of the study area. The studied drill cores exhibit highly broken rock in most parts and only rarely the cores are uninterrupted for more than couple of tens of cm. That is because of the ongoing slumping into the underlying dolomites which are ceaselessly being dissolved. Generally, the host rock of the iron ore consists of highly cracked, fractured, in places faulted rocks displaying rhythmic banding, zones of intense brecciation, horizons of silica enrichment, abundant veins of different scales and mineralogy, overall implying multiple episodes of alteration.

For the present study four drill cores were selected and studied. The main focus was given on the newest drill-core material from the Kumba exploration camp (cores SLT207 and SLT284) (Fig. 1.4). Additionally, two older cores from the Sishen mine (SLT2491E and SA2072) exhibiting more typical stratigraphical appearances of the Manganore BIF and the laminated iron were studied. The following section provides a detailed description of the lithostratigraphic columns made for the logged cores with the main focus given on one from each region (SLT207 and SLT2491E) along with some hand-specimen macroscopic observations. The lithostratigraphic logs created for the other two cores as well as a complete legend including the different Gamagara lithologies can be found in Appendix I.

2.2 Stratigraphic profiles and macroscopic observations

2.2.1 Drill core STL207

This drill core presents the most extensive profile of the altered BIF among the four studied and covers almost the whole palette of different textures observed in these rocks. The approximately 364 m of this core cover most of the typical regional stratigraphy, starting with the Ongeluk Formation at the top (111.19m) and ending within BIF at a basal depth of 475.51m from surface. The top of the core consists of the greenish altered andesitic lavas of the Ongeluk Formation overlying the Gamagara Formation, represented here by alternating dark red shales and pinkish white quartzites which both exhibit faulting and fragmentation. The sharp nature of the contact and the current arrangement of the older lavas on top of the younger sediments points to a thrust contact in agreement to what has been generally accepted by others (Carney & Mienie, 2003). The Gamagara shales grade downwards into a section consisting of slightly to highly ferruginized reddish brown to brownish grey shales. Within this part, shale horizons of 1-2m thickness are enriched up to ore quality in terms of iron content (>60 wt. %) comprising an essentially shale derived iron deposit (SID). The Gamagara Formation shales and quartzites are expected to unconformably overlie the underlying iron ore or BIF based on the regional geology presented in the previous chapter. The presence of an angular unconformity was not observed though in neither of the SLT cores, possibly due to present heavy fragmentation. At this point it bears mentioning that the ferruginous shale part described above was not sampled or further studied but macroscopic properties proved to be very helpful with the identification of the shales and their discrimination from BIF-derived massive ore. The total absence of banding, the reddish or brownish colouration and the brittleness which is expressed by the possibility of breaking by hand are features shared only by the ferruginous shales. The specific weight is also a nice tool for the determination of the relative iron-enrichment with higher values implying higher enrichment. Additionally, whole-rock geochemical data shared by Kumba Ltd. show high aluminum and potassium values reaching up to 17.4 wt. % and 4.1 wt. % respectively in ferruginous shales while in the shaley ore aluminum reaches up to 4.6 wt. % and potassium up to 1.1 wt. %. Such high values in these two elements are not observed lower in the stratigraphy from the point that the main iron orebody is found and they further represent the clay minerals present which provide the more reddish colours to the shaley ore compared to the typical bluish grey of the BIF-derived iron deposit (BID). Towards the bottom of the shale section, two thin (0.5m) horizons of greyish green igneous rocks intersect the shales showing sharp fault contacts and evidence of slickensides. The bottom fault contact also marks the top contact of the main iron orebody which is developed for ~100m (166-260m) and it can be broadly subdivided into two types based on macroscopic properties.

The first type comprises a massive ore that commonly shows impressions of irregular and discontinuous thick banding of alternating brighter metallic grey and darker dull grey hematite bands. Rarely, this ore can be also highly brecciated in places with hematite clasts mostly being large, although some mm-size clasts can also occur and cemented primarily by specular hematite and lesser quartz. The second ore type can be broadly defined as brecciated and its distinct feature is the small to medium scale irregular portions (~5-20 cm) of unenriched rock contained within it. The lateral restrictions which result from working on core do not always allow for the outlines of these unenriched or more precisely “less enriched than the ore” portions to be constrained. Nevertheless, when observed, the contacts of these two are generally very sharp. Indications of alteration textures are rare and of very small scale. These ore “impurities” are highly variable in terms of texture ranging from enriched (up to 60 % Fe_2O_3) dark red portions which resemble remnant banding, white to pinkish grey quartz chunks or bands frequently exhibiting secondary brecciation by specularite which develops from small scale micro-breccias to larger scale breccias with angular quartz clasts, to finally silica-rich portions or BIF-like remnants with alternating banding in very sharp contact with the hematite matrix. A peculiar texture of such BIF-like fragments giving the impression of floating in the hematite-rich matrix with very sharp contacts to it was scarcely observed. Mineralogical and geochemical study on various unenriched portions (Chapter 3 & 4) led to their verification as BIF-remnants and the name *BIF-bearing impure iron ore* was attributed to this second ore type. It must be also noted that occasionally, breccias in both ore types seem to have been reworked and include more abundant angular silica-rich clasts along with hematite-rich clasts within a fine-grained dark red matrix thus comprising a type of chaotic secondary breccia. Brick-red or even greenish vein-type infills, locally in parallel orientation to the irregular ore banding were also recognized apart from the common specularite veining which mostly shows cross-cutting relationships to earlier textures. Furthermore, small crystals of pyrite were noticed in hand-specimen within small vugs.

The iron ore gradually gives way to a less enriched section of ~30m (260-289m) which cannot be labeled as an iron ore using economical terms. It texturally resembles the

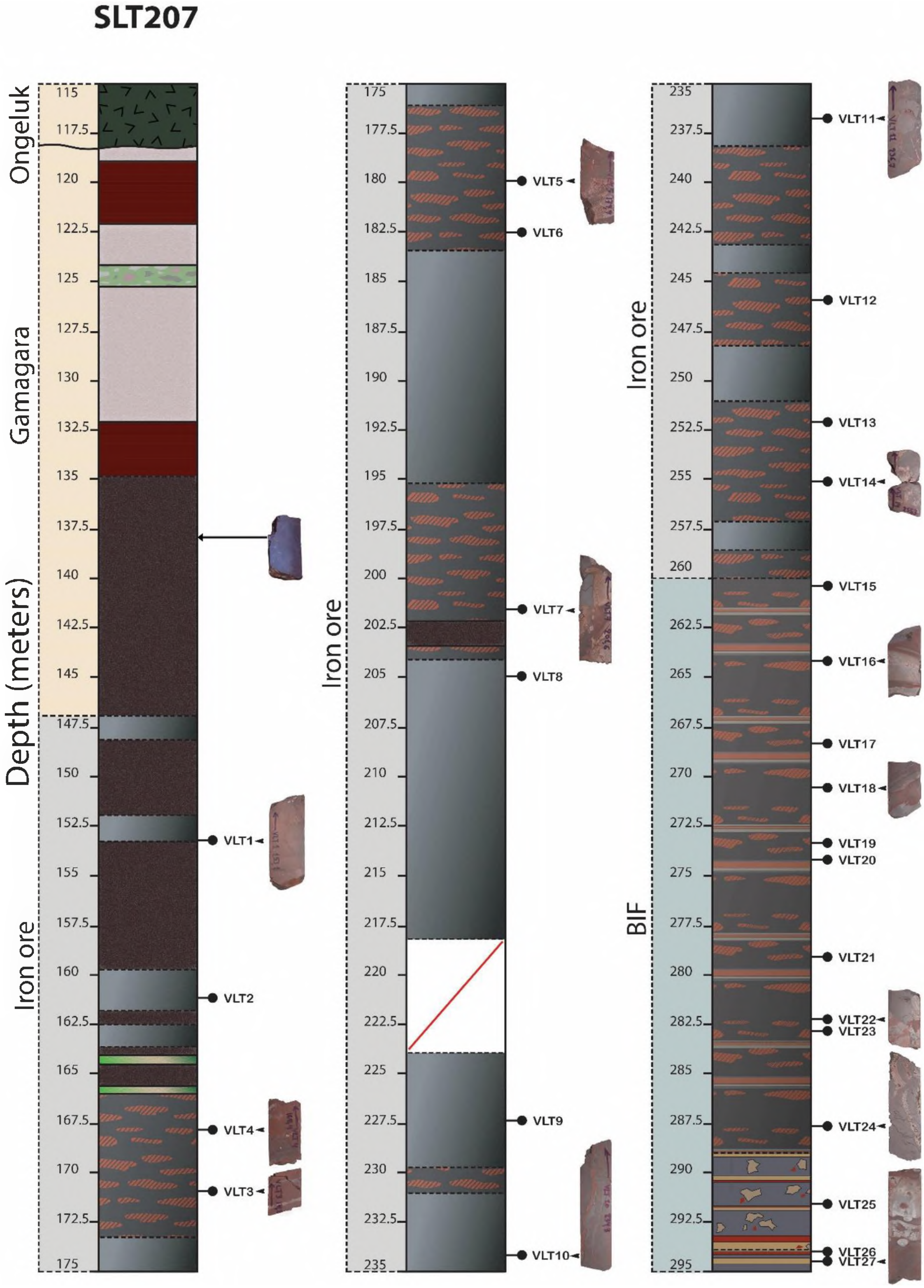

Figure 2.1. Stratigraphic log of drill core SLT207 continued in Figure 2.2. Legend describing lithologies can be found in Figure 2.3 as well as in the Appendix I.

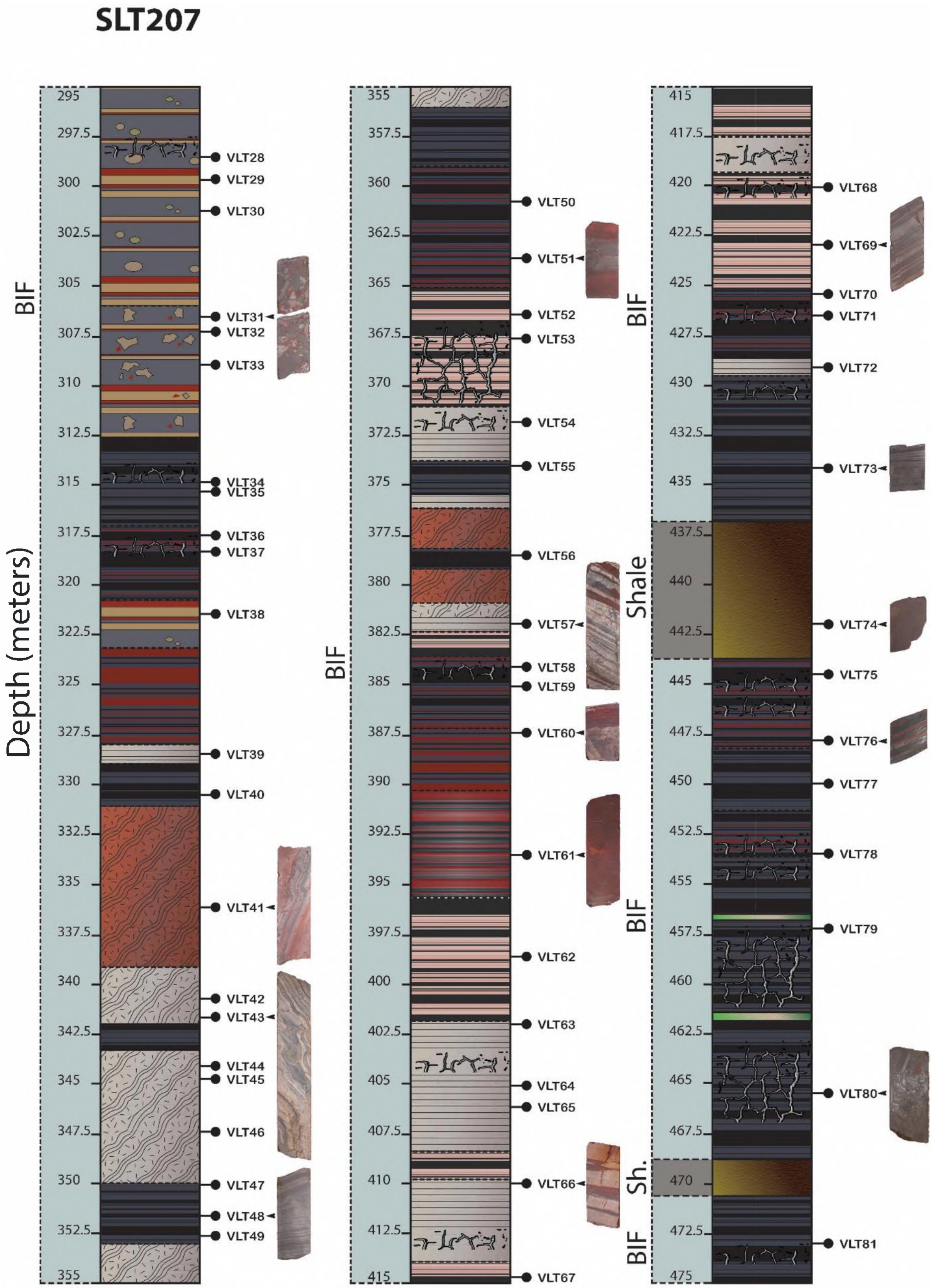

Figure 2.1. (continued) Stratigraphic log of drill core SLT207. Legend describing lithologies can be found in Figure 2.3 as well as in the Appendix I.

BIF-bearing impure iron ore found above it but the unenriched fragments here become more common and the banding more pronounced. This breccia with *highly enriched Fe-matrix and BIF-clasts* composes the transitional lithology between the iron ore and the Manganore BIF below. At ~289m, this lithology gradually changes into brecciated BIF with abundant lensoidal textures or pods which consist mostly of siliceous material and occasionally breccias with poorly sorted angular clasts of later origin. This part gives way to laminated BIF of grey-coloured alternating bands at ~312.5m. It is at this point that continuous and dominantly undisturbed rhythmic mm- to cm-scale banding becomes the main distinctive feature of the BIF. It appears that there is a general increase-downward trend of microlamination with micro-bands being more common than meso-bands, a characteristic that strongly resembles the pristine Kuruman Iron Formation. The laminated BIF are represented by different horizons of generally ~ 5 meters in thickness which are characterized by different colouration of banding (amount of hematite or quartz present), intensity of colouration and appearance or not of metallic luster. It must be noted that there are small variations of the above characteristics in each of these horizons but still the defining characteristics are dominant. Brecciation is more intense in specific parts of the stratigraphy where veins are also more abundant; however no relationship with lithology or any structural feature was recognized.

One very conspicuous characteristic of the BIF is the presence of siliceous rocks concentrated along horizons. The transition between the laminated BIF and these siliceous horizons is fairly abrupt. The silica-enrichment is easily recognized macroscopically by different attributes such as specific weight and pale colouration but it is expressed by very distinct textures. Layering is a feature shared nearly by all siliceous rocks of this core although it can be disrupted in many cases where clear replacement textures are developed. One of the most pronounced textures is that of undulating banding of alternating colouration and thickness in vertical orientation across the core. Even on a core-specimen scale greenish and brownish minerals can be observed. The term silicified BIF will be used to describe these rocks since ample evidence for silica addition were found during their meso- and microscopic study. Generally, three silica-rich horizons stretching for ~5 to ~15 meters accommodate the majority of silicified rocks in this drill core. Another feature of the laminated BIF is the occurrence of meter-thick portions exhibiting intense reddish colouration and occasionally metallic luster. These parts seem macroscopically very iron-rich. Finally, thin slices of dark grey-brownish shales seemingly ferruginous are found in sharp contact to laminated BIF in high stratigraphic depth (~437.5-443m and ~469-470.5m). Closely above the shale intersections, greyish green rocks of less than half a meter in thickness, reminiscent of the ones marking the transition from ferruginous shales to the main ore body occur.

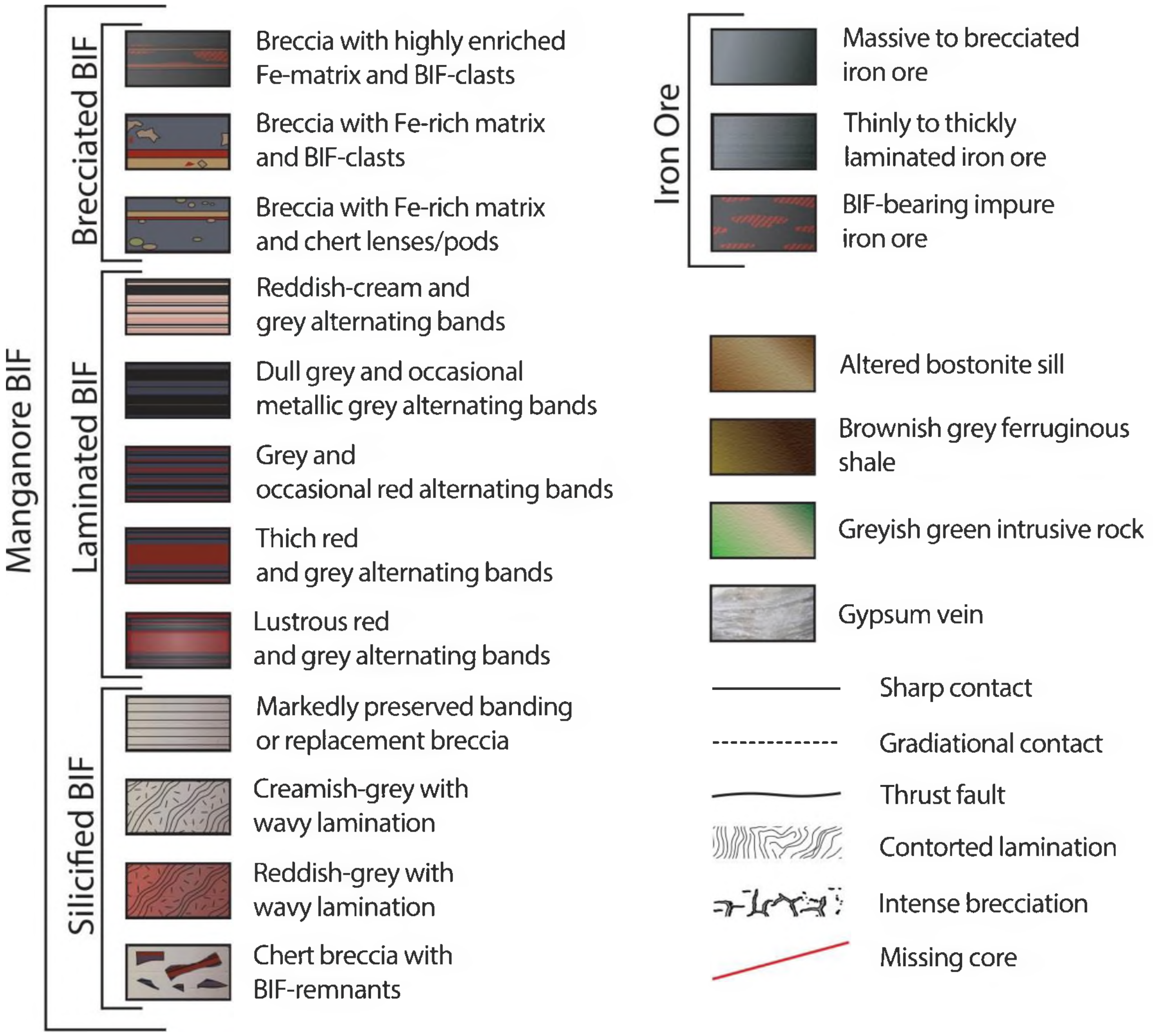

Figure 2.3. Detailed legend for all stratigraphic logs of this chapter.

2.2.2 Drill core STL284

Most of the observations described above apply also for drill core SLT284 which has essentially similar stratigraphy with SLT207 despite the comparatively thinner profile of the BIF that was drilled (~133m) and the smaller variety of textures exhibited. Some of the main differences are the following: i) the main iron ore body is again intercalated with ferruginous shales but shows less "impurities" while the transition from iron ore to the underlying laminated BIF is more abrupt than in drill core SLT207. This transition is expressed by brecciated BIF with Fe-rich matrix and abundant chert lenses/pods which resemble the Griquatown iron-formation. ii) Occurrences of easily observable gypsum veins and breccias of considerable thickness (up to ~1m) are found within the brecciated BIF in the direct footwall of the iron ore as well as nearby horizons of silicification. iii) Some different textures are observed concerning the silicified BIF such as silica-rich rocks containing “floating” BIF fragments.

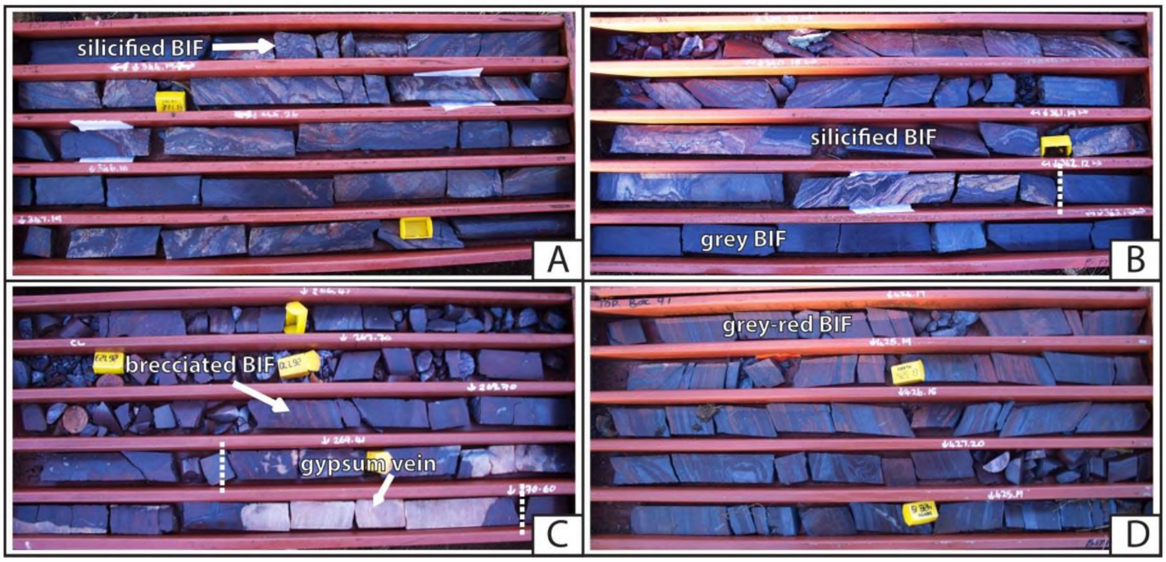

Figure 2.4. Core boxes from drill cores SLT207 (A, B and D) and SLT284 (C) illustrating diferent attributes observed in the BIF.

2.2.3 Drill core SA2491E - Sishen

The studied drill cores from Sishen generally display different attributes in comparison to the drill cores from the Kumba exploration camp. The two sampled cores show a much thinner profile of BIF exhibiting much lesser textural variations. In SA2491E, the bottom of the drill core is at a depth of ~340 m below surface. Ongeluk lava is found thrusted on top of the Gamagara Formation which is represented by a considerably thicker and more texturally variable stratigraphic profile consisting of pinkish white to grey-black quartzites, greenish white shales, red shales with white laminae, an horizon of thinly laminated ferruginous sandstone and finally the ferruginous breccia of Doorfontein. The latter is only developed in this core for ~2 meters and contains some slightly roundish unenriched BIF-clasts along with rounded iron-rich pebbles within a hematite-rich matrix. The beginning of the iron ore is marked by a fairly abrupt contact with the overlying conglomerate at a depth of ~245m. The upper two meters of the iron ore show a massive appearance and then gradually lamination is starting to develop. Further below, an intrusion intercepts the laminated ore and displays sharp contacts to it. This intrusion is locally known with the informal name bornite and has been altered to a clay-rich rock-type containing sericitized feldspar crystals in a matrix of hematite, calcite, muscovite, chlorite and quartz (Van Schalkwyk and Beukes, 1986). Highly altered pre-Gamagara mafic sills and dykes that have intruded prior to mineralization are common in Sishen deposit and have been also reported from the Sishen south at the other extremity of the Maremane dome (Carney and Mienie, 2003).

The bottom contact of the iron ore at a depth of ~260m is marked by the appearance of laminated BIF which stretches for approximately 80m and is intercepted by another two horizons of laminated ore. The laminated BIF is broadly microbanded with alternating cherty and oxide-rich bands. Within two thin intersections enrichment in silica can be observed (at ~267.5 and ~280) and is mainly expressed by conspicuous replacement textures. The main iron ore body begins at ~289m and it exhibits pronounced microlamination for almost 12 meters. Some brecciation occurs in places, expressed mainly by wrinkling of banding but the iron ore broadly preserves the typical laminated texture. Specular hematite occurs in fractures, such as veins and secondary pore-fillings within the ore body. Quartz or calcite veins are also seen in cross-cutting relationship to lamination of the ore. Closely to the bottom contact of the laminated ore with the underlying BIF three thin intervals of unenriched or less enriched BIF are found. The appearance of these BIF-slices suggests that there is a grading from the unenriched BIF to the iron ore. From that bottom contact of the ore body at ~310.5m and till the end of the core at ~340m, laminated BIF of monotonous appearance occurs. Only for an interval of ~ 4m (~324-328) there is a sense of more abundant grey (hematite-rich) banding and less cherty material.

2.2.4 Drill core SA2072 - Sishen

This core displays essentially the same characteristics as the previous one. The Doorfontein conglomerate exhibits a significantly thicker profile right above a core loss which occurs for about ten meters. The main ore body is conspicuously laminated and undisturbed for almost 30 meters. The laminated BIF occurs only for ~ 13m below the laminated iron ore and is rather monotonous. Nevertheless, right below the ore, the BIF shows no sign of lamination for ~ 1m and is silica-rich which highlights the importance of examining the BIF in closer detail.

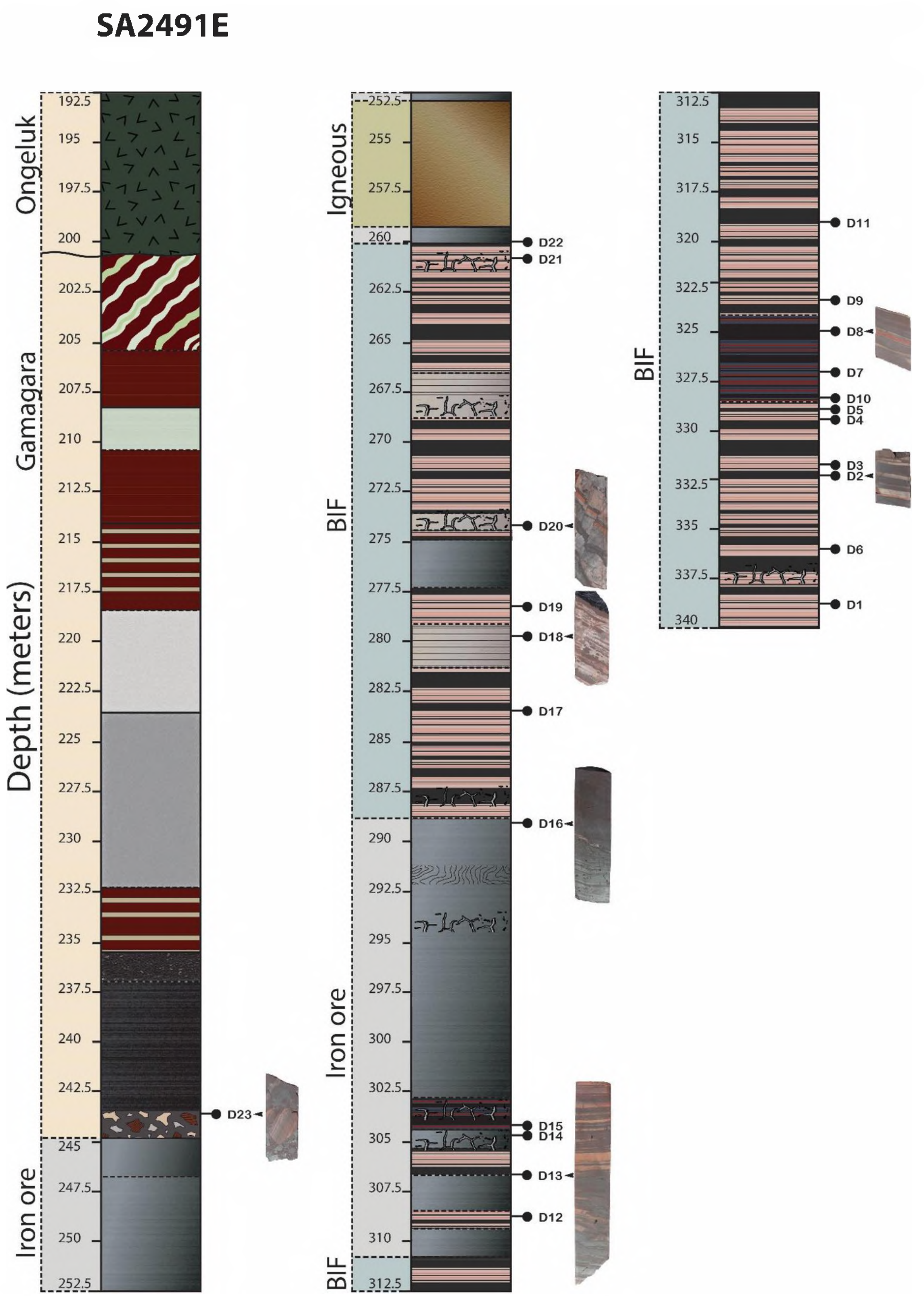

Figure 2.5. Stratigraphic log of drill core SA2491E. Legend describing lithologies can be found in Figure 2.3 as well as in the Appendix I.

2.3 Sample selection, petrographic description and classification

A total of 158 samples were collected from the four drill cores, although not all were further processed with analytical methods. The bulk of the sampling was carried out on the SLT cores (129 samples) while the Sishen cores were only included later in the study (29 samples) as a proxy of the MIF in the upper extremity of the Maremane dome and were mainly sampled for the purpose of expanding the existing whole-rock geochemical data. Owing to the large thickness of the SLT cores and the excessively wide variation in lithological textures both in the ore and the BIF, high resolution sampling proved to be impossible. Despite that, the selection of samples collected covers a fairly adequate range of BIF textures from the whole stratigraphy, including both relatively homogenous specimens for whole-rock geochemical analysis and texturally or mineralogically intriguing samples with conspicuous brecciation, veins and infills, intended exclusively for petrographic study.

For the purpose of presentation, mineralogical study, textural-geochemical comparisons and investigation of alteration stages the samples were initially grouped according to hand-specimen observations. The basic macroscopic properties that served as criteria for determining the sample groups are textural (brecciation, lamination, hints of banding, lensoidal textures), colour of banding which implies the mineralogical content (quartz/hematite ratio) and finally evident enrichments in either iron or silica that could be followed for a sufficient extent (hematitization, silicification). All the above facilitated the subdivision of the altered BIF in three main groups, namely: laminated, brecciated and silicified BIF. Each of these groups is further subdivided in greater detail into subgroups which outline the distinct predominant characteristics (Fig. 2.6). Since the iron ore was fairly discussed previously in section 2.2 it is not included in the current sample classification. Figure 2.7 illustrates the three main different ore types. Laminated BIF contains the following subgroups which are defined by contrasting alternating bands:

- i) BIF with *reddish/cream and grey bands*, characterized by chert bands of largely cm-scale and scarcely mm-scale alternating with hematite-rich bands of corresponding thickness. The chert bands (creamish) are usually coloured red in a striped pattern producing distinct micro-lamination though sometimes this colouration is more diffused and concentrated at the boundaries with the hematite-rich bands. On the other hand, the grey hematite-rich bands show reddish micro-laminae and rarely can be thick extending undisturbed for 5-10 cm. This type of altered BIF is found to be the most common in the Sishen cores while in the SLT cores its occurrence is of lesser extent.

- ii) BIF with *dull grey and occasional metallic grey bands*, comprising essentially of cm-scale alternating bands showing different shades of grey. BIF composed chiefly of dull grey bands occur only in core SLT207 near or within the silicified horizons and appear to be rich in silica. The presence of alternating metallic grey bands mostly at the bottom of SLT207 core apparently increases the modal abundance of iron as it is also implied by the increase of the specific weight. Reddish- or greyish-white bands of mm-scale can be also present which in most cases represent secondary micro-veining parallel to banding as is was shown by subsequent petrographic analysis.
- iii) BIF with *grey and occasional red bands*, containing abundant grey chert-rich bands or frequently metallic grey hematite-rich bands alternating with lesser mm- to cm-scale red bands. The latter can be either chert-rich showing minor discolouration by hematite and locally clear replacement textures or hematite-rich of darker red colour which along with the grey bands compose a more ferruginous end-member. This lithotype shows a considerable abundance in the SLT cores while its occurrence in only one of the Sishen cores is somewhat equivocal.
- iv) BIF *with red and grey bands*, which differs from the previous mainly in that the distinctive feature being in abundance are the red bands, varying from brick-red to dark red and reaching uninterrupted intervals of 5 cm in thickness. The alternating grey bands are thinner and widely spaced. Once more, this BIF-type is scarcely observed only in the SLT cores.
- v) BIF with *lustrous red and grey bands*, consisting essentially of brick-red bands alternating with only minor mm-scale grey bands. This lithotype appears to be very ferruginous, exhibits a strong luster and is limited only in the vicinity of the red-grey BIF.

It should be emphasized that a separate group of laminated BIF was considered if the distinct feature (colour banding-mineralogical content) was persistent for more than two continuous meters and was found for more than once in the studied cores. Silicified BIF are largely a characteristic of the SLT cores. Textural differences allow for their classification into four subgroups:

- i) Silicified BIF with *markedly preserved banding* which occasionally can be defined as *replacement breccias*. The alternating bands consist almost entirely of quartz and show

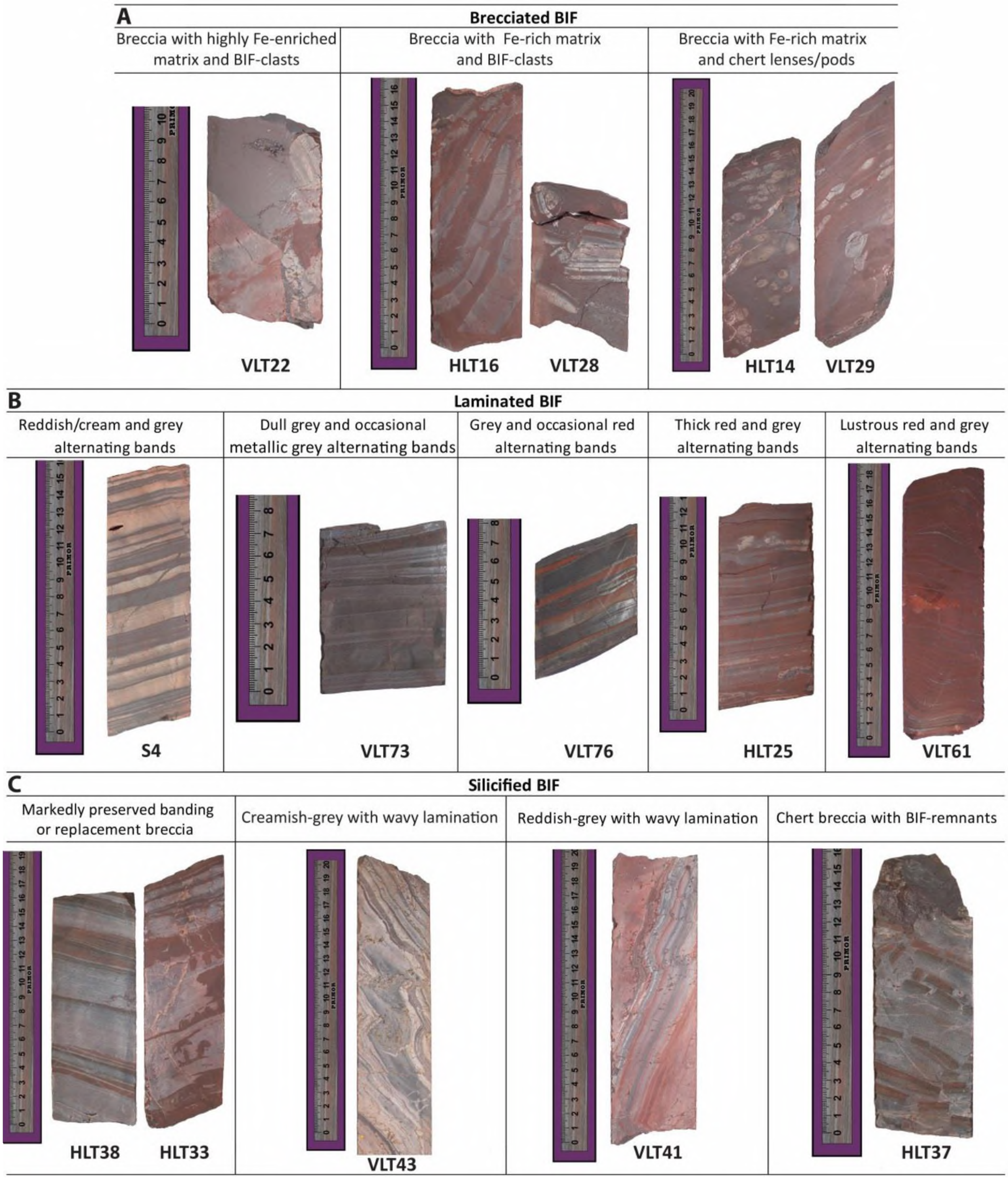

Figure 2.6. Representative photographs covering all three textural sample groups defined, i.e. a) brecciated BIF, b) laminated BIF, c) silicified BIF as well as all the associated subgroups.

contrasting colouration. Grey bands are commonly thicker (of several cm) while reddish-brown bands can be also of mm-scale. Hematite seems generally insignificant and its abundance increases only within reddish or grey bands which appear as being replaced by quartz leaving behind remnants of discontinuous banding. BIF of this type are the most representative of silica alteration found in all cores studied, even though sometimes brecciation is more intense and banding less pronounced. A yellowish-brown mineral occurring mostly within and parallel to banding as well as a green mineral appearing within cross-cutting veins were visible with the naked eye in samples of this lithotype.

- ii) *Creamish-grey BIF with wavy lamination*, characterized by colloform banding alternating with subordinate BIF banding that seems to have been largely replaced by quartz. The colloform-textured quartz shows a variety of colours from milky- or pinkish-white to grey. The wavy appearance is primarily produced by the colloform bands and is enhanced by secondary brecciation that generally dislocates the banding along the fold axes. This brecciation is related to secondary mineralization, easily detectable by the unaided eye. Thick veins showing concentric layering and botryoidal grains of quartz are fairly abundant and in sharp contact to minor but thick hematite-rich areas. A reddish-brown mineral is also noticeable. This peculiar lithotype is found only in the SLT207 core and is closely associated to the dull grey laminated BIF.
- iii) *Reddish-grey BIF with wavy lamination*, sharing broadly the same characteristics with the previous group with the exception of colour which seems to be related to higher hematite content. Despite the slightly red colouration these rocks are light and can be easily identified macroscopically as being silica-rich. As with the previous group this type of silicified BIF is observed only in the SLT207 core.
- iv) *Chert breccia with BIF-remnants*, characterized by siliceous BIF-fragments that compose a discontinuous or fragmented banding. The BIF-remnants are abruptly fragmented showing no sign of replacement and dislocation and/or rotation is mostly minor so that one can easily trace back the original position of the fragments. It appears that cross-cutting coarser-quartz veins might be responsible for the formation of this breccia although these are not always easily visible owing to their same colour. Rocks of this type are only observed in the SLT284 core.

Finally, brecciated BIF are distinguished into the following subgroups:

- i) Breccia with *highly Fe-enriched matrix and BIF-clasts*, containing unenriched or even siliceous BIF-derived fragments usually in sharp contact with enriched up to iron ore quality hematite-rich matrix. Irregular bands of several cm in thickness occur in places and consist of either reddish-white siliceous material or more hematite-rich red material. Specularite veins and vugs are also quite common. As discussed earlier in section 2.2.1 the only difference between this type of brecciated BIF and BIF-bearing impure iron ore is the higher content of BIF fragments as well as of irregular banding intervals shown by the first so that it cannot be considered as high-grade iron ore under today's standards. This lithotype occurs in a strict sense only in core SLT207 while in SLT284 the transition from ore to BIF is comparatively more abrupt.

- ii) Breccia with *Fe-rich matrix and BIF-clasts*, comprising of BIF-fragments or individual BIF-bands, both of which are commonly silica-rich, within a hematite-rich matrix. Grey colouration in the matrix implies a higher iron-content while red colour indicates the presence of a fair amount of silica. Intervals where irregular banding prevails are common. Replacement textures of red iron-rich material replacing grey or greyish-white siliceous material are also observed. Brecciated BIF of this as well as of the next type are present in both SLT cores always below the ore and above the laminated BIF. Detailed petrographic investigation showed that siliceous portions with vague outlines and irregular shapes might be also considered to an extent as secondary, indicating silica mobilization also in this part of the stratigraphy as it is discussed later.
- iii) Breccia with *Fe-rich matrix and chert lenses/pods* characterized mainly by the presence of lensoidal structures within a grey or reddish hematite-rich matrix. The lenses can be of mm- to cm-size, vary from roundish to very elongate and are chiefly composed of silica although rarely red lenses within a white siliceous matrix are observed. Occasionally, smaller angular fragments occur within the lenses. A well-developed fabric of red micro-laminae regularly wrapping around lensoidal structures is an additional feature that can be seen with the naked eye.

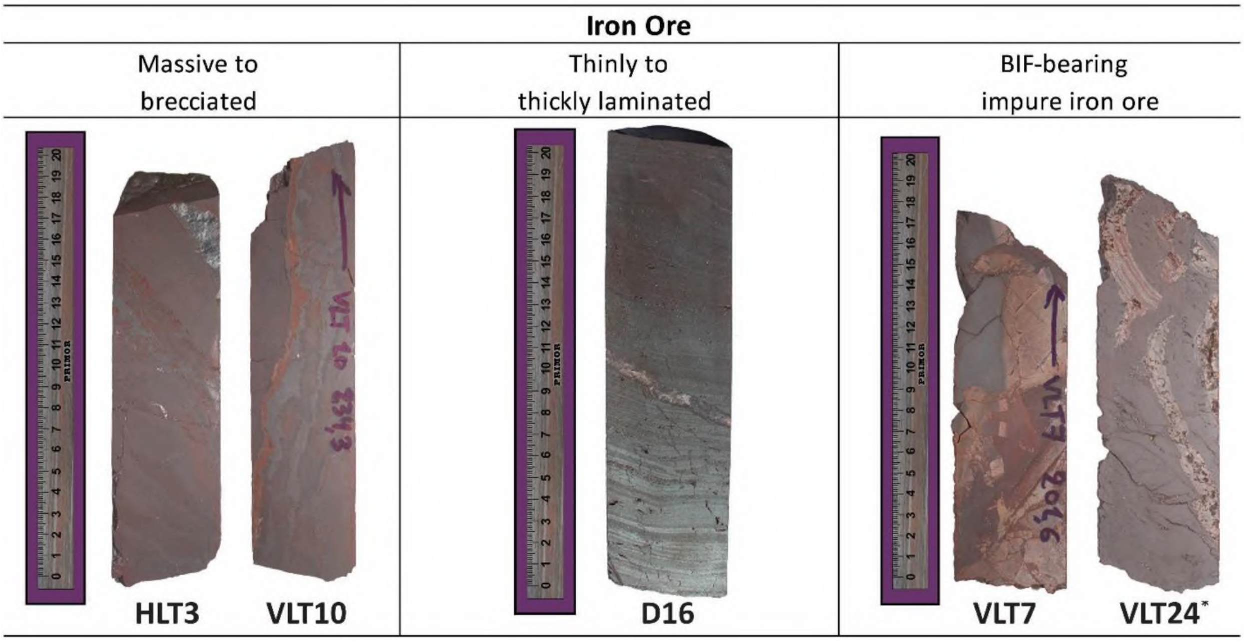

Figure 2.7. Representative photographs of the three main iron ore types.

The brecciated BIF discussed above are very inhomogeneous and do not constitute typical, for example crackle or mosaic breccias that can be described and classified easily using existing schemes. These rocks preserve a variety of textures that resemble the primary ones found in the BIF, such as the chert lenses and the banding but are now altered apparently by metasomatic processes. Their formation also seems to precede that of other later hydrothermal breccias found within these same lithotypes or lower within the laminated BIF. Finally, their overall appearance is completely different from the laminated BIF below and their occurrence is always transitional from the iron ore to laminated BIF. Typical hydrothermal breccias where one can characterize as matrix- or clast-supported or fairly accurately describe the shape, size and composition of matrix and clasts, are commonly found with the MIF but are excluded from the above classification since they definitely have formed later and consequently are discussed separately. It should be further noted that there is no intention of the author to recommend the aforementioned classification as a formal scheme for wider use. Its role is restricted within the borders of this study and it will form the ground for the petrographic discussion in the next chapter while it will also constitute a useful tool for geochemical-petrographic comparisons and the synthesis in the final chapter.

2.4 Summary

Detailed logging and macroscopic observations on the Manganore iron-formation from four different cores deriving from two separate regions reveal differences concerning mainly: i) the thickness and variability of textures of the overlying Gamagara Formation, ii) the occurrence or not of ferruginous shales intercalated with the iron ore, iii) the appearance of the iron ore bodies which ranges from laminated to massive or brecciated in places, iv) the occurrence or absence of igneous intrusions, v) the textures presented by altered BIF which are closely related to the members of the pristine BIF which are present, vi) enrichments in silica or iron in certain intersections which are expressed by different textures vii) the intensity of brecciation and the presence of vein and open-space infill material. Despite the excessive brecciation and wide variation in textures it is evident from the first observations that the MIF bears strong textural resemblance to the pristine Griquatown and Kuruman BIF in its upper and lower stratigraphy respectively.

The conspicuous lack of basic petrographic data from the MIF can be attributed to the high degree of alteration, intense brecciation and textural variety which may discourage detailed logging and sampling. A thorough petrographic analysis is presented next based on the sample groups defined earlier. The reader is asked to show patience during the pages of the following chapter since it holds key information on the alteration of the MIF and is crucial for understanding the complexity of the successive and ongoing processes that might be also intimately connected with the ore genesis. Table 2.1 presents simplified terminology for laminated BIF which keeps only the basic colouration features for brevity and is chiefly used in the next chapters.

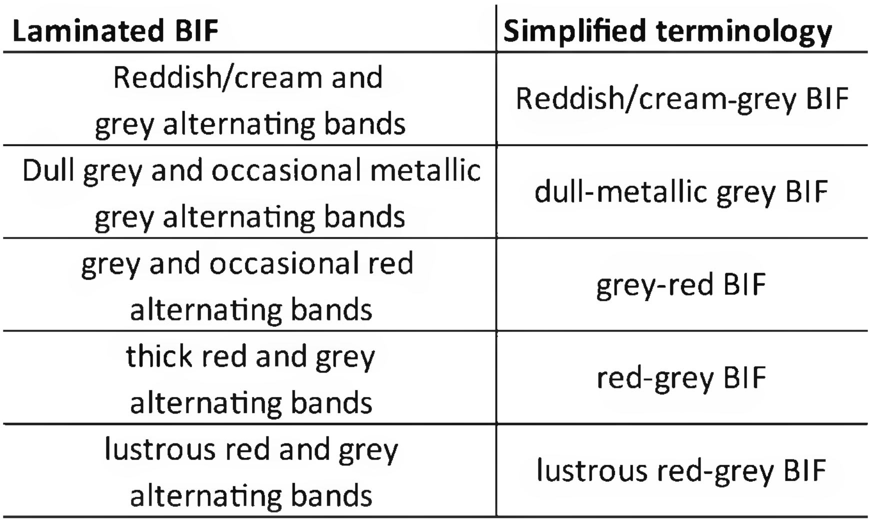

Laminated BIF	**Simplified terminology**
Reddish/cream and grey alternating bands	Reddish/cream-grey BIF
Dull grey and occasional metallic grey alternating bands	dull-metallic grey BIF
grey and occasional red alternating bands	grey-red BIF
thick red and grey alternating bands	red-grey BIF
lustrous red and grey alternating bands	lustrous red-grey BIF

Figure 2.8. Table displaying simplified terminology for the defined sample groups used in the next chapters.

Petrography

Chapter 3

3.1 Analytical methods

The petrographic characteristics of the Manganore iron-formation were studied on polished thin sections which allowed for microscopic investigations to be conducted under both transmitted and reflected light. Sample selection was based upon a number of macroscopic criteria which focused on covering as much textural varieties as possible, encompassing domains that exhibit vein and vug-filling material and finally including representative samples from all the macroscopically determined groups. X-Ray diffraction (XRD) analysis was performed on powdered samples selected from the same material used in the whole-rock geochemical investigations (see also section 4.1). Diffraction patterns of 23 samples revealed only the presence of quartz and hematite, since other mineral phases proved to be in very low modal abundance within the bulk-rock powders. Three separate powders prepared only for XRD analysis allowed also the detection of gypsum. It is noteworthy that neither quartz nor hematite were detected by XRD in most iron ore and silicified BIF samples respectively. Identification of other mineral phases was done mainly by means of energy dispersive spectrometry (EDS) on a scanning electron microscope (SEM). Spot analyses were performed using this set-up in order to determine qualitatively the different mineral constituents encountered. SEM studies formed an extremely useful tool not only for identifying the plethora of the accessory minerals presented in this chapter but also for allowing meticulous descriptions and was decisively found to be the most effective way to fathom the petrography of such fine-grained rocks. Electron probe micro-analyzer (EPMA) techniques were later adopted for element mapping and quantitative mineral chemical analyses. A total of 66 thin sections were studied using standard optical microscope and 30 of these sections were also investigated under the SEM. The author had also access to a large suite of thin sections from Kuruman and Griquatown iron-formations which were examined for comparison purposes. Further detailed descriptions of instrument specifications and analytical techniques applied are available in Appendix II.

3.2 Hematite and quartz in the MIF - Classification of different forms

The Manganore BIF and iron ore are essentially composed of a binary mixture of quartz and hematite in agreement to what has already been documented by Van Schalkwyk and Beukes (1986). As much as diversity in quartz forms can be easily recognized and characterized, identification of the different hematite varieties proved to be more demanding. The challenge arises because of its largely very fine nature, it's intricately and densely arranged crystals in conjunction with the first and finally the lack in literature, to the author's knowledge, of a detailed and comprehensive classification of the distinct habits encountered in high-grade iron ores and protores. Classification schemes for hematite in iron ores have been produced to some degree only by Morris (1985). The generation of a formal scheme of classification following for example that of Van Deventer (2009, MSc Thesis) and Mukhopadhyay et al. (2008) while at the same time incorporating iron oxide generations from a large number of ore localities, accompanied by thorough and descriptive terminology, would prove very valuable in high-grade iron ore studies, however this is beyond the scope of the present study.

According to crystal size, hematite in MIF is subdivided in three groups, namely: crypto (< 4μm), micro (4-50μm) and fine (>50μm). Hematite of micro-size is further subdivided into platy and crystalline. In general, platy habit is the most commonly encountered in iron ore regimes. Microplaty hematite occurs as flattened and thin crystals of equant to subequant hexagonal shape. Different orientation of platy crystals produces shapes from spindle to splinter or needle-like which can be easily discriminated under microscopic examination. Individual hematite platelets are rather scarce contrary to bundles or laths of small micaceous plates which is the norm. In such aggregates, microplaty habit can locally be discerned, especially when hematite is pseudomorphing preexisting minerals. On the other hand, microcrystalline in this study, is a term employed for aggregates where individual crystals are hard to discern. Even though hematite aggregates may be composed of very fine and densely packed platy-like crystals it is considered preferable to describe them as an assemblage since their origin and formation might differ from coarser and easily distinguishable microplaty crystals.

Fine-grained hematite is also platy to tabular or bladed when its c axis is more elongated and is widely known as specularite (Hagemann et al., 2008). It commonly occurs as paragenetic late hydrothermal vein or vug infill providing a metallic luster on the macroscopic scale while in terms of size can be as coarse as one or more millimeters. The cryptocrystalline variety is characterized by tiny white specks within quartz observed under reflected light and by the abundant internal reflections easily noticed in the impregnated chert. Martite, which is a term used to describe the product yielded upon conversion of magnetite into hematite (e.g. Cornell and Schwertmann, 2003), is quite common and exhibits either dense and solid textures or more hollow and skeletal ones where only the crystal outline is preserved. Finally, hematite in the MIF may occur in granular or spheroidal form which typically shows sizes of less than 50 microns. The main hematite forms present in the Manganore iron-formation are depicted in Figure 3.1.

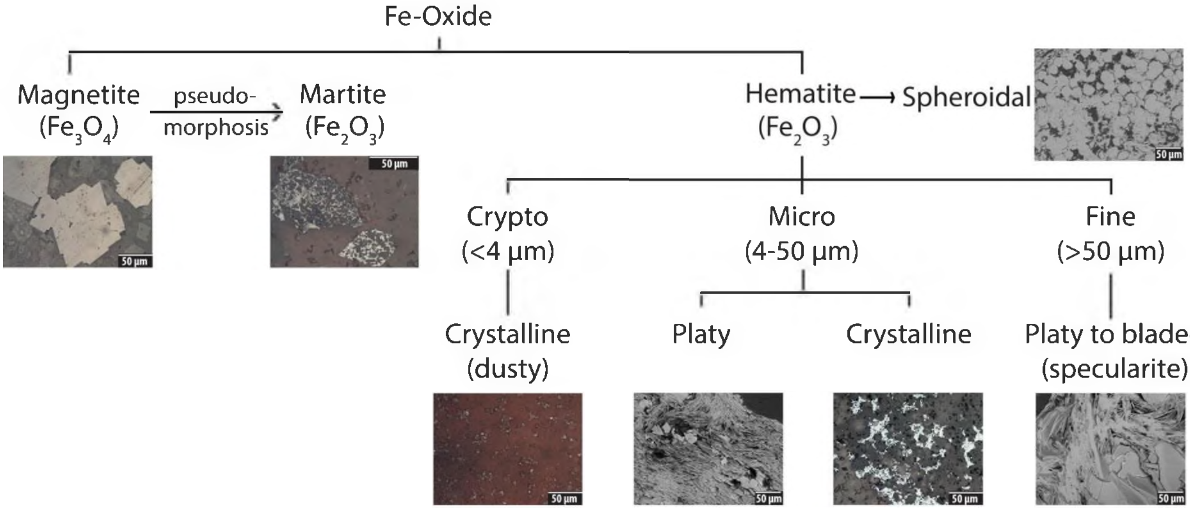

Figure 3.1. Textural generations of hematite present in the Manganore iron-formation defined by differences in shape and size. Magnetite shown here is from the Kuruman iron-formation and was never found in the studied rocks. This informal scheme was developed only as an auxiliary tool for this thesis and was crudely based on a corresponding scheme found in the MSc Thesis of Van Deventer (2009), hematite grain sizes used in other studies (e.g. Figueiredo et al., 2008), as well as on observations made by the author. A **larger version** of the current figure is available in Appendix II.

Quartz in this study is also subdivided in three groups according to size, namely: crypto-, micro-, and macrocrystalline. This subdivision depicts only the relative changes in crystal size and does not intend to use numerical values to strictly define each group. Following the old classification schemes, as cryptocrystalline is defined quartz which structure cannot be resolved in an optical microscope and is common in silicified BIF as it will be shown later. The microcrystalline variety displays a range of grain sizes commonly in groups of 5-10µm, 40-50µm or even grains of 100µm or more. Generally, it shows the characteristic “cherty” appearance seen in most unmetamorphosed or slightly metamorphosed iron-formations around the world, though in places it can be considerably coarser. Comb-textured quartz which is quite common in the MIF is considered as microcrystalline sensu lato. Finally, as macrocrystalline is characterized quartz that conspicuously stands out showing sizes of 500-1000μm or more than 1mm, sub- to euhedral crystal faces and usually forms as cement in breccias.

Chert is a term widely used in iron-formations and in this study is preferred only when describing layering or banding. This term is not so strictly defined and has been associated among other things with dense varieties of quartz showing chemical impurities which have been embedded during its formation and cause a noticeable colouration. Hence it is utterly suitable when describing bands consisting almost always of both quartz and hematite even if the latter is sometimes in negligible amounts. Additionally, the terms mesoband(-ing) or lamination and microband(-ing) or microlamination are employed to describe banding of millimeter to centimeter scale and banding of submillimeter scale respectively, in correspondence to similar use in band nomenclature in other iron-formation studies (Trendall, 1965a, Beukes and Gutzmer, 2008).

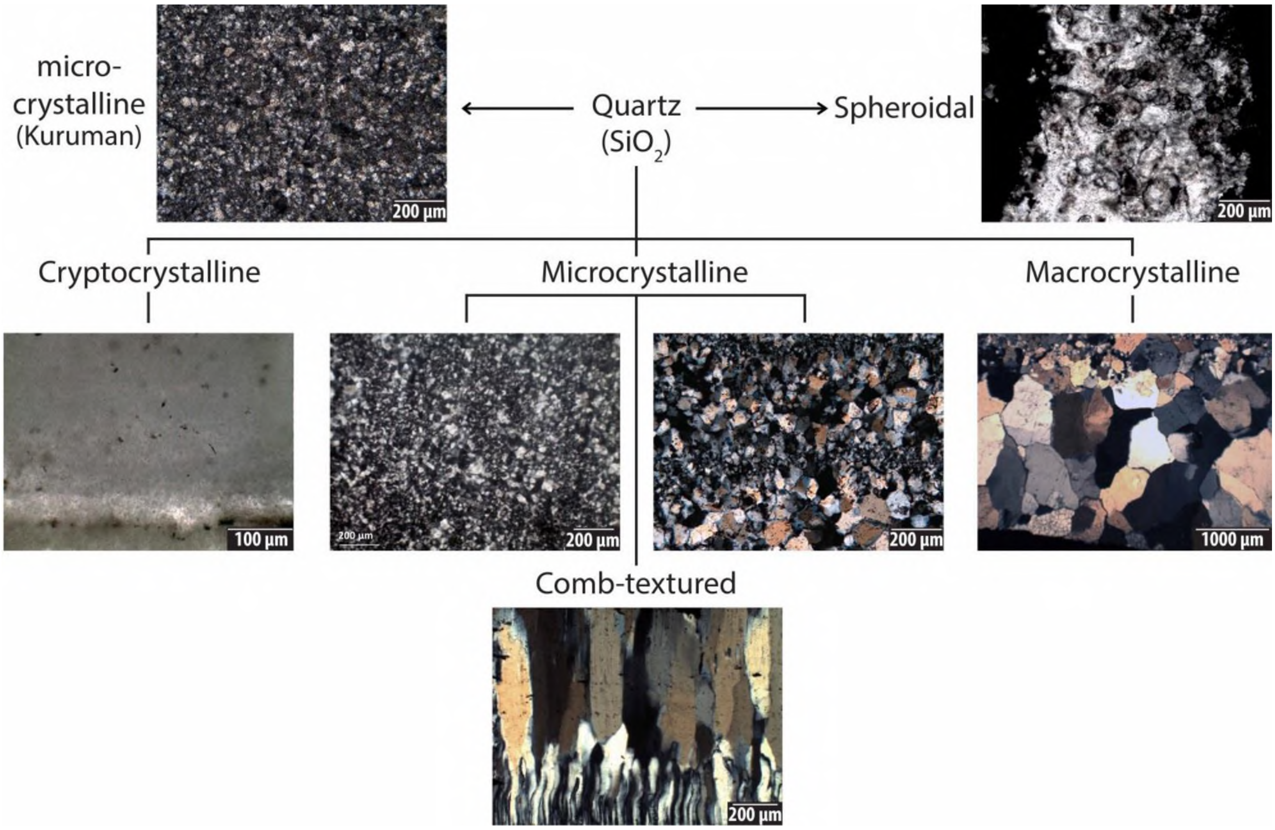

Figure 3.2. Different forms of quartz as seen in the Manganore iron-formation. The most commonly observed is that of microcrystalline quartz which strongly resembles the typical “cherty” appearance seen in most iron-formations around the world. The upper left image depicts this common occurrence of quartz in Kuruman iron-formation, possibly together with stilpnomelane which provides the

Figure 3.2. (continued) brownish colouration. Despite that, coarser varieties as well as cryptocrystalline quartz are not nearly rare, especially in silica-enriched BIF, veins and breccias.

3.3 Mineralogy and petrographic textures

The extensive section presented below forms the main body of the thesis and displays the obtained petrographical data in great detail. Although the use of interpretation is generally not recommended during data presentation, the role of interpretive passages within the text was believed to be important for three reasons: i) to examine things that would otherwise be impossible to bring back and discuss in the final chapter due to the extremely large number of different textures recorded and furthermore without the use of microphotographs, ii) to render this chapter as a mean of recording of most of the observations made during the protracted period of microscopic examination of these rocks which will further serve as a database for future studies and finally ii) to allow the text to breathe since plain description can be quite heavy at times and the reader can struggle. A plethora of microphotographs and selected microprobe analyses are included to support the text and illustrate the most representative and interesting features of these rocks.

3.3.1 Laminated BIF

Laminated BIF are mainly discussed through the first group since the main features are quite similar for the others and only the essential differences regarding the colouration of the banding or any additional features are further mentioned in the following groups.

BIF with reddish/cream and grey alternating bands

Cherty mesobands of cream to reddish/cream colour are composed primarily of microcrystalline quartz and regularly contain microbands of microcrystalline or microplaty hematite and/or occasionally martite. Quartz exhibits bulging recrystallization along grain boundaries which is clearly noticeable even in the finer-grained areas. The sutured contacts between quartz grains denote the very low grade metamorphism that has affected the protolith (Passchier and Trouw, 1996) although later recrystallization during the subsequent alteration cannot be excluded, especially where grains are comparatively coarser within marked lensoidal domains or in entire bands (Fig. 3.3, D). The different grain sizes quartz displays range from 5-10μm grains, which comprise the bulk of the chert mesobands, to 30-

50μm crystals that commonly form abundant lensoidal structures parallel orientated to the banding or are associated with chert mesobands rich in hematite microlaminae.

The distinct pigmentation of the chert bands is a result of finely disseminated hematite while the intensity of the colouration relates to the abundance and morphology of hematite crystals. The term *jasper* has been used to describe rocks in iron ore regimes consisting of microgranular quartz of reddish colour which is caused by iron inclusions (Hagemann et al., 2008). This term though is not preferred in this study since more importance is given to the mineralogy and precisely to the different habits of the quartz and hematite constituents. Hematite occurring as irregular to subrounded clusters of microcrystalline grains in the interstices between quartz, as thinly disseminated microplates or rarely as tiny inclusions in quartz (Fig. 3.3, entire E) does not impart any significant reddish colouration to banding. Brownish-stained quartz is usually found close or in contact with hematite microbanding and seems to be associated with the presence of dusty hematite suggesting iron mobilization during alteration (Fig. 3.3, A, inset). Transport of iron during the alteration processes is more conspicuous in the reddish chert mesobands where abundant dusty hematite impregnates quartz and possibly replaces or leaches it (Fig. 3.3, entire D). It is noteworthy that this type of hematitization develops in an almost linear fashion leaving in between hematite-poor areas (Fig. 3.3, C), something that might be related to differences in protolith's mineralogy and in the relevant to this porosity which is produced during incipient oxidation and leaching of the BIFs earlier (sedimentary or diagenetic) minerals.

The commonly observed texture of undulating and discontinuous martite or microplaty hematite streaks within the chert matrix (Fig. 3.3, A, inset in B) resembles the characteristic appearance of magnetite overprinting carbonates in the Kuruman iron formation, a texture that supports the widely accepted late diagenetic origin of magnetite (Klein and Bricker, 1977) and is still preserved to a large extent in the MIF. Comb textured quartz is also common in the laminated BIF and develops layers where grains are almost perpendicular to banding (Fig. 3.3, A). Comparable textures exist in the parent rock but quartz crystals are typically more fibrous, finer-grained, not so well-aligned perpendicularly to banding and are usually associated with other minerals, thus it is likely that comb quartz in the MIF is rather of a later origin.

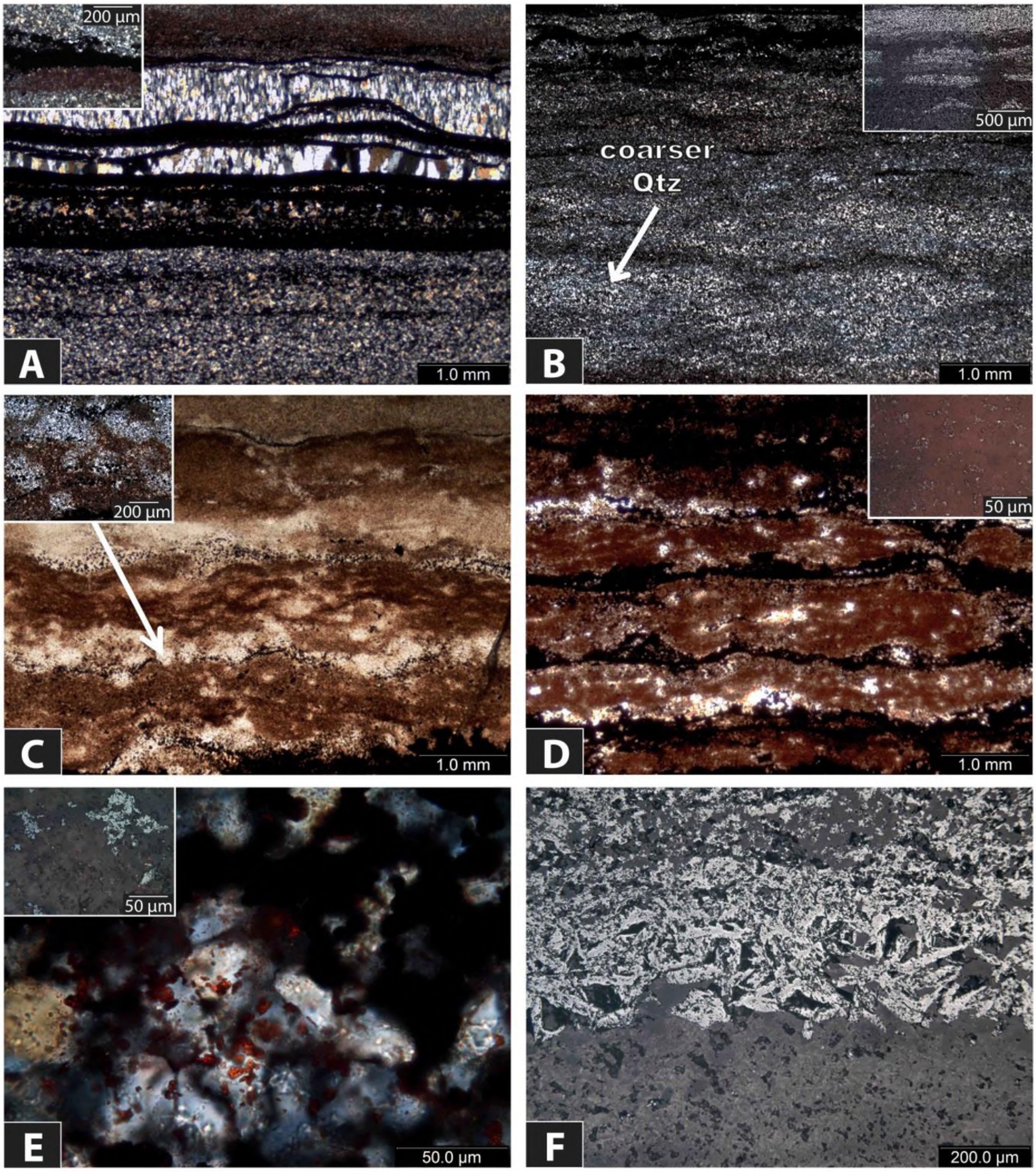

Figure 3.3. All photos were taken under transmitted light except from F and insets in B, D and E which are shown in cross-polarized reflected light. A) Typical hematite macrolaminae in a chert mesoband and associated comb-textured quartz. *Inset*, red-coloured quartz in vicinity of a hematite microband. B) Lensoidal domains of coarser quartz in a chert mesoband (XPT). *Inset*, laterally discontinuous microbands composed mainly of martite. C) Chert mesoband pigmented by dusty and microplaty hematite in a linear fashion and preserved rhombohedral textures resembling markedly those of ankerite from Kuruman iron-formation (PPT). *Inset*, detail in XPT showing the coarser quartz variety of the rhombs. D) Reddish chert mesobands with hematite microbanding. Note the bright areas which represent "ghosts" of carbonates surviving the hematitization (PPT). *Inset*, dusty hematite is responsible for the pigmentation of the chert bands. E) Tiny hematite inclusions in quartz (XPT). *Inset*, same area depicting microcrystalline hematite developing in the interstices between quartz. F) Coarse microplaty hematite in the transition between a chert and a hematite mesoband. Qtz = quartz.

Grey-coloured mesobands are hematite-rich and exhibit dense concentrations of microcrystalline and microplaty hematite. Martite, although not prevalent, can be commonly conspicuous, especially when sparsely set in a contrasting quartz matrix (Fig. 3.5, A). Well-defined bands and laminae with martite that parallels the bedding indicate the relationship with the previous magnetite layering. Quartz is also present in these bands either as grains arranged in narrow parallel strips or as irregular assemblages, intricately mixed with microcrystalline hematite. Despite of the interlocking nature of hematite crystals, closer inspection using scanning electron microscopy reveals the well-developed microplaty habit of the individual hematite grains in these irregular hematite clusters (Fig. 3.5, B). Microcrystalline hematite assemblages could possibly represent martite grains whose original shape has been destroyed by the progressive alteration. However the possibility of hematite pseudomorphing other primary/diagenetic minerals such as silicates or even the presence of authigenic hematite cannot be excluded. The contacts between chert and hematite mesobands range from relatively sharp to more diffuse depending also on the scale of observation. On a smaller scale, the boundaries appear irregularly serrated while most of the diffuse contacts are related to the presence of dusty hematite. Frequently, the contacts are characterized by the development of coarser microplaty hematite (Fig. 3.3, F). Finally, the transition between a hematite and a chert mesoband can be marked by disseminations of martite within the chert progressively becoming sparser, a feature commonly observed in the parent rock.

Apart from martite, preservation of other original BIF textures is quite common and can be easily recognized from the mesoscopic to microscopic scale. One of the more pronounced is that of preserved rhombohedral textures which markedly resemble the carbonate minerals in the considered protolith. These rhombs now consist either of quartz, which is coarser relative to the surrounding finer chert matrix (Fig. 3.3, C, inset) or of microplaty hematite. Both varieties show similar proportion in the laminated BIF as well as identical distribution within the chert bands as that in the parent rock (Fig. 3.5, C).

Carbonates replaced by microplaty hematite can exhibit also skeletal textures (Fig. 3.5, entire D) in which the platelet’s arrangement in parallel planes can be locally seen, since oxidation and replacement tends to follow cleavage patterns. The most common carbonate compositions in the Kuruman iron formation range from that of ferroan dolomite to magnesian ankerite while siderite is less common and very fine-grained relative to ankerite (Beukes and Klein, 1990, Rafuza, Msc Thesis 2015). Therefore the observed rhombs in the

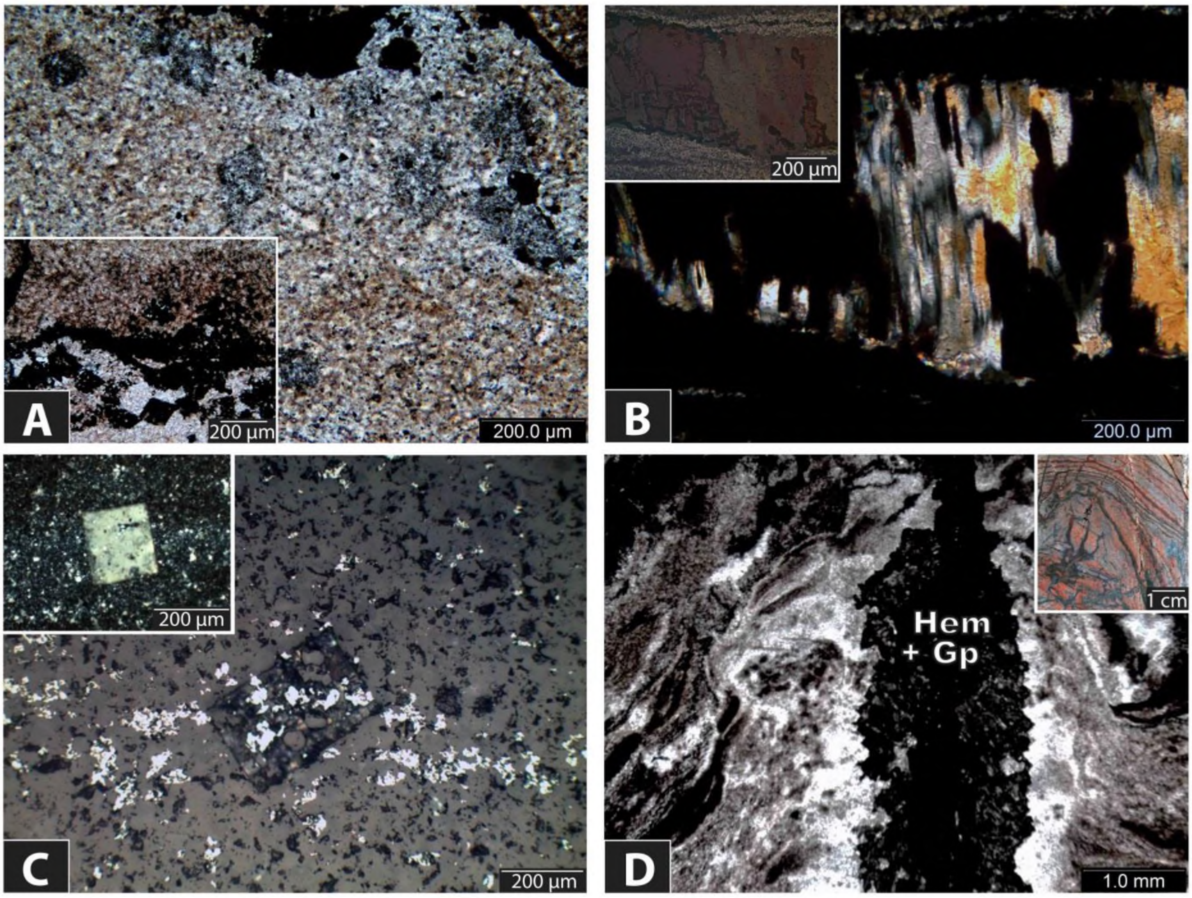

Figure 3.4. A) Pseudomorphs of quartz after possibly ankerite (PPT). *Inset*, the same pseudomorphs being replaced by hematite in the vicinity of a later microplaty hematite vein (PPT). B) Comb quartz showing partial replacement by hematite (XPT). *Inset*, same, hematite seems to be of dusty habit (XPR). C) Euhedral gypsum crystal set in a quartz matrix with disseminated hematite. Note the sharp crystal faces and the lack of vein-feeding channels in the surrounding area (XPT). *Inset*, another gypsum crystal showing quartz and hematite inclusions and/or overprints (XPR). D) Gypsum + hematite vein deforming banding by the development or dilation of pre-existing micro-fractures (PPT). *Inset*, a wider depiction of the same area (rock slab). Hem = hematite, Gp = gypsum.

MIF possibly represent former ankerite crystals which have been metasomatically pseudomorphed, a process that requires at least 50% or more of iron addition (Trendall and Morris, 1983). Pseudomorphs of quartz after carbonates are locally observed to have been partially or fully replaced by hematite in the vicinity of later hematite veins (Fig. 3.4, A). Hematite is also found impregnating and replacing comb quartz crystals which further supports a later iron mobilization (Fig. 3.4, B).

Siderite is very rare comparatively to pseudomorphs of carbonates described above and occurs as isolated grains both in the chert as well as in the hematite-rich matrix. Its size ranges from 100 to 300 microns. Crystal faces are sharp but occasionally somewhat serrated and in the surroundings of some anhedral grains, a lot of tiny dispersed bits of siderite can occur (Fig. 3.5, entire E). Although the scenario of siderite in the laminated BIF representing coarser crystals from the original rock that have resisted alteration cannot be disproved, as it was mentioned earlier siderite is very fine-grained relative to other carbonate counterparts in the protolith. In fact, its small size makes it indiscernible from the associated ankerite most of the times in the Kuruman BIF. The different occurrences of siderite in the MIF are discussed in the following paragraphs and further point to a secondary origin, at least for the bulk if not all of it.

Apatite is mainly found as scarce minute specks within chert while coarser grains or aggregates are usually associated with the rhombohedral “ghost” textures. It either occurs as tiny inclusions within the rhombs or as assemblages overprinting the pseudomorphs (Fig. 3.5, entire F). Coarser and euhedral grains of apatite are found in abundance within secondary microplaty to specular hematite veins brecciating the laminated BIF. Apatite’s distribution pattern points mostly to a secondary origin and suggests co-precipitation of iron and phosphorus from solution or adsorption of phosphorus on the surfaces of the iron oxide (Graham, 1973, Trendall and Morris, 1983). Further details on the different appearances of apatite and its close association with hematite are presented in the discussion.

Common minerals lining open spaces and veins are hematite, gypsum and berthierine. The latter is a relatively scarce iron-rich phyllosilicate, chemically related to chlorites and structurally related to serpentine that is usually associated with ironstones and iron ores (e.g. Rivas-Sanchez et al, 2006, Veena, 2009). The three aforementioned minerals share a strong paragenetic affiliation and the possible mechanisms for their formation involve undoubtedly hydrothermal processes (Fig. 3.6, A and B). Hematite in these assemblages forms randomly orientated microplaty crystals usually not exceeding 50 microns, while minute inclusions of euhedral quartz occur often within gypsum and berthierine. In some cases, small-scale intrusive veins of gypsum and hematite deform lamination in a way that resembles plastic deformation on mesoscopic observation (Fig. 3.4, D). Such structures apparently are controlled by micro-cracks and minor dislocations along them which produce the observed curves in lamination. In some areas around these veins, quartz exhibits a spherical texture, with the rounded grains ranging from 50 to 100 microns in size and usually being outlined by extremely fine-grained hematite (Fig. 3.2). Sub-millimeter quartz spheres from veins have been interpreted to originate from silica gel both in modern hydrothermal and synthesized

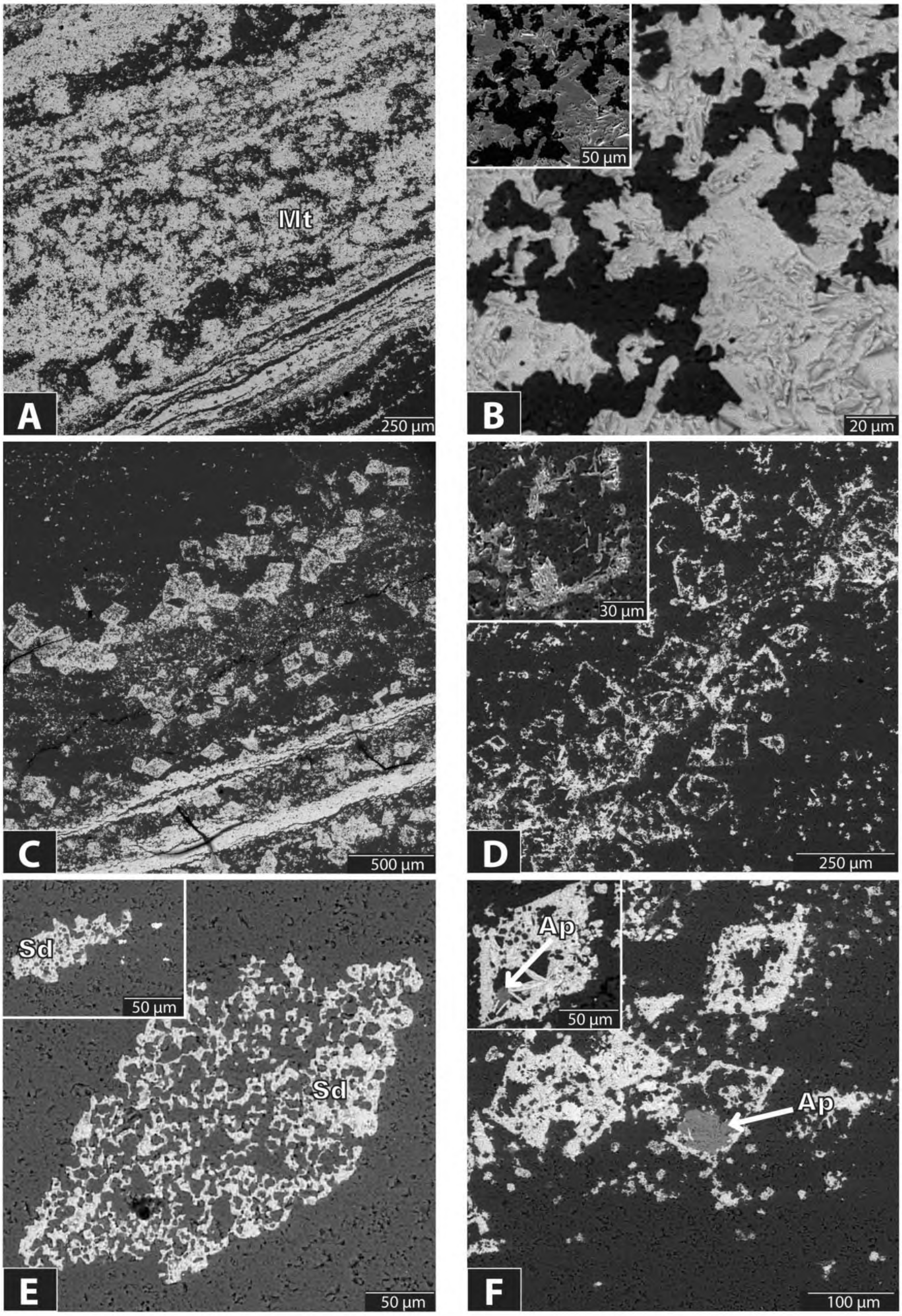

Figure 3.5. Back scattered electron (BSE) images of the laminated BIF, apart from the insets in B and D which were captured using secondary electron detection. A) Hematite mesoband with clear indication of martite. B) Anhedral aggregates of densely packed hematite in a mosaic with microcrystalline quartz. The microplaty habit of hematite is clearly discernable in BSE and SED

Figure 3.5. (continued) imaging under SEM inspection. C) Conspicuously preserved pseudomorphs of hematite after carbonates are common in the MIF. D) Carbonate pseudomorphs with only their outlines preserved, linearly arranged as in the parent rock. *Inset*, hematite replacing ankerite is of platy habit and possibly follows cleavage patterns. E) Common appearance of siderite in a chert matrix within the laminated BIF. *Inset*, anhedral siderite. Note the tiny sideritic specks in vicinity of the main grain. F) Apatite aggregate associated with hematitized carbonates. *Inset*, tiny apatite enclosed within carbonate pseudomorph. Mt = martite, Sd = siderite, Ap = apatite.

systems (Lebedev, 1967, Saunders, 1990). Ample evidence for silica of colloidal origin in the MIF is presented later.

Gypsum veins running through veins of microplaty hematite and vice versa emphasize the close relationship of the two minerals or in other cases the different succeeding hydrothermal events altering the BIF (Fig. 3.6, C and D). What raises difficulties in providing a solid interpretation is the rather scarce presence of individual isolated gypsum crystals with sharp faces set mostly in the matrix of chert mesobands (Fig. 3.4, entire C). Hematite overprints and quartz inclusions in gypsum as well as the apparent lack of feeding channels for fluids, further complicates things. The only sulfur-bearing mineral phase mentioned in the parent BIF is that of pyrite which has been never clearly shown in a study. If present, it should be an accessory constituent in extremely small amounts since sulphate concentrations were only 1 mM before the GOE compared to more modern levels, showing no specific distribution in concert with the majority of other iron-formations (Klemm, 1979, Hälbich, 1993, Lowenstein et al., 2003). Móricz et al (2012) have shown that pyrite oxidation in the presence of calcite can form secondary iron minerals as well as needles or tabular crystals of gypsum mostly as coatings on calcite. Although the required constituents are present in the BIF (ankerite instead of calcite) and large-scale oxidation does take place, there is no evidence for the aforementioned very unlike scenario. Instead, the abundance of gypsum in veins and breccias covering the whole stratigraphy points to a clearly secondary origin. The involved fluid could possibly pass through the pore space and precipitate gypsum in areas of higher permeability. It is also important to bring attention to the nature of silica in the chert bands during alteration and maybe consider the presence of a silicate gel which would allow for true solutions to pass through (Marinova et al., 2013). Otherwise, gypsum presence could be interpreted only through recrystallization of the initial quartz and subsequent co-precipitation of the two minerals.

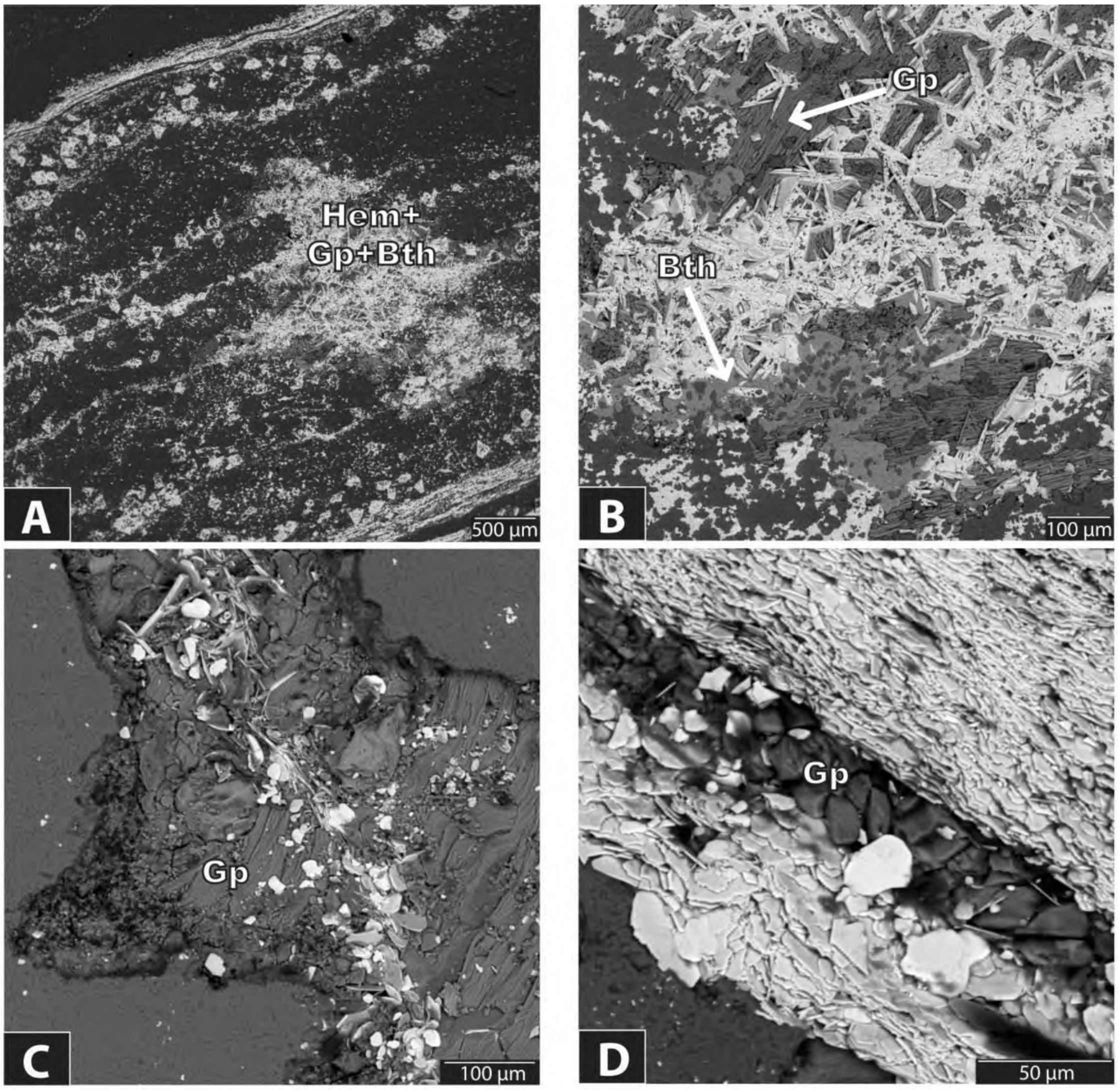

Figure 3.6. Back scattered electron (BSE) images. A) Vug-filling of hematite, gypsum and berthierine in crosscutting relationship with the banding. B) Gypsum, microplaty hematite and berthierine are common and closely associated. Note the microscopic quartz inclusions in gypsum and berthierine and the euhedral quartz crystals at the top and bottom left, which imply recrystallization of the surrounding quartz or transportation of silica through the fluid. C) Gypsum vein associated with microplaty hematite. Unidentified microscopic silicates bearing Na, K and Al are also present (bottom left). D) Gypsum-microplaty hematite association, with abundant hematite clearly lining the walls of the vein. Gp = Gypsum, Hem = Hematite, Bth = Berthierine.

Summing up, *reddish/cream-grey* BIF exhibit a variety of preserved and metasomatized textures. Inherited banding, microlamination and occasional truncation of bands (see also Appendix II, Fig. 2.2), the latter being a diagenetic texture, link these rocks to Kuruman iron-formation. Excellent preservation of the outward shape of the original ankerite, the sometimes degraded but mostly pronounced martite grains as well as the characteristic laterally discontinuous oxide microlaminae, strengthen this relationship. The origin of minerals such as siderite or apatite is more ambiguous though a secondary is more likely for most of the observed appearances. The presence of abundant vein-associated minerals accentuates the hydrothermal events involved during the alteration process. The degree of oxidation in these rocks is high as it is implied by the total absence of earlier mineral phases found in the pristine BIF and by the complete martitization of magnetite leaving behind no kenomagnetite relics (Kullerud et al., 1969), which suggests the addition of oxygen rather than loss of iron.

BIF with dull grey and occasional metallic grey alternating bands

Dull grey mesobands represent quartz-rich, hematite-poor bands, very similar to the chert mesobands in *reddish/cream-grey BIF*. The main difference is the absence of dusty hematite or its presence in such small amounts, insufficient to provide any significant red colouration to the banding. Instead, the chert bands have generally a brownish tint, caused by impurities of mostly randomly orientated microcrystalline to microplaty hematite. Scattered martite remnants are also present within the chert bands although their most pronounced appearance is usually in the graded contacts with the metallic grey bands (Fig. 3.7, D). Quartz is typically microcrystalline, exhibiting small variations in size and clear bulges along grain boundaries. In certain areas, mostly of lensoidal form, quartz has a more “cloudy” appearance which masks the boundaries of it’s widely euhedral grains (Fig. 3.7, C). Very fine-grained hematite is found as inclusions within this type of quartz or in the interstices between its crystals (Fig. 3.7, C, inset). This quartz-hematite assemblage is broadly reminiscent of a similar assemblage commonly found in the silicified BIF and presented in a later paragraph. Additionally, minor layering consisting of cryptocrystalline quartz was observed in *dull-metallic grey BIF*, stratigraphically close to silica-rich horizons.

Metallic grey mesobands consist of ample hematite but internally are finely microbanded by abundant layers composed of quartz. Quartz in these layers varies from microcrystalline, to coarser blocky grains, to comb quartz, most of them representing possibly recrystallized forms (Fig. 3.7, B). These well-defined microlaminae highlight the metasomatic replacement altering the BIF which leads to the visual enhancement of banding due to the strongly contrasting layers of the binary mineralogy (Fig. 3.7, entire A). Hematite mesobands usually show planar sharp contacts with adjacent chert mesobands. Hematite composing the metallic grey bands is represented by: i) clusters of martite grains arranged in bands which a lot of times are being finely separated by quartz (Fig. 3.7, E) and ii) microplaty hematite and/or martite assemblages with dispersed crystals of quartz, overall composing

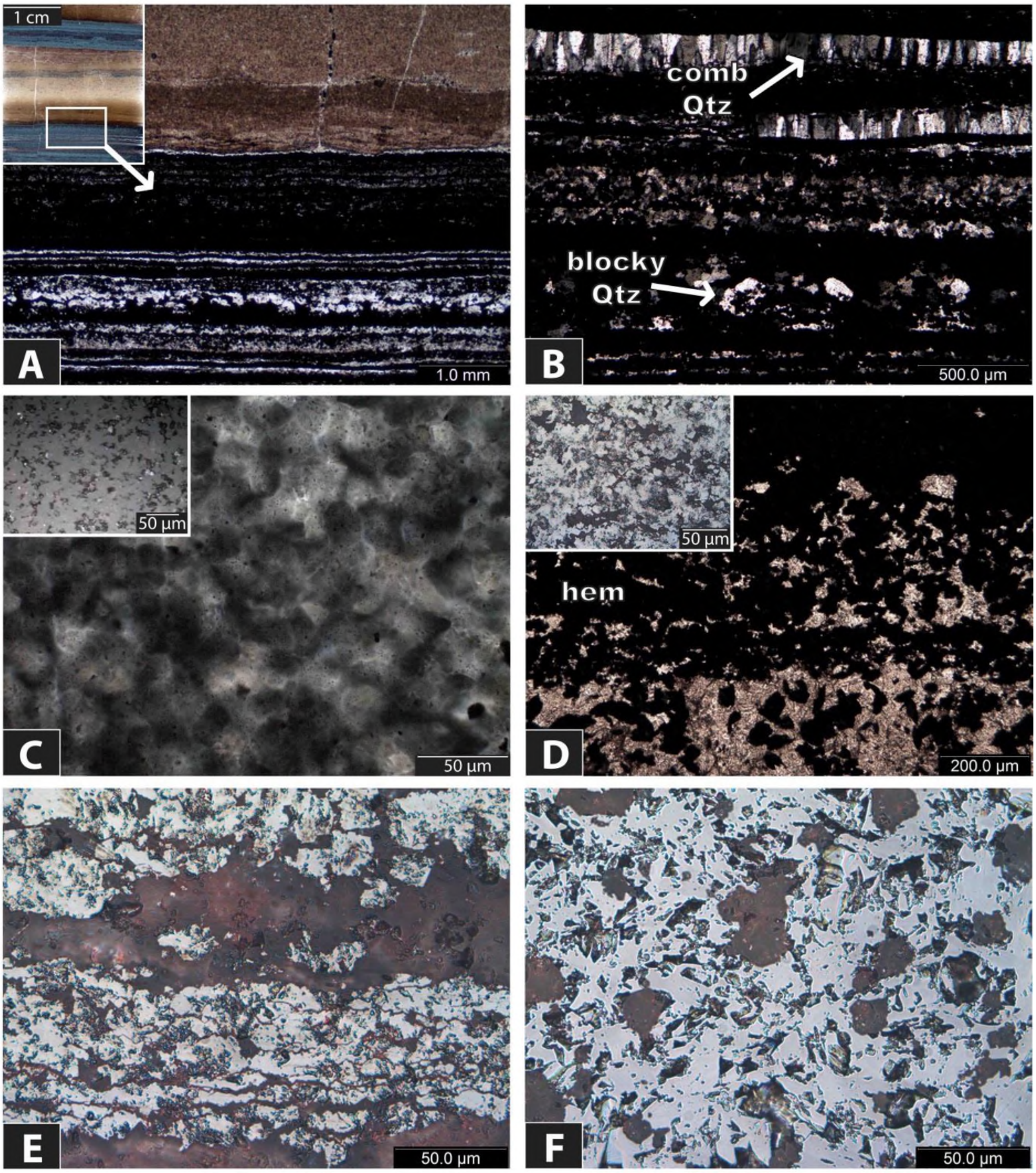

Figure 3.7. A) Sharp planar contact between a chert and a hematite-rich mesoband, the second containing conspicuous quartz microlaminae (XPT). *Inset*, thin section scan of the same sample. B) Microlamination within a metallic grey (hematite) mesoband consists of quartz showing different forms, from microcrystalline, to coarser blocky quartz or comb quartz; the latter being regularly fragmented (XPT). C) Quartz of "cloudy" appearance with masked crystal boundaries and tiny hematite inclusions within a chert mesoband (XPT). *Inset*, same in XPR. Note the fine-grained microcrystalline hematite occurring in the interstices between quartz. D) Graded contact between a chert and a hematite-rich mesoband with evident martite (PPT). *Inset*, detail of the same in XPR. E) Martite microbands. Note the finely separation by quartz layers at the bottom of the image (XPR). F) Microplaty hematite and dispersed sub- to euhedral quartz form the matrix of hematite-rich bands (XPR). Qtz = quartz, Hem = Hematite.

denser and more iron-rich bands.

Siderite is randomly distributed in all kinds of banding showing an average size of 100 µm. Despite its scarcity, a couple of grains were identified in almost every thin section studied for the laminated BIF. Unequivocal evidence of hematite overprinting siderite is shown in Figure 3.8, B. Gypsum shows the same distribution described so far, being present as euhedral single crystals within chert or forming veins with apparent crosscutting relationships to banding. Pyrite co-occurs with gypsum in some veins mostly as small subhedral crystals (Fig. 3.8, A). This assemblage has been well-demonstrated across the whole stratigraphy and an explanation for its formation is presented in the discussion. Occasionally, small cavities or vugs appearing within chert or hematite mesobands allow for the observation of quartz exhibiting hexagonal prismatic crystals of up to 50 µm which line these cavities (Fig. 3.9, A). The same is observed in similar vugs with hexagonal plates of hematite of usually 10-20 µm (Fig. 3.9, A, inset). Secondary micro-brecciation of these rocks by a network of dense veins and vugs is very common. This system of micro-fractures is filled by gypsum and celestine which were both identified using EDS (Fig. 3.9, entire B).

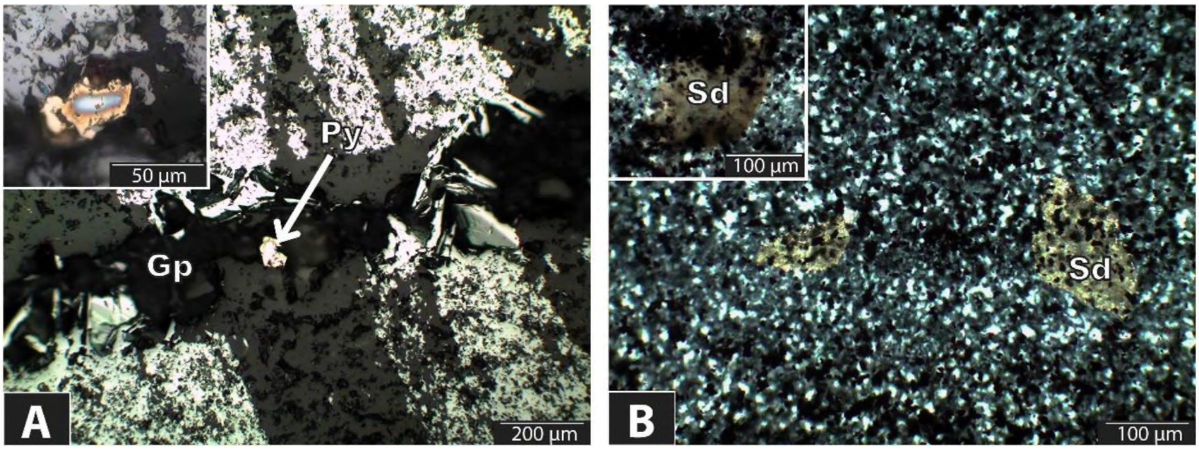

Figure 3.8. A) Gypsum vein clearly crosscutting and displacing banding and co-existing subhedral pyrite (XPR). Note the coarser, recrystallized microplaty hematite at the contact of the microbands with the vein. *Inset*, pyrite crystal (XPR). B) Sub- to euhedral siderite grains within chert being undoubtedly overprinted by hematite (XPT). *Inset*, the same. Gp = gypsum, Py = pyrite, Sd = siderite.

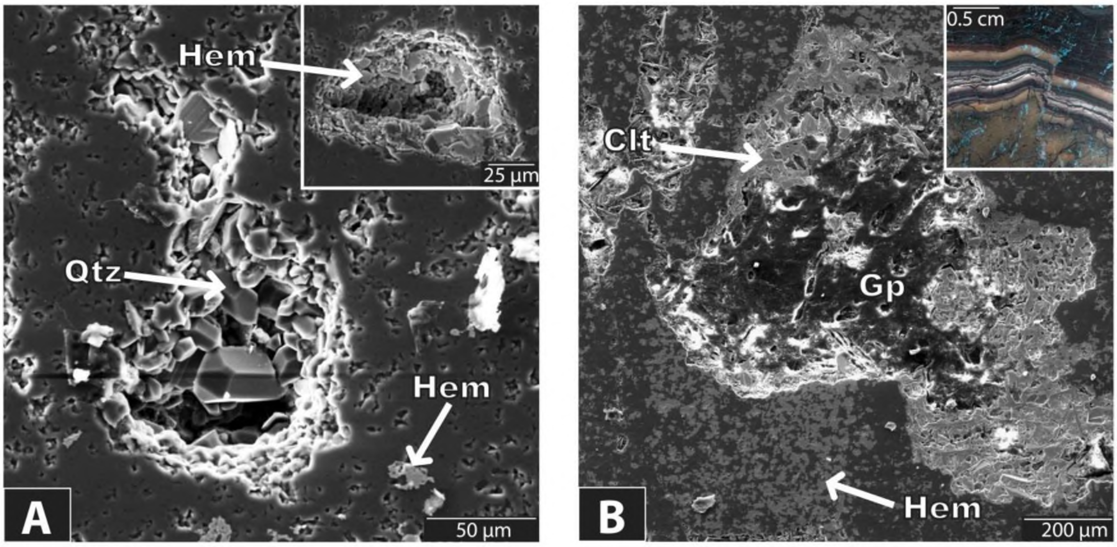

Figure 3.9. Both images shown were taken using secondary electron detector (SED). A) Small cavities within banding demonstrating well-crystallized hexagonal prismatic crystals of quartz. B) Mineral zonation in a vug lined by densely packed crystals of euhedral celestine in the outer zone and gypsum in its core. Note the crosscutting relationship to the hematite microband at the bottom left. *Inset*, part of a scanned thin section, showing the plethora of micro-fractures filled by sulphates brecciating and displacing the pre-existing banding. Clt = Celestine, Hem = Hematite, Gp = Gypsum, Qtz = quartz.

BIF with grey and red alternating bands

Grey-red BIF are more related texturally with the two groups already discussed than with the following two. These rocks were grouped separately due to: i) the lack of abundant chert mesobands, which when present always show intense red colouration (red bands) and ii) the prevailing presence of hematite-rich mesobands (grey bands), texturally very similar to the ones already described. These two features give a more iron-rich appearance to these rocks, based solely on petrographic observations. The metasomatic alteration is again well-documented by many characteristics such as the presence of carbonate pseudomorphs or the preservation of pinch and swell bedding which is clearly of diagenetic origin (Fig. 3.10, entire A). Hematite mesobands consist of martite and microplaty hematite along with quartz and range between more dense or porous bands (Fig. 3.10, C), very similar to the ones observed in the laminated ore. Gypsum veins were commonly observed running parallel to banding, causing brecciation and promoting recrystallization of hematite if not also quartz. Sporadically, some rather large, mostly sub- to euhedral pyrite crystals were found precipitated (Fig. 3.10, entire D). Investigation of one sample showed clusters of euhedral martite with very sharp crystal faces set in a quartz matrix impregnated by dusty hematite.

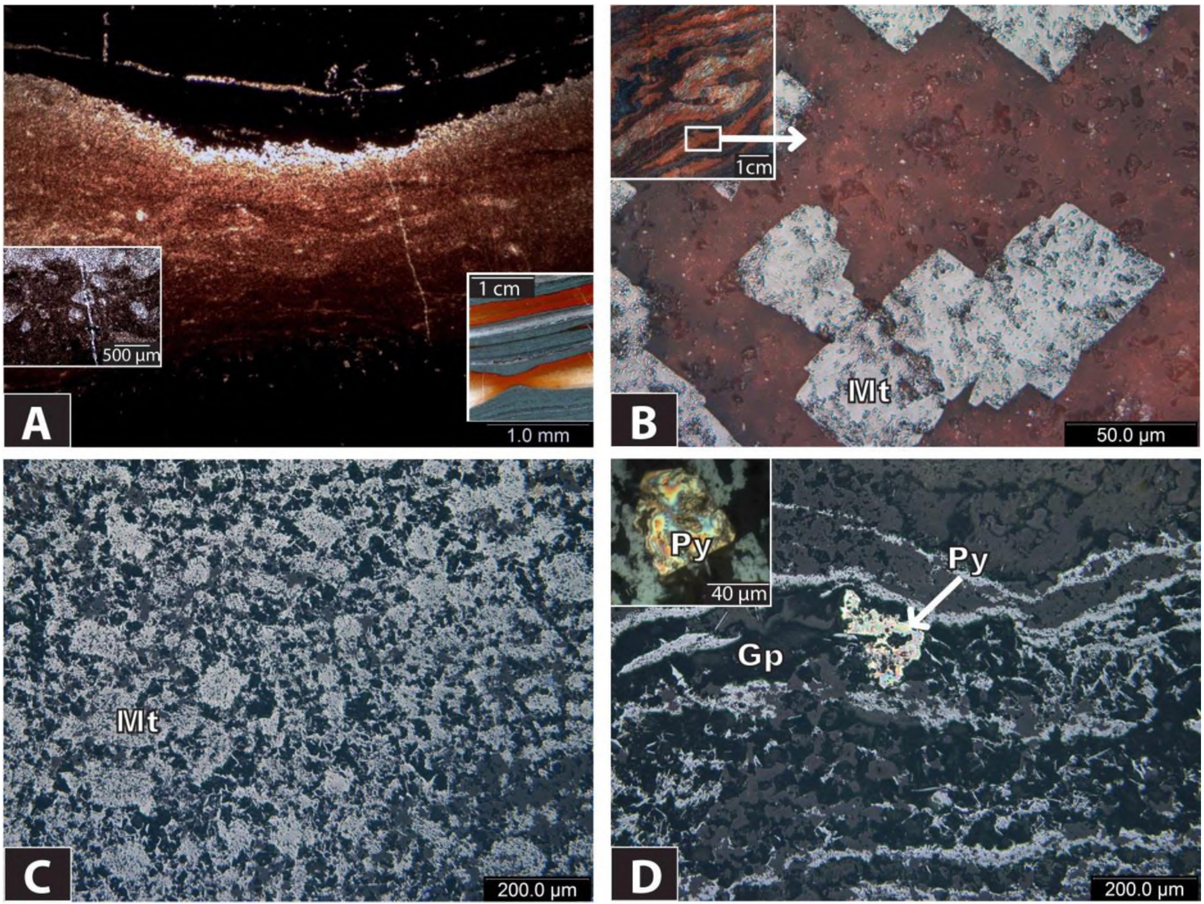

Figure 3.10. A) Chert mesoband impregnated by cryptocrystalline hematite, maintaining the original pinch and swell bedding of the BIF (PPT). *Inset a*, a wider depiction of the same sample (thin section scan). *Inset b*, quartz pseudomorphs after carbonates are more conspicuous in XPT, especially when set in a quartz + dusty hematite matrix. B) Martite aggregates with very sharp crystal surfaces set in a quartz matrix with abundant dusty hematite (XPR). *Inset*, scanned thin section of the same sample. C) Large martite grains intergrown with quartz in a rather porous band (XPR). D) Gypsum veins intruding parallel into banding are common and so as co-precipitating pyrite. *Inset*, euhedral pyrite of 40 µm in size (XPR). Gp = gypsum, Mt = martite, Py = pyrite.

The same sample records also remarkably well the diagenetic deformation structures of the parent rock (possibly a type of soft sediment deformation) being metasomatized by replacement alteration which largely follows and retains them, along with textures of specific mineralogical content i.e. banding, carbonates, magnetite (Fig. 3.10, entire B).

BIF with thick red and grey alternating bands

Red-grey BIF show evident textural differences compared to the other groups, which may provide some insights into their origin. As with the other groups, this type of laminated BIF can be followed in intersections for couple of meters. Despite some rare cm-scale intervals of chert bands, these rocks consist of either: i) red-coloured mesobands

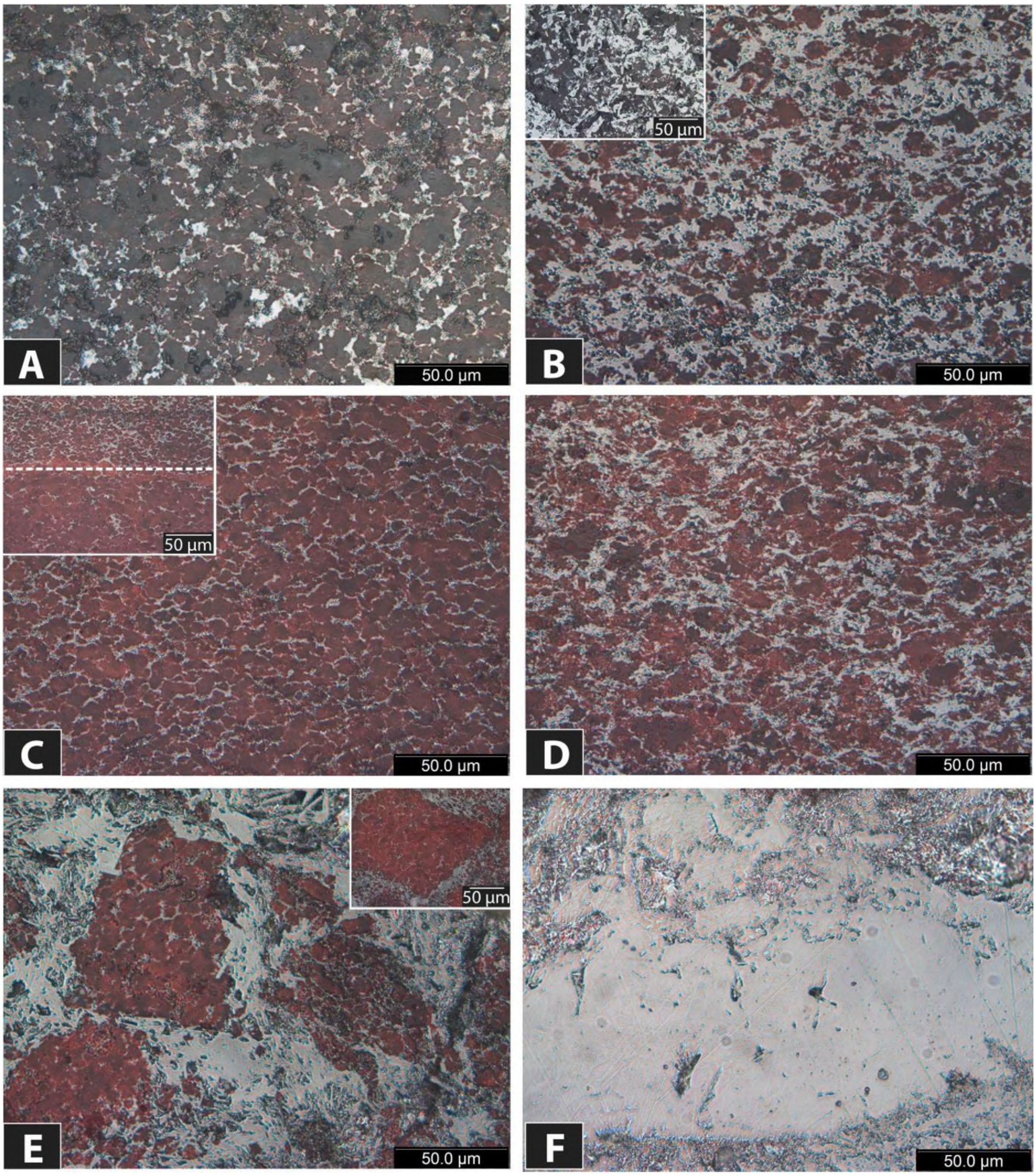

Figure 3.11. All images shown were taken under cross polarized reflected light (XPR). A) Part of a red band (quart-rich) exhibiting increased porosity. B) A typical grey band, rich in microplaty hematite and anhedral quartz showing dissolution textures. *Inset*, area with coarser microplaty hematite and increased porosity. C) A typical red band consisting of sub- to euhedral quartz within a meshwork of microcrystalline to microplaty hematite. Note the individual crystals enclosed by hematite. *Inset*, transition between a red (bottom) and a grey band (top). D) Transitional zone between a grey and a red band showing intermediate hematite content. E) Clasts or remnants possibly deriving from the red banding seem to have been further reworked and dissolved by an iron-bearing fluid. *Inset*, the same. Note the abundant and minute quartz remnants surrounding the clast. F) Vein-filling hematite showing a more tabular habit that it may also be the result of densely packed specularite crystals.

microlaminated by grey bands or ii) continuous microlamination of alternating red and grey bands, which is essentially very similar to the first. What is really intriguing though, is the mineralogical textures observed in these bands. A typical red band is composed of a mosaic of equigranular sub- to euhedral grains of microcrystalline quartz, almost each one of them bounded by its own well-developed crystal faces, as well as by a meshwork of microcrystalline to microplaty hematite surrounding and enclosing them (Fig. 3.11, C). Regularly, these bands exhibit areas with increased porosity (Fig. 3.11, A) and dissolution textures of quartz. As one moves towards the grey metallic bands, the hematite content increases and its microplaty habit becomes observable in most cases. The transition between the two types of banding is generally diffuse on the microscopic scale and the transitional areas are characterized by intermediate hematite content (Fig. 3.11, D and inset in C). Within the grey bands hematite develops dense laths of finer or coarser microplaty crystals that cumulatively form an iron-rich matrix (Fig. 3.11, entire B). Quartz is obviously lesser showing generally anhedral, stretched and elongated remnants and more pronounced dissolution textures than in the red bands.

Clasts or remnants of the red banding might have been reworked by hematite exhibiting larger microplaty grains, further brecciating them and dissolving silica (Fig. 3.11, entire E). The later mobility of iron is also recorded by veins of a more tabular hematite which may be also the result of densely packed specularite (Fig., 3.11, F). Thick gypsum + microplaty hematite veins usually with an outer lining of recrystallized quartz are also present. Based solely on textural observations, the alteration of the *red-grey* BIF gives the impression that it may have been caused by infiltration of an iron-rich fluid passing through the pore-space while dissolving and/or recrystallizing quartz. If true, this process is responsible for a significant iron-enrichment of some laminated BIF on a local scale. Higher amounts of magnetite within the original banding could partly control the high iron content observed. However, lack of martite textures allows to consider also a fluid-related introduction of iron in some stratigraphic horizons which might be related to: i) differences in primary mineralogy, i.e. comparatively lesser chert bands and a higher percentage of fine-grained iron silicates and carbonates, which are more susceptible to dissolution and which in turn would increase secondary porosity, ii) secondary structures of different scales or iii) a combination of both along with the nature of the fluid, capable of transferring iron and dissolving minerals in the parent rock and maybe even quartz. The lack of metasomatized textures, apart from the preservation of the general layering, is something also worth mentioning.

BIF with lustrous red and grey alternating bands

This final group of laminated BIF shows no significant differences compared to the *red-grey BIF* discussed above apart from the larger proportion of dense, hematite-rich grey bands, which are responsible for the metallic luster of these rocks. Specularite veins were also very common in the studied samples.

Laminated BIF - Summary

mineral	**Laminated BIF**				
	reddish/cream-grey	dull-metallic grey	grey-red	red-grey	lustrous red-grey
microcrystalline quartz	●●●	●●●	●●●	●●●	●●●
cryptocrystalline quartz		●			
microplaty hematite	●●●	●●●	●●●	●●●	●●●
cryptocrystalline hematite	●		●●	●	●
martite	●●	●●	●●		
specularite	●	●	●	●●	●●
siderite	●	●			
gypsum	●	●	●	●	
celestine		●			
pyrite		●			
berthierine	●				●
apatite	●		●		

Table 3.1. Mineralogy recorded in the various textural subgroups of the laminated BIF. The black dots (one to three) represent the observed relative abundance of the minerals in each group.

3.3.2 Silicified BIF

BIF with markedly preserved banding or replacement breccias

These are the most commonly observed silica-rich BIF in the Manganore iron-formation and display banded texture with usually thick (of several cm), almost hematite-free quartz mesobands alternating with more scarce and thinner (mm to cm-size) brownish-red mesobands which also contain minor hematite (Fig. 2.4, sample HLT38). Subordinate horizons exhibiting continuous micro-layering that consists of the aforementioned bands also occur in places but the high silica content of these rocks can be easily perceived due to the low specific weight and the very pale pigmentation of quartz comparatively with all the other groups of laminated BIF discussed above (see also Appendix II, Fig 2.3, sample HLT39).

Quartz is generally anequigranular and shows the following two textural varieties: i) microcrystalline quartz (5-30 μm) which is the chief constituent of the banding and ii) macrocrystalline grains of typically 100-200μm in size which form a dense interconnected network of subparallel layers within the microcrystalline quartz matrix (Fig. 3.12, A). Occasionally, blocky quartz veins traverse across this layered texture and the scarce reddish hematite-poor bands. Macrocrystalline quartz reaches up to 0.5mm in size and appears in polygonal shapes that allow for triple junctions to be easily seen. The microcrystalline varieties signify either the original or most likely recrystallized quartz of the chert bands of the parent rock while macrocrystalline quartz has formed certainly later and is strongly believed that it is connected with the silicification process. Small anhedral apatite and traces of submicroscopic REE-phosphates, xenotime and siderite are occasionally found in the quartz groundmass.

Hematite crystallizes in the interstices between quartz as minute plates or as anhedral to subhedral microcrystalline masses (10 to 30μm) and is generally rare (Fig. 3.12, A, inset). In the same way, sporadic martite grains exhibiting typical octahedral shapes are seen to have been fully replaced by cryptocrystalline hematite. The presence of the reddish-brown bands appears to be controlled by the original oxide-rich banding although the current texture and mineralogy produced by alteration is striking different. These bands consist of microcrystalline quartz with clear crystal boundaries and triple junctions as well as of abundant dusty hematite embedded in quartz (Fig. 3.12, B). This very fine-grained hematite is arranged in roundish or locally hexagonal shapes which indicate its close relationship with quartz and its possibly prior or synchronous crystallization after the dissolution of the prior magnetite or martite by a silica-rich fluid. These bands also contain interstitial anhedral to subhedral microcrystalline hematite of minor quantities.

In some samples, the breakup and dissolution of the iron oxide bands by a silica-bearing fluid is clearly manifested, thus leaving behind a type of replacement breccia (Fig. 3.12, C). Close inspection under reflected light shows that quartz grains tend to follow the pattern of the prior martite lamellae although it is not quite evident if replacement by quartz takes place in a metasomatic manner or as void filling after leaching of the iron oxides (Fig. 3.12, entire D). The relationship between quartz and hematite is very intricate as commonly, with needle-like inclusions of platy hematite within quartz and visa-versa. In a silicified

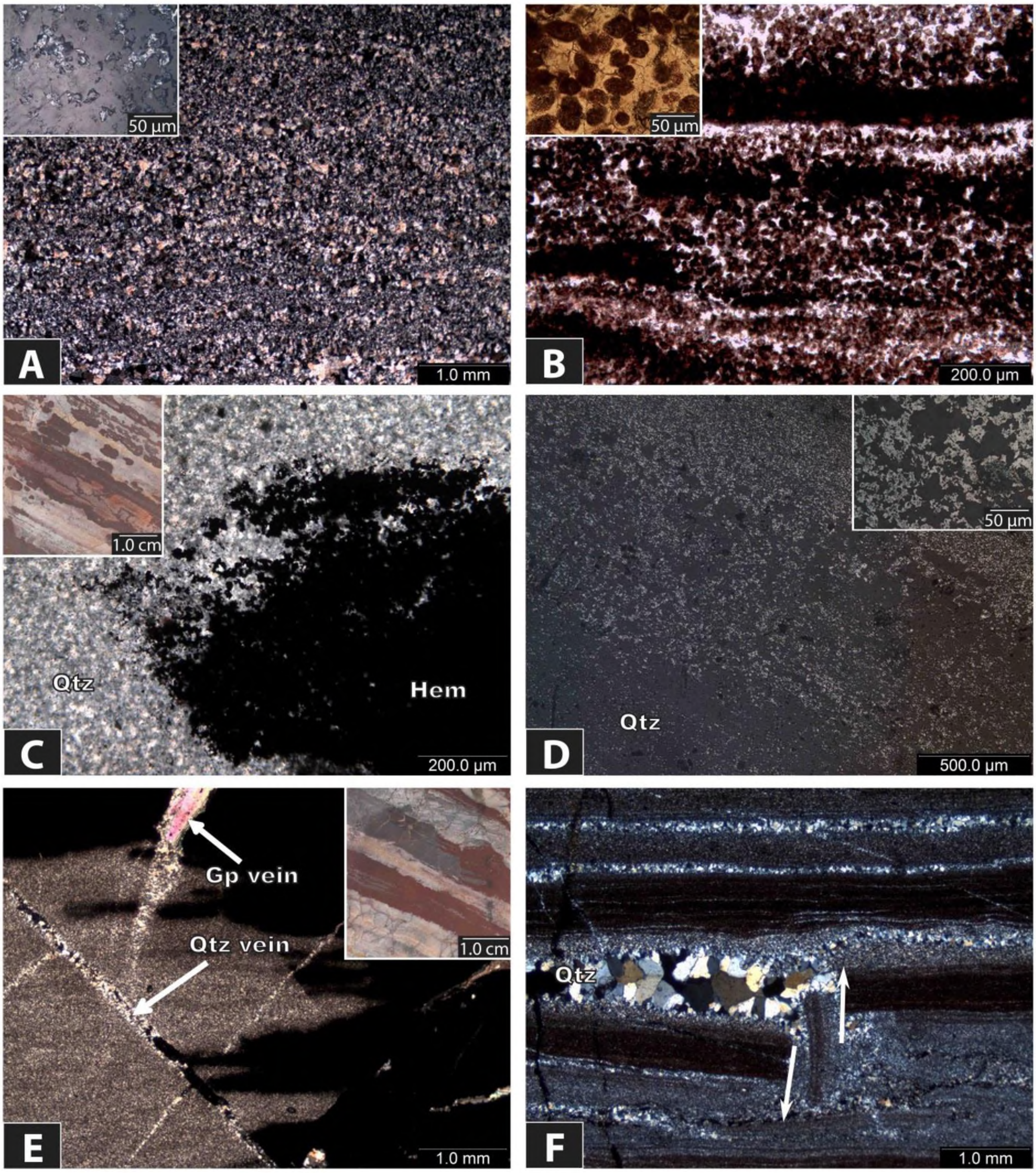

Figure 3.12. All photos shown were taken under transmitted light except inset in A and the entire D which is shown in reflected light. A) Typical layered texture of micro- and macrocrystalline quartz, the second forming a parallel and interconnected network (XPT). *Inset*, microplaty or microcrystalline hematite is occasionally filling the pore space between quartz (XPR). B) *Inset*, detail from (B). Hematite-poor mesobands consist of a peculiar appearance of euhedral quartz and microscopic hematite embedded within it (PPT). *Inset*, detail of the same band (PPT). C) Quartz apparently dissolving the existing banding and forming a replacement breccia (XPT). *Inset*, wider depiction of the same area (rock slab). D) Quartz replacing oxide banding (XPR). *Inset*, detail showing euhedral quartz grains of up to 50 µm in size. E) Hematite + quartz layer (right) replacing silica banding (left) within a silicified BIF. Crosscutting veins consists of gypsum and quartz (XPT). *Inset*, wider depiction of the same area (rock slab). F) Chert breccia with BIF-remnants showing crackle-style brecciation and rotation of a small fragment (XPT).

sample from Sishen (D20), porous hematite pseudomorphs after possibly carbonates showing evidence of leaching were observed within remnant banding (Fig. 3.13, C). Bands exhibiting kink folding in the same sample on the mesoscopic scale, have been exploited by later hematite veining and contain equant hexagonal quartz crystals of various sizes within a matrix of microplaty hematite (Fig. 3.13, D). This quartz might be either recrystallized or of detrital origin.

Although the presence of abundant replacement breccias allows for the conversion from altered/oxidized to silicified BIF to be clearly traced within a single thin section, sometimes the interpretation of certain replacement textures can be more ambiguous. In Fig. 3.12, E, (see also Appendix II, Fig 2.3, sample VLT57) it is believed that the iron-rich (red) material intrudes and replaces the silica-rich (grey) material. Quartz in the iron-rich front is rather anhedral, very fine-grained and it is surrounded by microcrystalline hematite. If this is the case, layered controlled hematitization may also occur after silicification. Iron mobilization postdating silicification is evident from crosscutting hematite veins, not necessarily specularitic, which also develop approximately parallel to bedding relationships and occasionally show small-scale wall rock alteration. Textures as the one seen in Fig. 3.13, B, of intricately associated microplaty hematite and quartz overprinting siderite veins of syn- or post-silicification origin further support the late-stage iron mobility.

Mineralization in veins that largely seem to postdate the silica enrichment is very common. Siderite showing concentric zoning is found both within quartz groundmass as well as a vein infill mineral (Fig.3.13, A). Sub- to euhedral crystals of berthierine and tourmaline are found in close association with siderite masses and gypsum (Fig. 3.14, A, B, C). The latter forms plenty of veins which rarely comprise celestine. Veins containing abundant rutile, zircon and xenotime along with silicates are quite frequent. Muscovite occurs mostly within the quartz matrix, infilling interstitially around some grains in the vicinity of vein boundaries and forming sericitized domains. Occasionally, it contains apatite and alumino-phosphate-sulphate minerals (APS), identified as svanbergite and woodhouseite by EDS. Minute chromite, cuprite and galena were also recognized using EDS and appear disseminated within the quartz bands or are closely associated with silicates and gypsum.

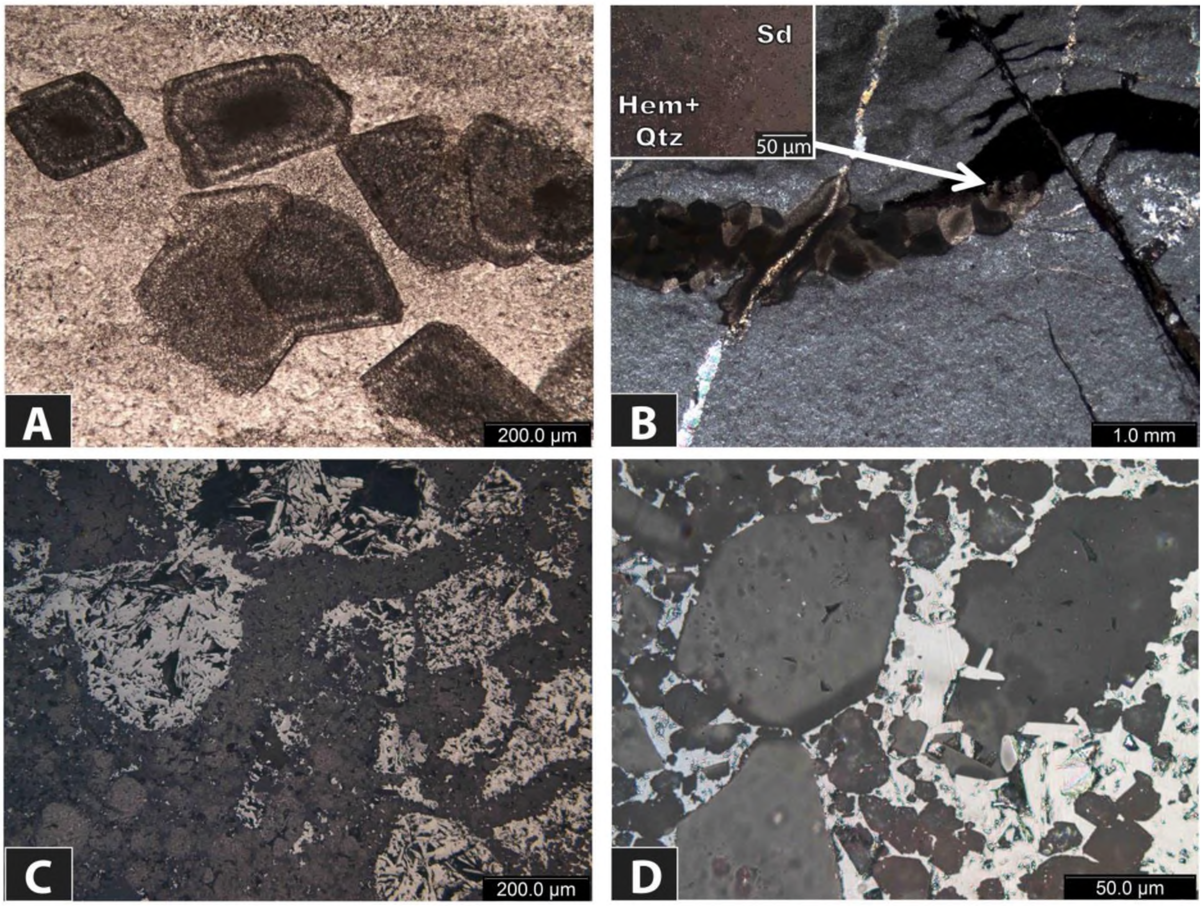

Figure 3.13. A) Siderite of 200 µm exhibiting concentric zoning within quartz matrix (PPT). B) A microplaty hematite vein containing abundant quartz (deriving possibly from the surrounding matrix) replaces a sideritic vein. Note hematite infiltrating into small cracks at the right left corner. Crosscutting veins consist mostly of gypsum (XPT). *Inset*, detail of the replacement front (XPR). C) Porous hematite pseudomorphs possibly after carbonates (XPR). D) Equant, variable in size quartz of possibly recrystallized or detrital origin within a microplaty hematite matrix filling a vein (XPR). Hem = Hematite, Qtz = Quartz, Sd = siderite.

To summarize, the retention of banded texture and especially of microbanding in these silicified BIF as well as their stratigraphic position suggests that the protolith is the Kuruman Iron Formation. Preservation of original BIF textures which are still recognizable such as martite, further proposes that silicification of these BIF is most likely to have occurred after an initial oxidation and metasomatic alteration and was possibly accompanied by mineralization which also followed silicification with a series of succeeding hydrothermal events.

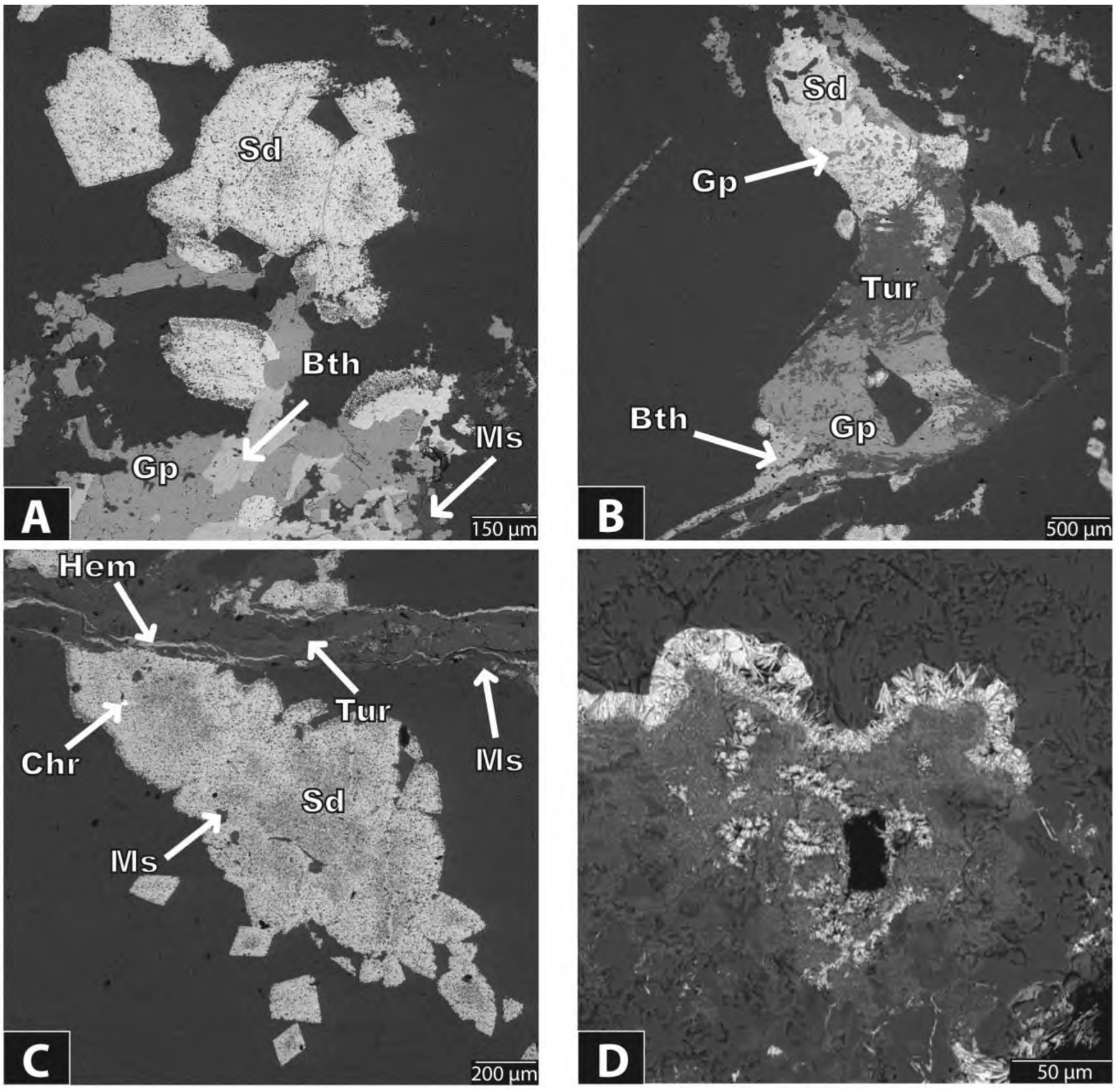

Figure 3.14. Back scattered electron (BSE) images. A) Subhedral siderite associated with prismatic crystals of berthierine and gypsum. B) An assemblage of berthierine, tourmaline, siderite and gypsum showing the close relationship of these minerals within the MIF. Textural observations suggest that siderite is the last constituent crystallizing between these four. C) Tourmaline vein showing crosscutting relationship with an aggregate of siderites and minor chromite. Muscovite is also present in the matrix and seems to predate the formation of siderite. D) Zoned textures with rims of microplaty hematite and cores of dusty hematite and quartz, probably representing former chalcedony or even siderite. Bth = Berthierine, Chr = Chromite, Gp = Gypsum, Hem = Hematite, Qtz = Quartz, Ms = Muscovite, Sd = Siderite, Tur = Tourmaline.

Chert breccia with BIF-remnants

The principal difference of these BIF from the previous group is that the existing blocky quartz veins which are thought to be related to the silica enrichment cause significant brecciation of the reddish hematite-poor bands (Fig. 3.12, F). Banding fragmentation ranges from crack-style with minor dislocation to more intense with rotation of the fragments, the latter giving the impression of BIF-clasts floating within a silica matrix on mesoscopic observation. Sporadically, veins or patches that consist of concentric layering are found within the microcrystalline quartz matrix. These zoned textures show well-developed microplaty hematite rims and quartz-rich interiors with dusty hematite, overall resembling collomorphous chalcedony which could have crystallized from an iron-bearing fluid or might have been later replaced by it (Fig. 3.14, D). Another possible explanation for these textures assumes that they represent former siderites as their spindle-like shape, zoning and distribution might suggest. Crosscutting veins containing either tourmaline or berthierine together with microplaty hematite are quite common.

Creamish-grey BIF with wavy lamination

The main constituent of the undulating banding is cryptocrystalline quartz alternating with much lesser microcrystalline quartz (Fig. 3.15, A, B). The former is thought to represent an open space infill phase which develops colloform bands or veins composed of milky, pinkish-grey, pale-grey or beige-coloured quartz varieties (Fig. 3.15, A, inset). As stated by Taylor (2009), any form of layering or banding in altered rocks should be seriously considered as a potential infill texture, especially when it is formed by silica. There is ample evidence to suspect a void-filled origin as it will be made clear. On the other hand, microcrystalline quartz is generally equigranular and is believed to be both secondary as well as component of the original banding which regularly alternates in between the colloform bands. The width of the individual colloform bands varies from a few millimeters up to several centimeters and they usually display a finer inner banding of contrasting colour. The boundaries of layers in this inner banding are clear but are usually obscured rather than sharp. Colloform-banded textures seem to be most of the times more widespread than the preserved original layering in these rocks. Furthermore, its distinction from the original banded-texture can be also challenging. The finely layered manner of the colloform bands is more conspicuous in colloform-banded veins, usually adjacent to contrasting hematite-rich areas (see also Appendix II, Fig 2.2, sample VLT45). Coarser quartz grains are rare and limited only to veinlets that form a dense interconnected network around finer-grained quartz.

The retention of the original banding is supported by the presence of scarce martite grains and their layered distribution within microcrystalline quartz matrix. Pseudomorphs of quartz after carbonates also occur. Veinlets of cryptocrystalline quartz rarely form bulges which overprint remnant martite-banding, thus suggesting that at least part if not all of the

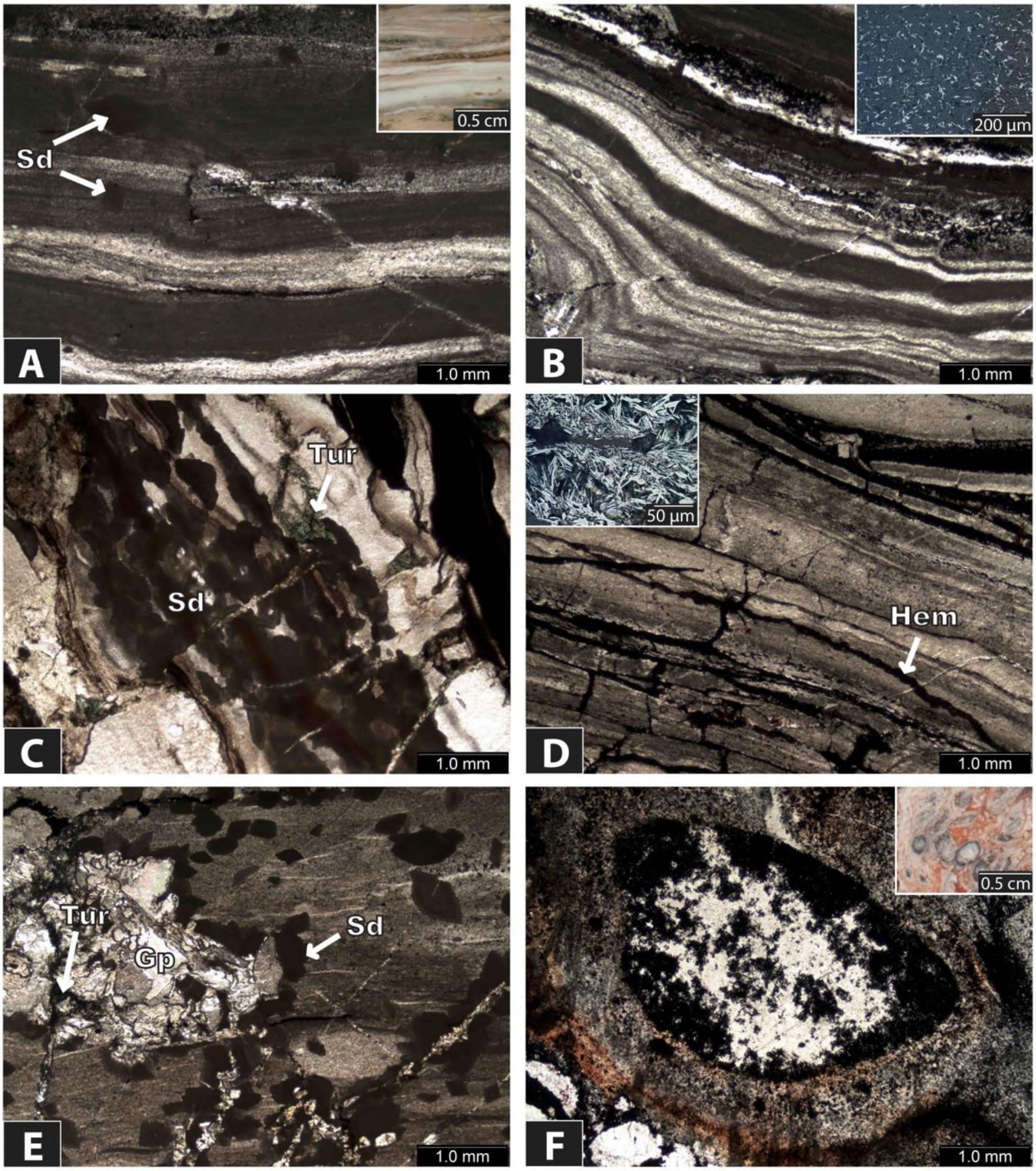

Figure 3.15. A) Bands of cryptocrystalline and microcrystalline quartz, the former most likely representing an open-space infill. Note the dispersed siderite (PPT). *Inset*, a wider depiction of the same area presenting the different pinkish and beige colours quartz displays (rock slab). B) Undulating banding is believed to be an entirely infill texture. Possible remnants of the pre-existing banding can be seen at the top right (PPT). *Inset*, randomly orientated needle-like microplaty hematite (XPR) within quartz. C) Assemblage of densely packed siderite crystals layered within cryptocrystalline quartz matrix. Veins of mainly tourmaline crosscut the banding (PPT). D) Veins of microplaty to specular hematite occasionally crosscutting the banding support mobilization of iron after the silicification event (PPT). *Inset*, detail of the same hematite (XPR). E) Gypsum, tourmaline and siderite vug and subparallel veins at the bottom right. Siderite is found at the rims, lining open spaces or within the matrix (PPT). F) Globular textures within colloform veins exhibiting concentric layering. They might reflect either the nature of the colloidal solution or the facies transition from the

Figure 3.15. (continued) microbanded Kuruman to the granular Griquatown iron-formation (see also text) (PPT). *Inset*, a wider depiction of the same area (rock slab).

silica was introduced through fluids after the initial oxidation of the rock. Apart from martite, hematite is also found as needle-like microplaty hematite of mostly very small size, scattered in all types of silica bands and rarely as microcrystalline grains (Fig. 3.15, B, inset). Despite the sparse distribution of hematite, the hematite-to-quartz ratio controls to some extent the pigmentation of banding which is otherwise governed by the different habit quartz displays. The random grain orientation of quartz, microplaty hematite and of occasionally present siderite supports a colloidal origin for the majority of the bands. The lack of periodicity in the width and composition of bands is also an argument that colloform banding is of primary deposition rather than of diffusive origin, although it must be also noted that any observation of radiating manner or periodicity in the colloform layering is limited to some degree when studying core samples.

Siderite in these rocks shows the highest concentrations compared to all the other studied groups. It is found disseminated in both microcrystalline and colloform quartz banding as subhedral to euhedral, equant to sub-rounded individual grains of typically 300-500 μm size and rhombohedral shape or as assemblages of densely packed crystals (Fig. 3.15, C). The latter are mostly associated with veins and vugs filled with gypsum and tourmaline (Fig. 3.15, E). Crystal zoning is rather conspicuous and is defined by a margin high in silica content, an intermediate zone of high siderite content and a silica-rich core. Microprobe analyses of siderites performed on silica-free areas of the intermediate zone from various silicified BIF showed a consistent composition (Table 3.2). Comparison with available microprobe data from siderites deriving from the Griquatown and Kuruman iron-formations (Rafuza, 2015), showed broadly similar compositions but with a noticeable deficiency in magnesium. Siderite in iron formations is typically very fine-grained (Klein, 1974, Ewers and Morris, 1981) and especially in the well-considered protolith it appears associated with much coarser-grained ankerite or as inclusions within it. Furthermore, siderite in the protolith does not show an analogous zoning to that noted in the MIF, instead this zoning is common in ankerite from the Kuruman iron-formation (Rafuza, 2015). All of the above in conjunction with the common appearance of siderite being associated with sulphate-bearing veins or occurring as an amorphous infill of sparitic siderite, point to a clearly secondary origin for the bulk of it found in the Manganore iron-formation.

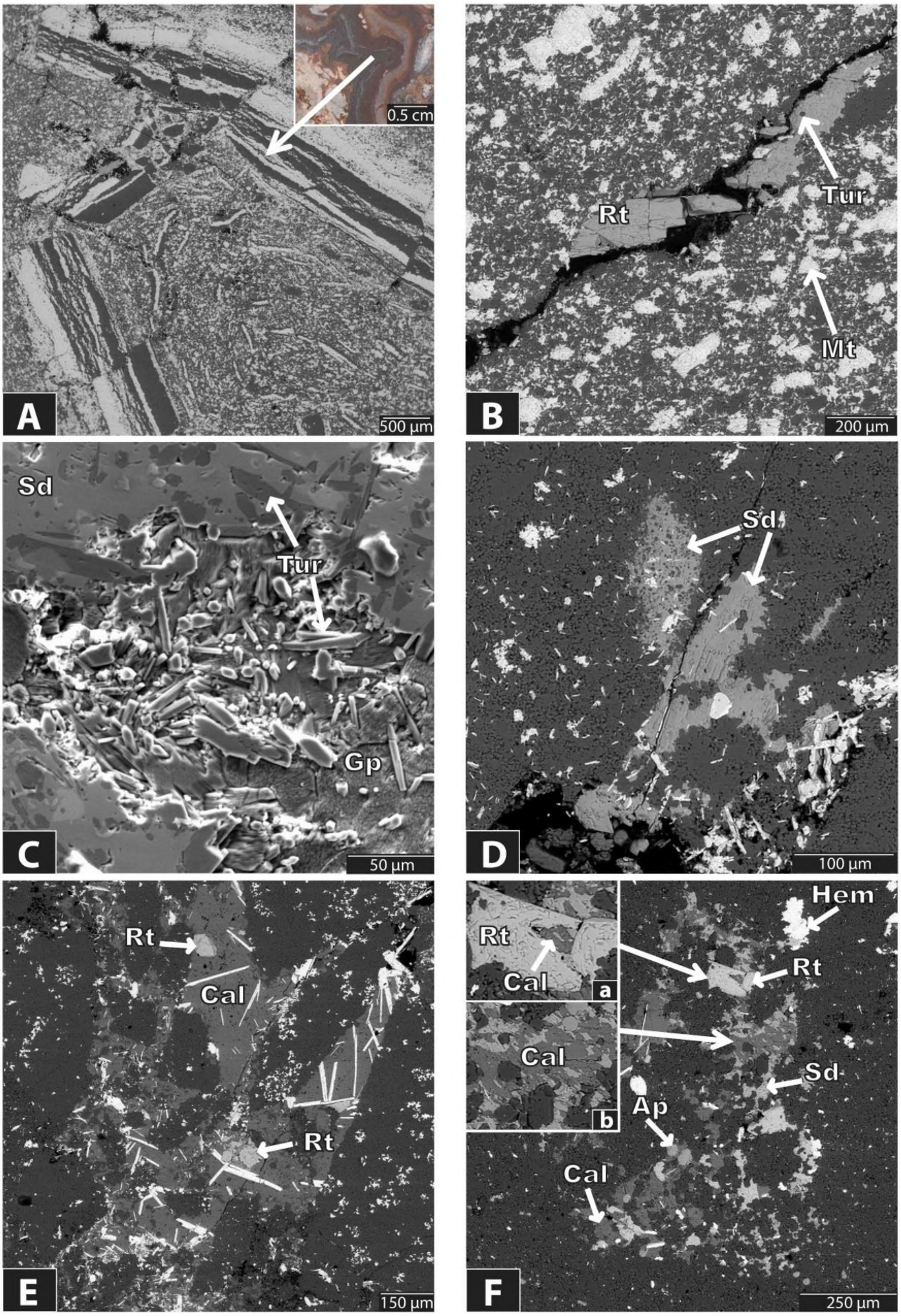

Figure 3.16. Back scattered electron (BSE) images except from (C) which was obtained using secondary electron detection (SED). A) Kink-bands and folding exhibited by ferruginous BIF-clasts follow the geometry of the surrounding colloform veins. *Inset*, a wider depiction of the same area (rock slab). B) Rutile with tiny tourmaline inclusions filling cracks within a quartz matrix with abundant microplaty hematite and martite. C) Tourmaline needles embedded in gypsum and siderite.

Figure 3.16. (continued) D) Siderite at the left of the fracture resembles the common occurrence of subhedral spindle-like crystals with abundant quartz inclusions and/or crystal zoning, while right of the fracture sparitic siderite is infilling pore space. E) Calcite as infilling cement together with rutile and specular hematite. F) An assemblage of carbonates, apatite, rutile and hematite within colloform banding. *Inset a*, rutile enclosing calcite with a hematite inclusion. *Inset b*, calcite showing inclusions of siderite. Ap = Apatite, Cal = Calcite, Gp = Gypsum, Hem = Hematite, Mt = Martite, Rt= Rutile, Sd = Siderite, Tur = Tourmaline.

Oxide wt. %	n = 24	STD	Kuruman*
MgO	3.69	0.66	6.69
MnO	3.08	1.73	2.65
CaO	0.44	0.46	0.87
FeO_{tot}	51.10	2.73	49.17
SrO	0.04	0.03	n.a.
Total	58.46	1.65	59.75
Calculated on the basis of 3 O			
Mg	0.32		0.55
Mn	0.15		0.12
Ca	0.03		0.05
Fe	2.5		2.27
Sr	0.001		n.a.

Table 3.2. Average microprobe analyses of siderite form different stratigraphic occurrences. Also included are average analyses (n=25) from siderites deriving from the Kuruman iron-formation. (Rafuza MSc Thesis, 2015). n.a. = not available.

Despite the fact that these rocks are largely iron depleted compared to the protolith, hematite-rich areas of sometimes considerable thickness can be found adjacent or even enclosed by wavy colloform-textured silica. These iron-rich portions consist of microplaty hematite and martite set in a quartz matrix. Occasionally, ferruginous BIF-clasts are also present and show a type of folding, produced by a series of clasts exhibiting kink bands. These micro-folds follow the geometry of the colloform banding to which they are adjacent to (Fig. 3.16, entire A). Rutile-bearing cracks with prismatic crystals up to 300 μm in size usually showing rutile inclusions are also common (Fig. 3.16, B). Hematite of microplaty to specular habit is found in veins running subparallel to the silica banding and locally forming a dense stockwork of micro-veins that crosscut and brecciate the banding, overall supporting a late-stage iron mobilization event (Fig. 3.15, entire D). It is also found cementing micro-breccias with siliceous angular fragments by filling triangular-acute angle textures, suggestive of late fracturing. Moreover, hematite appears overprinting siderite as observed in other silicified BIF.

Another commonly encountered texture is that of globular structures enclosed within colloform-banded veins and consisting of silica-rich cores outlined by hematite rims (Fig. 3.15, entire F). These structures range from roundish to more elongate and from several millimeters up to more than 1 cm. The contrasting concentric layering composing and surrounding them could reflect the overall colloidal regime, since these structures are ubiquitous and very close to each other within the colloform veins. However, the presence of hematite resembling pseudomorphs after carbonates or magnetite in the rims or in the surroundings of these structures complicates their origin interpretation (Fig. 3.17, B). There is a strong resemblance of these globular textures with pods/lenses found further upwards in the stratigraphy and which are thought to be altered equivalents of the lensoidal structures (pods or pillows) encountered in the Griquatown iron-formation (Beukes, 1984). If the globular structures seen in the silicified BIF are related to primary structures found in the protolith, then this could reflect the graded faces transition in the stratigraphy from the microbanded Kuruman to the granular Griquatown iron-formation. The large size of these structures excludes transportation through a fluid from upwards, i.e. a detrital origin. Similar textures of pods/lenses are discussed later in the *brecciated BIF* section.

The presence of abundant accessory minerals not related to the mineralogy of the protolith constitutes another significant characteristic of this group. Generally, the highest abundance and variety of secondary minerals filling veins and voids occurs in the silicified BIF. The chiefly gently curved surfaces of the colloform banding are distorted by brecciation and minor dislocation of the bands along the axes of the folding, a process that overall enhances the wavy appearance of these rocks. The open space that is created is occupied by secondary minerals and minute angular fragments from the silicified rock. Mineralization found in the colloform-banded silica veins consists mainly of siderite, calcite, rutile and hematite (Fig. 3.16, E, F). These minerals compose assemblages of closely related sub- to anhedral grains embedded in a silica matrix that also contains tiny hematite plates, apatite and traces of alumino-phosphate-sulphate minerals (APS) (Fig. 3.17, A). Needle-like specularite or microplaty hematite occurs as inclusions in all kinds of minerals. Siderite and calcite seem to be closely associated with each other, with the latter often showing siderite inclusions which suggest a later crystallization for calcite (Fig. 3.16, F, inset b). Rutile is abundant and is found in assemblages with any of the other existing minerals or is individually filling voids within the quartz matrix. Veins of muscovite (Table 3.3) almost always containing rutile, apatite, zircon or xenotime seem to represent a former event, as emerges from the apparent crosscutting relationships.

Oxide wt. %	n = 8	STD	Muscovite*
SiO_2	49.71	1.09	45.83
Al_2O_3	34.59	0.47	34.84
TiO_2	0.02	0.02	0.53
FeO_{tot}	1.65	0.2	1.47
MnO	0.05	0.03	n.d.
MgO	0.42	0.06	0.49
CaO	0.21	0.13	0.18
Na_2O	1.80	0.05	0.92
K_2O	9.70	0.19	9.98
Total	96.57	1.48	94.24
Calculated on the basis of 22 O			
Si	6.40		6.17
Al	5.24		5.53
Ti	0.002		0.05
Fe	0.18		0.17
Mn	0.01		n.d.
Mg	0.08		0.1
Ca	0.03		0.03
Na	0.45		0.24
K	1.59		1.71

Table 3.3. Average microprobe analyses of muscovite from sample VLT57 (silicified BIF). A muscovite* from literature is also included (Konings et al., 1988). n.d. = not detected.

Tourmaline occurring as inclusions both in gypsum and siderite was identified as a member of the schorl-dravite series (Table 3.4).

Concluding, meters of rock consisting of fine to massive colloform-banded textures of primary deposition amalgamated possibly with banding and remnant textures from the parent rock suggests that part of the silicification is caused by silica of colloidal origin. The colloform bands differ in quartz-to-hematite ratio as well as in colour and texture of quartz, which collectively provide the overall striped appearance to these rocks.

Oxide wt. %	n = 6	STD	Tourmaline 1*	Tourmaline 2*
SiO_2	37.11	0.87	38.10	36.59
Al_2O_3	33.60	0.94	35.50	33.18
TiO_2	0.06	0.04	0.95	0.75
FeO_{tot}	11.53	1.00	9.65	7.06
MnO	0.06	0.05	n.a.	0.03
MgO	4.42	0.69	4.32	6.47
CaO	0.19	0.37	0.37	0.44
Na_2O	2.28	0.28	1.92	2.09
K_2O	0.01	0.01	n.d.	0.05
Total	89.29	1.20	90.81	86.66
Calculated on the basis of 29 O				
Si	7.06		7.03	7.02
Al	7.53		7.72	7.51
Ti	0.01		0.13	0.11
Fe	1.83		1.49	1.13
Mn	0.01		n.a.	0.005
Mg	1.25		1.19	1.85
Ca	0.04		0.07	0.09
Na	0.84		0.69	0.78
K	0.002		n.d.	0.01

Table 3.4. Average of 6 microprobe analyses of tourmaline from the silicified BIF (samples VLT43, VLT57). Tourmaline 1* represents a schist-hosted metasomatic tourmaline (Gallagher, 1988) and Tourmaline 2* is from metapelites (Henry and Guidotti, 1985). n.a. = not available, n.d. = not detected.

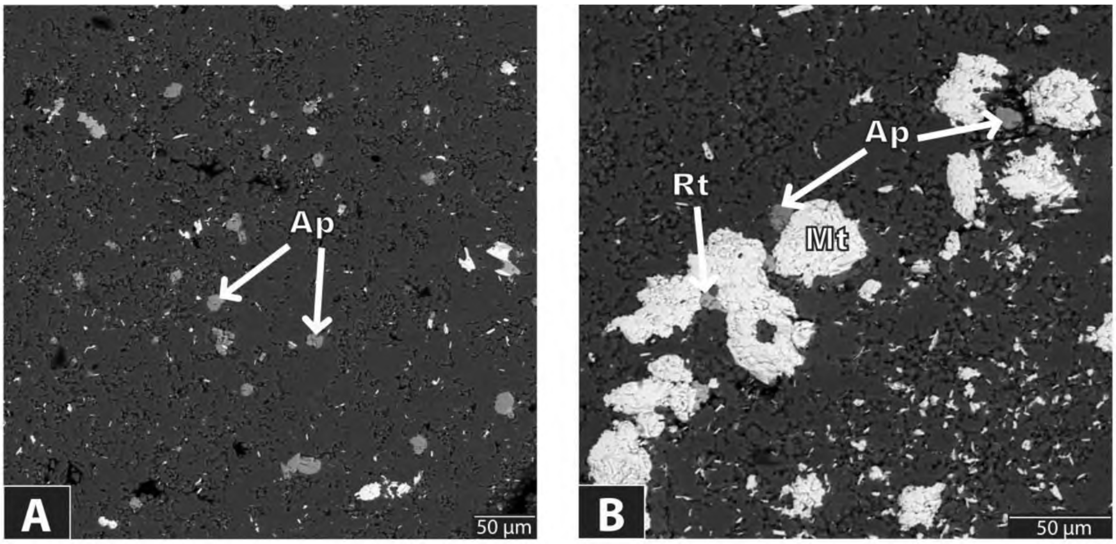

Figure 3.17. Back scattered electron (BSE) images. A) Small sub- to euhedral apatite disseminated within colloform quartz along with microplates of hematite. B) Martite at the rim of a globular structure exhibiting concentric layering. Ap = Apatite, Rt= Rutile, Mt =Martite.

Reddish-grey BIF with wavy lamination

These BIF strongly resemble the rocks of the previous group. The undulating banding consists chiefly of microcrystalline quartz alternating with bands of cryptocrystalline quartz and the overall texture is enhanced by later brecciation (Fig 2.4, sample VLT41). The main difference is the ample amounts of hematite contained in these rocks which also defines a marked directional fabric, visible only on the microscopic scale (Fig. 3.18, entire A). Hematite is distributed almost evenly within the bands and despite its presence, these BIF are still very silica-rich as macroscopic observations and later whole-rock geochemical data also confirmed (up to 83.95 SiO_2 wt. %). The planar fabric is more pronounced in specific microbands, yet it is well-developed in almost every band. The well-aligned hematite particles seem embedded in quartz, are very fine-grained and generally show a platy habit. Patches of coarser microplaty hematite exhibiting broadly parallel orientation to the main fabric also occur (Fig. 3.18, C). Strips of microcrystalline quartz showing grains stacked in a specific manner on closer observation also stand out as a feature of this preferred orientation (Fig. 3.18, B).

Development of schistose-like fabrics can result in hematite-rich rocks where constituent grains of platy shape are present and share a preferred orientation which was imposed to them by metamorphic processes or tectonic stresses (Rosière et al, 2001). The observed fabric may have formed for example in shear zones, under tectonic stresses, in the presence or not of pressure solution which would dissolve any earlier oxide and form platy hematite elongated in the plane of maximum compression. The crystallographic *c* axis of hematite is shorter than the *a* axes, thus the planes of the fabric coincide with the hematite c-faces (Blake et al, 1966). Even though this texture cannot be resolved with certainty, it is most likely not related to any primary fabric and is indeed a secondary feature associated with stresses build during or after silicification.

Siderite is scarcely found disseminated in the bands and ranges from 50 to 80 microns in size (Fig. 3.18, D, inset b). Apatite is rather common and occurs as sub- to euhedral tabular crystals of 20-40 μm though rarely it reaches sizes of 80-100 μm. Locally apatite crystals are arranged in a linear fashion which might be related to the overall orientated texture (Fig. 3.18, E). Although it is rather appealing to explain this distribution of apatite as a sedimentary or diagenetic feature, these rocks show an intense alteration which is texturally retentive only

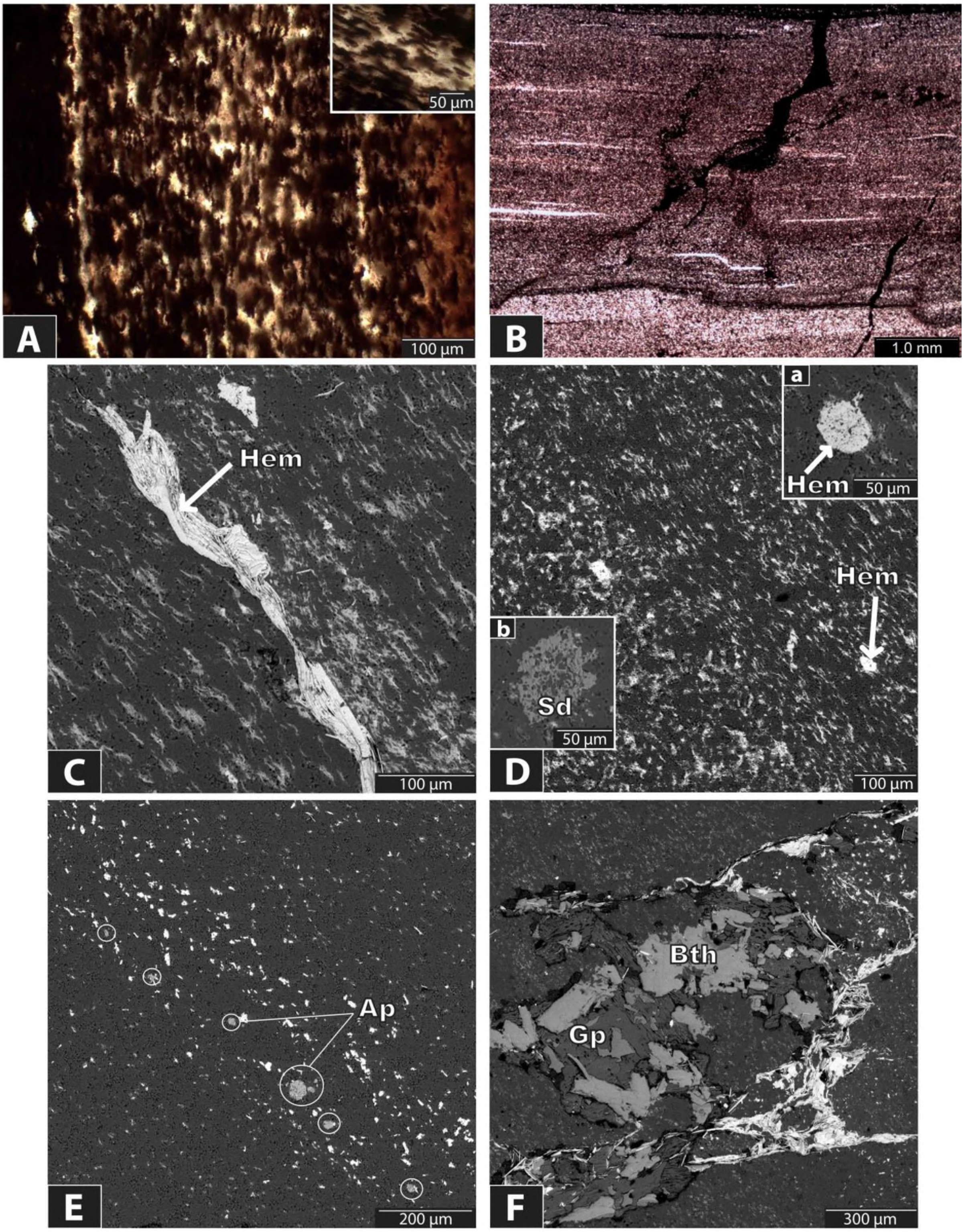

Figure 3.18. Back scattered electron (BSE) images except from A and B which were taken under transmitted light. A) Hematite microplates defining a marked directional fabric, most likely stress-related (PPT). *Inset*, detail of the same texture. B) Microcrystalline quartz crystals are also arranged in a specific manner and form parallel strips (PPT). C) The crystallographic c- axes of the individual hematite grains lie roughly parallel to each other, thus forming a preferred orientation which is also followed by coarser hematite plates. D) The shape and distribution of some hematite aggregates (bright spots) suggests that they might represent former apatite that has been replaced.

Figure 3.18. (continued) *Inset a*, possible pseudomorph of hematite after apatite. *Inset b*, siderite of 50 μm disseminated within banding. E) Linearly arranged apatite is thought to represent a secondary feature related to the general preferred orientation rather than a diagenetic characteristic. F) Gypsum + berthierine assemblage and associated hematite are commonly filling open space. Ap = apatite, Bth = Berthierine, Gp = Gypsum, Hem = Hematite, Sd = Siderite.

in terms of a still recognized layering. The size, shape and distribution of some coarser hematite grains, all reminiscent to that of apatite found in the same rocks, suggests that hematite might have metasomatically replaced apatite grains (Fig. 3.18, D, inset a). This is further supported by small amounts of phosphorus that was detected by EDS at the rim of some of these grains. Gypsum and prismatic berthierine of typically 150-200 μm in size are very common and have infilled almost every open space produced by brecciation (Fig. 3.18, F). Microplaty to specular hematite is found either associated with the above or forms separate veins. Rotated micro-fragments from the rock usually occur within these mineralization assemblages.

Silicified BIF - Summary

mineral	**Silicifired BIF**		
	markedly preserved banding, chert and replacement breccias	creamish-grey with wavy lamination	reddish-grey with wavy lamination
microcrystalline quartz	●●●	●●	●●
macrocrystalline quartz	●●		
cryptocrystalline quartz		●●●	●●●
microplaty hematite	●	●	●●
cryptocrystalline hematite	●		
martite	●	●	
specularite	●	●	●
siderite	●	●●	●
calcite		●	
gypsum	●	●●	●
celestine	●		
tourmaline	●	●	●
berthierine	●	●	●
muscovite	●	●●	
rutile	●	●	
zircon	●	●	
xenotime	●	●	
APS minerals	●	●	
apatite	●	●	●
REE phosphates	●		
chromite	●		
cuprite	●		
galena	●		

Table 3.5. Mineralogy recorded in the various textural subgroups of the silicified BIF. The black dots (one to three) represent the observed relative abundance of the minerals in each group.

3.3.3 Brecciated BIF

Analytical petrographic examination revealed that part of these rocks most likely represents metasomatized equivalents of the unaltered Griquatown iron-formation. This is indicated by many of the textures presented below and their stratigraphic position further supports it. Nevertheless, brecciated BIF were grouped as such because of: i) the presence of a sufficient number of textures showing clearly portions of BIF within an iron-rich matrix, ii) an ubiquity of different textures creating a highly variable stratigraphic profile, iii) the existence of silica-rich portions, chiefly identifiable as BIF-remnants, in sharp contact to iron-rich or even highly iron-rich portions, especially when moving upwards closer to the iron ore, iv) the change in the appearance of banding which is characterized by a general absence of microlamination in a strict sense and synchronous domination of an irregular type of banding and finally v) the higher occurrence of secondary breccias of different types (see also paragraph 3.3.5) compared to the lower stratigraphic parts.

Breccia with Fe-matrix and BIF-clasts

These rocks essentially consist of: i) a matrix showing variable iron content and ii) BIF-clasts represented by whole BIF-portions of variable size or even individual bands, as far as it can be drawn from the limited lateral observation. The grey (occasionally metallic) matrix seen in these rocks has typically higher content of iron and is composed of ubiquitous randomly orientated hematitized grains representing possibly martite grains set in a groundmass of quartz and microplaty hematite (Fig. 3.21, F). Similarly distributed magnetite, rather dispersed than concentrated in layers, can be seen commonly in the Griquatown iron-formation. Small grains of apatite were observed in lensoidal quartz-rich zones (Fig. 3.21, F, inset). The more reddish matrix observed in other samples consists either of i) cryptocrystalline (dusty) hematite impregnating quartz along with some dispersed oxidized grains, possibly of martite (Fig. 3.20, entire E), or ii) a very fine-grained mesh of hematite and quartz which most likely reflects fronts of hematitization (Fig. 3.20, A) and will be further discussed below. Within the BIF-clasts, there is evidence for martite developed in microlaminae, sometimes wrinkled, or disseminated in a chert matrix along with microplaty hematite (Fig. 3.20, entire F).

The most striking feature of what could represent alteration fronts bringing in iron is the presence of relatively unenriched silica portions showing diffused contacts with iron-

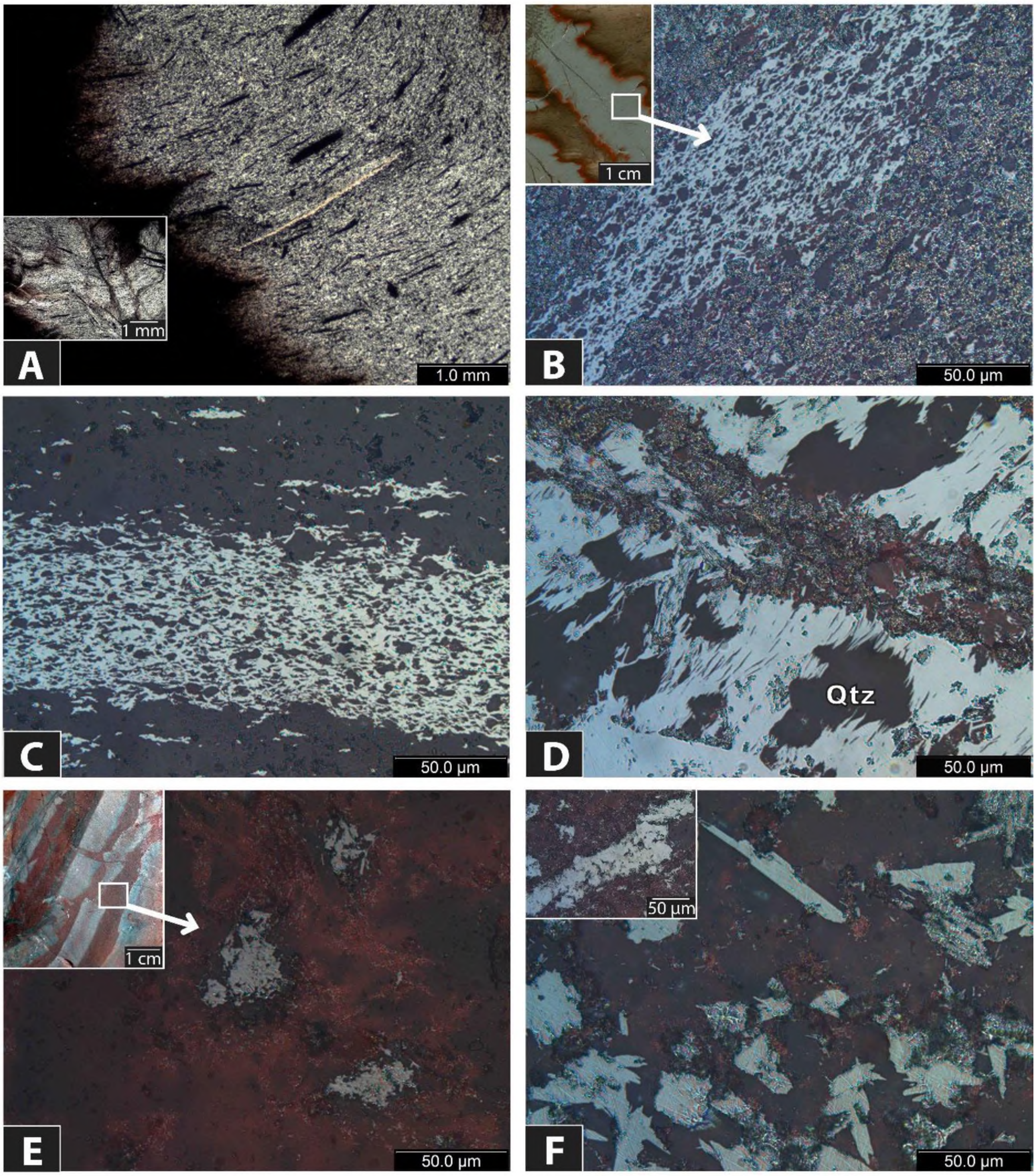

Figure 3.20. A) An iron-rich front (left) hematitizing part of the BIF. Note the preferred orientated fabric shown by hematite aggregates that might be controlled by primary mineralogy (PPT). *Inset*, a brittle structure resembling crenulation cleavage, produced by subparallel hematite-filled cracks superimposed on the main fabric (PPT). B) On the microscopic scale, the directional fabric consists of an orientated interconnected meshwork of microplaty hematite within a groundmass of very fine-grained hematite and quartz (XPR). *Inset*, scanned thin section of the same sample. C) Same as B, but within the quartz matrix of an unenriched portion (XPR). D) Parallel orientated hematite microplates and quartz with a peculiar feathery appearance filling veins (XPR). E) Red matrix (iron-rich) consisting of dusty hematite impregnations and possibly martite (XPR). *Inset*, BIF-clasts within iron-rich matrix (rock slab). F) Microplaty hematite appearance within a BIF-clast (XPR). *Inset*, martite microlaminae in the same sample (XPR). Qtz = Quartz.

enriched parts (red matrix) while a directional fabric, very similar to those observed under presence of stress in metasomatized and deformed rocks, preserves the lateral continuity between them (Fig, 3.20, A). Furthermore, this developed fabric of preferred orientation is expressed by parallel streaks consisting of an orientated interconnected meshwork of hematite microplates (Fig. 3.20, B and C). On a mesoscopic scale, the alteration front is developed in all directions, intruding the BIF and brecciating it (see also Appendix II, figure 2.4). Sedimentary or diagenetic characteristics of the Griquatown iron-formation can be considered as an explanation for the observed fabric. Parallel orientation on the micro-scale in the protolith is defined by discontinuous magnetite streaks, slightly thicker layers of possibly fine-grained carbonates and abundant very thin and discontinuous bands of unspecified mineralogy. This diagenetic feature of the protolith could be not only preserved in the brecciated BIF but also enhanced during alteration, becoming more conspicuous. A possible explanation involving preservation of the primary fabric could be the development of a type of chemical brecciation (Sawkins, 1969) causing dissolution, which could be superimposed upon the previous anisotropy (i.e. mineralogical banding of the protolith) that controls also the infiltration of the solution on a larger scale. Alteration controlled by primary textures, dissolving primary minerals and replacing them by the contrasting binary mineralogy of quartz and hematite can enhance greatly such a preferred orientated fabric in concert to other similarly enhanced textures that were described earlier.

Some specimens show structures resembling that of an asymmetric crenulation cleavage visible in deformed rocks (Fig. 3.20, A, inset). In detail these are actually subparallel sets of brittle cracks now filled mainly by hematite, suggesting that they have been utilized by the introduction of a pressurized fluid. These fractures are superimposed on the main directional fabric described above, creating this cleavage effect. The possibility of such fabrics to have been developed or at least affected by the presence of stress in shear zones cannot be excluded since regional scale folds and thrusts are not rare in the region. The reason for stress concentration could be either directly tectonic or a fluid pressure build up related to tectonism.

The paragenesis of gypsum + berthierine ± tourmaline was commonly observed in these rocks. Large euhedral gypsum crystals up to 500 μm in diameter have been noted within a quartz matrix with planar fabric displayed by hematite (Fig. 3.21, entire A). These crystals almost always contain berthierine, quartz and hematite inclusions. Again, their

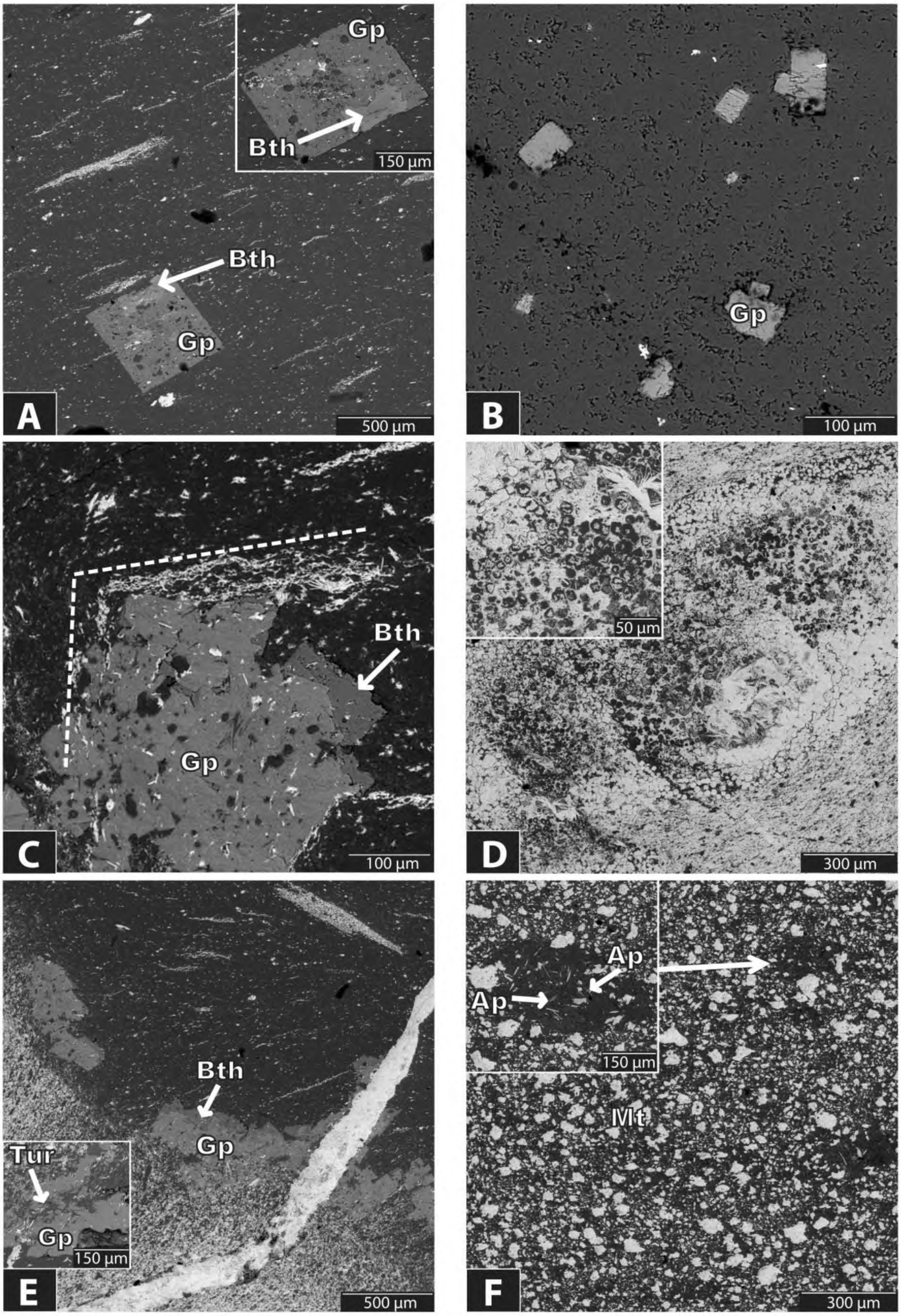

Figure 3.21. Backscattered electron (BSE) images. A) Euhedral gypsum with berthierine, quartz and hematite inclusions within a quartz matrix with parallel orientated hematite aggregates. *Inset*, another similar crystal. B) Occurrence of euhedral gypsum in an almost hematite-free quartz groundmass is common in irregular silica-rich portions found in the brecciated BIF. C) Hematite-fabric wrapped around gypsum and berthierine suggests a syn- or post-genetic origin for the first.

Figure 3.21 (continued). D) Spheroidal hematite and quartz with hematite inclusions contained in a larger lenticular structure. *Inset*, detail of the same area. E) Gypsum + berthierine occurring along the contact of the hematitization front with an unenriched silica-rich area and a later crosscutting hematite vein. *Inset*, tourmaline needles associated with gypsum. F) The grey matrix consists of abundant dispersed martite and microplaty hematite set in a quartz groundmass. *Inset*, apatite is more easily visible within quartz micro-lenses. Ap = Apatite, Bth = Berthierine, Gp = Gypsum, Mt = Martite, Tur = Tourmaline.

occurrence is enigmatic. The planar fabric can be locally seen being deflected around large gypsum grains which suggests a synchronous or later formation with that of gypsum (Fig. 3.21, C). Assemblages of gypsum, tabular berthierine and acicular tourmaline are usually concentrated within or along the edge of the hematitization front, proposing that they might be related to it (Fig. 3.21, entire E). In other cases, gypsum is found in an almost hematite-free quartz matrix which is part of irregular silica portions within the brecciated BIF (Fig. 3.21, B). These crystals might have co-precipitated with quartz, suggesting a secondary or recrystallized origin for at least some of the silica in these rocks.

On the other hand, these silica-rich portions could be part of the lenticular (podded) bedding found in the upper stratigraphic horizons of Griquatown (Beukes and Klein, 1990) and hence gypsum might have formed later. Apart from gypsum and specularite veins, a set of crosscutting veins consisting of parallel orientated needle-like microplaty hematite and quartz of “feathery” appearance were noted (Fig. 3.20, D). Finally, microscopic concretions of hematite enveloped by quartz and spheroidal hematite were found contained in large lenticular structures of up to 1 mm in size (Fig. 3.21, entire D). It is likely that these represent an oxidized equivalent of textures found in the Griquatown iron-formation, some type of allochem (intraclasts, pelloids, ooids) described by Beukes (1980), although hematite oolites with concentric layers can also form as hematite precipitates from fluids (Edson, 1950).

Breccia with Fe-matrix and chert lenses/pods

The distinguishing characteristic of this group is the presence of chert lenses or pods chiefly composed of silica (Fig. 3.22, insets in B and C). There is no doubt that these structures represent metasomatized relicts of the protolith, since they are very common in Griquatown iron-formation and have been explained as starved ripples deformed by compaction (Beukes and Klein, 1990). The main difference is that these pods now consist entirely of microcrystalline quartz and rarely by finely disseminated hematite whereas in the parent rock the main constituents are mainly carbonates and lesser magnetite, quartz and iron silicates such as riebeckite. Sparitic euhedral ankerite or magnetite is preferentially concentrated along the margins of the primary chert pods, a texture that is preserved in the altered rock as hematite pseudomorphs showing the same distribution. Moreover, the mineralogy of smaller clasts contained within these pods is now changed to coarser microcrystalline quartz, further indicating the silica alteration affecting these structures (Fig. 3.22, A, inset).

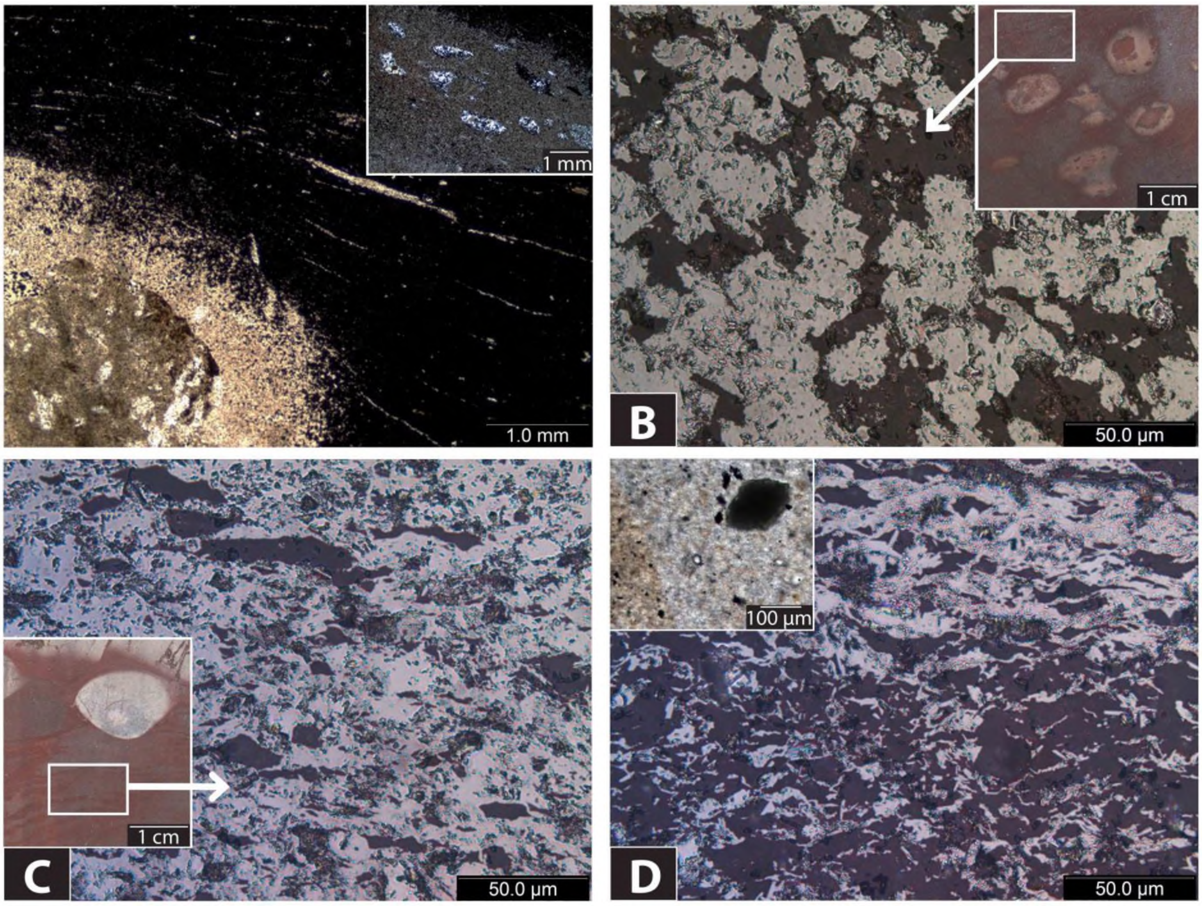

Figure 3.22. A) Silica-rich pod within an iron-rich matrix (PPT). *Inset*, smaller clasts within the pods/lenses consisting of coarser microcrystalline quartz (XPT). B) Abundant conspicuous grains of martite are found in the matrix along with microplaty hematite around the pods (XPR). *Inset*, iron-rich matrix containing these metasomatically replaced lenticular structures (scanned thin section). C) Quartz grains and aggregates in an almost parallel orientation defining a fabric that occasionally wraps around the lenses (XPR). *Inset*, a wider depiction of the same area (rock slab). The appearance of microplaty hematite forming a dense interconnected meshwork, anastomosing around quartz grains resembles the main texture observed in the so-believed enriched *red-grey* laminated BIF (XPR). D) *Inset*, siderite grains of secondary origin within chert pods suggest a possible relationship with the alteration of the pods (PPT).

The planar fabric described in the previous group is seen in many cases being deflected around the chert pods and is defined mainly by parallel orientated quartz aggregates or individual grains (Fig. 3.22, A, C). The iron-rich matrix is characterized by the presence of conspicuous martite (Fig. 3.22, B) and microplaty hematite. The latter is seen wrapping around quartz grains creating a dense mesh that resembles the textures noted in the iron-rich *red-grey laminated* BIF (Fig. 3.22, D). Macrocrystalline quartz veins are common and show crosscutting relationships with clearly later hematite veins which allows the possibility of their involvement in the silica enrichment of the chert pods. Siderite, although scare, is also found enclosed within these lenticular structures (Fig. 3.22, D, inset) and provides further clues for the involved fluid. Finally gypsum + berthierine veins are ubiquitous and in some samples they fill extensive open space.

Breccia with highly enriched Fe-matrix and BIF-clasts

This section describes the mineralogy and textures found in the direct footwall of the high-grade iron ore. The two discriminant features are: i) the matrix of these breccias which is believed to be highly enriched in iron content, up to almost iron ore quality (> 60 % w.t.) in places, based on macroscopic observations and ii) the very sharp contacts shown between some clasts or fragments and the matrix. There are many indications suggesting that clasts and irregular bands found in these rocks are BIF-derived, rather than shaley material slumped from above. The latter scenario though cannot be excluded and in fact it might be the only way of explaining some of the geochemical signatures presented in the next chapter.

Red iron-rich material usually seen as thick irregular bands exhibiting relatively sharp contacts with a highly iron-enriched (grey) matrix is indicative of BIF presence. Occasionally, these contacts are marked by fractures filled with microplaty or specular hematite. The red bands contain scarce martite grains which become very dense and abundant within the iron-rich portions (Fig. 3.23, C). The matrix consists also of euhedral quartz, microplaty hematite and sparsely dispersed microscopic grains of apatite. The characteristic discontinuous martite macrolaminae are present in both the unenriched and enriched parts. Apatite is also found associated with microplaty to specular hematite veins which brecciate former blocky quartz veins in these rocks (Fig 3.23, D). Generally, the highly iron-enriched matrix resembles texturally the massive iron ore but it has additionally higher quartz content while the red portions or bands have very high quartz content and are clearly BIF-derived.

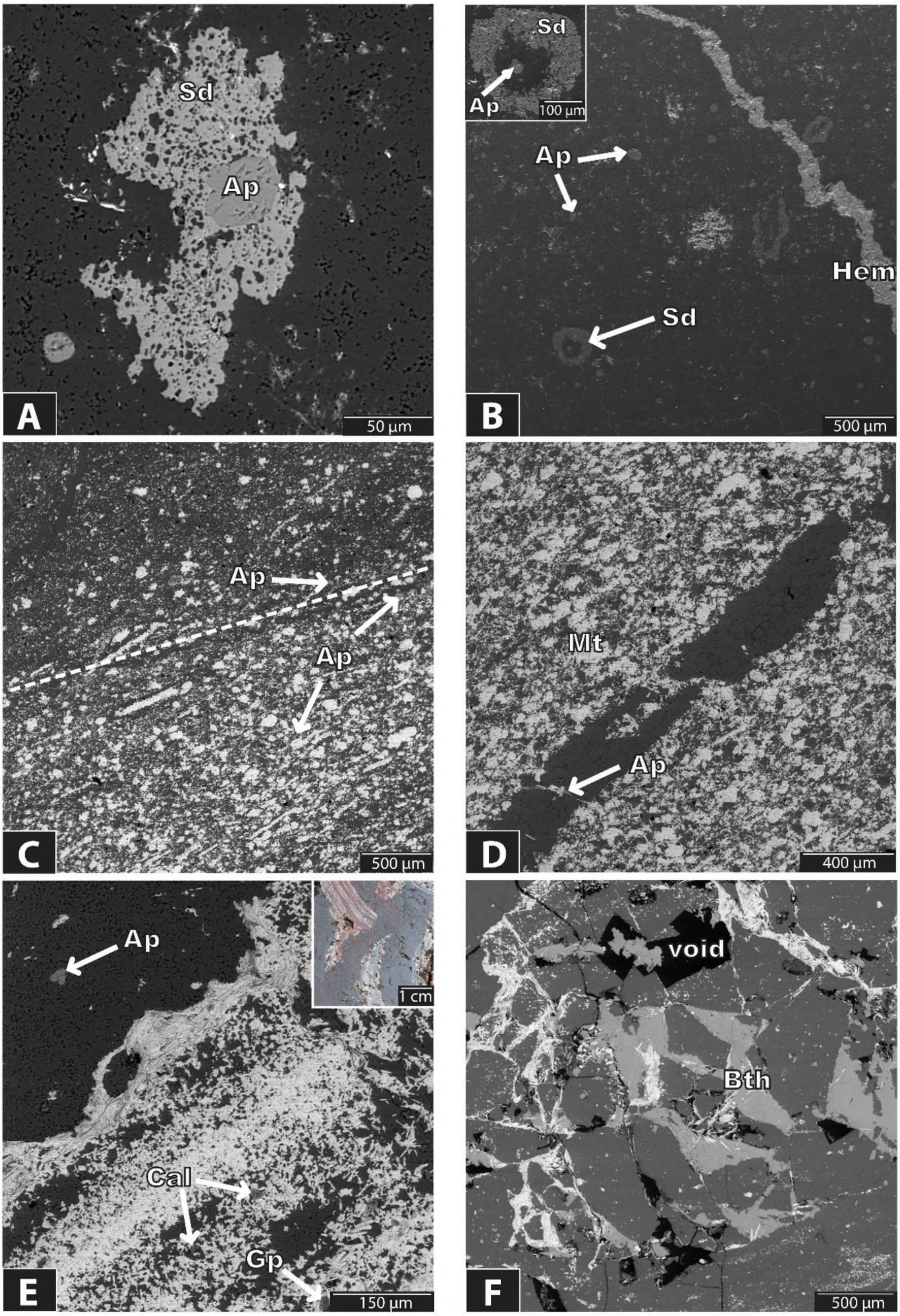

Figure 3.23. All photos shown are backscattered electron (BSE) images. A) Siderite grain with very irregular edges in close relationship with a subhedral apatite. B) Chert matrix with ubiquitous apatite locally enclosed within siderite, the latter showing a silica-rich core. *Inset*, detail illustrating the later formation of siderite compared to apatite. C) Graded contact between the highly iron-enriched matrix (down) and an irregular band of red colour (up). Martite arranged also in macrolaminae is a common

Figure 3.23. (continued) characteristic of BIF. D) Blocky quartz vein being fragmented by later hematite veins in which apatite is also commonly present. E) Alternating microbands of chert and hematite containing microscopic calcite, apatite and gypsum. *Inset*, wider depiction of the same area showing BIF-clasts “floating” within a highly iron-enriched matrix (rock slab). F) Berthierine and microplaty hematite filling open space and causing heavy brecciation to a BIF-clast. Voids of euhedral shape could also represent former gypsum. Ap = Apatite, Bth = Berthierine, Cal = Calcite, Gp = Gypsum, Mt = Martite, Sd = Siderite.

Within some cherty BIF-clasts, high amounts of sub- to euhedral apatite of 50-100 microns occur together with abundant siderite. The siderite can be as large as 500 μm in diameter and is undoubtedly secondary. Most of the times siderite exhibits a pronounced silica-rich core and it might be seen enclosing apatite which supports that it was formed later (Fig. 3.23, B) or during the same event. Locally apatite seems to overgrow siderite (Fig. 3.23, A) but whatever the case is there is definitely a shared affiliation between these two minerals. Although apatite appearance is not well documented in the unaltered BIF such high concentrations within the chert matrix are not very likely to occur in the protolith. Similar occurrences of high apatite content was found within colloform banding or associated with muscovite further down in the stratigraphy. Hence, it is likely that part of the phosphorus present in these rocks is related to a hydrothermal event introducing it or at least remobilizing it. Siderite and apatite are set within a matrix of quartz and finely disseminated microplaty hematite while they are both being clearly crosscut by later quartz or hematite veins. Within or close to some hematite veins microscopic chromite incorporating Ni was picked up by EDS.

Clasts of cherty appearance exhibiting conspicuous banding are locally found in knife-sharp contact with the matrix which macroscopically resembles a massive iron ore (Fig. 3.24, A). In other cases, unenriched BIF-clasts appear to be “floating” within the same matrix (Fig. 3.23, E, inset). A possible explanation is that fragments of the already formed iron ore have slumped below due to the intense collapse brecciation and have been mixed with the altered but not upgraded BIF of the Griquatown. The contacts between the two different types of fragments could have been cemented by iron-rich material during or later of the collapse. In Figure 3.24, A, it can be seen that between the so-considered ore (left) and the BIF-clast (right) there is an iron-rich area with somewhat increased porosity and slightly coarser plates of hematite (see also *inset a* in the same figure). The problems with this scenario though are: i) the “iron ore” fragments have considerably higher content of quartz compared to the high-grade iron ore, as it can be seen from microscopic investigation (Fig. 3.24, B). Furthermore, they consist mainly of randomly orientated microplaty hematite and martite was rarely found whereas in the massive iron ore martite is an important component. ii) This intermediate area of cementation between the two fragments does not always exist and for example in the case of abundant “floating” curved BIF-clasts within a highly enriched matrix the proposed scenario is not so convincing, despite the presence of some coarser hematite around the clasts. One could argue that if the iron ore was completely upgraded before the formation of these breccias, the highly iron-rich fragments should represent part of the ore and should show the exact similar textures. Instead, they show different textures forming a type of low-grade iron ore. Investigation of more samples is required if one wants to provide an elegant explanation for the formation of this section.

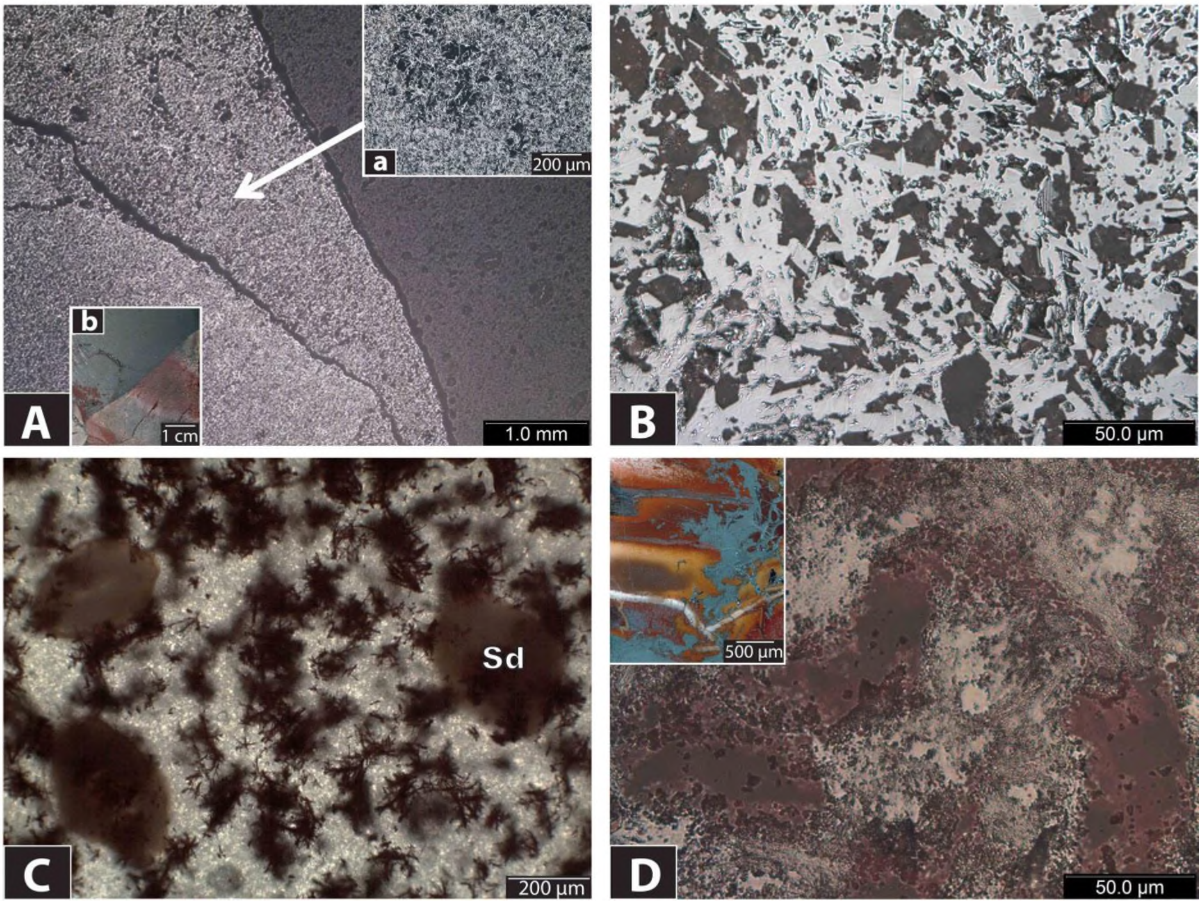

Figure 3.24. A) Sharp contact between a BIF-clast (right) and the highly iron-enriched matrix (left). Note the intermediate area which might be cementing the two fragments (XPR). *Inset a*, detail of this area showing the increased porosity and the slightly coarser hematite plates (XPR). *Inset b*, a wider depiction of the same area (rock slab). B) Microplaty hematite and abundant quartz composes the highly-enriched iron matrix (XPR). C) Siderite and laths of needle-like microplaty hematite impregnating quartz matrix in BIF-clasts (PPT). D) Microplaty to specular hematite vein crosscutting a BIF-clast is accompanied by brecciation and/or leaching of quartz (XPR). *Inset*, a wider depiction of the same area (scanned thin section). Sd= Siderite.

The BIF-clasts frequently show lamination. Apatite was found in the chert bands and gypsum and calcite in the oxide bands (Fig. 3.23, E). Very characteristic is also the appearance of hematite forming laths or sprays of randomly orientated needle-like crystals, impregnating quartz, sometimes together with siderite (Fig. 3.24, C). A possible relationship with resembling iron silicates from the parent rock can only be speculated.

Oxide wt. %	n = 39	STD	Range	Berthierine 1*	Berthierine 2*
SiO_2	22.30	1.75	16.64 - 24.54	22.04	22.40
Al_2O_3	22.62	3.65	13.25 - 26.38	23.01	23.34
TiO_2	0.02	0.01	n.d. - 0.05	0.07	n.d.
FeO_{tot}	42.43	5.95	35.23 - 61.31	42.70	39.63
MnO	0.14	0.05	0.064 - 0.2603	0.26	1.69
MgO	2.67	0.67	1.24 - 3.78	1.13	2.01
CaO	0.02	0.02	n.d. - 0.08	0.02	n.d.
Na_2O	0.04	0.03	n.d. - 0.12	0.08	n.d.
K_2O	0.02	0.01	n.d. - 0.05	0.04	0.29
Total	90.25	1.68	88.16 - 95.58	89.35	90.02
Calculated on the basis of 28 O					
Si	5.03			5.04	5.12
Al	6.01			6.20	6.29
Ti	0.003			0.01	n.d.
Fe	8.00			8.17	7.58
Mn	0.03			0.05	0.33
Mg	0.90			0.39	0.69
Ca	0.005			0.005	n.d.
Na	0.02			0.04	n.d.
K	0.01			0.01	0.08

Table 3.6. Average microprobe analyses of berthierine from different stratigraphic occurrences. Also included are analyses of hydrothermal berthierines from different ore deposits (Slack et al., 1992 and references therein). Berthierine 1^{*} is associated with tourmaline, pyrite, quartz, sericite and minor sphalerite. Berthierine 2^{*} is associated with chlorite in Ag-Pd-Zn veins. n.d. = not detected.

Berthierine was commonly found filling open-space in monomineralic veins or along with hematite. EPMA analyses from berthierine occurring in this as well as in other groups are shown in Table 3.6. Locally, this assemblage is heavily brecciating BIF-clasts (Fig. 3.23, F). Specularitic veins are also very common and can form dense stockworks. The iron-rich fluid forming these veins can be clearly seen micro-brecciating the rock, while possibly dilating the existing fractures and leaching quartz (Fig. 3.24, D). Small-scale wall rock alteration is also noticed when these veins pass through chert. Additionally, whole macrocrystalline quartz crystals within brecciated blocky quartz veins were found completely hematitized in the vicinity of specularitic veins.

Brecciated BIF - Summary

mineral	**Brecciated BIF**		
	highly Fe-enriched matrix and BIF-clasts	Fe-rich matrix and BIF-clasts	Fe-rich matrix and chert lenses/pods
microcrystalline quartz	●●	●●●	●●●
macrocrystalline quartz	●	●	●
microplaty hematite	●●●	●●●	●●●
cryptocrystalline hematite		●●	●●
martite	●●	●●	●●
specularite	●●	●	●
siderite	●●		●
calcite	●		
gypsum	●	●	●
berthierine	●●	●	●
tourmaline		●	
apatite	●●	●	●
chromite	●		

Table 3.7. Mineralogy recorded in the various textural subgroups of the brecciated BIF. The black dots (one to three) represent the observed relative abundance of the minerals in each group.

3.3.4 Iron ore

BIF-bearing impure iron ore

This is essentially a continuation of the previous lithotype. Because of its higher stratigraphic position, the high enrichment in iron and the scarcer unenriched portions it can be considered as an iron ore with random impurities. It is also discussed separately because the samples presented in this section derive from this part of the stratigraphy.

Again cherty BIF-clasts containing abundant apatite and/or siderite are very common. Some apatite grains found within chert are equant, euhedral and reach up to 200 μm in size (Fig. 3.25, B). Siderite is also found filling pore space generally as small anhedral masses usually associated with calcite of similar habit. The BIF-clasts are cemented by a dense matrix consisting chiefly of microplaty hematite as well as of dispersed sub- to euhedral quartz and martite of variable amounts. Unlike the previous group, portions of massive iron ore comprised of dense microplaty hematite and scarcer martite were also noted. Observation of their margins, when possible, allows for them to be characterized as angular to sub-angular fragments, which proves that later collapse brecciation has brought together pieces of the high-grade iron ore with parts of the BIF. Berthierine is a common constituent of the matrix, also filling pore space as anhedral aggregates and possibly dissolving quartz in places (Fig. 3.25, A). Fragments of macrocrystalline quartz veins showing a recrystallized halo are frequently found along with ferruginous BIF-clasts within an iron-rich matrix.

Another mineral noted only from samples deriving from the iron ore is baryte. It is mainly an infill of open space developing large tabular crystals or amorphous masses, the latter seen mostly when filling pore space. Baryte is found always associated with other minerals. Hematite is a typical co-existing phase showing a platy habit and usually occurring as vug linings, similarly to typical gypsum + hematite parageneses described in the previous sections (Fig. 3.25, D). Other minerals associated are berthierine, tourmaline and calcite. The most common and abundant is berthierine which is found as large prismatic crystals within baryte (Fig. 3.25, E). Calcite is rarer but also forms large crystals and is considered as part of the paragenesis. Tiny inclusions of gypsum within baryte were also recorded.

Muscovite is found as small euhedral grains and is associated other with baryte or hematite. It also occurs in the surrounding matrix hence it can be possibly of detrital origin, related to the overlying shales. It represents the main K-bearing phase in the iron ore, the same as in the BIF. Baryte can be seen filling open space up to 5 mm in diameter. Euhedral apatite and quartz are occasionally found enclosed within large baryte masses (Fig. 3.25, C). Baryte is found also as an accessory phase of microscopic grains in specular hematite veins. Ilmenite occurs randomly within brecciated chert matrix and is usually associated with hematite (Fig. 3.25, F).

Specularitic veins are abundant and in places form a dense stockwork of subparallel orientated veins of usually 1-3 mm thickness. These veins are generally composed solely of hematite and only microscopic sulphates or muscovite were found associated. This vein-system develops a type of micro-breccia and within them one can see from small mm-scale chert clasts to individual, possibly recrystallized, quartz grains. Veins of specular hematite can be quite thick reaching cm-scale and when relatively denser can cause a considerable

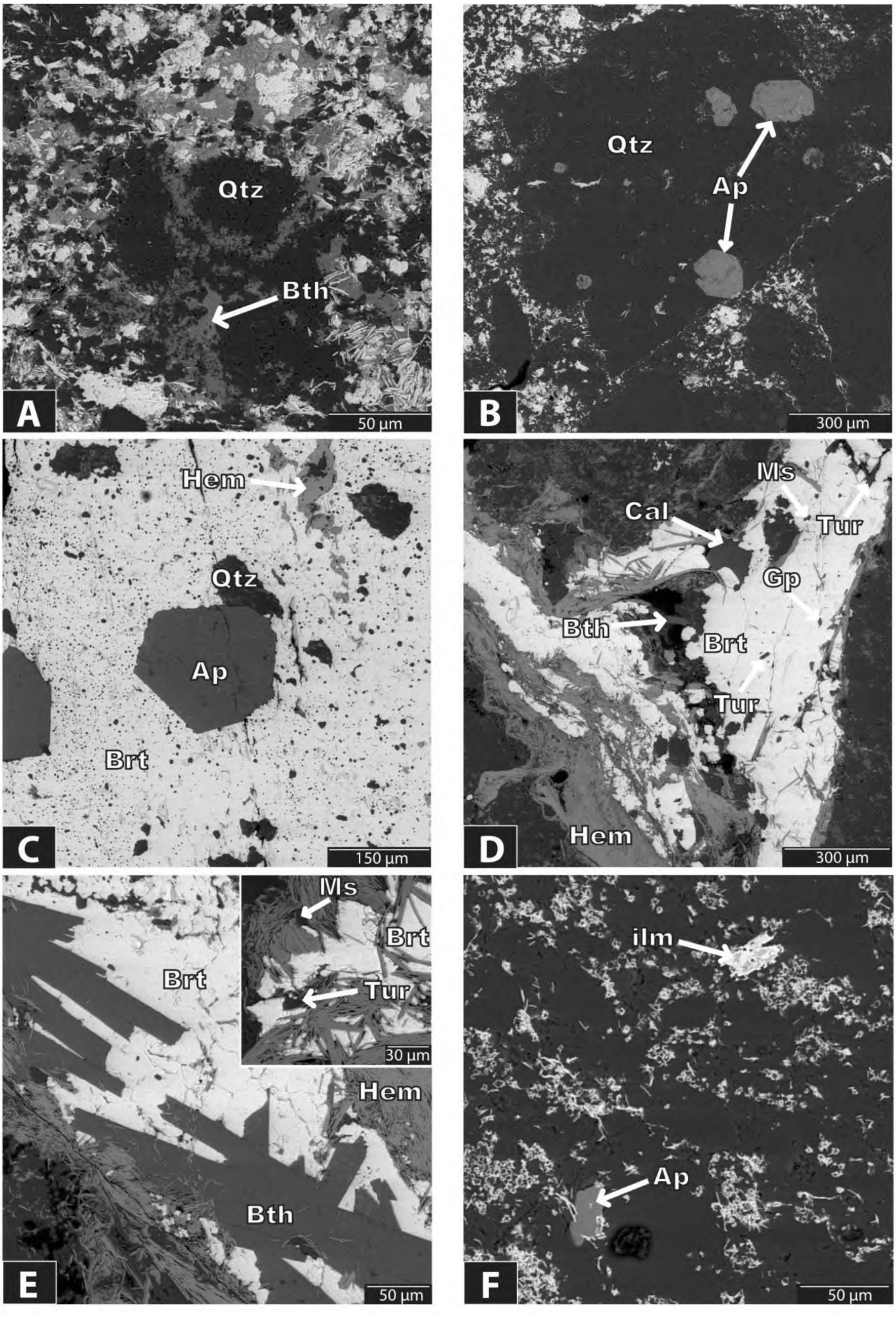

Figure 3.25. Backscattered electron (BSE) images. A) Berthierine as an open-space infill mineral along with quartz, microplaty hematite and martite. B) Large equant to sub-equant apatite within a BIF-derived chert clast. C) Subequant apatite within baryte. Note the distinct microscopic quartz inclusions and the larger grains deriving from the nearby chert clast. D) Baryte + hematite assemblage with lesser berthierine, tourmaline and calcite. Note the microplaty hematite lining the vug and the

Figure 3.25. (continued) microscopic inclusions of gypsum and muscovite within the baryte. E) Euhedral prismatic berthierine crystals associated with baryte. *Inset*, similar assemblage with tourmaline and muscovite. F) Ilmenite associated with hematite within a brecciated chert matrix filled with randomly orientated microplaty hematite. Ap = Apatite, Brt = Baryte, Bth = Berthierine, Cal = Calcite, Gp = Gypsum, Hem = Hematite, ilm = Ilmenite, Ms = Muscovite, Tur = Tourmaline, Qtz = Quartz.

secondary enrichment to the iron ore. It must be noted though that since they are partly related to collapse-induced brecciation, their presence could also indicate mixing of upgraded with non-upgraded material.

Massive to brecciated iron ore

The main iron body has a massive appearance, meaning that only some poorly defined bands of cm-scale can be rarely observed. The reason behind this in not the obliteration of the original layering but the mainly granular appearance of the Griquatown iron-formation and the overlying shales from which it is assumed it was mainly formed. Brecciation of variable intensity is also an important characteristic. In places, unenriched material is still present and later reworking by brecciation and fluid flow is evident. The iron ore matrix can be generally subdivided into: i) dense areas of low to no porosity and ii) areas with higher porosity. Bands consisting of a porous framework of microplaty hematite and martite were scarcely observed in the studied samples. Furthermore, hematite microplates are easily visible in these bands, generally coarser (up to 50 μm) and usually associated with accessory minerals such as berthierine and muscovite which seem to fill the porous space between hematite grains (Fig. 3.26, C and D).

On the other hand, the dense iron matrix comprises compacted hematite microplates which can show size variation (usually between 10 and 30 μm) and martite grains which can be discerned mainly by the different orientation of their hematite plates. It is interesting that martite or even remnants of martite microlaminae can be very conspicuous when found dispersed within a dense matrix of very fine-grained microplaty hematite (Fig. 3.26, B). It can be speculated that compaction of these areas with subsequent dissolution-reprecipitation of hematite can lead to the formation of the denser matrix where martite is most of the times hard if not impossible to discern and hematite appears to be slightly coarser.

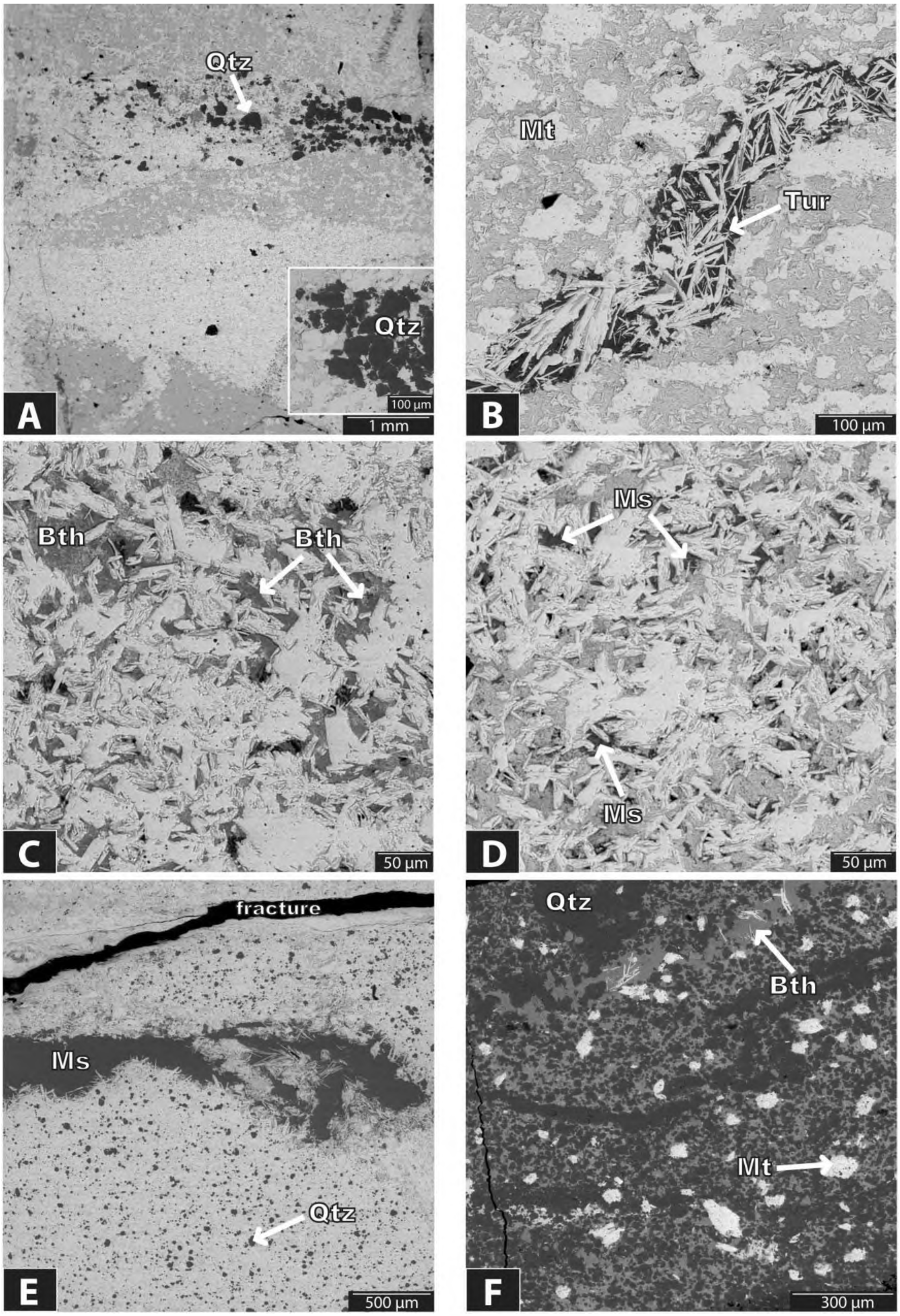

Figure 3.26. Backscattered electron (BSE) images. A) Coarse quartz grains concentrated in a hematite-rich (bright) area comprising martite, microplaty hematite and berthierine. Another distinct (dull) area consisting of very fine-grained hematite and occasionally martite exhibits sharp contact with the first, overall establishing a brecciated appearance for the ore in places on the micro-scale. *Inset*, detail from a similar quartz occurrence. B) Small tourmaline vein with abundant microplaty

Figure 3.26. (continued) to specular hematite. Note the conspicuous martite which seems to preserve in places the characteristic macrolaminae of the original BIF (bottom part). C) Microplaty hematite within a porous area of the ore filled with berthierine. D) Same as C but with muscovite infill. E) Large infill of muscovite and recrystallization of hematite along the margins of the vug. Abundant sub- to euhedral quartz is dispersed within the iron ore matrix. F) Extensive berthierine infill associated with quartz and most likely transported martite. Bth = Berthierine, Qtz = Quartz, Ms = Muscovite, Mt = Martite, Tur = Tourmaline.

Another interesting and common feature observed in places is that of brecciation of the massive iron ore on the micro-scale. In Figure 3.26, A, one can see two distinct areas with sharp, usually fractured contacts in between them: i) a bright area comprising of abundant densely packed martite, coarse and distinct microplaty hematite, berthierine and sub- to equant, sub- to euhedral large grains of quartz and ii) a more dull but equally dense area of very fine-grained hematite and dispersed martite as the one described earlier. This distribution of quartz is typical and along with its coarse size (up to 500 μm) suggests recrystallization if not transportation associated possibly with the fluid which is also responsible for the deposition of berthierine. Quartz is generally in very small amounts but in places ample sub- to euhedral grains can be seen dispersed within the iron ore matrix (Fig. 3.26, E). Finally, quartz in the iron ore is found as aggregates, individual crystals or filling pore space within irregularly unenriched areas or within berthierine-rich infills (Fig. 3.26, F and Fig. 3.27, D, E).

From the silicate minerals present berthierine was identified as the most ubiquitous. It occurs mostly as extensive anhedral masses filling vugs or veins which are subparallel to the poorly defined irregular layering (Fig. 3.27, E). Needle-like acicular or prismatic crystals are also recognized. Berthierine co-exists with quartz and hematite, the latter present also as martite which in cases seems to be transported. Muscovite is also found filling open space but not as frequently as berthierine. Tourmaline + microplaty to specular hematite veins regularly occur within the ore. Apatite is found as sub- to euhedral crystals of variable size within the iron matrix or inside quartz infill. Usually it can be also observed as large infilling masses (Fig. 3.27, F). Baryte was also identified in some samples.

Zircon is commonly found irregularly distributed throughout the iron ore either within veins and brecciated areas or within the matrix (Fig. 3.27, B). Most crystals present distinct core-rim structure and reveal zoning characteristics while they range in size from 10 to 60

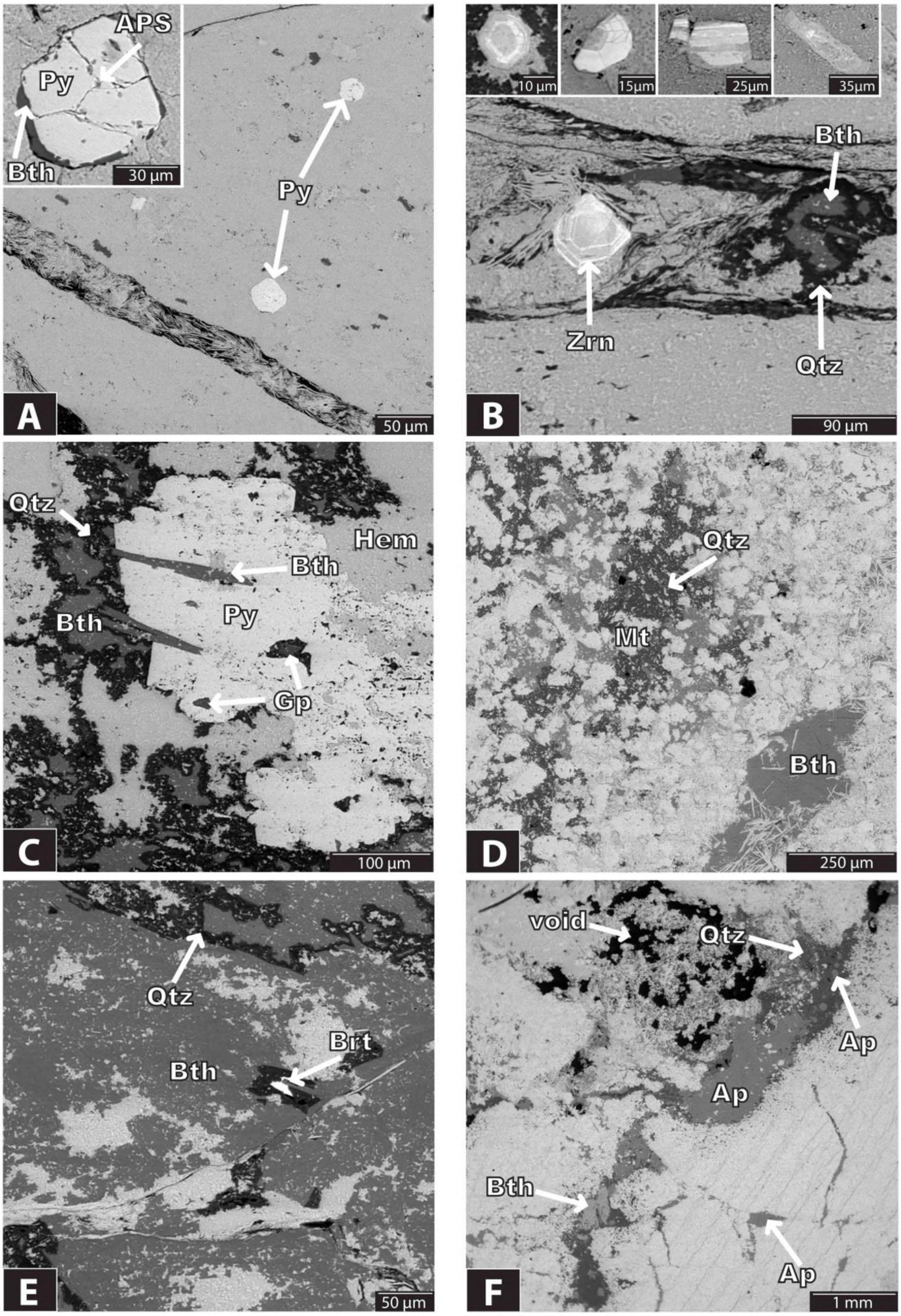

Figure 3.27. Backscattered electron (BSE) images. A) Subhedral pyritohedra within the hematite matrix. *Inset*, pyrite exhibiting a rim of berthierine and extremely fine APS inclusions. B) Zircon showing well-developed crystal faces and zoning within a hematite vein with silicates (muscovite, not shown here). Also shown are zircons of different shapes found in the iron ore suggesting both a

Figure 3.27. (continued) detrital and a hydrothermal origin (see also text). C) Sub- to anhedral pyrite intergrown with acicular berthierine, enclosing small crystals of gypsum or hematite within its mass. D) Quartz associated with berthierine infilling pore space within the iron ore and conspicuous martite. E) Another extensive berthierine infill with disseminated hematite aggregates and tiny baryte within quartz. F) Apatite is seen as individual euhedral crystals within quartz or hematite matrix, as aggregates of densely packed grains or amorphous masses filling open space. Ap = Apatite, APS = Alumino-phosphate-sulphate minerals, Bth = Berthierine, Brt = Baryte, Gp = Gypsum, Hem = Hematite, Mt = Martite, Py = Pyrite, Qtz = Quartz, Zrn = Zircon.

microns. Fractured zircons with slightly rounded shapes that are usually associated with veins might be of detrital origin deriving from the overlying shales. The appearance though of crystals with well-developed faces, sometimes exhibiting prismatic shapes and intergrown with hematite of the iron ore matrix suggest *in situ* crystallization.

Finally, pyrite is common appearing either as sub- to euhedral crystals of 30-50 μm set in the hematite matrix or as large anhedral masses, with occasionally a few well-developed crystal faces, infilling open space (Fig. 3.27, A, C and Appendix II, Fig 2.5). Sub- to euhedral tabular gypsum crystals of up to 50 μm are found as inclusions within pyrite, though usually they range between 10 and 20 μm. Pyrite is also associated with berthierine which locally forms a rim around euhedral crystals. The presence of extremely fine APS minerals occurring as inclusions within pyrite was noted using EDS (Fig. 3.27, A, inset). Coarser grains of APS were furthermore found within quartz infills close to tiny gypsum crystals. All the above emphasize the relationship of the pyrite with the sulphate-bearing fluid which also carries the ingredients for the deposition of silicates as well as phosphorus. Copper sulphides like chalcopyrite were also identified intergrown with and usually being enclosed by pyrite but they are rare comparatively to the second.

Laminated ore

The reader is being reminded that laminated iron ore was seen only in the Sishen cores. Its typical characteristic is the alternation of dense shiny hematite bands showing low to no porosity with dull hematite bands exhibiting higher porosity. Both types of bands are of mm-scale and the produced microlamination is believed to be intimately associated to that of the protolith, which in this case is most likely the Kuruman iron-formation.

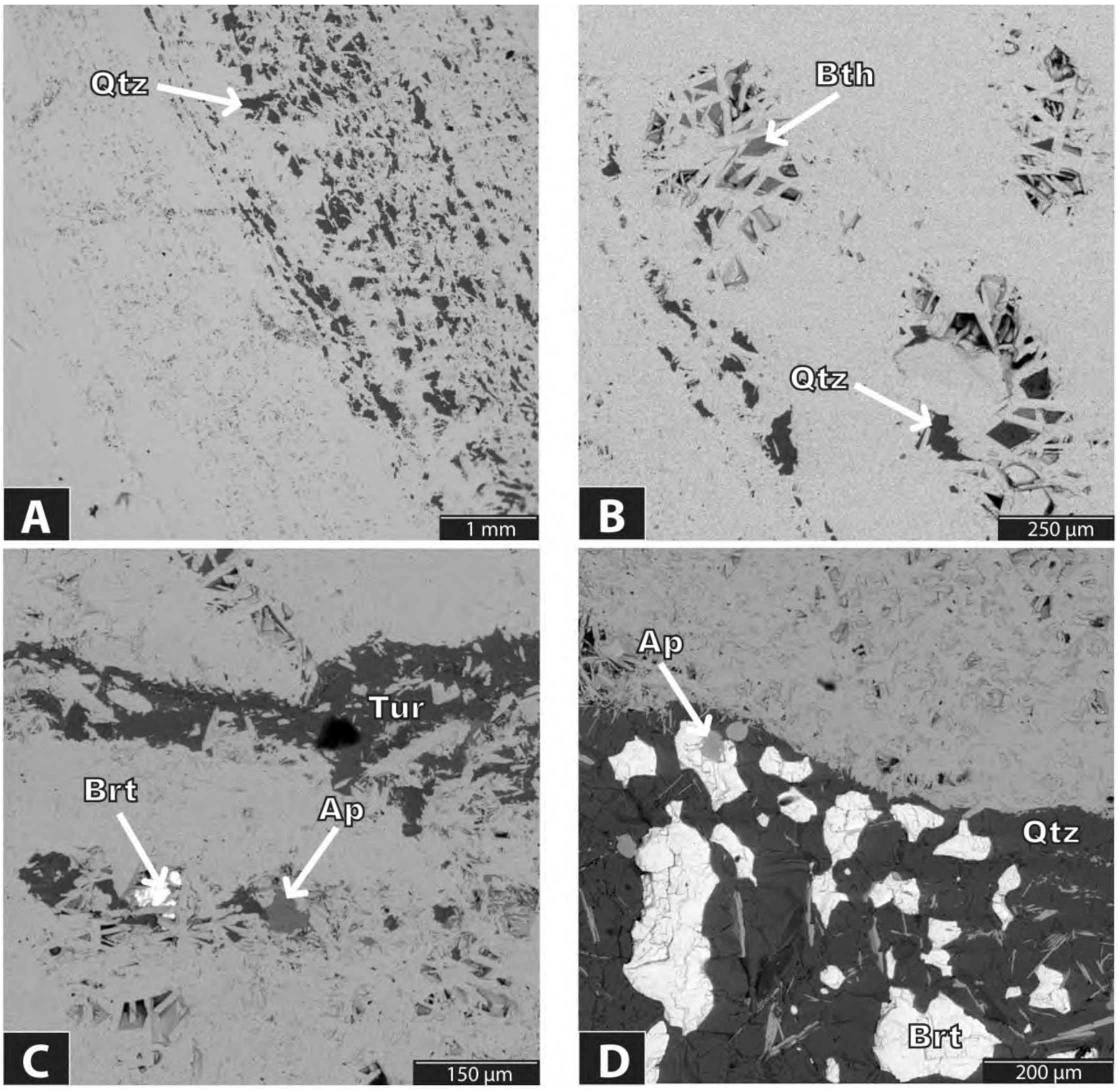

Figure 3.28. Backscattered electron (BSE) images. A) Planar to slightly wavy contact between a dense (shiny) quartz-free hematite band and a band containing ample quartz in the interstices between the microplaty hematite and the martite. B) Small pores within the laminated ore filled with berthierine and quartz. C) Tourmaline vein transecting across lamination and pore space showing specularite, baryte and apatite. D) Crosscutting quartz vein with associated baryte. Ap = apatite, Brt = Baryte, Bth = Berthierine, Qtz = Quartz, Tur = Tourmaline.

The matrix of the dense bands comprises closely packed, interlocking microplaty hematite. Despite being intricately associated with each other, a lot of times the hematite microplates are leaving in between very fine intergranular micro-pore spaces and a faint hint of microlamination can be observed. These bands are widely believed to represent earlier chert mesobands from which the silica has been leached to form secondary porosity. In the studied samples though, macrolaminae of microplaty hematite and martite with significant amounts of quartz were also rarely observed (Fig. 3.28, A, right part). Specularite is found in crosscutting veins and generally in areas of increased porosity. Berthierine occurs within small pore spaces (Fig. 3.28, B). Baryte is a common open-space infill or it might be associated with thick macrocrystalline quartz veins transecting across the iron ore (Fig. 3.28, D). Finally, tourmaline was found developing monomineralic veins (Fig. 3.28, C) or veins containing ubiquitous small xenotime of mostly 5-10 µm in size.

Iron Ore - Summary

mineral	**Iron Ore**		
	Laminated	Massive to brecciated	BIF-bearing impure iron ore
microcrystalline quartz	●	●	●●
macrocrystalline quartz	●		●
microplaty hematite	●●●	●●●	●●●
martite	●●	●●	●●
specularite	●●	●●	●●
zircon	●		
siderite			●●
calcite		●	●
berthierine	●	●●	●●
tourmaline	●	●	●
xenotime	●		
baryte	●	●●	●
muscovite	●	●●	●
ilmenite			●
apatite	●●	●●	●●
REE phosphates	●	●	
pyrite		●	
chalcopyrite		●	
gypsum (inclusions)		●	●
APS minerals		●	

Table 3.8. Mineralogy recorded in the various textural subgroups of the iron ore. The black dots (one to three) represent the observed relative abundance of the minerals in each group.

3.3.5 Veins and secondary breccias

Veins

The establishment of a vein classification falls to the same limitations induced by studying cores. Their development in space and the relationships between veins of different mineralogical content can be only studied on the meso- or micro-scale. Nevertheless, veins were investigated in an attempt to identify the main mineral parageneses and define the major events related to their deposition. Generally, the overall complexity of the hydrothermal vein system and mineralization found in the BIF can be explained to a large degree through continuous hydrothermal circulation of fluids of very similar chemistry for protracted periods of time.

The **first set of veins** that can be grouped together involves muscovite as the main constituent and additionally rutile, zircon, apatite, xenotime, monazite or other REE phosphates which might be present. Zircon found even in acicular shapes and in textural equilibrium with rutile is indisputably of hydrothermal origin (Fig. 3.29, C). The same applies for xenotime (Fig. 3.29, D). Such veins are reported from the whole stratigraphy, however they were found in ubiquity within horizons of silicified BIF. One thing that can be said with relative certainty is that these veins crosscut the banding of the BIF but are in turn being crosscut by the sulphate and silicate associations (Fig. 3.29, A, E). This observation places generally the muscovite associated parageneses to an earlier event within the alteration history of the MIF.

Apatite can be quite abundant within these veins showing well-developed hexagonal or acicular shapes implying direct crystallization from a fluid. In places, abundant APS minerals occur together with lesser apatite almost linearly arranged within muscovite veins that are being transected lengthwise by later gypsum + silicate veins which usually develop in the center of the former (Fig. 3.29, E). The APS were identified using EDS as members of the svanbergite-florencite and woodhouseite-florencite solid solutions, meaning that they contain either Sr or Ca or neither of the previous when being richer in REEs (mainly La, Ce, and Nd). The elements necessary for the build-up of the APS can be traced in their surroundings. The introducing sulphate-bearing fluid can provide the required sulphur, calcium, strontium and possibly aluminum while the phosphorus and the REEs derive from the breakup of the coexisting apatite which furthermore partly survives the alteration. Hence indirectly, the

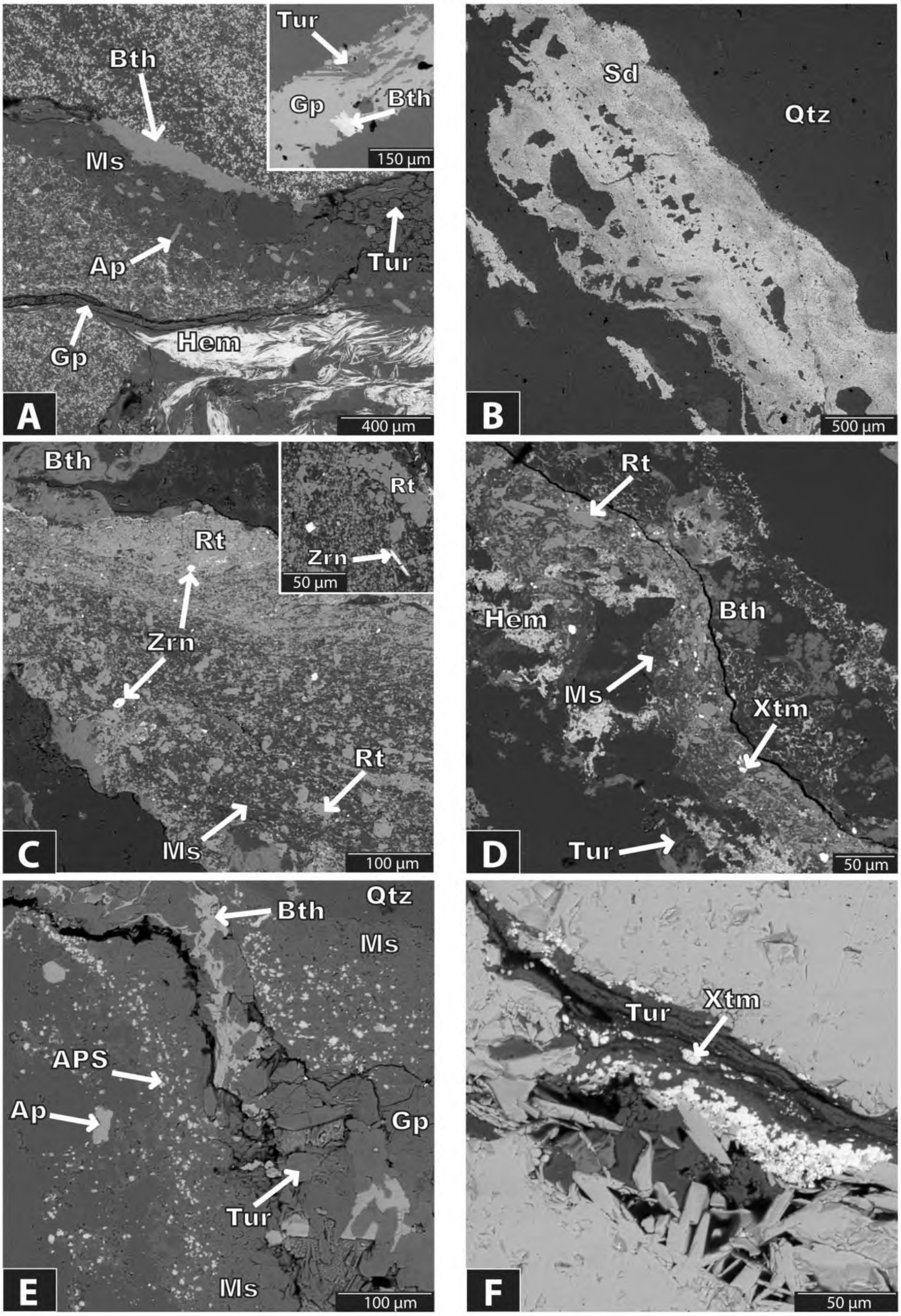

Figure 3.29. Backscattered electron (BSE) images. A) An earlier muscovite + apatite association showing crosscutting relationships with a gypsum + berthierine + tourmaline paragenesis. The presence of specular hematite implies transportation of iron along with the aforementioned fluids. *Inset*, another typical paragenesis of gypsum and silicates. B) Siderite vein with incorporated chert clasts from the surrounding matrix. C) Muscovite vein with abundant rutile and hydrothermal zircon.

Figure 3.29. (continued) *Inset*, detail of the same vein showing zircon of acicular habit. D) Similar muscovite + rutile vein containing xenotime instead of zircon. E) APS (alumino-phosphate-sulphate) minerals linearly arranged along the margins of a gypsum + silicates vein, responsible for their formation (see also text). F) Tourmaline vein containing small subequant xenotime concentrated mostly along the margins of the vein. Ap = Apatite, APS = Alumino-phosphate-sulphate minerals, Bth = Berthierine, Gp = Gypsum, Hem = Hematite, Qtz = Quartz, Ms = Muscovite, Sd =Siderite, Rt = Rutile, Tur = Tourmaline, Xtm = Xenotime, Zrn = Zircon.

presence of these APS minerals provides additional evidence for the earlier origin of the muscovite veins. Muscovite has been also noted from the iron ore in veins containing additionally specularite and minor sulphates. Occasionally, it is also an accessory phase in hematite veins. Remobilization of potassium or a different origin cannot be excluded for some of the muscovite occurrences.

The **second set of veins** that seems to be related to a major event comprising several successive stages includes sulphate minerals (gypsum, celestine, baryte), silicates (berthierine, tourmaline), carbonates (siderite, calcite) and lesser sulphides (mainly pyrite). The close relationship between these minerals has been demonstrated in the previous sections of the petrography. In Figure 3.29, A, a gypsum micro-vein is seen crosscutting a former muscovite + apatite vein, depositing larger gypsum crystals in the open-space along with tourmaline and berthierine. In the inset of the same image, a gypsum vein containing prismatic to tabular crystals of tourmaline and berthierine is shown. Siderite is commonly part of the paragenesis and is found lining the walls of vugs but it also forms monomineralic veins of mm-scale in thickness (Fig. 3.29, B). Calcite might be present instead of siderite in berthierine + hematite veins. Calcite is relatively rare compared to siderite and it was found in slightly higher amounts in the upper parts of the stratigraphy as vein constituent where siderite was only present within BIF-fragments. Moreover, mm-scale monomineralic veins of calcite occur within the ore. Evidence supporting the carbonates association with the sulphate-bearing solution can be seen in Fig. 3.30, D, where siderite and calcite coexist within a perfectly prismatic shape reminiscent of gypsum that was most likely abraded during thin section preparation. The minerals could have also replaced the gypsum crystal later. Veins consisting entirely of silicates and/or hematite are also very common. Microplaty to specular hematite usually forms internal selvages to these veins or is found as randomly orientated plates in their center. The same occurs with sulphate veins even if hematite is not present in the immediate surroundings which clearly shows that iron is being transported

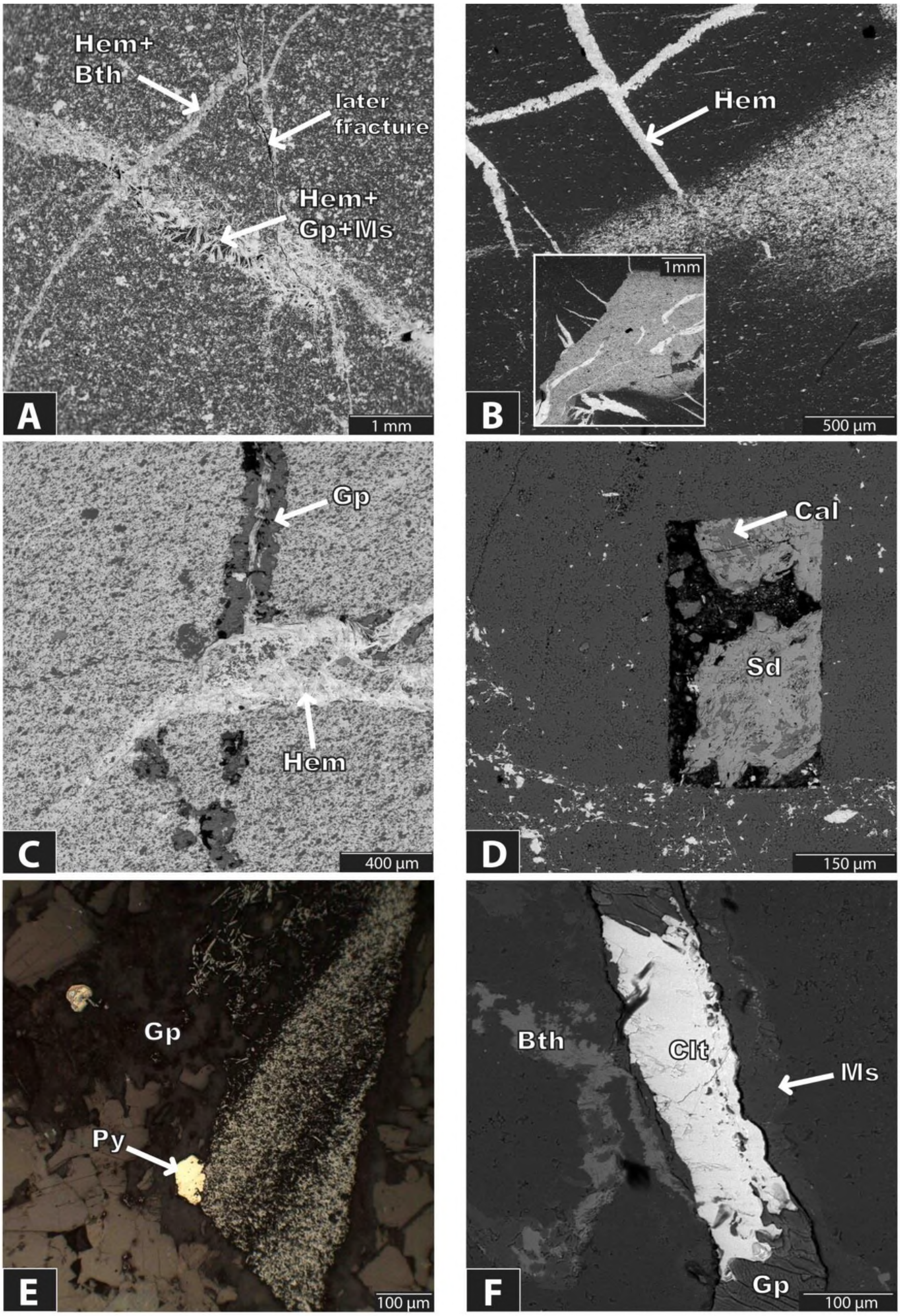

Figure 3.30. All images shown are backscattered electron (BSE) images except from (E) which was taken under reflected light. A) Specularite vein being crosscut by a berthierine + hematite vein of later origin. B) The displacement of a hematite vein favors a later origin for the hematitization front occurring at the right of the image. *Inset*, another area showing the same relationships. C) Specularite veins might propagate across preexisting gypsum veins. D) Calcite and berthierine syn-crystallized

Figure 3.30. (continued) within a remnant gypsum crystal which was either replaced or abraded during thin section preparation. E) Pyrite associated with gypsum suggests crystallization from the same solution. F) Celestine filling partly a gypsum vein. Bth = Berthierine, Cal = Calcite, Clt = Celestine, Gp = Gypsum, Hem = Hematite, Ms = Muscovite, Py = Pyrite, Sd = Siderite.

through these fluids (Fig. 3.31, D). Tourmaline + xenotime veins are also common (Fig. 3.29, F). Although tourmaline is found in assemblages with siderite and gypsum, tourmaline veins overprinting siderite suggest it is also involved in later events (Fig. 3.31, B). Finally, quartz micro-veins are seen crosscutting silicate and gypsum veins proving that silica is mobile even at the latest stages of alteration.

Celestine is relatively rare but occasionally can be seen partly filling gypsum veins or vugs (Fig. 3.30, F). Pyrite is generally scarce within the BIF and only small anhedral to subhedral crystals were observed whereas within the iron ore its size and abundance are increasing. Its close association with gypsum, the sharp contacts between them and its occurrence directly next to gypsum veins imply synchronous crystallization from the same solution (Fig. 3.30, E and Fig. 3.31, A).

Specularite veins are commonly believed to be of late-stage hydrothermal origin in iron ore regimes (Hagemann et al., 2008). The apparent crosscutting relationships are generally in agreement with the above but it can be confirmed that they don't represent the latest stage of alteration observed in the studied rocks. Since iron seems to be carried along with the components required for deposition of the silicate minerals and gypsum, it can be associated with different stages. For example in Figure 3.30, A, a berthierine + microplaty hematite vein dislocates a specularite vein containing small amounts of gypsum and muscovite while in turn it is being dislocated by a later fracture. Hematite veins are also seen being crosscut by the later hematitization front affecting the brecciated BIF of the upper stratigraphy, demonstrated earlier in section 3.3.3 (Fig. 3.30, entire B). Generally, it is common for fracture reactivation to propagate across preexisting veins. Moreover, if the mineralogical content can be easily dissolved as in the case of gypsum it can be assumed that microplaty or specular hematite veins are using preexisting veins or areas filled with gypsum for their propagation (Fig. 3.30, C and Fig. 3.31, C). This could explain the common occurrence of the first traversing along the center of the second. Summarizing, the main mineral parageneses identified are listed in Fig. 3.32 and can be broadly attributed to the **two**

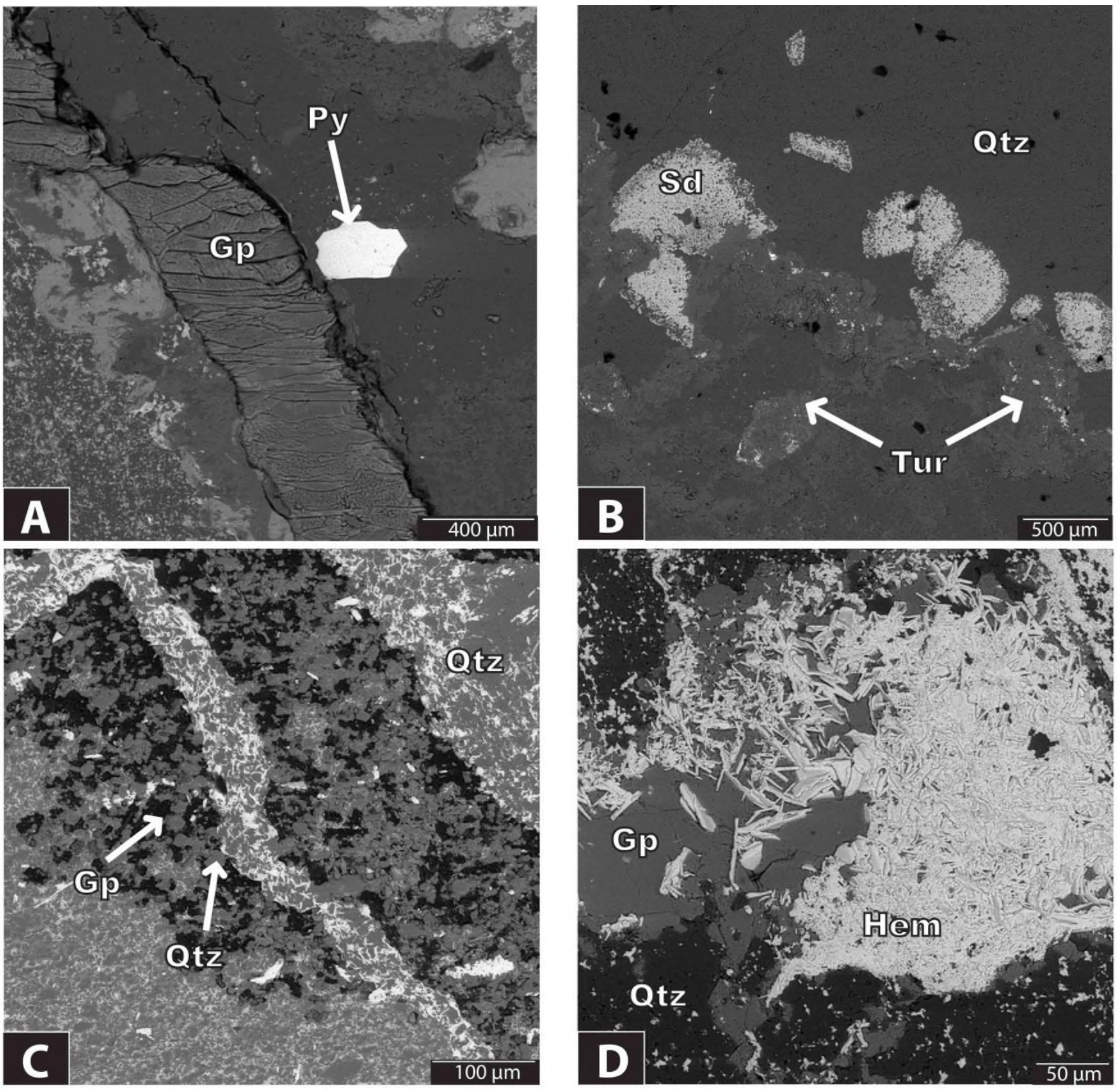

Figure 3.31. Backscattered electron (BSE) images. A) Subhedral pyrite associated with gypsum vein. B) Later tourmaline vein overprinting preexisting siderite within quartz matrix. C) Microplaty hematite veins with silica content brecciates an earlier gypsum micro-breccia implying that later fluids might use easily dissolved preexisting areas for their transportation through the rock. D) Microplaty hematite coexisting with gypsum within a vug proves that iron is being transported through sulphate-bearing fluids. Gp = Gypsum, Hem = Hematite, Qtz = Quartz, Py = Pyrite, Sd = Siderite, Tur = Tourmaline.

major events described above as well as to the successive and possibly ongoing hydrothermal stages of these events. Most monomineralic veins of specularite or macrocrystalline quartz with clearly crosscutting relationships to the previous assemblages represent the latest events recorded.

Manganore BIF	***Iron Ore***
Gypsum assosiated parageneses	*Gypsum assosiated parageneses*
Gypsum (*monomineralic vein*)	Hematite + Gypsum + (Muscovite)
Gypsum + Hematite (+ Quartz)	Pyrite + Gypsum + (Hematite)
Gypsum + Berthierine +Tourmaline	
Gypsum + Berthierine + Hematite	
Gypsum + Celestite	
Gypsum + Pyrite	
Carbonate assosiated parageneses	*Carbonate assosiated parageneses*
Siderite (*monomineralic vein*)	Calcite (monomineralic vein)
Siderite + Gypsum +Tourmaline + Berthierine	Calcite + Bethierine + (Hematite)
Calcite (*monomineralic vein*)	
Calcite + Siderite ± (Rutile) + (Hematite)	
Calcite + (Rutile) + (Hematite)	
Tourmaline assosiated parageneses	*Tourmaline assosiated parageneses*
Tourmaline + Hematite	Tourmaline + Hematite
Tourmaline + Berthierine + Hematite	Tourmaline + Xenotime
Tourmaline + Berthierine	
Tourmaline + Rutile	
Berthierine assosiated parageneses	*Berthierine assosiated parageneses*
Berthierine + Hematite	Berthierine + Hematite
Muscovite assosiated parageneses	*Muscovite assosiated parageneses*
Muscovite + Rutile + Zircon	Muscovite + (Hematite)
Muscovite + Rutile + Xenotime	*Baryte assosiated parageneses*
Muscovite + Apatite + (Hematite)	Baryte + Quartz ± Apatite + (Hematite)
Muscovite + Apatite +APS	Baryte + Berthierine + Hematite ± Calcite ±
	± Turmaline + Gypsum ± Muscovite
	Baryte + Apatite + (Hematite) + (Quartz)
Quartz assosiated parageneses	*Quartz assosiated parageneses*
Quartz (monomineralic vein)	Quartz + Apatite (*veins-pore space infill*)
Quartz + APS + Apatite (*colloform veins*)	*Hematite assosiated parageneses*
Hematite assosiated parageneses	Hematite (monomineralic vein)
Hematite (monomineralic vein)	Hematite + Apatite (*veins-pore space infill*)

Figure 3.32. List of the main mineral parageneses observed in the Manganore BIF and the iron ore. Minerals given in parenthesis show a degree of uncertainty on whether they are part of the paragenesis or not. Hematite and quartz sometimes represent detrital or recrystallized grains from the immediate surroundings of the veins.

Secondary breccias

Secondary breccias are partly the expression of veins presented earlier but on a larger scale and partly the result of the intense karstification and associated slumping of the whole stratigraphy into the underlying carbonates of Campbellrand. These breccias were grouped in four different facies, the main characteristics of which are presented in Fig. 3.34. The three main cements or matrix constituents are: i) gypsum, ii) macrocrystalline quartz and iii) microplaty hematite, quartz and occasionally muscovite (sericite). The fragments in all breccia types are mostly angular and display from crack-style to major rotation. Moreover, the clasts can be cherty or ferruginous fragments of BIF or even vein fragments. It is interesting that some *gypsum breccias* are being clearly crosscut by gypsum veins of certainly later origin, which further supports the multiple successive hydrothermal stages. A very common texture observed is that of smaller crystals of same composition as the mineral cement lining the outlines of each fragment (Fig. 3.33, A). Gypsum crystals are also found in *silica breccias* and seem to be the last to crystallize which suggests that silica supersaturated fluids also carry sulphate. Brecciation is also fluid-assisted as it is proposed by locally relocated BIF fragments which can be traced to their original position and are clearly seen to have moved stratigraphically slightly upwards.

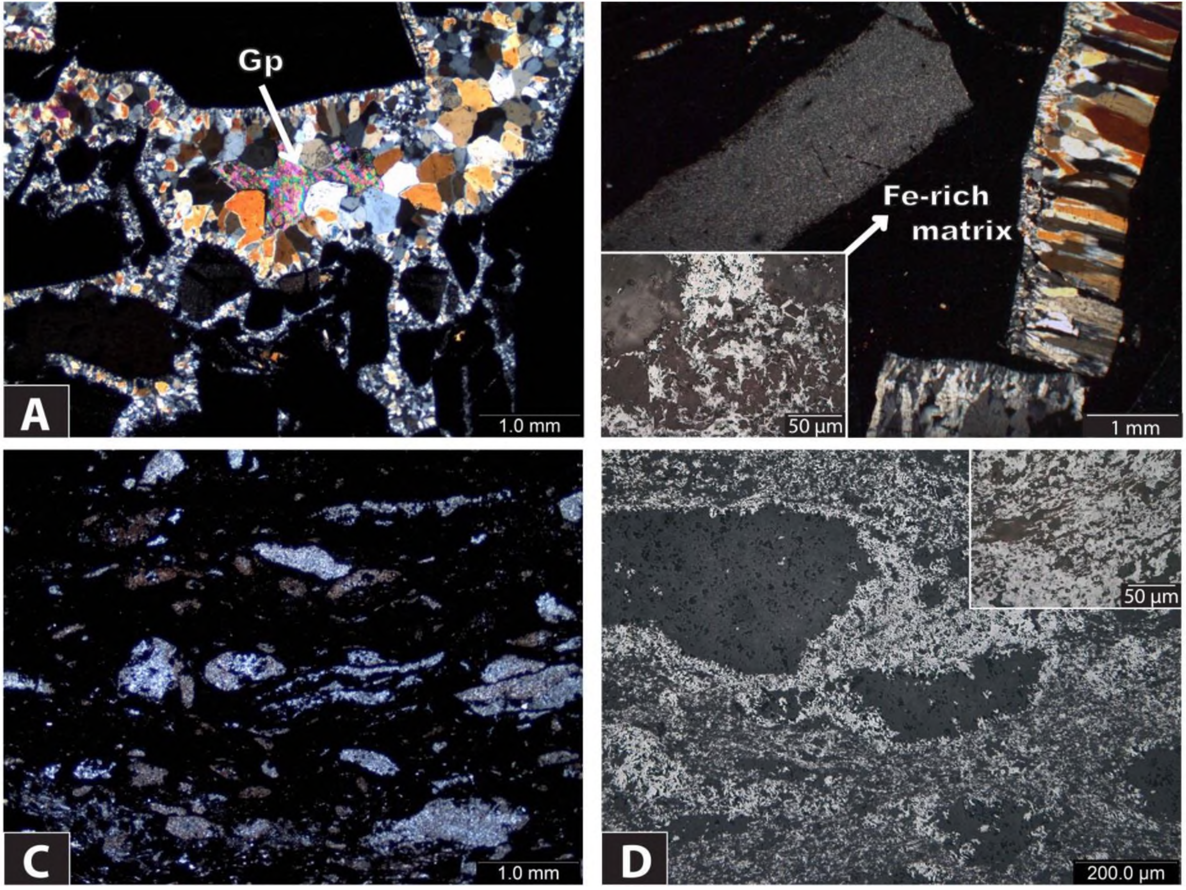

Figure 3.33. A) *Silica (quartz) breccia* with ferruginized and cherty BIF-clasts containing also gypsum crystals in the cement. Note the smaller quartz crystals forming selvages around the clasts (XPL). B) *Hematite breccia* (type 3) with BIF clasts and pieces of fragmented comb quartz vein (XPL). *Inset*, iron-rich matrix consists of microplaty hematite and smaller chert fragments (XPR). C) *Hematite breccia* (type 4) showing generally well-sorted chert clasts (XPL). D) Same breccia type as

Figure 3.33. (continued) C in XPR illustrating the chert clasts being attacked by hematite. *Inset*, dissolution of quartz and a sense of orientated fluid flow is apparent in the matrix (XPR). Gp = Gypsum.

Silica breccias may also show red pigmentation produced by co or post-precipitated dusty hematite. Sericite + hematite matrix in secondary breccias is believed to be related to introduced Al and K from the overlying shales during brecciation collapse. *Hematite breccias* (Type 4) observed in the bottom part of the stratigraphy in core SLT207 show generally well-sorted chert fragments being attacked by microplaty hematite within a hematite-rich matrix, the overall appearance of which indicates enrichment via fluid-flow (Fig. 3.33, C and D). This type could be defined as a solution breccia and although its timing is uncertain it is included in secondary breccias.

Breccia Facies	**Internal Organization**	**Clast shape and type**	**Matrix/Cement**	**Alteration**	**Interpreted Origin**
Type 1 Gypsum 	monomictic, matrix- to clast-supported breccia, crack-style to major rotation, poorly sorted	angular fragments of ferruginous and cherty BIF	cemented by coarse gypsum crystals	unaltered, crosscuted by later gypsum and/or hematite veins	collapse brecciation, intrusion of sulphate-bearing hydrothermal fluids
Type 2 Silica 	monomictic, quartz cemented breccia, heavily rotated fragments, poorly to well-sorted	angular to sub-rounded ferruginous and cherty BIF fragments	coarse quartz cement	may be hematitized by co- or post-precipitated cryptocrystalline hematite	collapse brecciation, dissolution and mobilization of silica from the BIF, later exploited by iron-rich solutions
Type 3 Hematite 	monomictic, matrix- to clast-supported breccia, heavily rotated fragments, poorly sorted	angular to sub-rounded ferruginous and cherty BIF fragments, quartz vein fragmetns	microplaty hematite-rich matrix together with quartz, both mostly clay-sized, sericite sometimes present	generally unaltered, red-coloured matrix has higher quartz and sericite content, specularite veins	collapse brecciation, introduction of iron-rich fluid and Al and K to the system possibly from higher stratigraphic horizons (shales)
Type 4 Hematite 	monomictic, hematite-rich matrix-supported breccia, little to no rotation, poorly to well-sorted	angular to sub-rounded, elongated fragments mostly of chert band or enriched chert bands, minor hematite-rich clasts	hematite-rich matrix of platy and microcrystalline habit together with clay-sized quartz, martite also present	unaltered, crosscutted by hematite and gypsum veins	faulting + collapse, intrusion of iron-rich hydrothermal fluids and further in situ brecciation (chemical)

Figure 3.34. Different secondary breccia facies identified. Their main characteristics are also tabulated along with a suggestive scenario for their origin and/or alteration.

3.4 Summary

Detailed petrographic investigation of the Manganore BIF and iron ore presented above reveals different forms of hematite and quartz being responsible for localized silica or iron enrichment through a primarily layered-controlled metasomatic alteration combined with dissolution of primary mineralogy and deposition of infill material. The pronounced brecciation and the presence of veins and vugs of mineralization indicate the influence of fluid influx during alteration of these rocks. Nearly every mineral listed in Table 3.9. represents an exotic component in respect to protolith's mineralogy and cannot be attributed to residues from the parent rock without elemental introduction through brines.

Mineral Name	Mineral Formula	Iron Ore	Manganore BIF	SLT cores	Sishen cores
Quartz	SiO_2	X	X	X	X
Hematite	Fe_2O_3	X	X	X	X
Siderite	$FeCO_3$		X	X	
Calcite	$CaCO_3$	X	X	X	X
Apatite	$Ca_5(PO_4)_3(OH,F,Cl)$	X	X	X	X
Monazite	$CePO_4$	X	X	X	X
Svanbergite - Florencite	$SrAl_3(PO_4)(SO_4)(OH)_6$ - $(La,Ce)Al_3(PO_4)(OH)_6$	X	X	X	
Woodhouseite - Florencite	$CaAl_3(PO_4)(SO_4)(OH)_6$ - $(La,Ce)Al_3(PO_4)(OH)_6$	X	X	X	
Tourmaline (dravite-schorl series)	$NaMg_3Al_6(BO_3)_3Si_6O_{18}(OH)_4$ - $NaFe^{2+}{}_3Al_6(BO_3)_3Si_6O_{18}(OH)_4$ -	X	X	X	X
Berthierine	$(Fe^{2+},Fe^{3+},Al,Mg)_{2-3}(Si,Al)_2O_5(OH)_4$	X	X	X	X
Muscovite (sericite)	$KAl_2(AlSi_3O_{10})(F,OH)_2$	X	X	X	X
Gypsum	$CaSO_42H_2O$	X	X	X	
Celestine	$SrSO_4$		X	X	
Baryte	$BaSO_4$	X		X	X
Pyrite	FeS_2	X	X	X	
Chalcopyrite	$CuFeS_2$	X		X	
Rutile	TiO_2		X	X	
Ilmenite	$FeTiO_3$	X		X	
Zircon	$ZrSiO_4$	X	X	X	
Xenotime	YPO_4		X	X	X
Chromite	$FeCr_2O_4$		X	X	
Galena	PbS		X	X	
Cuprite	Cu_2O		X	x	

Table 3.9. Summary of minerals present in the four drill cores of this study within the BIF and the iron ore.

The difficult task of timing and grouping the events responsible for the observed mineralogy certainly requires examination of more drill cores and of larger lateral appearances of the stratigraphy which would allow observation of the magnitude of the alteration features as well as of the relationships between the different veins. However, the observed parageneses can be attributed to two major events with relative certainty. The first event includes rutile associated parageneses as shown in Figure 3.32 and has been observed in the silicified BIF and the iron ore (Table 3.10). The second event involves sulphate-carbonate-silicate parageneses (Figure 3.32) with the main representatives being gypsum, siderite and berthierine. This seems to be definitively a later event and has been recorded in the whole stratigraphy (Table 3.10). Several textures described in the previous sections

mineral	Laminated BIF	Silicified BIF	Brecciated BIF	Iron Ore
microcrystalline Quartz	●●●	●●	●●●	●
macrocrystalline Quartz		●●	●	●
cryptocrystalline Quartz	●	●●●		
microplaty hematite	●●●	●	●●●	●●●
cryptocrystalline hematite	●●	●	●●	
martite	●●	●	●●	●●
specularite	●	●	●	●●
apatite	●	●	●●	●●
REE phosphates		●		●
siderite	●	●●	●	●
calcite		●	●	●●
gypsum	●	●●	●	
celestine	●	●		
berthierine	●	●	●●	●●
tourmaline		●	●	●
baryte				●
muscovite		●		●
rutile		●		
zircon		●		●
xenotime		●		●
APS minerals		●		●
pyrite	●			●●
chalcopyrite				●
cuprite		●		
chromite		●	●	
galena		●		
ilmenite				●
	intercalated*		direct footwall	Ore
	high	stratigraphic depth →		low

Table 3.10. Summary of all minerals and textural varieties found within the four main rock types. The black dots (one to three) represent the observed relative abundance of the minerals in each rock type. Brecciated BIF form always the direct footwall to the iron ore while * laminated and silicified BIF are always below with the second usually forming two or three intercalated horizons of few meters.

suggest that this hydrothermal event might have been expressed by several stages. Meticulous petrographic study has also shown that iron has been mobilized during this event but also certainly later. The specularitic veins are undoubtedly one the latest events recorded but not necessarily the latest as it has been already shown by the presence of silicate + hematite veins crosscutting the first. It seems also that there is a greater abundance of specularite towards the upper part of the stratigraphy. Generally, the silicification textures point to a stage synchronous or later than the initial oxidation of the BIF. It is noteworthy that the silicified BIF are characterized by all different textures of quartz and especially by the cryptocrystalline variety. Late stage mobility of quartz is represented in the upper part of the stratigraphy in both brecciated BIF an iron ore by the occurrence of macrocrystalline quartz veins. The combined Table 3.10. further provides insights on the evolution of the recorded parageneses across stratigraphy. For example, siderite seems to be more rare within the upper stratigraphic parts whereas at the same calcite is more commonly found. Baryte and pyrite are recorded almost entirely from the iron ore while gypsum is found in the ore only as small inclusions in sulphates and sulphides. The implications of all secondary minerals to the overall alteration and possibly to the ore formation are discussed in the final chapter where a possible genetic model is also proposed.

Geochemistry

Chapter 4

4.1 Sample selection and geochemical groups

BIF are fairly heterogeneous rocks due to significant compositional differences between primary beds and thus bulk rock geochemical analyses can be strongly influenced by sampling. However, this has not discouraged researchers who have clearly demonstrated the general geochemical similarity between large-scale iron-formations of the Precambrian and defined averages such as the Superior type-BIF (McClung, 2006). Kuruman and Griquatown iron-formations are not an exception and show similar geochemical patterns to other iron-formations worldwide, while it is hard to distinguish them geochemically despite of the textural differences between them (Beukes and Klein, 1990, Horstmann, 1995).

Regarding altered BIF and related iron ores, most studies have made little use of whole-rock geochemical data in attempts to interpret and quantify the process of transformation of BIF to iron ore. (Gutzmer et al 2008). Morris (1983) mentions that precise silica-iron ratios of individual specimens have only broad significance, in view of the inhomogeneity of these rocks but also indicates that the importance of these two major components in understanding the origin of altered BIF cannot be disputed. The author strongly believes that geochemical data from a statistically adequate sample size collected on the basis of textural observations which consider the inhomogeneity issue, if combined with detailed textural and mineralogical examinations and a large geochemical dataset from the unaltered equivalent available for comparisons, can still provide meaningful insights into the alteration processes involved, despite any expected bias during sampling.

The main purpose of the geochemical investigation was to be able to directly compare the principal composing material or banding-constituent of the altered Manganore BIF with that of its considered protolith. For that reason, veins of any kind and intensely brecciated samples of clearly secondary origin were avoided as much as possible. The majority of samples selected for analysis were macroscopically categorized as laminated BIF. Thin slabs of ~10 or sometimes up to ~15 cm were cut across banding from as much as relatively homogenous material. Samples from all the other texturally determined groups were also analyzed, with only some of the brecciated BIF displaying a relative heterogeneity. Seven samples were intentionally sub-sampled and hence are not included in the calculated averages below. Whole-rock analytical data for all major element oxides and fourteen trace elements were obtained for a total of 114 samples (including sub-sampling) via x-ray fluorescence (XRF) using the method of Norrish and Hutton (1969). The majority of the analyses (n=66) were carried out on a Philips PW 1480 X-ray spectrometer housed in the Department of Geology, Rhodes University. Supplementary analyses were undertaken for the same elements plus Co, Ba, S, La, Ce and Nd for Sishen samples (n=48) and samples from the Kumba exploration camp (n=23) using a Philips 1404 DW X-ray spectrometer housed in the Central Analytical Facility, University of Stellenbosch. Further details on sample preparation, analytical techniques and raw analytical data are available in Appendix III.

According to the geochemical results obtained, the samples when then grouped on the basis of their dictating components, being SiO_2 and Fe_2O_3. To determine the Fe_2O_3 and SiO_2 values which define each of the four different geochemical groups, their respective concentrations in other iron-formation averages from literature were taken into account. Furthermore, an average for the Kuruman and Griquatown iron-formations was created for this study. The latter was based on analyses of major and trace elements from 98 samples deriving almost equally from both iron-formations and obtained by XRF and ICP-MS techniques (Paul Oonk unpublished data, see also Table 4.2. and 4.3. for more details). Kuruman and Griquatown are considered geochemically similar for the purpose of this study despite some possible minor differences. On the basis of different geochemical and statistical criteria explained below, the four following group were determined:

i) Ferruginous BIF (Fe_2O_3 > 50 wt. %). The total Fe content of BIF ranges from 20 to a maximum of 40 wt. %, where iron is expressed as a mixture of Fe^{2+} and Fe^{3+} and differs between distinct iron-formations (Klein, 2005). The average Fe_2O_3 content of the Superior type-BIF is 43.10 wt. %, the average obtained from the Kuruman and Penge iron-formations is 39.79 wt. % (Gutzmer et al., 2008) and finally the Kuruman-Griquatown Fe_2O_3 average determined for this study is 36.96 wt. %.

GEOCHEMICAL GROUP	HEMATITE CONTENT	SILICA CONTENT	TEXTURAL GROUP	TEXTURAL SUBGROUP
Iron ore	very high $Fe_2O_3 > \sim 90$ %	very low $SiO_2 < \sim 5\%$	Massive to brecciated iron ore	No Subgroups
			Thinly to thickly laminated iron ore	
			BIF-bearing impure iron ore	
Ferruginous BIF	high $Fe_2O_3 > 50$ %	moderate $SiO_2 < \sim 45\%$	Brecciated BIF	Breccia with highly Fe-enriched matrix and BIF-clasts
				Breccia with Fe-rich matrix and BIF-clasts
			Laminated BIF	Grey and red alternating bands
				Reddish-cream and grey alternating bands
				Dull grey and metallic grey alternating bands
				Lustrous red and grey alternating bands
			BIF-bearing impure iron ore	No Subgroups
Altered BIF	moderate $Fe_2O_3 < 50$ %	high $SiO_2 < 65\%$	Brecciated BIF	Breccia with highly Fe-enriched matrix and BIF-clasts
				Breccia with Fe-rich matrix and chert lenses/pods
				Breccia with Fe-rich matrix and BIF-clasts
			Laminated BIF	Grey and red alternating bands
				Reddish-cream and grey alternating bands
				Dull grey and metallic grey alternating bands
Siliceous BIF	low $Fe_2O_3 < \sim 30\%$	very high $SiO_2 > 65\%$	Silicified BIF	Replacement Breccia
				Creamish-grey with wavy lamination
				Reddish-grey with wavy lamination
				Chert breccia with BIF-remnants
			Brecciated BIF	Breccia with Fe-rich matrix and chert lenses/pods
				Breccia with Fe-rich matrix and BIF-clasts
			Laminated BIF	Dull grey and metallic grey alternating bands

Table 4.1. Geochemical groups defined for the analyzed Manganore BIF and iron ore samples and their relationship with the macroscopically and petrographically determined textural groups and subgroups. Note the significant overlaps between the groups owing, to some extent, to a minority of samples from a specific group showing divergent geochemical behavior, when laminated BIF are concerned. Some groups such as the *lustrous red-grey* BIF correlate only to one geochemical group (*ferruginous*), while for example, brecciated BIF show a higher overlap between different groups due to their expected inhomogeneity. Overall, geochemical data coincide well with petrographic observations (see text for more details).

Hence, it is reasonable to consider analyzed samples showing Fe_2O_3 values greater than 50 wt. % as *ferruginous*, regardless of the process responsible for this enrichment. Even if one considers some analyses from the Kuruman-Griquatown suite (Paul Oonk, unpublished data) exceeding 50 % of iron content (51,6, 53,7, 57,5 wt. %) it must be taken into account that these values were only three out of ninety-eight analyses and most likely reflect some biasing during sampling.

ii) Siliceous BIF ($SiO_2 > 65$ wt. %). SiO_2 in a BIF generally ranges from 34 to 56 wt. %, for the Superior type-BIF is 47.30 wt. % and for the Kuruman-Griquatown BIF is 43.88 wt. %. Samples with $SiO_2 > 65$ wt. % and hence low iron content (~ <30 wt. %) were grouped as *siliceous*, regardless of the alteration process involved.

iii) Altered BIF. Samples with $Fe_2O_3 < 50$ wt. % and consequently high SiO_2 but at the same time lower than 65 wt. %, were characterized as *altered BIF*. Most of these samples are not considered as significantly enriched in neither of the two elements and show only expected variations in iron and silica, with silica being always higher of course by definition.

iv) Iron Ore ($Fe_2O_3 > 90$ wt. %). Samples grouped as *iron ore* in this study represent typical high-grade iron ore which corresponds to a very high iron content (usually > 95 wt. %).

The geochemically determined groups were compared with the textural groups presented earlier in the petrography chapter in an attempt to identify relationships between them (Table 4.1). Despite the significant overlap between geochemical and textural groups and subgroups some fair points can be made. *Reddish/cream-grey* laminated BIF are geochemically represented by both *ferruginous* and *altered* groups but proportionally the majority of these rocks fall into the *altered* group (17 samples over 9). This coincides with petrographic observations, since their main characteristic is the presence of abundant chert bands showing variable hematite content. Things are more lucid with *grey-red* laminated BIF which are represented mostly by the *ferruginous* group (12 samples over 5 in the altered group). The higher iron-content is also reflected in petrographic textures displaying a significantly higher amount of hematite which penetrates throughout the whole mass of these rocks. Furthermore, *lustrous red-grey BIF* are clearly categorized as *ferruginous*. On the other hand, *dull-metallic grey* laminated BIF correlate with all three geochemical groups for BIF. Although most samples used in this study lack metallic bands and thus fall into the *siliceous* group it seems that a higher abundance of metallic layering (hematite-rich) increases notably the modal abundance of iron but again not as much as in the *grey-red* and *lustrous* *red-grey BIF*. Brecciated BIF are more heterogeneous and do not allow for useful insights to be drawn. As expected, breccias with highly Fe-enriched matrix fall into the *ferruginous* and *altered* groups while the *siliceous* group encompasses brecciated BIF with high abundance of chert pods and/or large chunks of silica-rich bands and fragments.

4.2 Major element geochemistry

4.2.1 Results

A summary of the major element composition of the different geochemical groups is presented in Table 4.2. Raw geochemical data as well as a complete table showing SiO_2 and Fe_2O_3 values of the geochemically grouped samples can be found in Appendix III. The average composition of Superior type-BIF, Kuruman-Griquatown and Kuruman-Penge are also included. The concentrations of SiO_2 and Fe_2O_3 are dominant and vary considerably between different groups. Na_2O shows consistently the lowest concentrations in all groups while the other major oxides show only minor variations. **Ferruginous BIF** are dominated by Fe_2O_3 (50.02 - 74.80 wt. %) followed by SiO_2 (22.13 - 48.80 wt. %). The higher Fe_2O_3 values (e.g. 74.80, 74,74, 72,78 wt. %) are associated with *red-grey* and *lustrous red-grey* laminated BIF or with brecciated BIF with Fe-rich matrix and 46 % of the samples have iron content higher than 55 wt. %. On the other hand, Fe_2O_3 values closer to 50 wt. % represent *reddish/cream-grey* laminated BIF. This is in good agreement with petrographic observations which show that BIF with high abundance of grey and red bands and no presence of reddish/cream chert bands have higher hematite content showing textural evidence of an enrichment process involving simultaneous quartz dissolution. The other elements are minor and generally account for less than 1 w.t. % of the bulk rock (excluding LOI and H_2O^-). These include in order of higher average value shown CaO (0.02 - 1.13 wt. %), Al_2O_3 (bdl - 1.51 wt. %), P_2O_5 (0.02 - 0.14 wt. %), MnO (0.02 - 0.09 wt. %), K_2O (0.01 - 0.38), TiO_2 (bdl - 0.08 wt. %), MgO (bdl - 0.06 wt. %) and Na_2O (bdl - 0.02 wt. %).

In the **altered BIF**, Fe_2O_3 concentrations range between 31.13 and 48.35 and those of SiO_2 between 49.62 and 66.75. The iron content of most samples is higher or close to BIF averages from literature but silica is consistently higher with 68 % of the samples showing $SiO_2 > 55$ wt.%. The other major elements are of very minor abundances, accounting in sum for less than 1 w.t. % of the bulk rock. In order of higher average these are: CaO (0.01 -

1.71), Al_2O_3 (bdl - 0.65 wt. %), P_2O_5 (0.01 - 0.11 wt. %), MnO (0.02 - 0.08 wt. %), TiO_2 (bdl - 0.09 wt. %), K_2O (0.01 – 0.10 wt. %), MgO (bdl – 0.05 wt. %) and Na_2O (bdl – 0.05).

Geochemical Group	Iron Ore (n=12)		Ferruginous BIF (n=37)		Altered BIF (n=31)		Siliceous BIF (n=23)		Superior-type BIF[1] (n=1073)
	Range	Average	Range	Average	Range	Average	Range	Average	
SiO_2 (wt%)	0.65 - 10.69	3.23	22.13 - 48.80	40.92	49.62 - 66.75	56.52	65.49 - 96.54	75.93	47.30
TiO_2	bdl - 0.68	0.15	bdl - 0.08	0.03	bdl - 0.09	0.02	bdl - 0.03	0.01	0.04
Al_2O_3	0.03 - 1.36	0.87	bdl - 1.51	0.22	bdl - 0.65	0.11	0.01 - 0.36	0.13	1.07
Fe_2O_3	86.67 - 99.10	94.51	50.02 - 74.80	57.16	31.13 - 48.35	41.41	2.91 - 33.23	13.73	43.10
MnO	0.01 - 0.08	0.04	0.02 - 0.09	0.04	0.02 - 0.08	0.04	0.03 - 0.36	0.06	0.44
MgO	0.01 - 0.08	0.03	bdl - 0.06	0.02	bdl - 0.05	0.01	bdl - 0.64	0.06	5.68
CaO	0.05 - 0.41	0.17	0.02 - 1.13	0.25	0.01 - 1.71	0.41	0.11 - 1.82	0.44	3.03
Na_2O	bdl - 0.03	0.01	bdl - 0.02	0.01	bdl - 0.05	0.01	bdl - 0.02	0.01	0.33
K_2O	bdl - 0.14	0.09	0.01 - 0.38	0.03	0.01 - 0.10	0.02	0.01 - 0.06	0.01	0.27
P_2O_5	0.05 - 0.30	0.13	0.02 - 0.14	0.06	0.01 - 0.11	0.04	0.01 - 0.09	0.02	0.10
LOI	0.24 - 0.96	0.56	-0.04 - 1.59	0.42	-0.02 - 2.32	0.65	-0.18 - 5.46	0.77	n.a.
H_2O^-	0.06 - 0.38	0.21	0.04 - 0.41	0.15	0.01 - 0.80	0.18	0.04 - 0.85	0.31	n.a.

Geochemical Group	Kuruman-Griquatown[2] (n=98)		Kuruman-Penge[3] (n=25)
	Range	Average	
SiO_2 (wt%)	19.92 - 67.56	43.88	51.68
TiO_2	0.01 - 0.20	0.03	0.02
Al_2O_3	bdl - 3.00	0.33	0.11
Fe_2O_3	10.12 - 57.50	36.96	39.79
MnO	0.06 - 5.90	0.86	0.30
MgO	0.63 - 5.96	3.08	5.14
CaO	0.10 - 15.58	3.48	5.65
Na_2O	bdl - 3.01	0.18	0.03
K_2O	0.01 - 1.69	0.33	0.03
P_2O_5	0.01 - 0.82	0.06	0.09
LOI	-0.16 - 26.03	10.72	n.a.
H_2O^-	0.02 - 1.13	0.20	n.a.

Table 4.2. Major element average composition and ranges for the iron ore (=12), ferruginous BIF (n=37), altered BIF (n=31) and the siliceous BIF (n=23) in wt. %. Whole-rock analytical data derive from samples collected from SLT207, SLT284, SA2491E and SA2072 drill cores. Average compositions for three iron-formations are also shown. (1) is from McClung (2006), (2) from Paul Oonk (unpublished data) and (3) from Gutzmer et al. (2008). bdl = below detection limit, n.a. = not available.

In the **siliceous BIF**, SiO_2 (65.49 – 96.54) is by far the most abundant component followed by Fe_2O_3 (2.91 – 33.23). The remaining element oxides are minor and are presented in order of higher average: CaO (0.11 – 1.82 wt. %), Al_2O_3 (0.01 – 0.36 wt. %), MnO (0.03 – 0.36 wt. %), MgO (bdl - 0.64 wt. %), P_2O_5 (0.01 - 0.09 wt. %), K_2O (0.01 - 0.06 wt. %), TiO_2 (bdl - 0.03 wt. %) and Na_2O (bdl - 0.02 wt. %). High-grade **iron ore** samples are dominated by Fe_2O_3 (86.67 - 99.10 wt. %) with the lower values being associated with quartz- and berthierine-rich domains in these rocks. Elements showing considerable concentrations in the iron ore are SiO_2 (0.65 - 10.69), Al_2O_3 (0.03 - 1.36), CaO (0.05 - 0.41), TiO_2 (bdl - 0.68) and P_2O_5 (0.05 - 0.30 wt. %). K_2O (bdl - 0.14 wt. %), MnO (0.01 - 0.08 wt. %), MgO (0.01 - 0.08 wt. %) and Na_2O (bdl - 0.03 wt. %) follow showing only minor abundances. The deleterious elements in the iron ore account on average for ~ 1.5 wt. % of the bulk rock excluding silica, which if added, these elements amount to a ~ 4.5 wt. % of the bulk rock. LOI is becoming progressively higher from iron ore (0.24 - 0.96 wt. %), to ferruginous BIF (-0.04 - 1.59 wt. %), to altered BIF (-0.02 - 2.32 wt. %) and finally to siliceous BIF (-0.18 - 5.46 wt. %). In view of the same trend recorded in CaO and a regression value of 0.68 resulting if these two are plotted together, it can be considered that the bulk of CaO analyzed resides in gypsum.

Standard deviation (STD) and relative standard deviation (RSD) were calculated for all averages and are available in Appendix III. As expected, there is a wide scatter of the values around the mean for such low concentrations. Fe_2O_3 and SiO_2 generally have the lower RSD values (Fe_2O_3 ranges from 3.43 to 83.31 % and SiO_2 from 7.64 to 89.35 %), with the highest values shown in the siliceous BIF and the iron ore respectively. On the other hand, the concentrations of the other major oxides are fairly variable as already shown and the RSD values, for example for K_2O or MgO can exceed 200 %. This is mainly due to the very low elemental concentrations and the presence of a small amount of samples which show considerably higher values in comparison to the average, e.g. MgO of 0.64 wt. % compared to 0.06 wt. % which is the average in the siliceous BIF. Such concentrations represent accessory minerals in the BIF, such as siderite and gypsum, appearing mostly as vein-filling material. As far as this is taken into account and individual samples with highly divergent concentrations are discussed, then reliable insights can still be drawn. It is quite evident that elemental averages used in this study to draw meaningful conclusions are not controlled by a couple of highly enriched or depleted samples, but instead show a clear pattern of higher or lower concentrations in the whole sample suite, as it is also clear from chemostratigraphic plots presented below.

To summarize, leaving out SiO_2 and Fe_2O_3, all types of BIF are very similar in composition regarding the rest of the major oxides, which generally show very low concentrations. If minor differences are considered then all three types of BIF show higher average abundances in CaO, Al_2O_3, P_2O_5 and MnO with the exception of siliceous BIF which have additionally higher MgO. Finally, the iron ore has inarguably higher Al_2O_3, TiO_2 and P_2O_5 concentrations than all the other BIF groups.

4.2.2 Chemostratigraphic plots

Chemostratigraphy is a useful tool for displaying changes in the elemental concentrations through cores, especially when crossing formation boundaries, or identifying related geochemical behaviors between different elements. Although it is usually applied in conjunction with high-resolution sampling and the studied drill cores were not sampled in such way, chemostratigraphic plots could still portray compositional shifts when crossing form BIF to iron ore, delineate geochemical relationships and contrasts between different textural types of BIF or help recognize mineralogical control on geochemical signals since

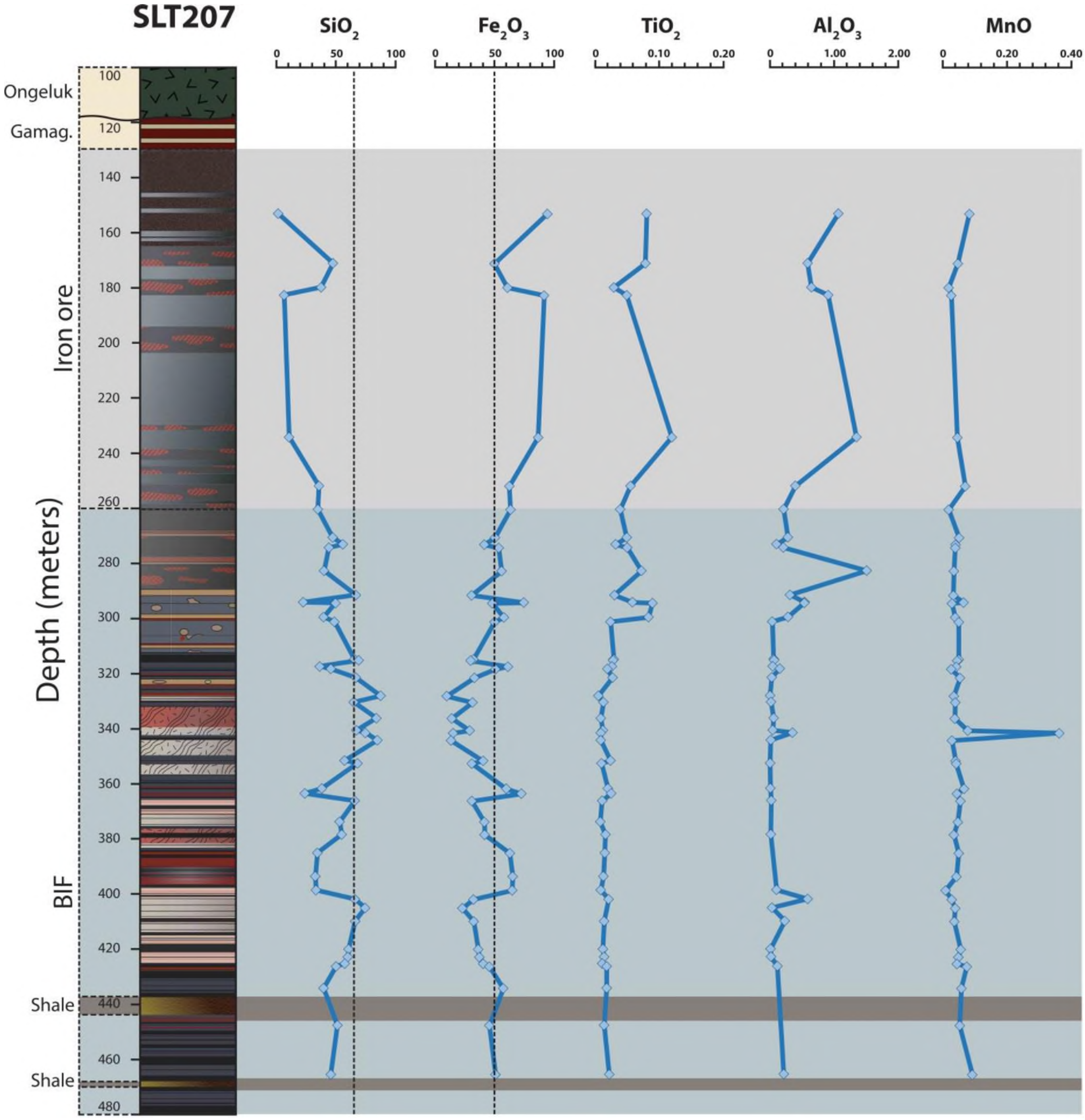

Figure 4.1. Geochemical variation plots for major element oxides (wt. %), created for drill core STL207. Iron ore samples are represented by light grey-fill and BIF samples by bluish grey-fill. A detailed legend for the stratigraphic column depicted can be found in paragraph 2.2 or in Appendix I.

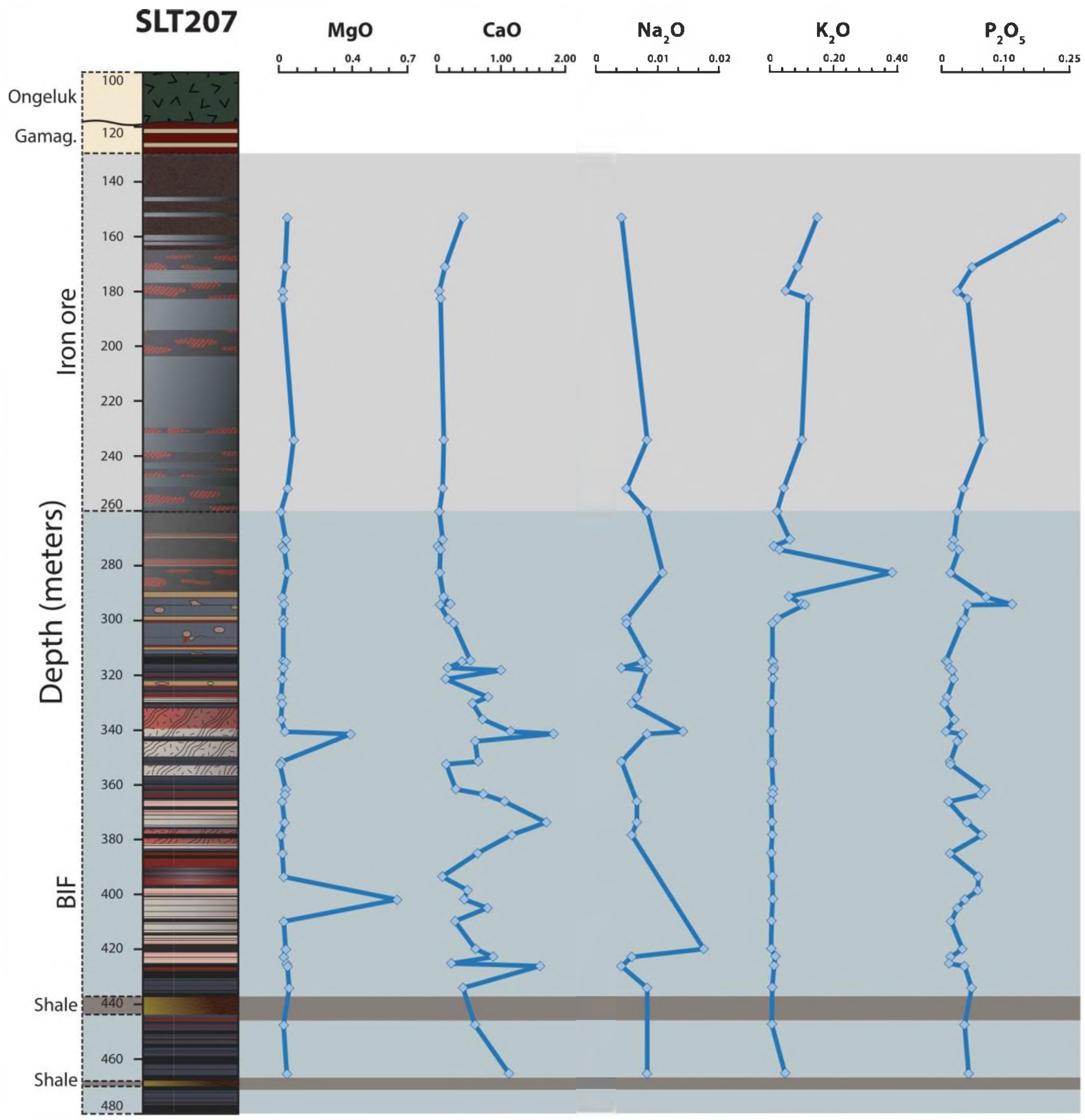

Figure 4.1. (continued).

individual samples are plotted. Chemostratigraphic plots were constructed for the selected drill cores STL207, SLT284 and SA2491E, for all major oxides and the basic fourteen trace elements analyzed in this study. Lithostratigraphic profiles presented in chapter 2 are included in each figure. Selected plots for major oxides are shown here and for trace elements in paragraph 4.3.3 while the rest of the plots are available in Appendix III.

All plots illustrate the pronounced antithetic relationship between Fe_2O_3 and SiO_2 which reflects the duomineralic nature of Manganore iron-formation, already confirmed and recorded by petrographic investigations. In drill core SLT207 (Fig. 4.1), increases of Fe_2O_3

(> 50 wt. %) and their correlation with the iron ore, the underlying brecciated BIF and horizons of *grey-red* and *(lustrous) red-grey* BIF is clearly depicted. Drop-offs in Fe_2O_3 concentration within the iron ore to values slightly above 50 wt. % are caused by "unenriched" portions or clasts. Similarly, SiO_2 increases drastically in horizons of silicified BIF. The transition from the BIF to the iron ore at the approximate depth of 260 meters is outlined by noticeable increases in concentrations of Al_2O_3, TiO_2, P_2O_5 and K_2O. A change in concentration of these elements occurs already from the underlying brecciated BIF which clearly exhibit higher values in comparison to the rest of the stratigraphy. Al_2O_3 and TiO_2 show strongly comparable chemostratigraphic behavior within and just below the iron ore whilst the geochemical trend of K_2O is more subtly related to the other two. Some geochemical signals possibly reflect vein -hosted and/or open space-filled mineralogy which has been described in the previous chapter. For example, the sharp increase of Al_2O_3 at the depth of 282.8 meters coincides with that of K_2O and most likely represents the presence of muscovite within brecciated BIF with highly Fe-enriched matrix. P_2O_5 does not show any drastic changes across BIF's profile but minor enrichments from ~360 to ~400 meters depth correlate with ferruginous BIF intervals. MnO and MgO are fairly invariant across stratigraphy and the sharp increases shown at 341.6 and 402 meters are related to CaO and Al_2O_3 which demonstrates the presence of siderite and berthierine. The elevated CaO especially in the silicified BIF parts which reaches up to 1.82 wt. % clearly indicates the high abundance of gypsum and/or siderite in these rocks. Finally, Na_2O shows extremely low concentrations and a rather invariable profile. The slightly higher values occurring only within the siliceous BIF which have high density of tiny veins (~340 and ~420m) could represent sodium silicates, such as tourmaline.

In drill core SLT284 (Fig. 4.2), the geochemical behavior of Fe_2O_3 and SiO_2 with depth is very similar, as expected, to the one already described in the previous core. It is noteworthy that SiO_2 in the siliceous horizon occurring from ~350 to ~370 meters depth is always above 95 wt. % and reaches up to 96.50 wt. %. Iron content within the ore is also consistently high, mostly above 95 wt. %. Again, Al_2O_3 and TiO_2 show the same shifts in elemental concentrations at the upper part of the BIF's stratigraphy and higher values within the iron ore. The chemical variation of K_2O is also comparable in most parts with that of Al_2O_3, despite the sharp decrease in one sample within the iron ore at 200.1 m. For example, there is an exact correlation between these two at the depths of 305.2 and 381.3 meters which points to the possible presence of muscovite. The iron ore seems again clearly enriched in

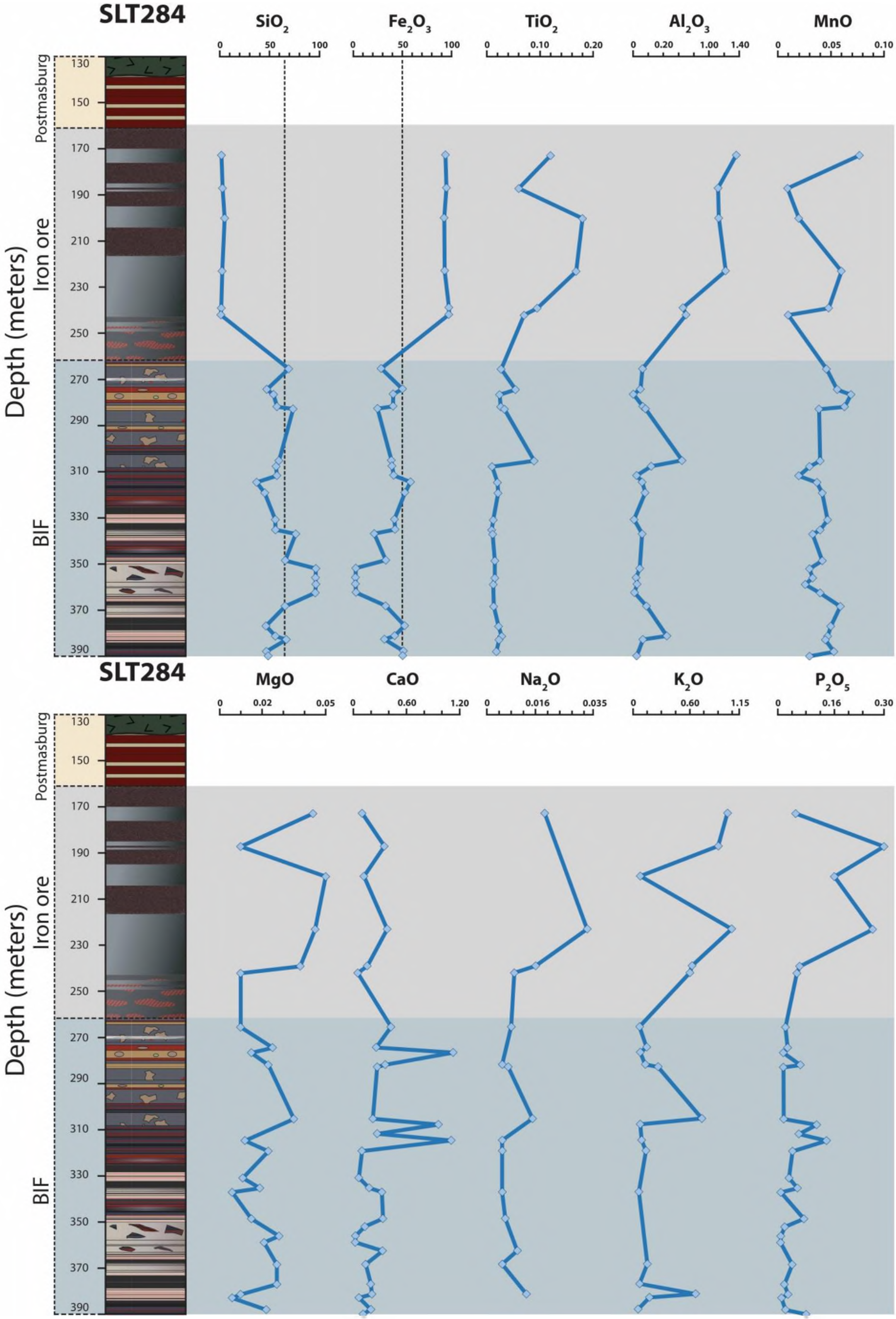

Figure 4.2. Geochemical variation plots for major element oxides (wt. %), created for drill core SLT284. Iron ore samples are represented by light grey-fill and BIF samples by bluish grey-fill. A detailed legend for the stratigraphic column depicted can be found in paragraph 2.2 or in Appendix I.

Al_2O_3, TiO_2, P_2O_5 and K_2O. Sharp shifts in CaO at depths of 276.5, 307.7 and 314.6 meters respectively are almost certainly related to elevated gypsum content. In plots of drill core SA2491E from Sishen, which is not shown here (Appendix III), Al_2O_3 and K_2O seem to behave in a similar manner throughout the core. Elevated concentrations are shown in the iron ore and in associated ferruginous BIF. CaO and P_2O_5 exhibit the most pronounced correlation observed in the chemostratigraphic plots that were constructed. Finally, TiO_2 concentration peaks only in one sample within the iron ore.

4.3 Trace element geochemistry

4.3.1 Results

Trace element composition of the four different geochemical groups is summarized in Table 4.3 along with the average concentrations of the Superior type-BIF, Kuruman-Griquatown and Kuruman-Penge. The raw geochemical data can be found in Appendix III. Generally, the trace element concentrations obtained are low and some elements such as U and Th are below detection limits for most of the samples. For the calculated averages to be of value, the following rule was followed. If more than 20 % of the samples in a group have values below detection limit for a specific element, then only samples with detected concentrations are used in the calculation of the elements average. Despite that, for most of the trace elements the same number of samples (n) was used in average calculations as in major elements. Standard deviations were generally lower compared to major oxides. The lower values are shown by Mo and Nb whereas Sr, Y and Zr exhibit almost the higher deviations among trace elements. Furthermore, Cr, Ni and V show divergent values from the average especially in the iron ore but it is apparently evident that these elements are generally in higher concentrations in the ore and the average is not controlled by the minority of samples.

The geochemistry of the **ferruginous BIF** is dominated by Cr (22 - 190.4 ppm), V (11 - 182 ppm), Ni (bdl - 121 ppm), Cu (bdl - 50) and Sr (4 - 58 ppm). The rest of the elements show low to very low concentrations and in order of maximum average shown are: Zr (bdl - 28 ppm), Pb (3 - 16 ppm), Th (3 - 12 ppm), Y (bdl - 27 ppm), Rb (1 -11.6 ppm), Mo (2.2 - 5.3) and Nb (1.8 - 6 ppm). U is constantly below detection. The **altered BIF** appear to share similar patterns with the ferruginous BIF except form the fact that their concentrations

Geochemical Group	Iron Ore			Ferruginous BIF			Altered BIF			Siliceous BIF		
	Range	Average	n	Range	Average	n	Range	Average	n	Range	Average	n
Mo (ppm)	bdl - 8.1	5.11	12	2.2 -5.3	3.52	37	bdl - 6.2	3.32	31	1.7 - 4.2	3.18	23
Nb	bdl - 6.0	3.92	12	1.8 - 6.0	3.37	28	1.5 - 5.0	3.15	18	bdl - 5.0	2.86	13
Zr	bdl - 42.0	22.58	12	bdl - 28.0	9.08	37	bdl - 22.0	7.05	31	bdl - 17.0	5.61	23
Y	4.0 - 20.0	10.21	12	bdl - 27.0	5.46	37	bdl - 15.0	5.38	31	1.0 - 12.2	5.93	15
Sr	5.3 - 148.7	55.14	12	4.0 - 58.0	18.98	37	5.3 - 53.8	20.98	31	2.1 - 66.3	15.58	23
U	bdl - 5.8	5.80	1	bdl	0.00	0	2.7 - 3.5	3.10	2	bdl - 3.0	3.00	1
Rb	bdl - 12.0	6.14	12	1.0 - 11.6	3.90	21	1.0 - 10.0	3.16	20	1.0 - 5.0	2.34	7
Th	10.0 - 14.0	11.50	8	3.0 - 12.0	7.78	18	4.0 - 12.0	7.90	13	3.0 - 10.0	5.83	6
Pb	bdl - 69.0	25.78	12	3.0 - 16.0	8.50	25	4.2 - 14.0	8.00	20	3.3 - 10.9	7.28	11
Cu	bdl - 74.0	40.12	12	bdl - 50.0	25.82	37	bdl - 46.0	21.22	31	bdl - 23.8	14.94	23
Zn	bdl - 26.0	15.40	12	6.0 - 14.0	9.80	23	3.0 - 14.0	7.80	23	2.0 - 9.0	4.50	12
Ni	15.0 - 1512.0	343.00	5	bdl - 121.0	29.61	37	bdl - 97.0	27.87	31	bdl - 61.0	18.99	23
Cr	6.0 - 174.0	86.83	12	22.0 - 190.4	54.19	37	19.0 - 129.6	50.28	31	26.0 - 63.1	44.23	23
V	15.0 - 726.1	152.57	12	11.0 - 182.0	42.02	37	5.0 - 52.6	26.73	31	4.0 - 39.2	22.64	23

Geochemical Group	Superior-type BIF[1] (n=1073)	Kuruman-Griquatown[2]			Kuruman-Penge[3] (n=25)
		Range	Average	n	
Mo (ppm)	n.a.	0.2 - 2.4	0.81	98	n.a.
Nb	3.00	1.0 - 3.0	1.90	37	7.32
Zr	38.00	bdl - 34.4	5.48	98	2.50
Y	25.00	1.2 - 16.5	5.53	98	9.35
Sr	25.00	4.0 - 144.6	30.76	98	3.45
U	1.70	bdl - 0.70	0.08	98	0.02
Rb	36.00	bdl - 311.6	39.43	98	2.15
Th	3.00	0.04 - 3.08	0.39	98	0.06
Pb	5.00	0.59 - 30.18	2.78	98	2.25
Cu	12.00	6.8 - 43.4	21.30	98	7.00
Zn	26.00	4.0 - 28.1	12.29	98	25.40
Ni	18.00	4.1 - 46.3	16.92	98	29.34
Cr	n.a	7.3 - 57.6	24.83	98	n.a.
V	26.00	5.8 - 61.0	18.86	98	10.00

Table 4.3. Trace element average composition and ranges for the iron ore (=12), ferruginous BIF (n=37), altered BIF (n=31) and the siliceous BIF (n=23) in ppm. Whole-rock analytical data derive from samples collected from SLT207, SLT284, SA2491E and SA2072 drill cores. Average compositions for three iron-formations are also shown. (1) is from McClung (2006), (2) from Paul Oonk (unpublished data) and (3) from Gutzmer et al. (2008). Trace element analyses presented here for (2) were obtained via XRF except from Mo, Y, U, Th, and Pb which were analyzed via ICP-MS. bdl = below detection limit, n.a. = not available.

are apparently more depleted. Again, there is dominance in Cr (19 - 129.6 ppm), Ni (bdl - 97 ppm), V (5 - 52.6 pm), Cu (bdl - 46 ppm) and Sr (5.3 - 53.8 ppm) while the rest of the traces follow exhibiting very low concentrations: Pb (4.2 - 14 ppm), Th (4 - 12 ppm), Zr (bdl - 22 ppm), Y (bdl - 15 ppm), Mo (bdl - 6.2), Rb (1- 10 ppm), Nb (1 - 5 ppm) and finally U omitted only from two samples (2.7 - 3.5 ppm). **Siliceous BIF** apparently reproduce the same relationships showing in turn higher depletions in comparison to the altered BIF. Cr (26 - 63.1 ppm), V (4 - 39.2 ppm), Ni (bdl - 61 ppm), Sr (2.1 - 66.3 ppm) and Cu (bdl - 23.8 ppm) have the higher concentrations. Pb (3.3 - 10.9), Y (1 - 12.2), Th (3 - 10 ppm), Zr (bdl - 17 ppm), Mo (1.7 - 4.2 ppm), Nb (bdl - 5 ppm) and Rb (1 - 5 ppm) follow in order of maximum average shown. The only element which does not follow the pattern of gradual depletion from ferruginous, to altered, to siliceous BIF is Y but this happens only on average and might be related to xenotime abundances in veins or phosphates in the matrix of the silicified BIF as it was presented in the petrography chapter.

The **iron ore** shows in comparison to the BIF the higher abundances in trace elements. Some high and divergent values like that of sample HLT3 which has Cu concentration of 1901 ppm might represent a copper mineral present, such as cuprite or most likely bornite and were not used in average calculations. During logging of the Sishen cores copper minerals with a bluish tint were observed macroscopically. The trace element geochemistry of the ore is dominated by Ni (15 -1512 ppm), V (15 - 726.1 ppm), Cr (6 - 174 ppm), Sr (5.3 - 148.7 ppm) and Cu (bdl - 74 ppm) which are also the prevailing trace elements in the BIF. The rest of the traces show very low concentrations and at the same time always higher than the BIF: Pb (bdl - 69 ppm), Zr (bdl - 42 ppm), Th (10 - 14 ppm), Y (4 -20 ppm), Rb (bdl - 12 ppm), Mo (bdl - 8.1 ppm) and Nb (bdl - 6 ppm). U is below detection limit apart from one sample which has a value of 5.8 ppm.

Summarizing, traces elements with consistently higher concentrations in the BIF and in the iron ore are transition metals (Ni, Cr, Cu, V, Zn) and Sr. The latter is mainly a carbonate- and sulphate-associated trace element. HFSE elements (Th, Y, Zr, Nb) along with Mo and Rb show lower concentrations and are mostly associated with silicate minerals or phosphates in the case of Y. Despite the fact that concentrations for most of the traces can be considered as very low or even negligible in cases, there seems to be a clear continuous pattern of enrichment in trace elements moving from silica-rich to iron-rich samples. One plausible explanation for this would involve hematite which is able of bearing a wide range of trace elements and is becoming by definition more abundant with elevated Fe_2O_3. Hensler et al. (2015) demonstrated that hematite in iron ore can inherit from the host rock, the precursor magnetite as well as from external fluids different elements in trace amounts such as Al, Mg, Mn, Ti, V, Cr and As. Another explanation for some of the observed enrichments in the ore could involve rutile which is the dominant carrier of HFSE (Zach et al., 2002) such as Nb, Ta, Sb and W while it can also carry considerable amounts of V, Cr, Mo and Sn. Rutile though was identified only in the BIF and never in the iron ore where only some scarce ilmenite was found. Other silicate minerals and even sulphates can also account for the higher trace element concentrations observed and they should not be neglected since it has been shown that they are systematically present in the ore. What is important to note is that the enrichment in elements such as Ni, Cr and V may be as well partly related to the overlying

Gamagara shales and not just to the potential hydrothermal evolution and alteration but also to their possibly mafic-ultramafic origin (Cousins, 2016).

4.3.2 Chemostratigraphic plots

Chemostratigraphic plots created for trace elements are somewhat less insightful than the plots for major oxides but quite a few interesting observations can still be made. Only selected plots are shown here and the rest can be found in Appendix III. An initial comment

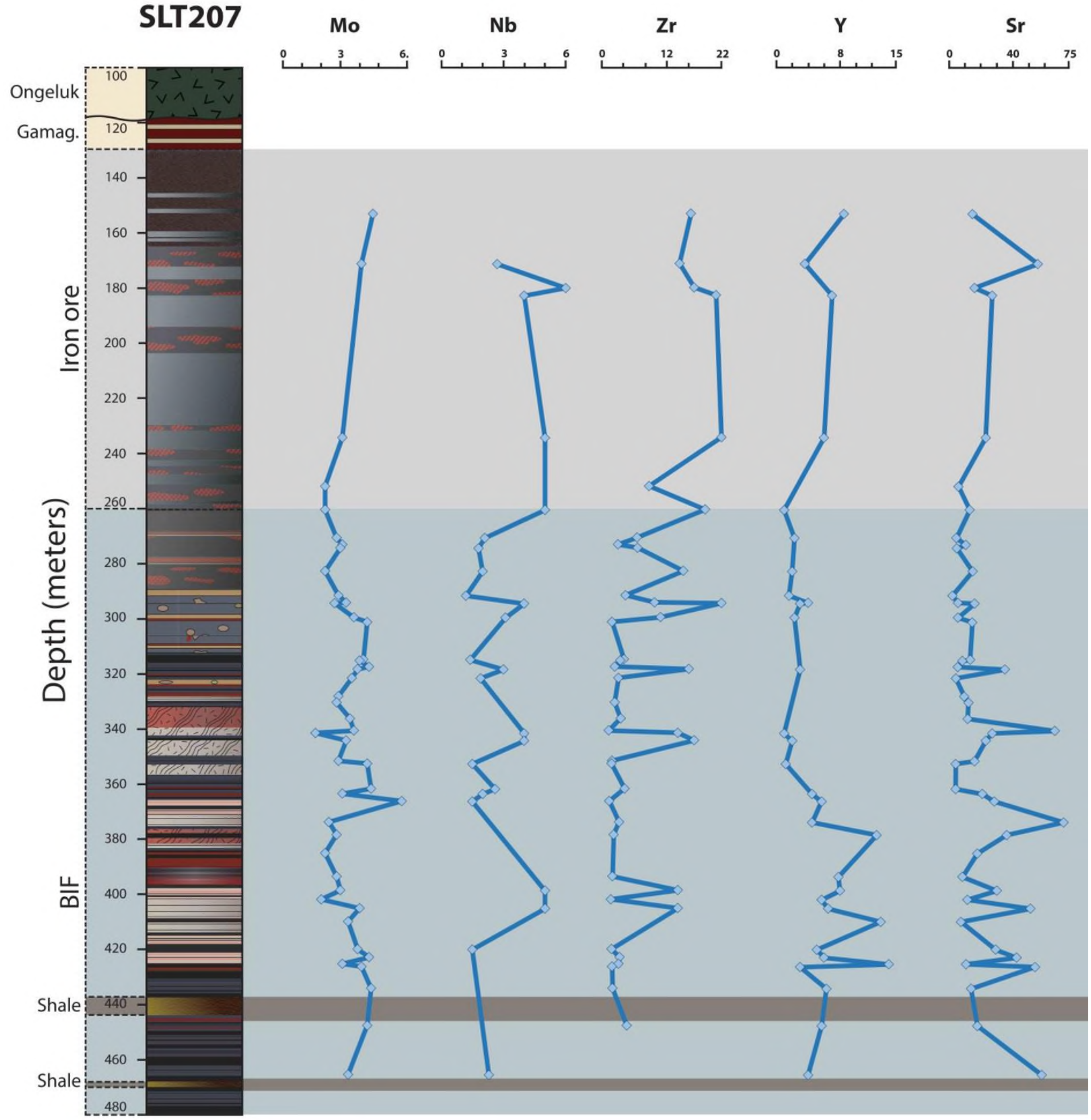

Figure 4.3. Geochemical variation plots for trace element (ppm), created for drill core STL207. Iron ore samples are represented by light grey-fill and BIF samples by bluish grey-fill. A detailed legend for the stratigraphic column depicted can be found in paragraph 2.2 or in Appendix I.

would be that the concentrations of trace elements are more invariant across stratigraphy than the respective of major oxides. In drill core SLT207 (Fig. 4.3), Sr seems to correlate well with CaO in most parts of the BIF (same anomalous peaks at 340.7 and 373.9 m) whereas in the ore some elevated values of Sr do not show any correlation with CaO suggesting the presence of baryte or celestine. Y shows increased concentrations within or near the silicified BIF possibly reflecting associated xenotime and phosphate content and furthermore in the iron ore it exhibits generally higher values compared to the rest of the stratigraphy. Zr concentration is highly variable but the greater values are observed in the ore and in brecciated BIF. Elevated concentrations within the silicified BIF most likely reflect hydrothermal zircon present in veins. Nb values are generally increased in the iron ore but samples with high values occur also within the silicified BIF which supports that Nb resides potentially in rutile found abundant in these rocks. However, TiO_2 and Nb are barely correlated in both SLT cores apart from specific samples. Rb correlates relatively well in places with K_2O (282.8 and 294.5 m) since it forms as a common substitution of the second and may reside in muscovite. Mo and Zn concentrations are generally erratic across stratigraphy. Cu and Pb show increasing shifts in the iron ore and comparable chemostratigraphic patterns, however it can be only speculated if these elements are primarily oxide or silicate-related. Ni behaves erratically across stratigraphy although it seems that higher values are associated with the ore, *grey-red* and *lustrous red-grey* (ferruginous) BIF. Cr and V have similar chemostratigraphic patterns in most parts (similar anomalous peak at 294.2 m) of the stratigraphy and slightly increased values in the ore.

In drill core SLT284 (Fig. 4.4), chemostratigraphic patterns and relationships between trace elements and lithotypes are essentially the same although enrichments in the ore are more pronounced. Mo, Zr, Y, Rb and Th appear to shift towards higher concentrations in the iron ore. The same trend is shown by Cu, Pb, Zn, Cr and V but in a more pronounced way. Cu and Pb appear to correlate strong in the ore. Cr and V are again broadly correlated across stratigraphy although in places they show antithetic relationships and Cr is better associated with Ni which suggests that Cr resides in different mineral phases. Elevated values of Y in the silicified *chert breccia with BIF-remnants* again suggest its association with phosphates.

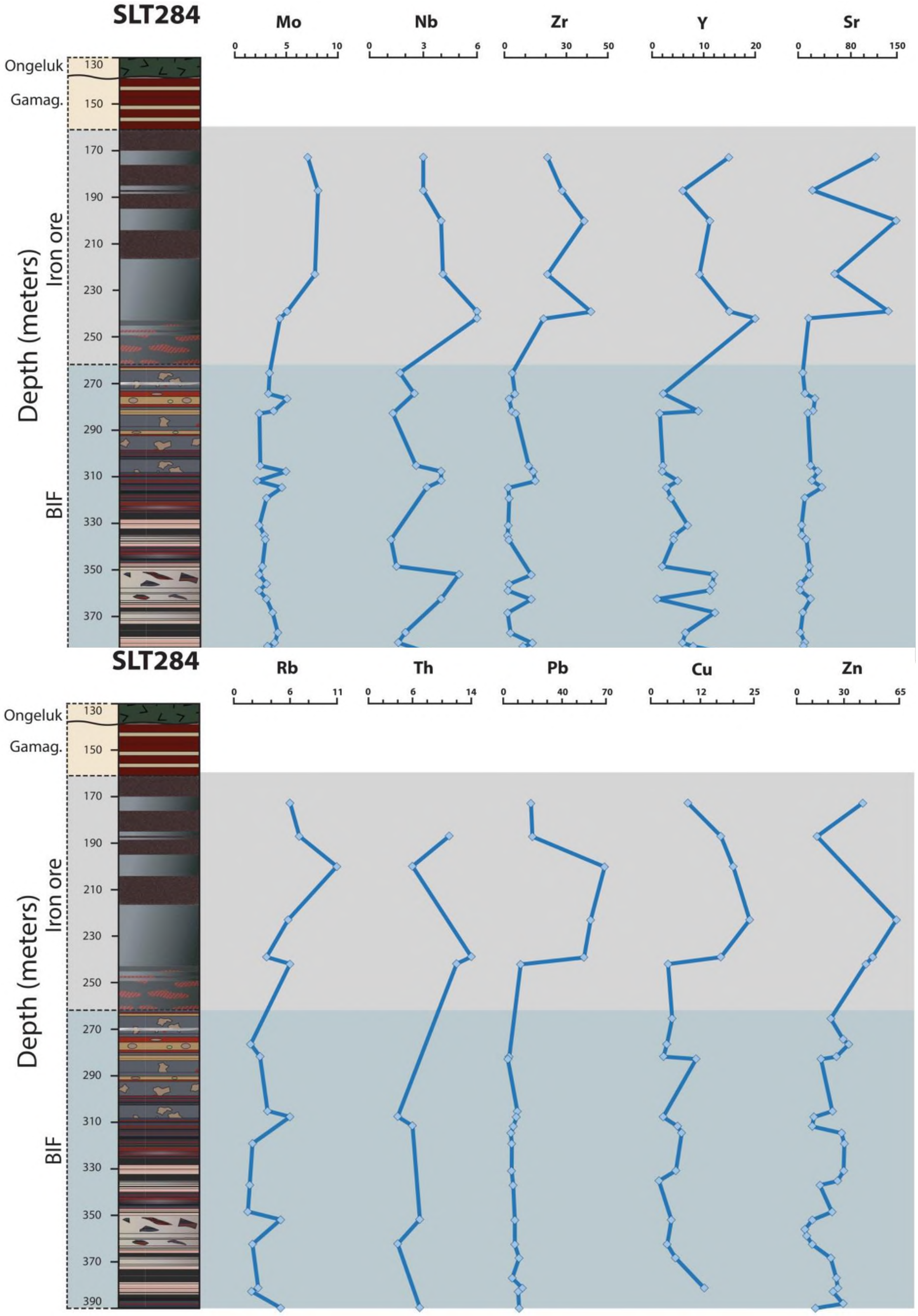

Figure 4.4. Geochemical variation plots for trace element (ppm), created for drill core STL284. Iron ore samples are represented by light grey-fill and BIF samples by bluish grey-fill. A detailed legend for the stratigraphic column depicted can be found in paragraph 2.2 or in Appendix I.

4.4 Geochemical comparisons

Average compositions and ranges of major oxides and trace elements for each geochemical group were normalized against three different averages: Superior type-BIF (n=1073), Kuruman-Griquatown iron-formation (n=98), and Kuruman-Penge iron-formation (n=25). The data are from McClung (2006), Paul Oonk (unpublished data) and Gutzmer et al. (2008) respectively. Normalization against the last two and especially against the Kuruman-Griquatown average composition is of greater value since their data derive from the considered protolith of both the Manganore iron-formation and the iron ore (Van Schalkwyk and Beukes, 1986, Beukes et al., 2003). The constructed spider diagrams allow for a convenient visual evaluation of enrichment and depletion patterns. Furthermore, the different magnitudes of enrichment or depletion in comparison to the protolith can be easily established using normalized values. The enrichment/depletion factors presented below refer to the average enrichment/depletion relative to the respective protolith used and within brackets is always shown the range of the factors.

In Superior type-BIF-normalized diagrams (Fig. 4.5, A), the **iron ore** is enriched in TiO_2 by a factor of 3.75 (up to 17). P_2O_5 has a concentration almost always enriched (0.5 - 3), by a factor of 1.30 on average. Al_2O_3 is slightly depleted by a factor of 0.91 (0.03 - 1.27), although half of the samples show higher values than the average Superior type-BIF. The smallest depletion is that of SiO_2 which has a concentration 14 times lower compared to Superior type-BIF and the higher depletion is that of MgO with a concentration at least 100 times lower respectively. In sample vs. Kuruman-Griquatown diagrams (Fig. 4.5, B), the iron ore shows an almost similar pattern with higher enrichments in some elements and variable depletions in others. The concentration of TiO_2 is higher by a factor of 5 (up to 22.7), Al_2O_3 is almost always enriched by 2.64 on average (0.09 - 4.12) and similarly P_2O_5 by 2.17 (0.83 - 5.00). Finally, in Kuruman-Penge-normalized diagrams (Fig. 4.5, C), the iron ore is further enriched in K_2O by a factor of 3 (up to 4.67) while the enrichments of Al_2O_3 by 7.91 (0.27 - 12.36), of TiO_2 by 7.5 (up to 34) and of P_2O_5 by 1.44 (0.56 - 3.33) are considerably higher compared to the ones observed when a Kuruman or Superior type-BIF protolith is considered. The significant differences in K_2O (depletions or enrichments) reflect the contrasting concentrations in the considered protolith which in turn might be attributed to differences in the degree of weathering. For example, the Kuruman-Penge samples could be weathered surface samples compared to the Kuruman-Griquatown fresh drill-core samples but that is a

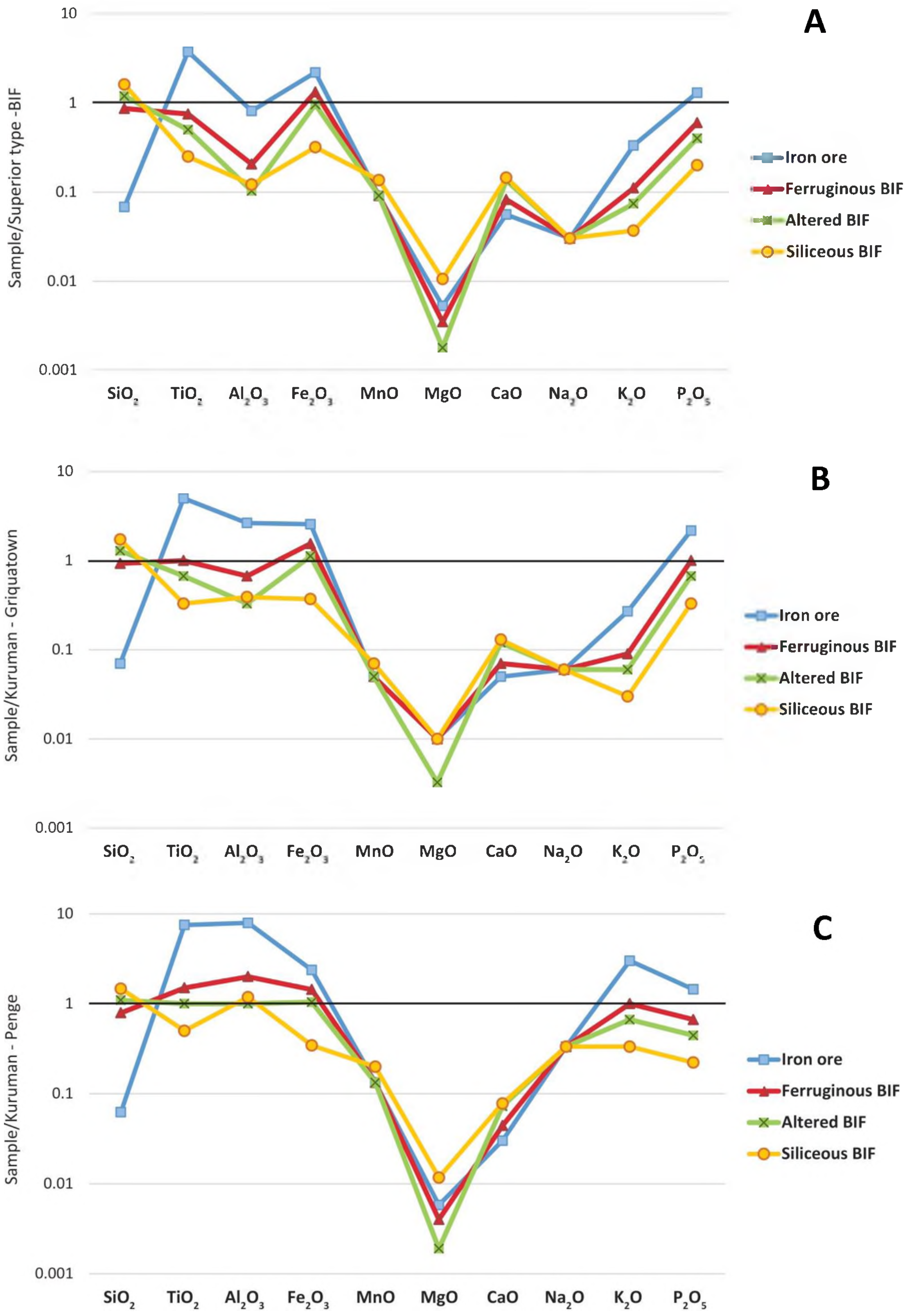

Figure 4.5. Average major element geochemical spidergram of iron ore and the different BIF groups normalized against Superior-type BIF (McClung, 2006), Kuruman-Griquatown BIF (Paul Oonk, unpublished data) and Kuruman-Penge comprising of both the Kuruman and correlative Penge iron-formations (Gutzmer et al., 2008).

hypothesis that has to be examined. The remaining major elements are always variably depleted.

The **ferruginous BIF** samples display comparable patterns between the three diagrams (Fig. 4.5), with the main differences concerning TiO_2, Al_2O_3, P_2O_5 and K_2O. TiO_2 is slightly depleted in sample vs. Superior-type BIF (although enriched up to 2 times in certain samples), but compared to Kuruman is relatively immobile and against Kuruman-Penge is enriched by a factor of 1.5 (up to 4). Al_2O_3 concentrations show relative depletions (0.21, 0.67) whereas in comparison to Kuruman-Penge it is enriched by a factor of 2. In Kuruman-normalized diagrams P_2O_5 is immobile on average (0.33 - 2.33) while for Superior-type and Kuruman-Penge considered protoliths is depleted by a factor of 0.60 (0.20 - 1.40) and 0.67 (0.22 - 1.56) respectively. Finally, K_2O is depleted on average by factors of 0.11 (0.04 - 1.41) and 0.09 (0.03 - 1.15) for Superior-type and Kuruman BIF respectively whereas when normalized against Kuruman-Penge it is immobile on average but can show enrichment up to ~13 times in certain samples. SiO_2 is depleted by a factor of 0.87, 0.93 and 0.79 on average for the three considered protoliths respectively. The concentrations of the other major oxides are depleted at all times and again MgO shows the highest depletion being an element of high mobility.

The **altered BIF** generally mimic the geochemical behavior of the ferruginous BIF in the constructed spider diagrams (Fig. 4.5) exhibiting slightly higher depletions in TiO_2, Al_2O_3, Fe_2O_3, K_2O and P_2O_5. SiO_2 is enriched by factors of 1.19 (1.05 - 1.41), 1.29 (1.13 - 1.52) and 1.09 (0.96 - 1.29) for the three accounted protoliths respectively. The rest of the major elements are depleted. CaO depletion is slightly lower than that of ferruginous BIF whereas MnO shows exactly the same depletion. **Siliceous BIF** display an expected enrichment of SiO_2 by factors of 1.61 (1.38 - 2.34), 1.73 (1.49 - 2.20) and 1.47 (1.27 - 1.87) against the three considered protoliths respectively. MgO despite being the most impoverished major oxide compared to the different protoliths, in the siliceous BIF it exhibits slightly lower depletions along with MnO and CaO which should be related to the abundant siderite whereas the remaining major oxides are significantly depleted.

In **trace element** spidergrams a lot of distinct enrichments are observed especially when the considered protolith is that of Kuruman-Griquatown (Fig. 4.6, B). Another interesting observation deriving from the constructed diagrams is that the siliceous BIF show

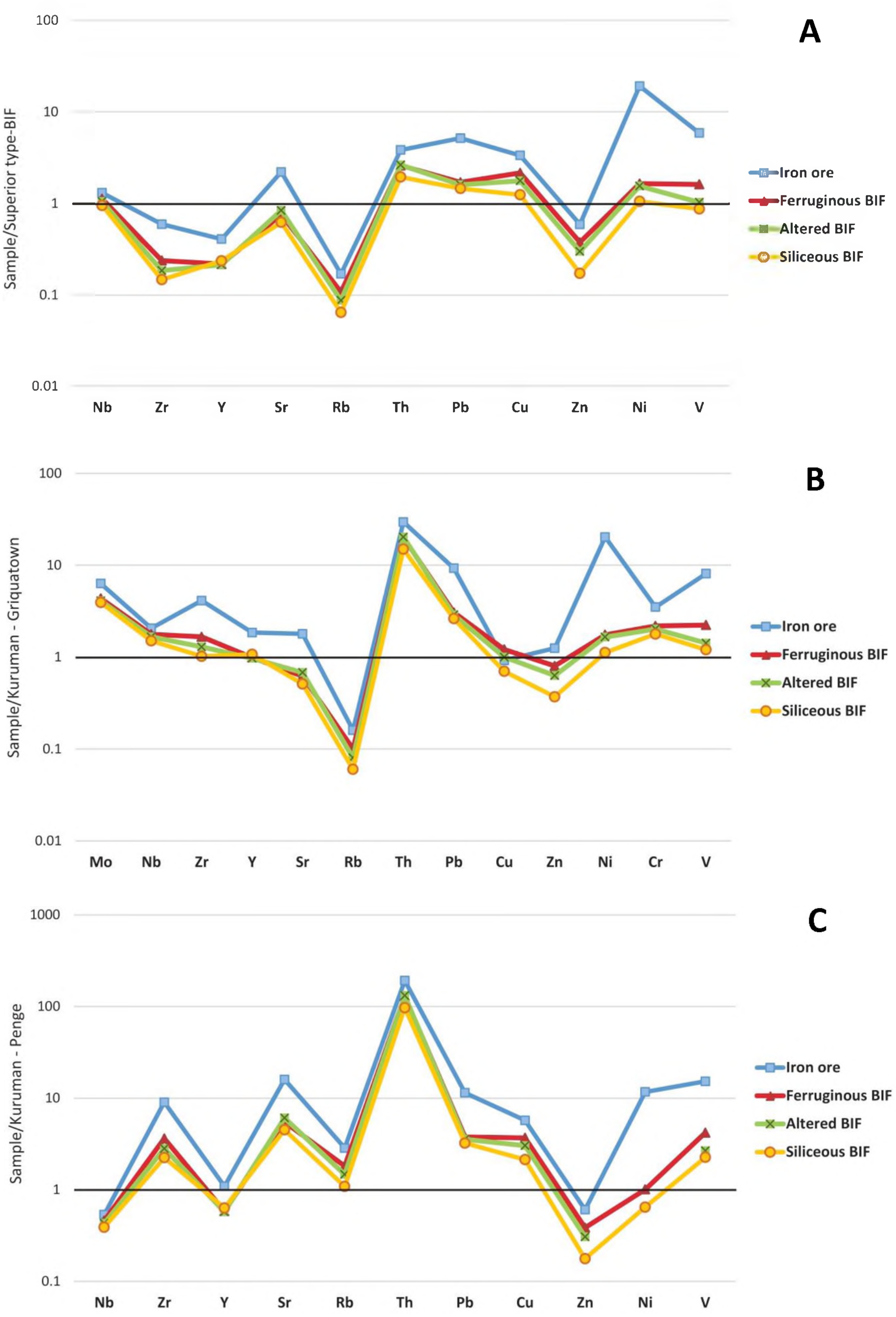

Figure 4.6. Average trace element geochemical spidergram of iron ore and the different BIF groups normalized against Superior-type BIF (McClung, 2006), Kuruman-Griquatown BIF (Paul Oonk, unpublished data) and Kuruman-Penge comprising of both the Kuruman and correlative Penge iron-formations (Gutzmer et al., 2008).

the most impoverished trace element concentrations and as moving towards higher iron content and to the iron ore, element concentrations are getting higher and nearly all of them are being enriched in comparison to all three protoliths. In Kuruman-Griquatown normalized diagrams (Fig. 4.6, B) the **iron ore** is enriched more pronouncedly in Th, Pb, Ni, Cr, V, Mo and Zr by factors of 29.5, 9.3, 20.3, 3.5, 8.1, 6.3 and 4.1 respectively. The only element in which it is depleted is Rb by a factor of 0.16 while Cu is enriched by the smallest factor (1.18). The different **BIF groups** follow the same geochemical fingerprints but with lower enrichment factors moving towards siliceous BIF. In all three BIF groups Y and Cu concentrations are either close to that of the protolith or slightly depleted whereas Sr and Zn show constantly small depletions. In Superior type-BIF normalized diagrams (Fig. 4.6, A), **iron ore** is again highly enriched in Th, Pb, Ni, V by factors of 3.8, 5.2, 19.1 and 5.1 but additionally the concentrations of Sr and Cu are also enriched (by factors of 2.2 and 3.3). The major differences are shown in Cu and Nb which are both enriched for all geochemical groups concerned as well as in Y and Zr which are systematically depleted. Finally, in Kuruman-Penge normalized diagrams (Fig. 4.6, C), the main differences involve Nb, Y and Zn depletions in different magnitudes and Sr, Rb and Cu enrichments for all four geochemical groups. Again the Th, Pb, Ni, V and Zr enrichments in the iron ore are very conspicuous and display enrichment factors of 191.7, 11.5, 11.5, 15.3 and 9.1 respectively.

Comparison between altered and ferruginous BIF samples from the SLT and the Sishen cores shows broadly similar patterns for major and traces elements (Fig. 5, Appendix III). Samples from Sishen seem generally more depleted in major elements and especially in TiO_2, Al_2O_3, CaO and MnO which might reflect lower abundances in rutile, sheet silicates, sulphates or siderite. On the other hand, trace elements from Sishen samples display very similar concentrations to the ones from the SLT cores with comparably increased values of Zr, Y, Zn and Ni.

To conclude, the important enrichments in Al_2O_3 and TiO_2 observed in the iron ore from this study have been also documented from other deposits such as Mt Tom Price in Australia (e.g. Webb, 2003) and have been used together with other findings to support that iron ore formation is predominantly a process of gangue removal. Whether the significant enrichments in these two elements and especially of TiO_2 (up to 17 times) in the iron ore of the MIF is a result of gangue removal or if it has been introduced by hydrothermal processes at some point during BIF's alteration history, is something that needs further investigation using mass balance calculations. Whatever the main process of iron mineralization is, the diagrams of Figure 4.6 suggest that concentrations of most trace elements analyzed are largely enriched in the altered samples (BIF and iron ore) but their relative concentrations do not significantly vary between all geochemical groups concerned (altered samples).

4.5 Additional geochemical signatures

Supplementary analyses and reruns on samples showing low totals led to the accumulation of some additional geochemical data from a different lab on S, Ba, and Co content as well as on some REEs (La, Ce, Nd). These are presented in Table 4.4. Raw data can be found in Appendix III. Co shows values above detection limit for almost all of the analyzed samples. It exhibits a slightly depleting pattern on average from the iron ore to ferruginous, to altered, to siliceous BIF. In comparison to Kuruman-Griquatown BIF, it is always enriched by a factor of 4.57 (up to 12.6), 3.53, 2.8 and ~2 for the iron ore, ferruginous, altered and siliceous BIF respectively. Co is possibly an oxide-related element along with Cu and Ni and if so it is expected to be enriched in the oxidized BIF and in the iron ore compared to the protolith although its source and processes of enrichment are unknown. Co may be also party controlled by baryte since it was commonly picked by EDS residing in it. Ba is always present in small amounts and occasionally it occurs in slightly increased concentrations (e.g. 736, 975 ppm) in samples where S is not present suggesting

Geochemical	Iron Ore			Ferruginous BIF			Altered BIF			Siliceous BIF		
Group	Range	Average	n	Range	Average	n	Range	Average	n	Range	Average	n
Co (ppm)	bdl - 41.0	14.86	8	bdl - 39.0	11.48	21	bdl - 40.0	9.07	14	bdl - 24.0	6.66	3
Ba	12.0 - 6906.0	1159.71	8	bdl - 736.0	90.57	21	4 - 47795.0	3465.2	14	2.0 - 26.0	14.83	6
S	bdl - 16930.0	3898.85	8	bdl - 16930.0	6125.5	6	bdl - 15739.0	6609	4	bdl - 21132.0	4886.83	6
La	bdl - 55.0	24	3	bdl - 42.0	7.63	8	bdl - 7 .0	3.8	5	bdl - 14.0	12.00	3
Ce	bdl -92.0	92.00	1	bdl - 54.0	17.00	5	bdl - 27.0	16	2	bdl - 11.0	8.00	2
Nd	bdl - 33.0	14.40	5	bdl - 24.0	9.31	13	bdl - 53.0	9.73	11	bdl - 8.0	6.00	4

Geochemical	Kuruman-Griquatown (n=98)		Superior-type BIF
Group	Range	Average	(n=1073)
Co (ppm)	1.0 - 7.7	3.25	24
Ba	bdl - 91.6	12.42	108
S	bdl - 0.9	0.12	n.a.
La	0.3 - 8.4	1.73	2.16
Ce	0.6 - 16.7	3.31	3.69
Nd	0.2 - 7.2	1.46	2.68

Table 4.4. Trace element and REE average composition and ranges for part of the sample suite deriving from all four studied drill cores. Results are reported in ppm although some elements show concentrations of wt. %. Average compositions of Kuruman-Griquatown BIF (Paul Oonk, unpublished data) and Superior type-BIF (McClung, 2006) are also included. bdl = below detection limit, n.a. = not available.

that it may also reside in carbonates or silicate minerals apart from baryte. The highest values of Ba (6906, 47795 ppm) are associated with respective enrichments in S in the same samples demonstrating clearly the presence of baryte. Although Ba is present in the protolith, its concentration is very low (12.8 ppm) in general concert to Superior type-BIF (108 ppm). On the other hand, S concentration is mostly below detection limit and when detected it generally exhibits very high concentrations in all different geochemical groups which are undoubtedly related to sulphates. It should be noted that S is absent (0.12 ppm) from the Kuruman-Griquatown protolith.

La and Ce are in undetectable concentrations for most of the samples whereas Nd is mostly above detection. The obtained Nd values from all groups are enriched compared to Kuruman-Griquatown and Superior type-BIF. In the iron ore its concentration is ~ 10 times higher on average. Although the obtained La and Ce values are very few it can be clearly seen that they are again enriched on average and in upper range concentration compared to the two considered protoliths. For example in the ore La is ~14 times higher and Ce 28~ times higher, the latter potentially producing a significant anomaly. The observed enrichments in REEs are higher in the iron than in BIF. Distinct enrichment of LREE has been reported from the high-grade iron ore of Maremane dome and has been attributed to mobilization of REE, fractionation of LREE from HREE and concentration of LREE in the weathering residue during intense chemical weathering (Gutzmer et al., 2008). Regardless of the cause of REE mobilization, which in the case of this study it has been clearly shown so far that it also involves hydrothermal fluids (APS minerals), these elements potentially reside in the different phosphate minerals. This is supported by EDS analyses from this study showing that LREE (La, Ce and Nd) are mostly found in APS, and monazite whereas MREE and HREE (Gd, Dy, Yb, Er) reside chiefly in xenotime and zircon.

Additionally, a sample from the ferruginous shales (VLT74) found juxtaposed against the BIF in depths of approximately 440 and 470 meters was analyzed for major and trace elements. The obtained data are presented in table 4.5 along with Post-Archean average Australian shale (PAAS) (Taylor and McLennan, 1985) and average Gamagara shale created for a study on the Gamagara Formation (David Cousins, MSc Thesis, 2016).

Shale	VLT74	PAAS	Average Gamagara
SiO_2 (wt%)	32.27	64.80	57.79
TiO_2	2.75	0.7	1.29
Al_2O_3	17.20	16.9	17.22
Fe_2O_3	38.39	5.66	12.88
MnO	0.07	0.06	0.06
MgO	0.19	2.86	0.87
CaO	0.12	3.36	0.32
Na_2O	0.41	1.14	0.15
K_2O	4.02	3.97	3.72
P_2O_5	0.08	0.13	0.17
LOI	3.29	n.a.	4.39
H_2O^-	0.61	n.a.	0.88

Shale	VLT74	PAAS	Average Gamagara
Mo (ppm)	bdl	n.a.	n.a.
Nb	28.00	19	35.77
Zr	280.00	210	310.03
Y	30.00	27	30.84
Sr	152.00	200	157.24
U	bdl	3.1	2.60
Rb	99.00	160	140.04
Th	11.50	14.6	18.64
Pb	38.00	n.a.	12.04
Cu	9.00	50	n.a.
Zn	5.00	n.a.	n.a.
Ni	35.00	55	n.a.
Cr	65	110	327.48
V	552	150	140.49

Table 4.5. Major and trace element average composition in wt. % and ppm respectively for a ferruginous shale occurring in the MIF in a stratigraphic depth of 442 meters. PAAS is from Taylor and Mclennan (1985) and average Gamagara from David Cousins (MSc Thesis, 2016). bdl = below detection limit, n.a. = not available.

In PAAS normalized-diagrams it can be clearly seen that the analyzed shale displays similar geochemical patterns with the average Gamagara shale both if major and trace elements are concerned and some considerable enrichments in TiO_2, Fe_2O_3, Nb and Zr in comparison to PAAS. In the studied sample Fe_2O_3 is enriched by a factor of almost 3 and Ti by a factor of 2.1 in comparison to average Gamagara shale. Consequently, SiO_2, CaO, MgO and MnO show higher depletions while Al_2O_3 and K_2O are essentially the same. Trace elements are very well comparable apart from Cr and V which show antithetic relationships.

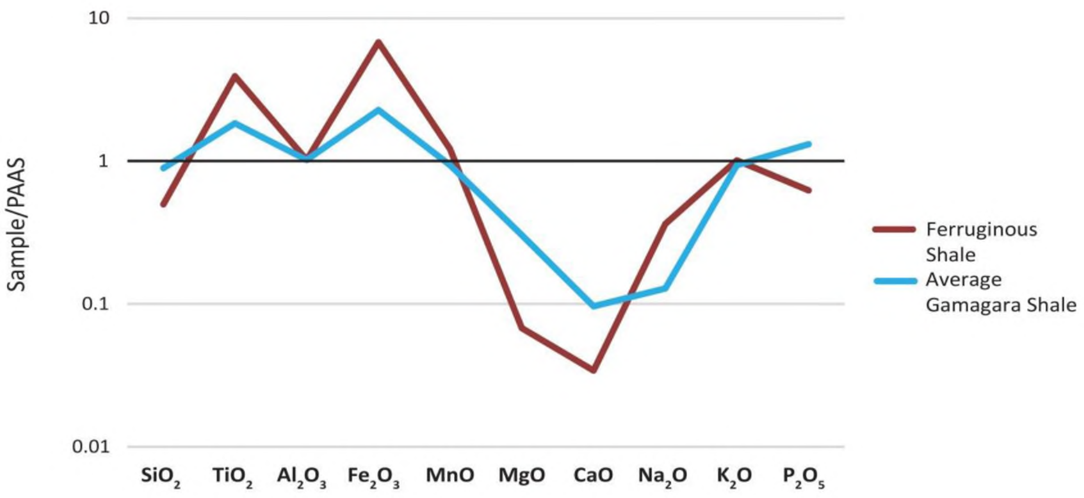

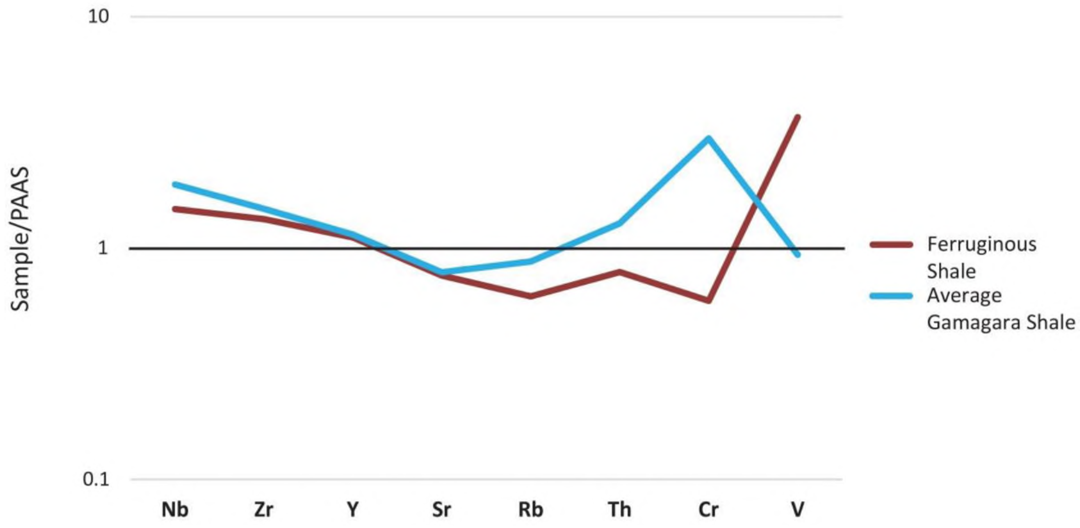

Figure 4.7. Average major and trace element geochemical spider-diagram of ferruginous shale (sample VLT74) and average Gamagara shale (David Cousins, MSc Thesis, 2016) normalized against PAAS (Taylor and McLennan, 1985).

The presence of shales sandwiched between the BIF by thrust faults in such high depths while showing the same geochemical signatures with shales from different regions found in the upper stratigraphy may be explained either by i) later thrusting after the main alteration of the shales which brings BIF upon shales and creates duplications or ii) thrusting-related fluid flow (shearing fluids) of similar geochemistry occurring in horizons of higher permeability and thus exploiting and altering shales found either in the upper stratigraphy or thrusted within the BIF. From the available data neither of the two scenarios is more preferable although it must be noted that Ti, Nb and generally HFSE enrichment has been documented by Tsikos et al. (2007) in the Gamagara Formation immediately overlying the ore and has been attributed to post-depositional alteration from an alkaline hydrothermal fluid the timing of which is believed to have occurred early in the diagenetic history of the shales (Land et al., in review).

Some of the studied samples deriving mainly from the BIF-bearing impure iron ore were further subsampled for different purposes such as to identify if the selected material is shale or BIF-derived based mainly on its Al_2O_3 content, to evaluate the iron content of red matrix (bands) commonly found in the ore or estimate the iron content responsible for pigmenting a silica-rich band (Fig. 4.8). The iron-rich matrix of the red bands apparently shows a consistent concentration of approximately 60 % wt. Fe_2O_3 whereas the quartz-rich portions have ~ 90-95 wt. % SiO_2 and consequently ~ 5-10 wt. % Fe_2O_3. Al_2O_3 is constantly low suggesting that no shale-fragments were present in the analyzed samples. The slightly increased Al_2O_3 of 2.70 wt. % in sample VLT4 is most likely related to silicates such as berthierine. Ba and S in the same sample account for almost 7 wt. % of the whole rock pointing to the presence of abundant baryte. In sample HLT26 a fragment of a siliceous BIF (73.15 wt. % SiO_2) is in sharp contact with a ferruginous (*lustrous red-grey*) BIF which shows 68.79 wt. % Fe_2O_3 and additionally CaO and S content accounting for ~ 4 wt. % of the whole rock. Gypsum was identified petrographically in the ferruginous portion as well as along the sharp contact between the two BIF-fragments. Finally, a sample from Sishen (D13) capturing a relatively gradual downward transition from a typical *reddish/cream-grey* (altered) BIF to the laminated high-grade iron ore was subsampled to evaluate the enrichment in Fe within the laminated BIF. Fe_2O_3 in the bottom part of the BIF is enriched only by 7 wt. % since chert mesobands and quartz within the oxide-band are apparently still present.

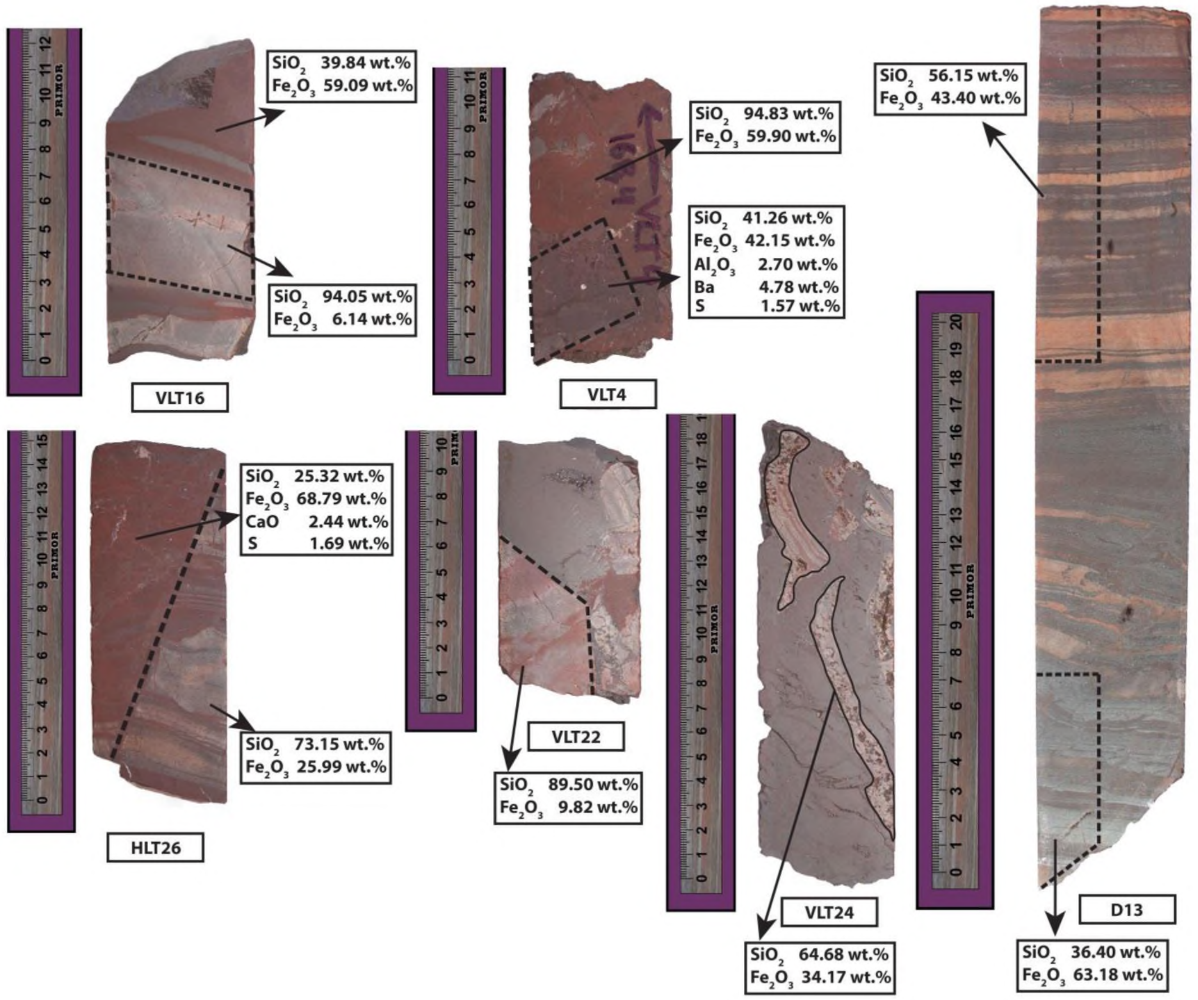

Figure 4.8. Geochemical signatures of subsampled portions from the studied samples. Only SiO_2 and Fe_2O_3 are shown in wt. % unless a concentration of another element is considerable. All geochemical data obtained are undoubtedly BIF-related. Samples VLT16, VLT4, VLT22 and VLT24 are from the BIF-bearing impure iron ore, sample HLT26 represents a *lustrous red-grey* (ferruginous) BIF in sharp contact to a *reddish/cream-grey* (siliceous) BIF and sample D13 derives from a transition from BIF to a horizon of laminated high-grade iron ore in Sishen.

4.6 Oxygen isotopes from quartz and hematite separates - results

Oxygen isotope analysis from hematite and quartz separates can yield insights in terms of the fluids responsible for the alteration of the BIF and the genesis of the iron ore. Samples analyzed for O isotopes in this study are in total 35 and were collected by micro-drilling. Further details on sample preparation and analytical techniques can be found in Appendix III.

Quartz separates collected represent different occurrences or generations of quartz from the BIF and the iron ore such as macrocrystalline quartz from veins, comb quartz, quartz form silica-rich portions in the ore and in chert lenses/pods, quartz from colloform banding and associated lensoidal structures, quartz from silicified replacement breccias and finally quartz from secondary silica-breccias. The $\delta^{18}O$ values for the quartz separates range from 19.8 ‰ to 25.2‰ with an average of 21.8‰ (n=17). The yields for the reported samples are between 82.6% and 102.2% except from two samples which gave a yield of 66% and 40.9%. Low yield values can be related to incomplete reaction during analysis or weighting errors. Sample HLT9 (66% yield) shows a reliable $\delta^{18}O$ value of 21.9‰ whereas sample D16b (40.9% yield) displays a very low $\delta^{18}O$ value of 8.3‰. For that reason, the later was excluded from the data set (although shown in Table 4.6) since as it was also found later by petrographic observations this sample contained baryte along with quartz.

Quartz		
Sample	**$\delta^{18}O$**	**Yield %**
VLT7a	23.71	96.0
VLT17	21.30	84.2
VLT27	21.00	84.7
VLT43	22.41	91.5
VLT44	20.40	90.4
VLT46	20.70	86.9
VLT49	19.80	82.6
VLT54	22.65	92.3
VLT57	20.90	87.8
VLT58	22.34	86.1
HLT9	21.90	66.0
HLT11	20.70	89.3
HLT17	22.20	102.2
HLT36	20.85	88.9
HLT38	21.45	88.7
D16b	8.30	40.9
D18	25.20	87.1
D20	23.40	95.1

Hematite		
Sample	**$\delta^{18}O$**	**Yield %**
VLT7b	-0.4	95.5
VLT10	1.7	94.7
VLT14	15.1	131.4
VLT21	4.1	98.9
VLT22a	9.4	100.4
VLT22b	0.4	98.4
VLT45	1.2	99.7
VLT75	-2.5	98.4
VLT76	3.8	101.4
VLT79	-0.9	97.5
HLT1	-2	91.8
HLT8	-1.2	93.2
HLT10	-0.3	95.9
HLT25	4.0	93.1
HLT44	0.5	91.0
S1	-1.4	96.9
D16a	-1.8	96.1

Table 4.6. Table displaying $\delta^{18}O$ isotope signatures and yield percentages from quartz and hematite separates of the BIF and the iron from all studied cores. $\delta^{18}O$ values are normalized to VSMOW and yield calculation assumes pure quartz (16.65 μmol/mg) and hematite (9.39 μmol/mg) respectively.

Despite the large range of different textures of quartz analyzed for O isotopes, the $\delta^{18}O$ values do not change significantly. The highest $\delta^{18}O$ isotope values (23.4‰, 23.71‰, and 25.2‰) are associated with macrocrystalline quartz from veins and silicified BIF with clear indications for replacement of banding. Secondary cryptocrystalline quartz of colloidal origin though shows lower values from ~20 to 22‰. Distinguishing values into different populations is difficult with the available data because there does not seem to be a clear pattern between quartz textures and oxygen isotope values. Generally, the isotopic diffusion rate between microcrystalline quartz from the original protolith and the fluid causing alteration is expected to be low because quartz displays the same texture in the MIF as in the protolith and is largely believed to be intact or *in situ* recrystallized in cases. However, it seems possible that the exchange rate of O isotopes between fluid and quartz is slightly changing for different generations of quartz being locally recrystallized or dissolved and regionally transported through the system before being precipitated in veins or horizons of silicification.

Hematite separates from the BIF found to be more difficult to select because of the intricate relationship of the mineral with quartz. Analyzed samples derive from the massive and laminated iron ore, the highly enriched Fe-matrix of the BIF-bearing impure iron ore, ferruginous clasts in secondary gypsum-breccias, Fe-rich portions in contact to silicified BIF and specularite veins. Additionally, some samples from hematite banding of ferruginous BIF which may show some quartz impurities were included. The $\delta^{18}O$ values for the hematite separates range from -1.8‰ to 4.1‰ with an average of 0.35‰ (n=15) except from two samples showing values of 9.4‰ (VLT22a) and 15.1‰ (VLT14). The yields obtained from all samples range from 91% to 101.4% except from sample VLT14 which gives a yield of 131.4%. This high value is caused definitely due to silicate impurities in the hematite separate. This sample petrographically represents a ferruginous clast within a secondary breccia in the iron ore but within its matrix quartz can be also found along with other silicates. Hence, this sample is also excluded from the isotopic data set. Higher $\delta^{18}O$ values (3.8‰, 4‰, 4.1‰ and 9.4‰) are associated with specular hematite. Ferruginous BIF from high stratigraphic depths (~450m) display negative $\delta^{18}O$ values, very close to that of the laminated and massive iron ore. Only sample HLT44 which is expected to bear some quartz impurities has a positive value (0.5‰). The $\delta^{18}O$ values of hematite from this study are compared to values from other major iron ore districts from around the world as well as to values from the protore BIF in the final chapter.

Synthesis and conclusions

Chapter 5

5.1 Alteration of the Manganore iron-formation

The Manganore iron-formation (MIF) has been considered as an altered equivalent of the Kuruman-Griquatown iron-formation sequence of the Asbestos Hills Subgroup (Van Schalkwyk and Beukes, 1986). Its association with the largest high-grade hematite ore resources on the Southern African continent renders its study essential for a better understanding of the iron ore origin and formation. Petrographically, MIF has been characterized as completely hematitized (oxidized), consisting entirely of hematite and quartz and only traces of greenalite and siderite have been detected by XRD within a horizon of laminated BIF (Van Schalkwyk, 1984). Martite has not been positively identified while any vein or vug-filling mineral possibly present has been systematically neglected, apart from the common mineralization of specularite occurring almost throughout the stratigraphy.

Detail investigation carried on four drill cores (SLT207, SLT284, SA2491E, SA2072) confirmed its close relationship with both the Kuruman and Griquatown iron-formations, providing further some insights into the complex alteration history it has undergone. Kuruman and Griquatown iron-formations consist of an assemblage of Fe_2^+ -bearing minerals which are: quartz, magnetite, Fe-carbonates (ankerite, siderite), calcite and Fe-silicates (greenalite, minnesotaite, stilpnomelane, and riebeckite), (Beukes, 1984). Hematite is only in such negligible amounts that its detection can prove to be very challenging. Protracted alteration has caused removal of primary mineralogy through dissolution and partly pseudomorphism in the MIF. The exact processes causing this mineralogical change though remain unclear as well as their relationship, if any, with the ore formation. Some reasonable questions arising could be the following: i) are there any mineralogical or sedimentary/diagenetic textures linking the MIF to its protolith and could one gain insight on the alteration processes through textural observation ii) what geochemical changes follow dissolution or replacement of primary minerals and are there any patterns of enrichment/depletion in the primary components of the BIF (silica and iron) across stratigraphy iii) Is it possible to explain the geochemical signature of the MIF and the overlying iron ore with elemental removal and redistribution or is a fluid-induced addition of elements necessary and finally iv) what is the nature of fluids responsible for the observed alteration and deposition of secondary mineralogy. This synthesis is trying to shed some light on the above by resuming the most important data presented earlier along with some new implications and concludes to a possible model for the alteration of the MIF and the genesis of the associated high-grade iron ore based on the available data.

5.1.1. Textural and geochemical evidence for hematitization and silicification of the BIF

Despite the extremely fine grain size of the MIF and its protolith insights can still be drawn from textural observation. There seems to be an excellent preservation of some of the original BIF textures differing only in mineralogical content. One of the most characteristic textures is that of discontinuous martite microbands reminiscent of the typical magnetite microbands of the Kuruman-Griquatown iron-formations (Fig. 5.1, A-B). Generally, the distribution of martite within mesobands and in contacts with chert bands where it becomes gradationally dispersed, are typical in the protolith. However, densely packed martite in the iron ore or in the iron-rich matrix of BIF breccias is a textured produced by leaching of silica, compaction and reworking of martite grains and is a drastically different distribution compared to the protolith. Pseudomorphic minerals exhibiting similar distribution with that of the parent rock are hematitized relicts of carbonates, typically of ankerite, arranged mostly in bands. Other pronounced relict textures linking MIF to Griquatown IF are the chert lenses/pods or pillows (Beukes, 1984) consisting almost entirely of quartz whereas in the parent rock the main constituents are Fe-carbonates, Fe-silicates and magnetite, regularly preferentially concentrated along the margins of the pods, a texture that is also preserved in the altered rock (Fig. 5.1, C-D). Even in cases where hematite-fronts appear to destroy primary textures, sedimentary/diagenetic fabric of orientation defined by primary mineralogy might have been texturally preserved and in fact might control the hematitization process itself through a type of chemical brecciation (Fig. 5.1, E-F). Fabrics exhibiting orientated microplaty hematite associated with previously silicified BIF are believed though to be of clearly secondary origin and most likely related to shearing.

From the above it is reasoned that alteration is to a large extent texturally retentive. The well-preserved banding and microlamination, the occurrence of comb quartz layers or

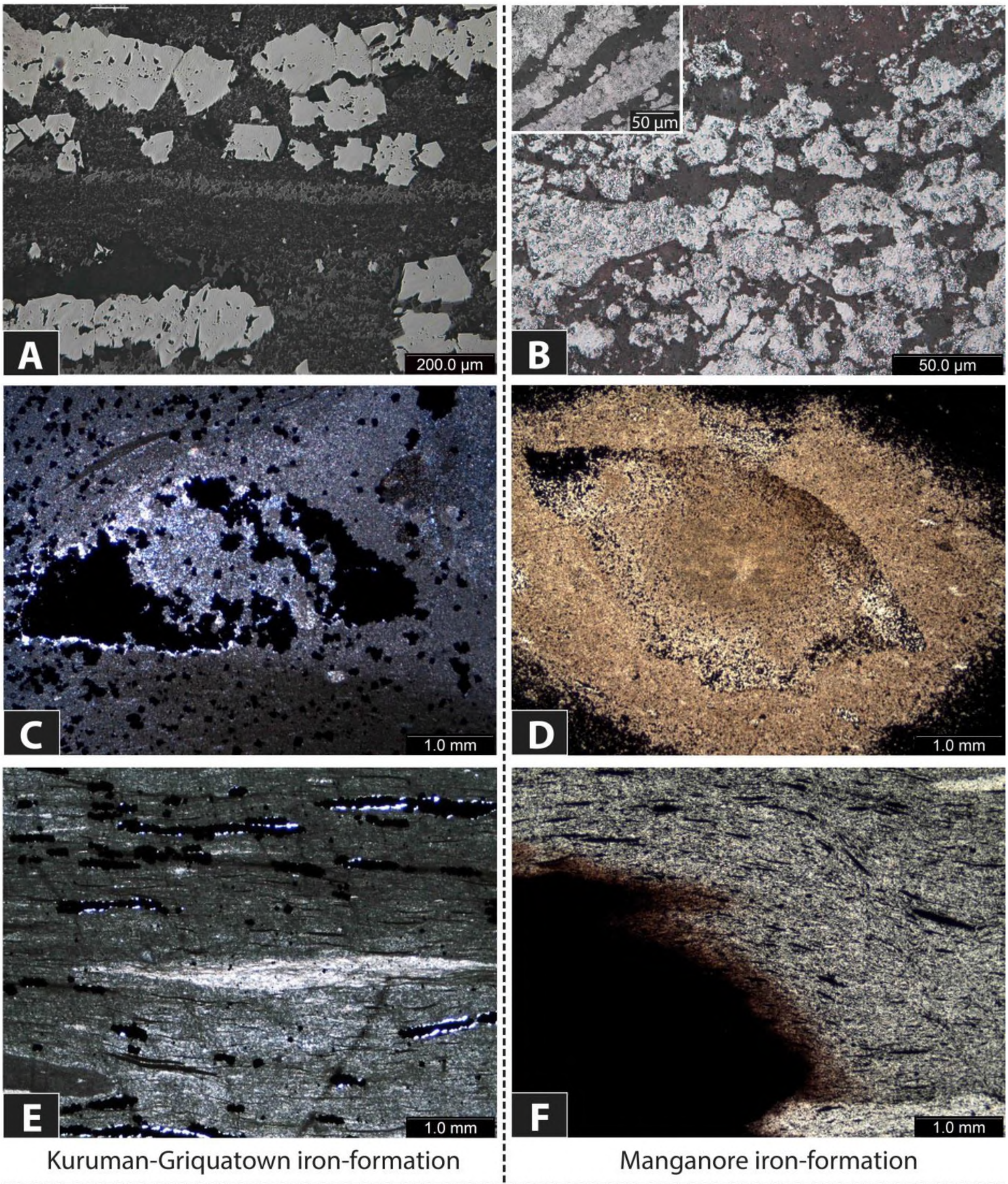

Figure 5.1. A-B is shown in reflected light whereas all other images were taken in transmitted light. A-B) Characteristic discontinuous magnetite microbands (left) preserved as oxidized martite microbands in the altered BIF (right) (XPR). C-D) Typical chert pods or pillows from Griquatown IF consisting of carbonate material and magnetite concentrated along the rims (left-XPL) transformed into a siliceous equivalent partly preserving the concentric structure (right-PPL). E-F) Planar fabric of sedimentary/diagenetic origin (left-XPL) retained in the altered rock despite the mineralogical differences and the hematitization front on the left of the image (right-PPL).

veins parallel to banding and the occasionally bedding-parallel development of microplaty to specular hematite or gypsum veins point to channeling of alteration fluids along susceptible horizons controlled by the marked lamination and structural discontinuities between the contrasting bands. Regardless of the nature of alteration (hematitization or silicification) it is suggested that it broadly occurs in layer-controlled metasomatic fronts.

In whatever way one interprets some of the textures presented in the petrographic chapter of this thesis, there is strong geochemical evidence coupled with textural observations which support that the dominant geochemical constituents of the BIF (silica and iron) are fluctuating across stratigraphy and in specific zones they are highly increased to a point where one can safely talk about ferruginous or siliceous BIF. Color variation of the BIF was used as a feature for macroscopic classification of the laminated BIF. Geochemical analyses showed that it can be a good indicator for the degree of iron enrichment since the pigmenting agent is hematite if also some other features are taken into consideration.

Removal of all major elements except from silica is expected to lead to a residual enrichment in iron. Dissolved carbonate and silicate minerals would release iron which would then precipitate as newly formed hematite, occasionally pseudomorphing pre-existing minerals. Things are way more complicated though as it can be seen from textures. For example, silica is also mobilized and plays a vital role in alteration since it is seen replacing same minerals as hematite (carbonates) and maybe even on a larger scale. The inhomogeneity of the laminated BIF renders any quantitative calculation difficult. It can be said that broadly a typical oxidized BIF (*reddish/cream-grey BIF, grey-red BIF*) seems to be only ~ 5 % (41.4 wt. % Fe_2O_3) more iron-rich on average compared to the protolith although large variations are shown because of the heterogeneity of samples. The total iron content of the BIF seems to be controlled chiefly from the occurrence and density of the oxide-rich mesobands and only minor from the dusty hematite impregnating and pigmenting pre-existing chert bands.

However, certain horizons of laminated BIF show high homogeneity because they consist to a large extent of alternating microbands (*red-grey BIF, lustrous red-grey BIF*). These BIF display higher iron content as expected due to absence of chert mesobands which reaches up to ~75 wt. % Fe_2O_3. Again, there are fluctuations between samples but the majority shows values above 60 %. The obtained geochemistry is in good agreement with textural observations which support that these laminated BIF have experienced an *in situ* enrichment in hematite by fluids while leaching of silica might be also taking place. Primary mineralogical composition possibly plays a crucial role in alteration in a sense that magnetite-rich horizons will lead to more hematite-rich BIF during alteration. The almost total absence of martite from the aforementioned enriched-BIF (ferruginous) suggests that other features such as structural might also control significantly the iron-enrichment, although this can only be surmised.

Iron released from primary minerals being dissolved might precipitate *in situ* as hematite but a lot of indications have been shown in the petrography chapter implying iron transportation. Hematitization as a process involving oxidizing solutions which further transport Fe on different scales within the MIF is supported by: i) pseudomorphic minerals the more conspicuous of being martite and pseudomorphs of hematite after ankerite (Fig. 5.2, A). Possible pseudomorphs after other minerals such as apatite were noted and most likely represent later remobilization of iron. ii) cryptocrystalline (dusty) hematite pigmenting chert bands in a linear fashion. iii) irregularly shaped hematite-fronts with diffused contacts to silica-rich portions within the brecciated BIF iv) laminated BIF showing textures of enrichment defined by microplaty hematite intruding between quartz crystals, enveloping them and in cases dissolving them (*red-grey BIF, lustrous red-grey BIF*). The same BIF show Fe_2O_3 up to ~75 wt. %. v) replacement textures of different kinds and possibly timing such as hematite replacing comb quartz or whole macrocrystalline crystals from secondary veins, hematite replacing pseudomorphs of quartz after carbonates or siderite being replaced by hematite. vi) microplaty to specular (>50 μm) hematite veining or vug filling which generally appears to be a late stage event, producing small-scale wall rock alteration, overgrowing and possibly replacing quartz and developing hematite-rich micro-breccias especially in proximity to the iron ore. Some localized hematite-breccias of unknown timing of formation display well-sorted chert fragments attacked by hematite in a hematite-rich matrix which indicates enrichment via fluid flow and vii) finally by hematite coexisting in veins with gypsum and/or silicates which supports transportation of iron through sulphate-bearing fluids.

It is also apparent that liberated silica most likely from the parent rock builds in places silica-rich zones within the BIF and beneath the ore. Silica alteration broadly follows the general alteration patterns suggesting that associated fluid flow percolates in a subparallel to banding manner and is preserving layering to a large degree although it can be also texturally destructive. Overall, silicification is expressed by: i) meso- to microbanded BIF of pale colouration and SiO_2 content of ~95 wt. % consisting almost entirely of micro and macro-crystalline quartz and a peculiar appearance of hematite as inclusions within quartz. Veins of quartz transecting these rocks are very common and may be responsible for brecciation of banding (Fig. 5.2, D) and occasionally intense rotation of remnant BIF-fragments. ii) replacement breccias where silica is actually seen replacing oxide banding leaving behind remnants of the initial banding ii) silica of colloidal origin precipitating as crypto- and microcrystalline quartz, filling open space and producing undulating colloform and concentric banding and veins interlayered with remnants of the primary BIF (Fig. 5.2, C). iii) replacement textures such as pseudomorphs of quartz after carbonate minerals or silicified structures such as pods/lenses of different initial mineralogy iv) whole-rock geochemical signatures reaching up to ~96.5 wt. % SiO_2. All of the above, point most likely to different silicification events. The difference in the susceptibility to silicification due to mineralogical and structural composition, the available open-space, degree of silica supersaturation and other physical parameters of the fluid may be related for the different textures observed.

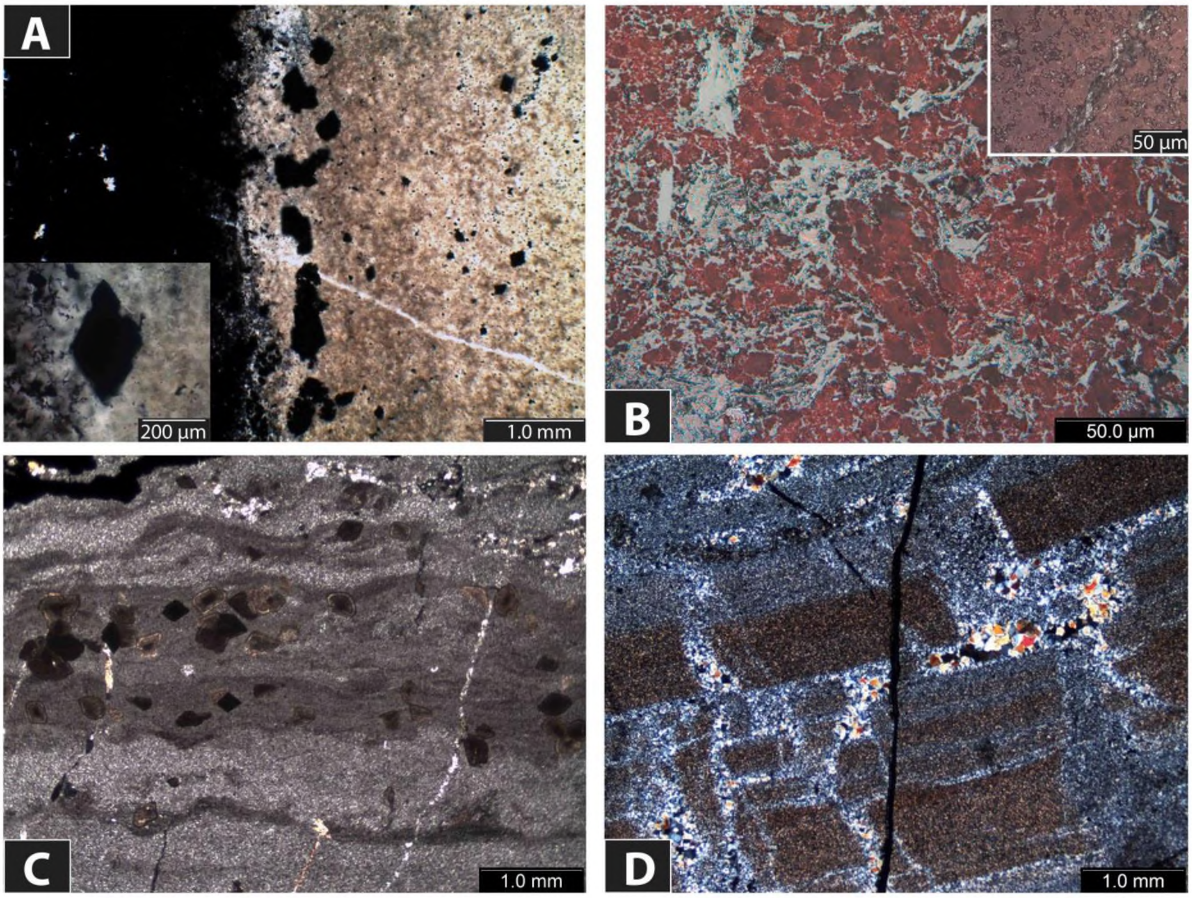

Figure 5.2. A) Linearly arranged pseudomorphs of hematite after carbonates next to a hematite mesoband (PPL). B) Hematite apparently brecciating and possibly dissolving quartz (XPR). *Inset*, hematite micro-vein and associated wall rock alteration defined by hematite microplates precipitating in the pore space as well as dusty hematite further impregnating quartz (XPR). C) Silicified BIF showing alternating crypto- and microcrystalline quartz banding and dispersed hydrothermal siderite (XPL). D) Quartz veins in a silicified BIF brecciating banding in a crackle-style fashion (XPL).

Mineralogically, there is no doubt of hematite and quartz being the chief constituents of the BIF. The first shows mostly micaceous habit while the latter is chiefly microcrystalline. Quartz is almost certainly recrystallized in various parts of the banding especially when is coarser and replaces pre-existing minerals. Different generations of quartz are further represented by macrocrystalline quartz veins and cryptocrystalline quartz of colloidal origin. Hematite-overprinted textures and crosscutting specularite veining points to at least two different generations of hematite although intricate relationships do not allow for further classification of microcrystalline and microplaty hematite.

Additionally, a variety of different assemblages of fluid-introduced secondary minerals have been described in detail from the BIF and the iron ore. Siderite and gypsum are two of the most abundant which also appear regularly within the chert or hematite mesobands of the laminated BIF and display euhedral individual crystals with no apparent relationship with veins. Different scenarios discussing their occurrence have been presented in the petrography chapter but their main implication is that their textural appearance relates the overall layered-controlled metasomatism of the BIF with the fluids responsible for their deposition. Carbonates, silicates, sulphates and sulphides appear commonly in veins and breccias and are a clear indication of fluids, irrespective of their origin. Many veins formed via mineral filling of open space from the contacts of veins toward their central part and propagated across pre-existing cracks or veins. Results of an attempt to widely discern the developed paragenetic sequences have been already presented although their complicated relationships limit determination of discrete stages. Nevertheless, it is certain that these parageneses represent a succession of hydrothermal pulses. Structural composition of the rocks played a major role in channeling groundwater or any type of hydrothermal brine related to the occurring mineral assemblages. Normal and thrust faults, fractures and cracks of different scales are very important structural features. Equally if not more important though is fragmentation caused by volume reduction of the BIF following dissolution of primary material and continuous brecciation collapse due to the intense karstification of the underlying dolomites. Fluid-assisted brecciation has been reported to also take place.

5.1.2. Apatite occurrence and phosphorus redistribution during alteration

Before continuing with a detailed evaluation of the geochemical changes during alteration it is considered valuable to briefly present the observed occurrences of apatite within the BIF and the iron ore, since the way in which phosphorus is generally found in iron ore is not well known (Pereira and Papini, 2015). Phosphorus is a contaminant that can be hard to remove and may need very different routes of treatment according to the mineralogy and distribution of phosphorus in the ore.

Phosphorus concentrations in the ores are thought to reflect the original amounts of apatite in the associated BIF (Morris, 1985). Whole-rock geochemical data from the different BIF groups in this study suggest that phosporus has relatively the same concentration in the altered rocks as that in the parent BIF or it might be slightly depleted. In more detail in ferruginous BIF it shows exactly the same concentration, in altered BIF it is depleted by an average factor of 0.67 and in the siliceous BIF it is depleted by a factor of 0.33. On the other hand, in the iron ore it can be enriched up to 5 times compared to the considered protolith. Apatite is the only significant P-bearing mineral in fresh BIF and although direct microscope evidence scarcely exist it has been reported that it is mainly distributed in bedding related patterns or scattered rounded micrometer-sized grains of <20 μm in diameter (Morris and Ewers, 1978, Morris, 1985).

In heavily altered or mineralized BIF and iron ore, microscope evidence for apatite is very scarce. Instead, reports for other phosphates are more common. For example Cochrane (2003) documented complex phosphate minerals and P-rich hydroxides along with secondary hydrothermal apatite occurring within the Mount Tom Price deposit of Hamersley Province. Xenotime and aluminium phosphates have been reported from the previous and other iron districts (Morris, 1985 and references therein). Authigenic REE phosphates (xenotime, monazite) documented by Rasmussen et al. (2007) and authigenic apatite are likely to represent the mineralogical reconstitution of P contained in the protolith BIF (Gutzmer et al., 2008).

In the studied samples apatite and other P-bearing minerals were observed commonly. The use of scanning-electron microscopy allowed for it to be easily detected while under optical microscope only large crystals were identifiable due to their characteristic hexagonal shape. That is said because in the massive iron ore apatite was commonly found filling open space as amorphous masses or as dense crystal aggregates (Fig 5.3, C) and one must be suspicious for such an occurrence if willing to identify it by means of standard microscopy. Apatite in the ore is also found as scattered grains of random distribution, especially in vuggy

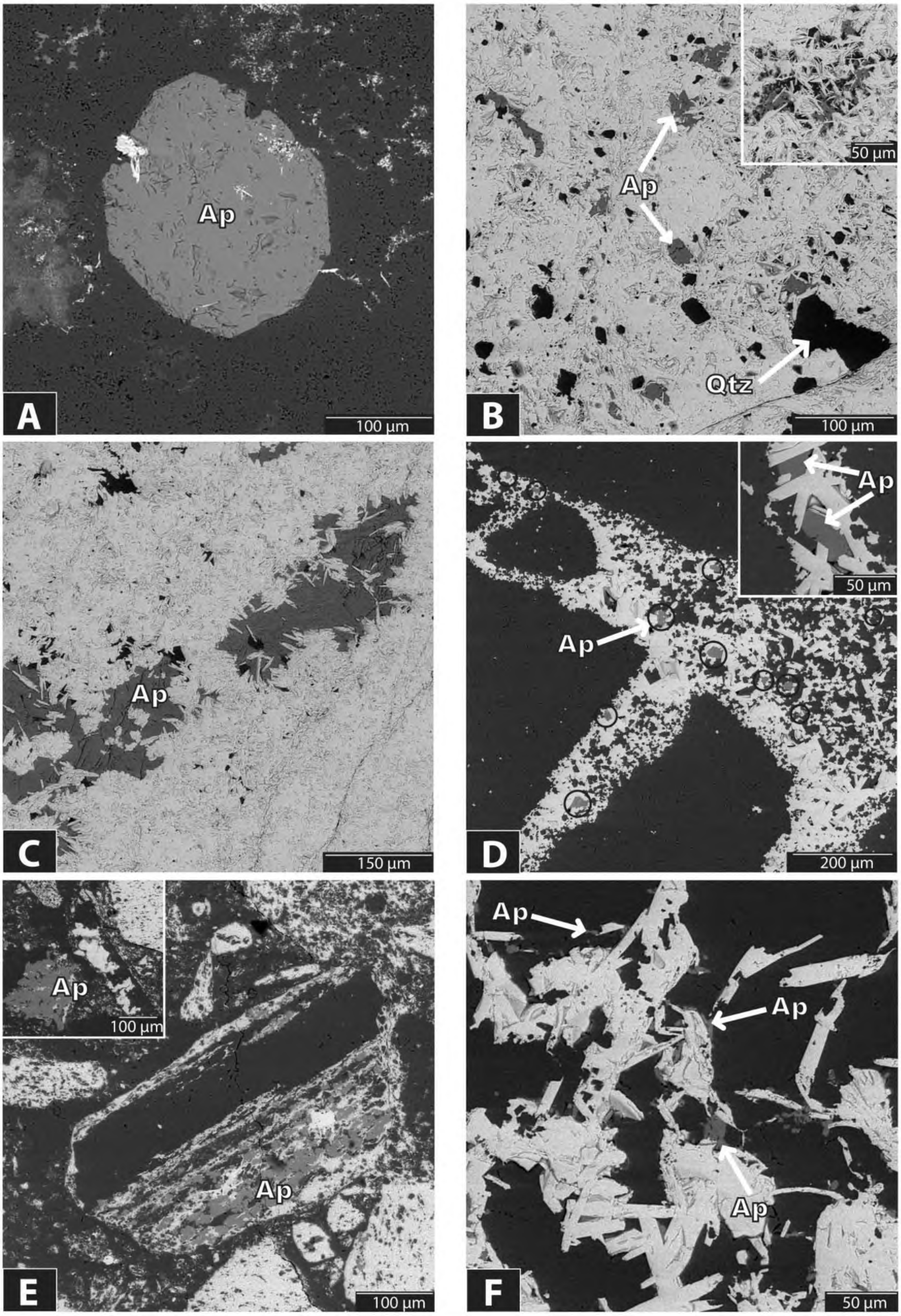

Figure 5.3. Backscattered electron (BSE) images. A) Large subequant apatite within the chert matrix of BIF-fragments in the direct footwall of the iron ore. B) Apatite randomly scattered as individual grains in the iron ore matrix. *Inset*, detail of a vuggy area. C) Apatite in the form of amorphous masses filling open-space within the ore. D) Abundant apatite grains present within microplaty to specular hematite-vein brecciating BIF. *Inset*, detail of the same area. E) Apatitized ferruginous BIF-

Figure 5.3. (continued) clast contained in a secondary quartz-breccia. *Inset*, another similar texture. F) Ubiquitous tiny apatite in close association with hematite microplates. Ap = Apatite, Qtz = Quartz.

areas intergrown with hematite (Fig 5.3, entire B). Apatite occurs also in the silicified BIF, in muscovite-veins and the largest euhedral crystals were observed within the chert matrix of BIF-fragments in the direct footwall of the ore (BIF-bearing impure iron ore) (Fig 5.3, A). A common pattern observed was the association of apatite with hematite in different textures. Hematite veins brecciating a typical altered BIF regularly contain abundant apatite intricately associated with the hematite plates (Fig. 5.3, D). Moreover, apatite seems to almost surround hematite in some cases (Fig. 5.3, F). Ferruginous BIF-clasts in secondary quartz-breccias are locally seen completely apatitized (Fig. 5.3, E). A relevant texture is that of apatite overprinting pseudomorphs of hematite after carbonates. In turn, apatite has been noted being metasomatically replaced by hematite, something that is presumably possible as stated by Morris (1985). The aforementioned textures could be characterized as preferential precipitation of P along with hematite. P becomes associated with goethite through surface adsorption of ions or complexes onto the growing surfaces of its precursors and might be incorporated into the goethite structure (Dukino et al., 2000). For synthetic samples, literature reports that goethite has a greater adsorption capacity of phosphate than hematite, certainly due to the higher surface area and porosity of the particles of goethite (Pereira and Papini, 2015). Although in the studied samples P is associated with hematite in the form of apatite it is suggested that there is certainly a geochemical reason behind this, related possibly to the transportation of Fe and P through the same solution using adsorption mechanisms as described above.

5.1.3. Geochemical mobility during alteration of the BIF and ore formation

Isocon diagrams provide one means to evaluate mass changes between an altered rock and its precursor as long as whole-rock geochemical data are available for both (Grant, 1986). The basic notion behind this method is that some elements are likely to behave as immobile during the alteration process and so these can be used to determine any volume change that may have taken place (Gresens, 1967). In the current study, precise mass-balance calculations are considered invaluable due to the insufficient data on thickness of the unaltered BIF and the overall collapse regime induced by the sinkholes which affects greatly the thickness of the MIF. However, isocon diagrams can be a useful tool for assessing geochemical mobility during alteration considering different scenarios of "immobility" isocons. A "constant mass isocon" is the simplest straight line that can be drawn through the origin at 45° and it assumes constant mass during the alteration from the original rock to the altered product. The "immobility isocon" is a line which is again drawn through the origin but it is generated using elements that are considered as immobile during alteration. For that reason, it provides greater insights into the geochemical mobility during alteration processes. The deviation of element data points from the relevant isocon defines the concentration change for that element relative to the protolith (Grant, 1986). Simply speaking, elements lying above the relevant isocon are gained during alteration and those lying below are being lost. Four isocon diagrams were constructed for all major element oxides and the majority of trace elements analyzed. The isocon method was applied to samples from the iron ore, from ferruginous BIF, altered BIF, as well as to samples from siliceous BIF. The considered precursor rock is no other than that of the Kuruman-Griquatown iron-formation, created for this study (Paul Oonk, unpublished data). All data were scaled for display purposes so that they plot between the values of 0 and 50 on the x and y axes.

The "immobility isocon" is usually determined by aluminum and titanium which are the most immobile elements among the major oxides and even in a supergene environment they are typically concentrated in the weathering profile whereas alkali earths and alkali metals are strongly mobilized (Grant, 1982, McLennan et al., 2003). Land et al. (in review) have shown that an alkali-HFSE metasomatism has affected the overlying shales and furthermore in this study, indications of a similar event are shown to have been recorded by BIF. If this event has happened before the main alteration of the BIF and its subsequent upgrade to iron ore as textures suggest, then one can assume that Ti, Zr and Nb were immobile after this event and during the supergene processes of ore formation. Hence, an "immobility isocon" can be drawn using the aforementioned elements. It has been already shown that compared to the considered protolith aluminum and titanium are either enriched in the iron ore or depleted in the BIF. Scatter plots constructed for these two elements do not show any significant correlation within the BIF. However, within brecciated BIF which compose the direct footwall to the ore and within the iron ore which is important in isocon diagrams evaluation, aluminum and titanium show comparable behavior in cores SLT207 and SLT284 (Fig. 5.4). Aluminum though displays a better linear relationship with potassium as it can be seen in Al_2O_3 vs. K_2O plots. Since potassium is considered as more mobile and may be introduced in the ore also later from the overlying shales, aluminum is not used in the determination of the "immobility isocon". The "constant iron" line displayed in the diagrams considers iron as being immobile and residually enriched during transformation process from BIF to iron ore, as suggested by most supergene models (Beukes et al., 2003). From the constructed graphs it can be seen that if iron is residually enriched in the ore, the immobile isocon is slightly deviating from constant iron which suggests that elements such as titanium and zirconium do not remain immobile during ore formation. Moreover, whatever isocon line one considers to be constant there is an observed enrichment in trace elements such as Cr, V, Ni, Pb, Mo and Th taking place during the transformation of BIF to high-grade iron ore. Relative mobility of iron against immobile elements or visa-versa is observed also in isocon diagrams constructed for BIF. Since altered BIF can be considered as the protore, during supergene processes effective removal of major elements such as calcium, magnesium and potassium is expected to take place while iron will remain immobile and will be residually enriched. At the same time, concentrations of elements defined by the immobility isocon are expected to remain unchanged. However, this is not the case for any of the isocon graphs involving BIF where it can be seen that Zr and Nb are being gained and titanium is being lost. The immobility isocon deviates more from the constant iron as one moves from ferruginous, to altered, to siliceous BIF as it is expected due to the significant changes in iron content. Most of the trace elements plotted are being gained during alteration in all BIF groups for all

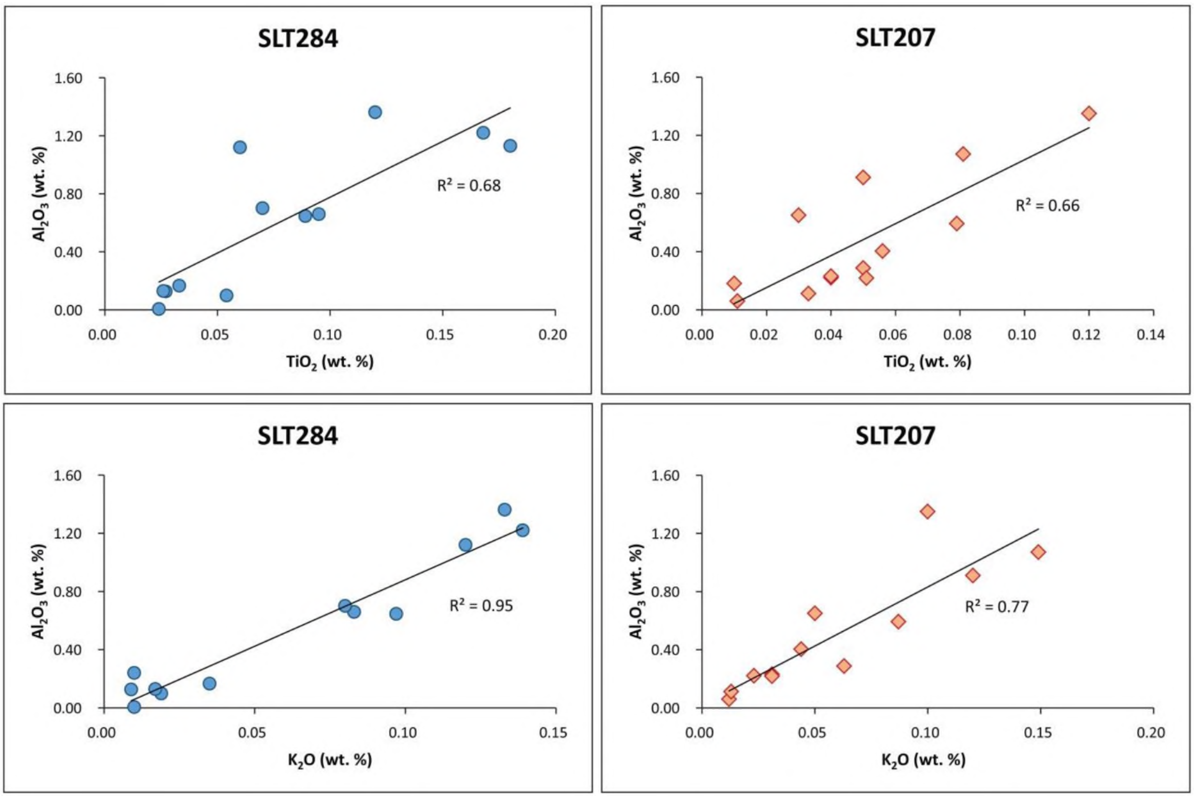

Figure 5.4. Bivariate plots of Al_2O_3 vs. TiO_2 and Al_2O_3 vs. K_2O for samples deriving only from the upper part of the stratigraphy of drill cores SLT207 and SLT284 which comprises brecciated BIF and iron ore. The higher concentrations derive from the iron ore and they decrease with increasing depth.

different isocon lines considered to be constant. Aluminum is constantly mobile if the immobility isocon held true during the alteration processes or if iron remained immobile during supergene enrichment. The highest loss of aluminum is recorded in the siliceous BIF. From all the above, it is suggested that supergene processes cannot account for the observed geochemical mobility during alteration of the MIF. Therefore, a fluid-induced redistribution of elements involving fluids of chemistry different from that of meteoric water would be required.

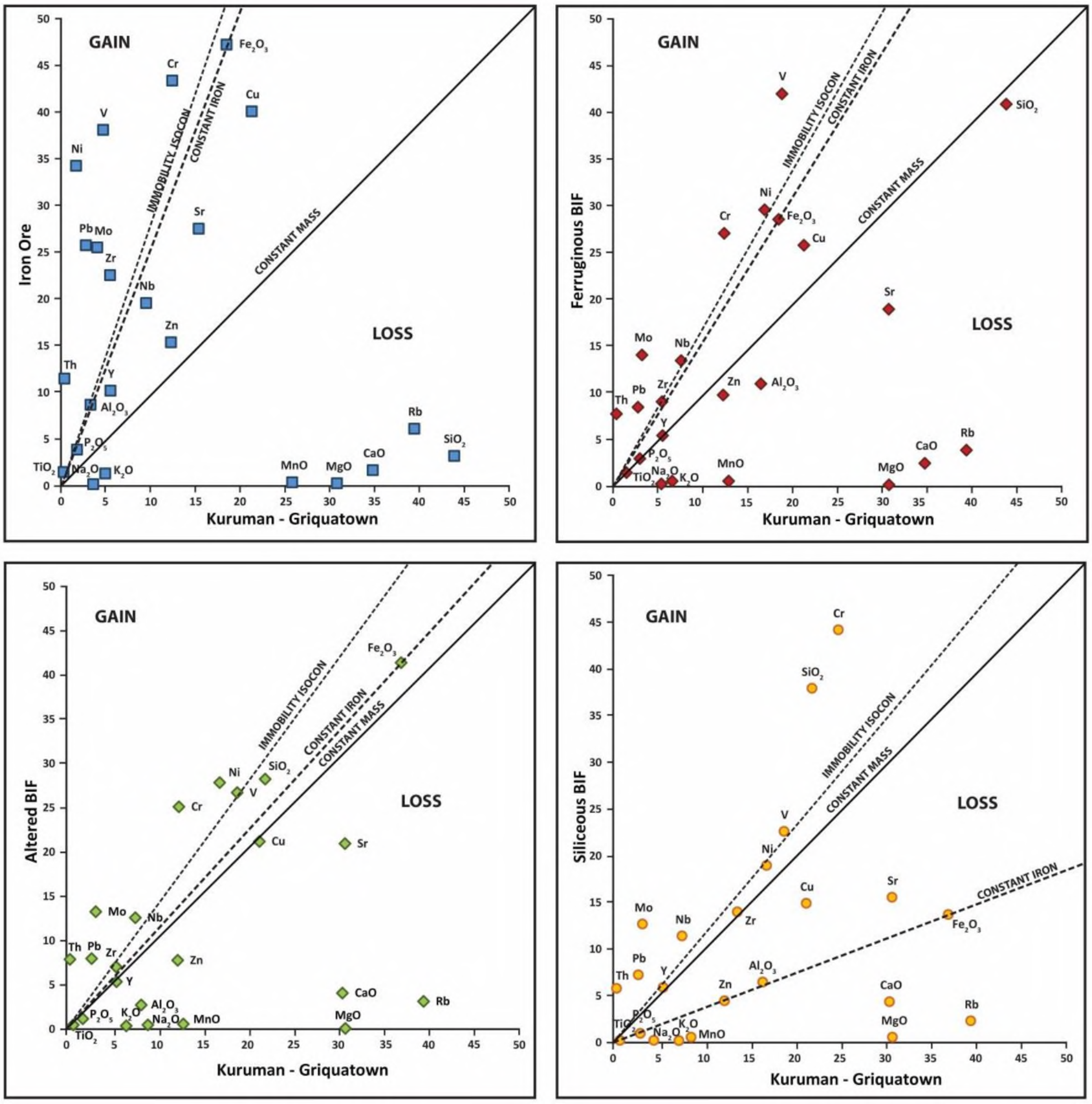

Figure 5.5. Isocon diagrams illustrating average whole-rock geochemical relationships between: A) iron ore, B) ferruginous BIF, C) altered BIF D) siliceous BIF and Kuruman-Griquatown iron-formation respectively. The average Kuruman-Griquatown iron-formation is from Paul Oonk (unpublished data). The three different isocon lines shown are for constant mass, constant iron and immobile elements (Ti, Zr, and Nb).

5.1.4. Constraints on the nature and evolution of fluids involved and deposition mechanisms

Establishment of the nature of the fluids responsible for depositing the vein and vug-filling mineral assemblages observed is difficult without fluid inclusion and stable isotope data. Generally such data are absent from literature apart from an unpublished fluid inclusion study on quartz form the underlying Wolhaarkop Breccia (Van Schalkwyk MSc thesis, 2005) which showed temperatures not exceeding 128^{o}C and a collection of published oxygen isotope data of hematite from the iron ore. The latter are discussed in the next section. However, textural relationships between minerals and mineral chemistry can provide a crude reading of the nature of the fluids involved.

The unaltered BIF contain some of the required components to produce the observed mineralization, such as Al, Ca, Mg, Na, Fe, Mn, and one could consider the possibility of fluid flow percolating through the bands, dissolving primary mineralogy and eventually becoming enriched in some of these elements which could be potentially involved in secondary mineral precipitation after being redistributed within the rock. However this cannot explain the presence of high amounts of S, Ba, B, Zr, Y, Nb and other traces elements which are either in minor quantities or truly absent from the protolith. The brecciation and slumping of the whole stratigraphy into the underlying carbonates caused by the continuous karstification of the latter made the MIF very permeable through secondary porosity and it is most evident that it was subject to a large through-put of fluid.

The crystalline, undeformed and euhedral nature and distribution of the silicate and sulphate minerals presented show affiliation to initial open spaces and deposition from hydrothermal fluids as vein and vug fillings and linings. These minerals formed under pronounced control by secondary porosity of the host rock which they might have further increased through dilation by elevated fluid pressure. Berthierine is essentially an iron-rich chlorite which requires high ferrous iron content in the fluids for it to be deposited. Other favorable factors for its formation are high alkalinity, slightly reducing conditions and additionally available Mg (Toth and Fritz, 1997). Harder (1978) noted also that low silica concentration in solution is the most important condition for low-temperature synthesis of iron clay minerals. All of the above point to an alkaline brine of low silica and high ferrous iron concentration being responsible for precipitation of berthierine possibly with the following reaction which progressively increases the acidity of the solution:

$$3Fe^{2+} + 3Mg^{2+} + 5Al^{3+} + 2H_4SiO_4 + H_2O \rightarrow \underset{\text{berthierine}}{(Fe^{2+},Fe^{3+},Al,Mg)_3(Si,Al)_2O_5(OH)_4} + 6H^+$$

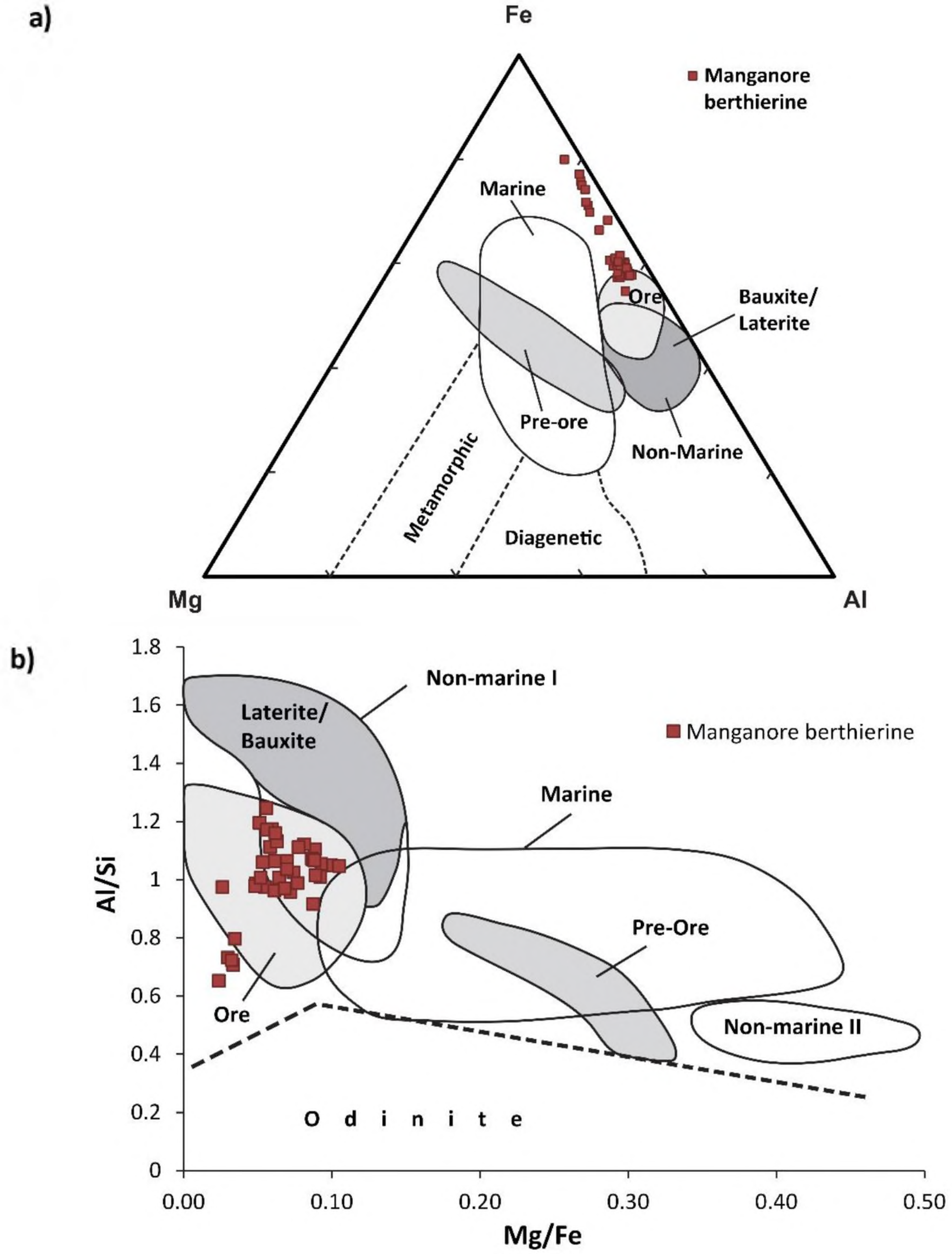

Figure 5.6. (a) Al - Mg - Fe triangle diagram (Velde, 1985, Damyanov and Vassileva, 2001). The plotted berthierine rarely falls within the ore field and exhibits very high iron content compared to berthierine from literature. The grey-shaded areas represent hydrothermal berthierine. (b) Mg/Fe vs. Al/Si diagram of compositional variations of berthierines formed in different geological settings (Damyanov and Vassileva, 2001 and references therein for the different fields). Ore field includes various deposits: Ag-Au epithermal, polymetallic, Au-quartz vein deposits, VMS, SEDEX, etc.

It has been shown that at temperatures of about 145°C berthierine converts into chamosite (Veena, 2009). Formation and conservation of the structurally metastable berthierine by hydrothermal solutions can be explained by sudden drops in temperatures or abrupt changes in acidity (Rusinova et al., 1986), both of which are plausible for berthierine in this study. Berthierine has been also used as an indicator of geological setting and it has been suggested that its composition depends more on the conditions than on the formation processes Damyanov and Vassileva, 2001). In the Mg-Al-Fe triangle diagram berthierine from Manganore iron-formation rarely falls within the ore field while most of the samples show very high iron content in comparison to berthierine from literature. It must be further noted that berthierine with the highest iron content derives from the iron ore. Al/Si and Mg/Fe ratios can reflect the initial geochemical relationships in solution/precursor because these pairs of elements are characterized by relatively close geochemical behavior in mineral systems related to isomorphic substitutions in each of the phases crystallized (Damyanov and Vassileva, 2001). In the Al/Si and Mg/Fe diagram the analyzed berthierine is clearly plotted within the ore field. This field includes hydrothermal berthierine from high temperature ore bodies (Au-quartz vein deposits, VMS, SEDEX, etc.) with higher Mg/Fe ratio and Mn content in comparison to pre-ore varieties. The Mn content is considered to be a mineralogical tracer implying the feeding channel of the hydrothermal ore-forming system (Rusinova et al., 1986) and hence it might show increases/decreases depending on the distance from the iron ore but the available analyses don not show any significant variations in Mn.

Tourmaline is a complex borosilicate with a considerable range of potential compositions, especially in hydrothermal environments. Its complex composition reflects changes in its chemical and physical environment in which it was developed, making it an ideal mineral to use for investigating differences between contrasting hydrothermal systems (Henry and Guidotti, 1985). The composition of the analyzed tourmaline from sample VLT57 plots near the iron-rich schorl member of the schorl-dravite series, showing almost constant aluminum. The associated rock types in which tourmaline of this composition is usually found are Li-poor granitoids and Fe^{3+} -rich quartz-tourmaline rocks (hydrothermally altered granites). Furthermore, tourmaline is host of boron and it is most likely formed in the studied system by reaction of a water solution bearing NaCl and H_3BO_3 with available Si, Fe, Al and Mg in the same solution. Boron has elevated concentrations in marine pelites and potassium-magnesium salts of marine evaporites (Walter, 2011) hence the presence of tourmaline in the studied rocks could potentially reflect brines with evaporitic characteristics. Its stable isotopes can be used as indicators of parent brine type, discriminating between marine and non-marine evaporites (Vengosh et al., 1991).

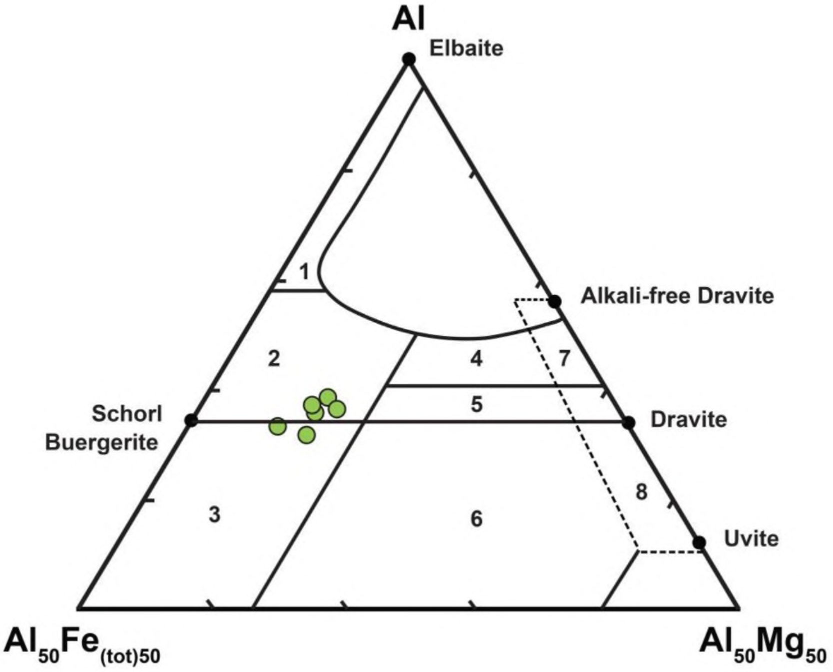

Figure 5.7. Al-Fe(tot)-Mg diagram for tourmalines from various rock types. The analyzed tourmaline from sample VLT57 is an Fe-rich member of the schorl-dravite series and is plotted in the field of Li-poor granitoids (2) and Fe^{3+} - rich quartz-tourmaline rocks (hydrothermally altered granites). For the rest of the fields the reader is referred to Henry and Guidotti, (1985).

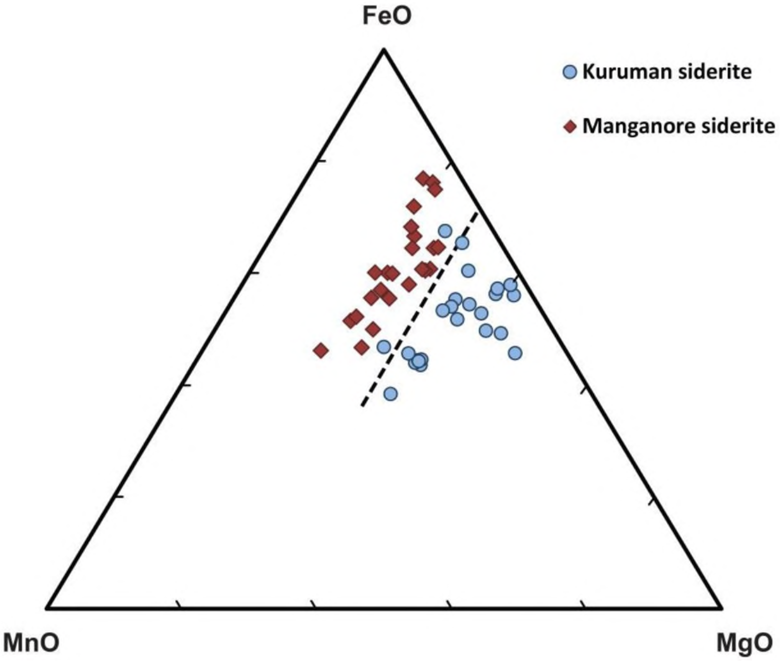

Figure 5.8. Mg-Mn-Fe triangular plot showing pronounced discrimination between siderite in the Manganore iron-formation and that in the protolith due to the lower Mg content of the first. Data presented here were scaled for display purposes, so that they do not plot very close to the upper apex due to very high FeO compared to MgO and MnO.

It has been already discussed that textures and distribution of siderite occurring in the MIF point to a secondary origin. In Figure 5.8, analyses of 24 siderites from the MIF were plotted along with 25 siderites from Kuruman. Mineral chemistry confirms textural observations as Manganore siderite has clearly lower Mg content. It is interesting that the average Mg/Fe ratio in the berthierine is consistent with that in the siderite (0.07 for both) which reflects high concentration of Fe compared to Mg within the fluid and points to crystallization from the same solution for the two minerals.

It is evident that the fluids involved are dominated by sulfur, most likely present as SO_4^{2-} which is the prevailing form in the usual pH rages of natural water and in alkaline conditions (Hem, 1960). Sulfur is also largely resistant to isotopic fractionation during burial alteration and transformation (Worden et al., 1997). Gypsum dehydration to anhydrite might not involve significant isotopic fractionation; therefore analyses of sulfur isotopes from different sulphates could shed some light into the origin of the fluids. Textural evidence has showed pyrite coexisting with gypsum as small crystals within the BIF. This implies the synchronous presence of oxidized and reduced sulfur in the same solution. Furthermore, pyrite in the ore was found as large anhedral crystals or pyritohedra, in cases even observable within vugs with the unaided eye. Reduction of sulfur species can occur through disproportionation reactions in hydrothermal fluids such as for example the ones related to the formation of sulphate (anhydrite) associated with porphyric copper deposits (Holland, 1965). The following reaction: $4SO_2 + 4H_2O \rightarrow 3HSO_4^- + H_2S + 3H^+$ can produce the required sulfur species if sulfur dioxide is present in the solution (Kusakabe et al., 2000) and thus explain the coeval formation of gypsum and pyrite and the commonly found inclusions of the first within the second. Experiments of SO_2 disproportionation made from the previous authors showed that it is favored when temperature drops, sulfur has low concentrations and the redox potential is low. A mixing of the fluids with downward percolating meteoric waters can also be assumed as partly being the cause of S disproportionation in the studied system. The produced H_2S could be used for the formation of pyrite while H_2SO_4 could be consumed to form the abundant baryte found in the ore through the following reactions:

(1) $Fe^{2+}_{(aq)} + 2H_2S \rightarrow FeS_2 + 4H^+$ (2) $H_2SO_4 + Ba(OH)_2 \rightarrow BaSO_4 + 2H_2O$

One can also draw insights into depositional conditions from the textural characteristics of pyrite, which are valuable because of the large variety of its morphological forms in hydrothermal environments (Murowchich and Barnes, 1987). The observed pyritohedra and anhedral shapes imply high to extreme levels of supersaturation in sulfur. Pyrite in the ore is believed to syncrystallize primarily with berthierine since prismatic crystals of the second are found penetrating the first. A WDS distribution map showing pyrite relationships with gypsum and berthierine can be found in Appendix II. Ferrous iron is not likely to be dissolved in a solution containing sulphide if equilibrium has been reached due to the very low solubility of pyrite, unless the pH and eh are relatively low (<6) (Takeno, 2005), therefore it will eventually precipitate forming mainly berthierine. Sulfur is not used up during the upward passage of fluids and synchronous deposition of abundant gypsum within the BIF as it is suggested by the presence of baryte within the ore. One the other hand, calcium concentration seems to falls below sufficient levels for large-scale gypsum precipitation. Baryte may be related to the final stage of the hydrothermal activity in concert to numerous other hydrothermal systems (Fig. 5.9).

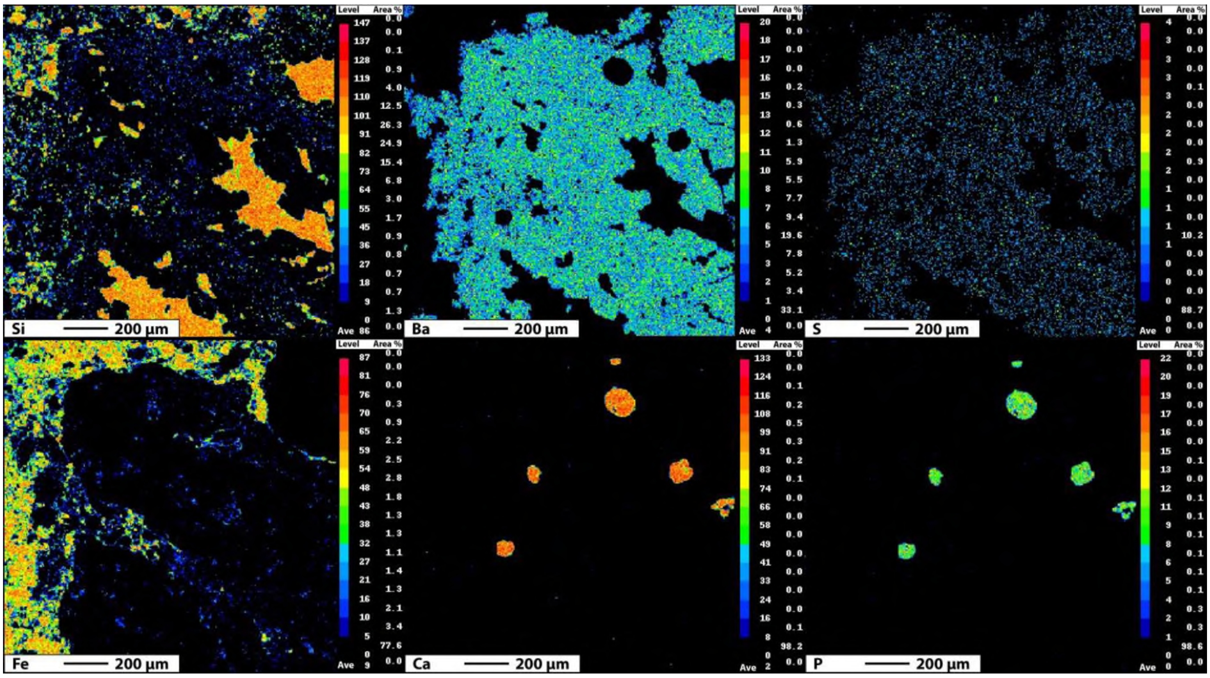

Figure 5.9. Elements distribution map obtained by WDS from an iron ore sample in drill core SLT207. Al and Mg not shown here are distributed within and around the baryte in small concentrations. The Ca-P areas represent apatite and the scales are in counts per second.

Berthierine and tourmaline seem to be present during all stages of hydrothermal activity. However, siderite was not found in the iron ore matrix but only within some associated unenriched BIF-fragments while lower in the stratigraphy it was commonly observed along with the silicates assemblage filling vugs and veins. Instead calcite, although relatively rare, seems to occur more often in the iron ore either with berthierine or baryte, or forming monomineralic veins. Siderite precipitation takes place under conditions of low sulphide-ion concentration, high carbonate-ion accumulation, high Fe^{2+}/Ca ratio, low eh and pH close to 7 (Curtis and Spears 1968, Maynard, 1983). The higher concentration of pyrite in the ore, lower calcium content in the fluid and a rise in the eh possibly by mixing with meteoric fluids could explain the dominance of calcite over siderite in the iron ore.

The presence of rutile up to 300 μm in size within colloform banding, vugs associated with ferruginous BIF or within veins with muscovite, zircon and/or xenotime (see also Appendix II) is believed to be a clearly secondary feature of the BIF. The introduction of Ti is thought to be related to an HFSE enrichment event involving alkaline oxidizing fluids that has affected the shales of the Mapedi formation during their early diagenetic history (Land et al., in review). Ti is generally considered immobile and rutile has very low solubility in water. However rutile solubility is critically depend on fluid chemistry and is increasing in chloride and fluoride-rich hydrous fluids as well as with increasing temperature (Rapp et al., 2010). In more detail, in chloride brines its solubility is 2-4 times higher than in water and in fluoride brines it can elevate 20-100 times. Hence, some occurrences of rutile associated with silicification could be explained by remobilization of Ti within the system caused by fluids with high concentrations of elements such Na, Cl, F, Si, Al, and K that influence Ti solubility (Antignano and Manning, 2008, Rapp et al., 2010). Furthermore, mobility of rutile has been reported to be defendant on sulphate and carbonate complexing agents carried by hydrothermal fluids (Purtov and Kotelnikova, 1993) which further supports the observed Ti mobility and parageneses of rutile + siderite + calcite found in the BIF. The partitioning of zirconium into rutile coexisting with zircon is strongly dependent on temperature which led to the presentation of an empirically calibrated Zr-in-rutile thermometer by Zack et al. (2004a), revised later by Watson et al. (2006). Qualitative analyses of rutile in textural equilibrium with zircons using EDS showed zirconium content in rutile as well as titanium content in zircon, therefore the aforementioned geothermometer could be applies if one proceeds with obtaining robust quantitative data.

Additionally, EDS-obtained chemical analyses of zircons from the iron ore demonstrated the presence of Ca, Sr, and Al mostly concentrated in the core of the crystals while the rim showed a somewhat purer composition. Although the provenance of these zircons is not clarified and a both detrital and hydrothermal origin is considered for the various crystals, mineral chemistry clearly shows metamictic zircons which could have been annealed by the introducing of the alkali fluids. Aluminium-phosphate-sulphate (APS) minerals occur in a wide range of environments including supergene and hypogene alteration (e.g. advanced argillic alteration, quartz-muscovite-tourmaline zones, supergene oxidation zones of epithermal deposits) and the important conditions for their formation are destruction of apatite, high activity of PO_4^{3-}, Ca^{2+} and Sr^{2+} the redistribution of which plays a major limitary role for the amount of APS, high oxygen potential and broad interval of pH (3-8) (Dill, 2000, Hikov et al., 2004). APS mineralization noted from the BIF and the iron ore is rather obviously related to the sulfur-bearing alkali fluids as it was demonstrated also in chapter 2 and furthermore to the destruction of either primary or secondary apatite occurring in the MIF. Scavenging the available ingredients svanbergite for example could form as shown below: $3Al^{3+} + H_2PO_4^- + SO_4^{2-} + Sr^{2+} + 6H_2O \rightarrow = SrAl_3(PO_4)(SO_4)(OH)_6 + 8H^+$. Most of the EDS analyses on apatite showed detectable amounts of fluorine which may also has important implications on the fluids involved since it is related to the conditions controlling Ti mobility as it was presented above.

Removal of SiO_2 from the BIF is fundamental for its transformation to high-grade iron ore and at the same time challenging to explain when considering supergene models and associated meteoric waters (Evans et al., 2013). On the other hand, there are scientists who propose that given a reasonable time and the right structural and topographic situations, rainwater will eventually dissolve quartz on the basis of the very good preservation of the parent textures, easily leached minerals and accelerated channeling of water through susceptible horizons such as BIF layering (Morris, 1980). Silica is most likely represented in the solution as molecules of monosilicic acid (H_4SiO_4). Mechanisms described for formation of colloids and banded veins in epithermal gold deposits involve vigorous boiling during rapid pressure drop and supersaturation with respect to amorphous silica (Simpson et al. 1995). Silica forming colloform-banded textures documented in this study could have originated from colloidal solutions formed by similar mechanisms for example of abrupt changes in physical parameters of the fluids. The solubility of quartz increases with increased temperature, pH and salinity. The pH is indeed the most crucial factor causing 4 orders of magnitude increase in solubility of quartz at pH 9 comparatively with solubility at pH 6 (Busey and Mesmer, 1977). The presence of NaCl in solution has been shown to cause a quartz solubility enhancement in higher temperatures (Newton and Manning, 2000b).

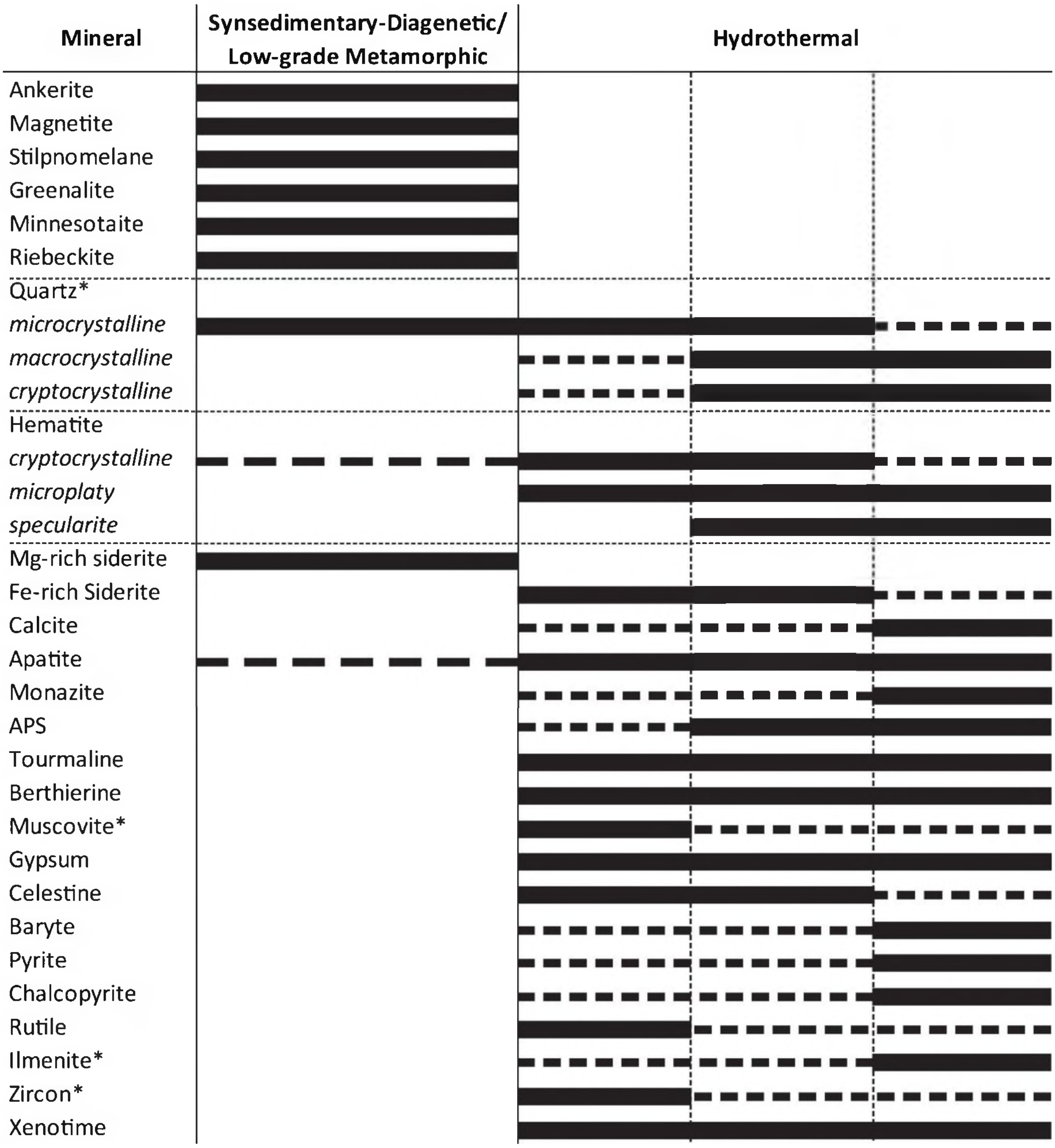

Figure 5.10. Interpreted paragenetic chart of the main minerals and textural varieties identified in all four studied drill cores. Minerals marked with an asterisk (*) can be also detrital, meaning that they might also have derived from the overlying shales during collapse brecciation.

Iron is commonly transported in solution by forming aqueous complexes with chlorine ($FeCl^+$, $FeCl_2^0$), the second becoming dominant at higher temperatures (Heinrich and Seward, 1990). Generally, reduced iron is mobile and oxidized iron immobile thus the valence of iron is Fe^{2+} in Cl-bearing aqueous fluids. Hydrothermal solubility of iron is positively correlated with fluid salinity and temperature (Fein, 1992). Elevated chlorine content of hydrothermal solutions is usually caused by dissolution of halite (Barton and Johnson, 1996). Furthermore, an increase in pH, from acidic to alkaline conditions would result in Fe^{2+} oxidizing to Fe^{2+}, whereas a change in Eh, from a reducing to a more oxidizing environment, would bear the same result (Ohmoto, 2003, Takeno, 2005). The latter is crucial for the transformation of magnetite to hematite during ore formation. From all the above it is inferred that alkali-bearing hydrothermal fluids provide an elegant mechanism to oxidized iron, transport SiO_2 out of the system and mobilize relatively immobile elements such as Al and Ti. The mineralogy presented earlier is in absolute concert with such fluids. Below, a paragenetic chart summarizing all textural observations made is presented.

Summarizing, the involved hydrothermal fluids contain appreciable amounts of dissolved SO_4^{2-} and CO_3^-, F^-, Cl^- and B^- as well as several ions of alkali earth and alkali metal elements. It is further noted that unidentified phases of silicate minerals found using EDS revealed always the involvement of Na and K in their structure during qualitative analyses. Although it is almost certain from crosscutting relationships with BIF banding that the occurrence of sulphates, sulphides, silicates and carbonates in veins is partly the product of hydrothermal overprinting at a later stage and their deposition follows largely the brecciation patterns developed by karstification of the dolomites as well as any other structural feature, their presence should not be neglected. In fact it is proposed that fluids associated with deposition of these minerals may have been the chief processes in the development of the observed BIF alteration and iron ore formation. The finding of berthierine, tourmaline and baryte in the iron ore of Sishen as well as sulfur content of almost 1 wt. % not associated with Ba, which implies the presence of gypsum (sample D14), suggests that these hydrothermal processes occur on a regional scale from one extremity of the Maremane dome to the other. It is also important to note that the fluids are seen circulating along a thick succession of BIF of at least 250 meters and end up affecting the iron ore as well.

5.1.5. Further insights from O isotope geochemistry

Quartz $\delta^{18}O$ values from texturally different occurrences from this study show only little variation. The measurements range from 19.8 ‰ to 22.7‰ with the exception of three values (23.4‰, 23.71‰, and 25.2‰) which represent secondary macro- and microcrystalline quartz from silicified BIF with pronounced replacement textures. Oxygen isotope geochemistry for Archean cherts displays values around 20‰, for example maximum values for Barberton cherts of the Swaziland Supergroup in South Africa are ~22‰ while Phanerozoic bedded cherts show comparatively higher values with the minimum being ~23%

(Knauth and Lowe, 2002). The only available quartz δ^{18}O values provided from literature for pristine and altered iron-formation in the wider Northern Cape Province derive from the Kalahari Manganese Field (KMF) and are similarly close to 20‰ (Tsikos et al., 2003). All of the above indicate that primary quartz broadly remains isotopically unexchanged during interaction with alteration fluids even if textures confirm that it is being recrystallized or dissolved, transported and reprecipitated within the system. Low isotopic exchangement further implies that these processes must have taken place at substantially low temperatures. However, the higher δ^{18}O values (up to 25.2‰) may be indicative of a higher isotopic exchange during secondary quartz formation under slightly higher temperatures from a brine potentially enriched in isotopically higher water.

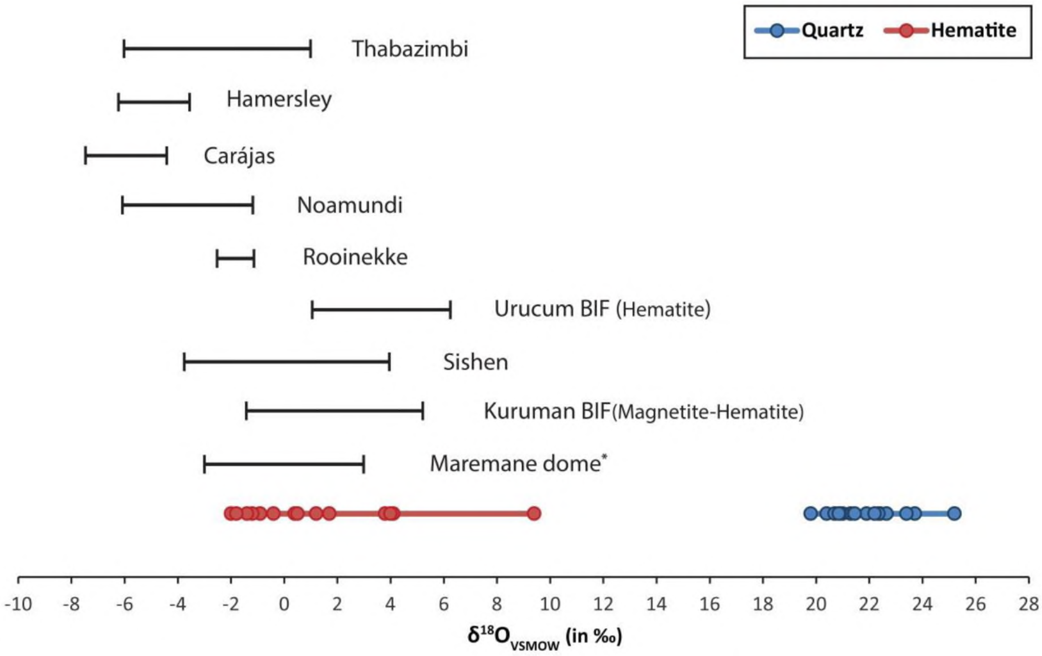

Figure 5.11. Diagram depicting ranges of hematite δ^{18}O values for various high-grade iron ore deposits. Data sources for Thabazimbi, Hamersley, Carájas, Noamundi, Rooinekke and Urucum are from Gutzmer et al. (2006), for Sishen is from Gutzmer et al. (2008) and Van Deventer (2009), for Kuruman BIF from Perry and Ahmad (1983) and for Maremane dome are from (Land, 2013). Hematite and quartz δ^{18}O values from this study are also plotted.

The oxygen isotope values of hematite from different BIF and ore-textures correspond very well with previously published data, excluding some high δ^{18}O values which represent microplaty to specular hematite veins. The first group of values (-1.8‰ to 1.7‰) corresponds markedly to values obtained from the Sishen iron ore deposit located on the northern part of the Maremane dome which is believed to be of supergene origin as well as to values from a previous study on the central part of the anticline (Land, 2013). Furthermore, the obtained

$\delta^{18}O$ range completely overlaps with values observed for the BIF protolith (Kuruman BIF) although the latter is slightly more enriched in $\delta^{18}O$ compared to the altered BIF and iron ore. The Thabazimbi, Hamersley, Carájas, Noamundi and Rooinekke deposits, which are interpreted to be hydrothermal or supergene-modified hydrothermal deposits, are on average distinctly more depleted than both Sishen and the samples from this study. Urucum BIF as a Neoproterozoic type example of supergene deposit displays comparatively enriched values.

Iron ore deposits of hydrothermal origin record depletions of up to 6‰ in comparison to the BIF protolith and the $\delta^{18}O$ values of hematite can be as low as -7‰ (Gutzmer et al., 2006). Summing up, oxygen isotope values of hematite in comparison to other ore districts point to a supergene rather than hypogene origin for the alteration of BIF and formation of the iron ore although this does not exclude the scenario of a later supergene overprint or invalidates the existence of the hydrothermal system presented earlier. Regardless of the above, hematite from veins as well as form an enriched laminated BIF show distinctively enriched $\delta^{18}O$ values which implies a different, most likely later generation of hematite and is in concert with values of specularite veins obtained from Sishen (Van Deventer, 2009).

5.2 Alteration history of MIF and iron ore genesis - A possible genetic model

In view of the above, a model can be proposed for the alteration of the BIF and the genesis of the high-grade hematite iron ore. It must be emphasized that the studied drill cores are part of a mineralization district expanding for at least 90 km N-S and possibly in other directions containing several different ore bodies while new are being and might be discovered in the future. Hence, an integrated model about formation of iron ore bodies on a regional scale, if possible, should involve more drill core and structural data from the whole region. The model proposed here encapsulates an endeavor to explain the new findings of this study on the basis of available data also from other studies.

The most plausible origin that could be proposed for the fluids associated with the alteration of the MIF is the underlying dolomites of the Campbellrand Subgroup. Since the nature of the fluids seems to involve also dissolution of evaporites besides that of carbonate rocks, a source of evaporites would be also favorable. The carbonates can act as a source of all alkalis observed in the studied parageneses and moreover of CO_3. The dolomites contain economic MVT-type Pb-Zn mineralization (Kesler et al., 2007) which could explain furthermore the enrichment in these elements in the ore as well as in some BIF groups. Pseudomorphs of former evaporitic minerals and typical evaporitic structures have been found within the upper parts of the Campbellrand Subgroup, in the Gamogaan and Kogelbeen Formations (Gandin et al., 2005). Field, petrographic and stable isotopic evidence indicate the former presence of extensive evaporites in the Campbellrand Subgroup. Pyrite is abundant in the Gamogaan Formation and is interpreted as a secondary mineral produced by bacterial sulphate reduction of earlier evaporitic species (selenite) (Gandin et al., 2005). Furthermore, all evaporites are ionic salts containing the major ions Na, Ca, Mg, K, Cl, SO_4 and CO_3. The hydrothermal model proposed bears similarities with the type model of Mississippi Valey-type deposits (MVT) which was also suggested by Thorne et al. (2004) for the North deposit in the Hamersley district. MVT deposits commonly occur where mineralizing brines are focused by the upward movement of hydrothermal saline ($NaCl-CaCl_2$) brines along inclined faults and associated fracture networks and laterally along the bedding planes of permeable lithologies. The temperatures of these brines are between 75 and 200^{o}C (Shelton et al., 1992). The sequence of events of the proposed model is summarized below and is illustrated in Figure 5.12:

- A) The first mineralization event affecting the BIF more or less synchronously with the overlying Gamagara/Mapedi shales is that of an alkali/HFSE metasomatism occurring early in the diagenetic history of the shales (Land et al., in review). This event possibly involved highly alkaline F-bearing brines and is recorded in the BIF by the presence of muscovite, rutile and zircon in veins across stratigraphy. The development of sinkholes in the dolomites in which BIF slumps into might have started already and could have helped the downflow of the alkali fluids.
- B) Subsequently, ongoing karstification of the Campbellrand dolomites by migrating groundwater of generally low pH, able to dissolve the carbonates leads to the production of large sinkholes and increases secondary porosity of the overlying BIF by its continuous collapse into the dolomites. Consequently, dissolution releases brines which start percolating through the BIF, carrying alkalis and CO_3^{2-} from the dissolution of the dolomites and becoming more alkaline progressively. The fluids are further enriched in Cl^- and B^- by the dissolution of the former evaporites of Campbellrand and in S deriving from dissolution of the abundant pyrite of the Gamogaan Member. Upward movement of

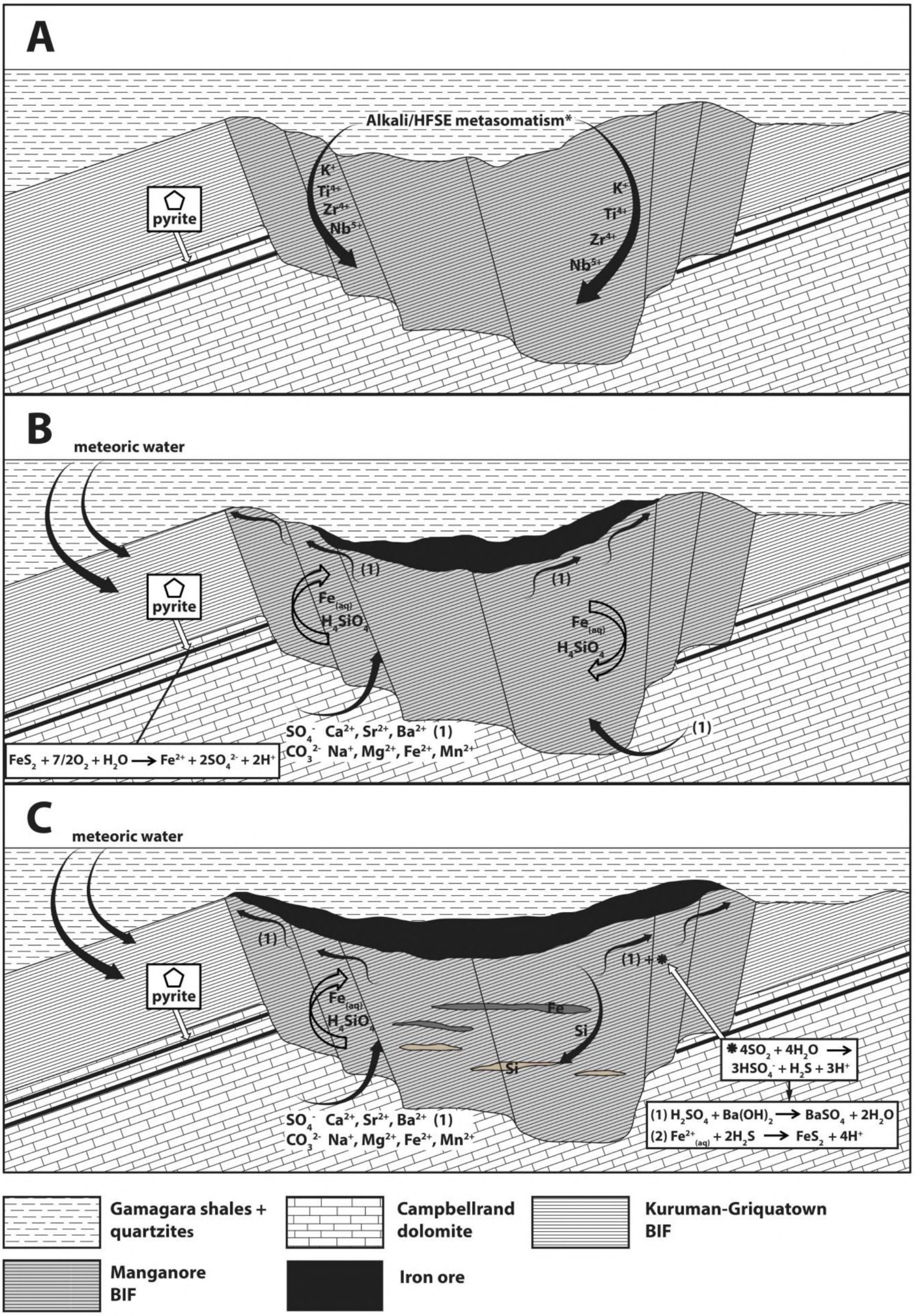

Figure 5.12. Suggested model for the alteration of the Manganore BIF and formation of the associated hematite high-grade iron ore. See text for details.

hydrothermal alkali-bearing saline brines possibly bringing in additional Fe starts dissolving primary BIF minerals and leaches SiO_2, inducing mineralization of the BIF. The brines convey through the BIF utilizing all kinds of discontinuities, causing dilation and further associated rock fracture, metasomatize the rock in layer-controlled fronts while at the same time more intense carbonate and sulphate metasomatism occurs in veins and breccias. Fluid infiltration successively exploits the unconformable contact between the BIF and the overlying shales and causes intense mineralization of both units along the contact. Hydrothermal fluids propagate though the whole mass of the BIF but the contact between the two units work as the most suitable fluid conduit for the iron enrichment process.

- C) Persistently circulating alkali-rich brines of successive hydrothermal pulses cause eventually complete leaching of silica from the upper stratigraphic horizons and hence development of a BIF and shale-derived iron ore (BID and SID). Fluids bearing iron and silica are convecting within the system during all stages of alteration. Susceptible horizons of BIF may be locally enriched in iron whereas silica supersaturated fluids build in places silicified zones. Liberated silica from desilicification during ore formation might be a likely source providing abundant silica for the development of such zones. The hydrothermal system is geochemically evolved as fluids pass through the BIF, dissolving and precipitating minerals while the physical parameters of the brines might also change by mixing with downward percolating meteoric water. This is expressed by disproportionation of sulphate and precipitation of major baryte and pyrite and lesser calcite in the iron ore, in contrast to major siderite and gypsum precipitating further down within the BIF stratigraphy. Specularite veins which produce micro-breccias and further upgrade locally the iron ore characterize one of the latest but not necessarily the last event of iron remobilization.

5.3 Conclusions and suggestions for further study

Some of the most significant conclusions reached in this study are the following:

(1) MIF has undergone a multi-event complex alteration history, as it can be withdrawn from overprint, replacement and crosscutting textures, in which hydrothermal activity is indisputably present.

(2) A series of preserved and metasomatized textures suggests that alteration occurs in layer-controlled metasomatic fronts, overall resulting in an altered rock which bears strong textural resemblance to Kuruman and Griquatown iron-formations in its upper and lower stratigraphy respectively.

(3) Whole-rock geochemical data can be used in conjunction with detailed petrographic observations to monitor potential patterns of enrichment/depletion in iron and silica in the altered BIF across stratigraphy. Hence, the Manganore BIF should not be considered as geochemically invariant since it is commonly enriched up to ~95 wt. % in SiO_2 and up to ~75 wt. % in Fe_2O_3 in meter-scale intervals.

(4) Enrichments of TiO_2 and Al_2O_3 by factors of 5 (up to 22.7) and ~2.5 respectively in the iron ore compared to the protolith and relative mobility of iron against immobile elements or visa-versa observed in isocon diagrams constructed for both BIF and iron ore suggests hydrothermal fluid-induced elemental redistribution during alteration.

(5) Trace elements display increasing enrichment patterns moving from silica-rich to iron-rich samples. Specifically, transition metals (Ni, Cr, Cu, V, Zn) and HFSE elements (Th, Y, Zr, Nb) are enriched in BIF and iron ore from ~4 up to ~30 times when compared to the Kuruman-Griquatown protolith.

(6) Secondary siderite is regularly recorded in the MIF both in banding as individual grains or within veins and open-space fillings along with gypsum, tourmaline and berthierine. Gypsum shows similar occurrence and additionally is more abundant.

(7) An alkali/HFSE alteration event that is believed to have affected the overlying Gamaraga/Mapedi shales is also recorded in the BIF by the occurrence of muscovite, apatite, rutile, hydrothermal zircon and xenotime down to high stratigraphic depths.

(8) A large-scale hydrothermal event has affected the BIF and the iron ore and it is expressed by sulphate, carbonate, silicate and sulphide associated parageneses appearing in veins and breccias.

(9) Most APS mineral occurrences have formed in response to the aforementioned hydrothermal event through redistribution of pre-existing muscovite and apatite. Phosphorus seems to be transported along with iron and secondary apatite bears a strong affiliation with hematite.

(10) Oxygen isotopes from different quartz textures reveal little to none isotopic exchangement during alteration whereas oxygen isotopes from hematite from BIF and iron ore coincide with values from literature obtained for Sishen and suggest two different generations of hematite, the later related with specularite veins.

(11) Upward movement of hydrothermal alkali-bearing saline brines originating from the underlying Campbellrand carbonates is proposed to be responsible to a large degree for the alteration of BIF and iron ore formation, without excluding involvement of synchronous or later supergene processes. Exploitation of the unconformable contact between BIF and the overlying shales is suggested as the most suitable fluid conduit for the iron enrichment process and the development of a BIF and shale-derived high-grade hematite iron ore.

In order to establish the nature of the fluids responsible for depositing the observed assemblages, set constraints on their possible origin and indirectly on the alteration of the MIF and formation of the associated high-grade iron ore, one has to employ more sophisticated methods. Some more high-tech analytical tools that could be used are: i) stable isotope geochemistry of boron and sulfur in tourmaline and the different generations of sulphate minerals respectively as a method to fingerprint the source of the mineralizing fluids, ii) geochronology of the different datable minerals that are found within the iron ore and the BIF such as zircon, xenotime, monazite and even tourmaline could set constraints on iron ore formation and timing of silicification and iii) fluid inclusions would potentially reveal more on the chemistry and temperature of the fluids. More detailed logging taking into account the textural and geochemical differences of the BIF could help in the development of new exploration tools. Emphasis should be also given on structural control through the development of maps. All of the above, can service to the refinement of the broadly accepted supergene models for the formation of the iron ores in the Northern Cape province which as it has been shown are inadequate of explaining new findings of this as well as of other recent studies.

References

Alchin, D., Lickfold, V., Mienie, P. J., Nel, D., & Strydom, M., (2008). An Integrated Exploration Approach to the Sishen South Iron Ore Deposit, Northern Cape Province, South Africa, and Its Implication for Developing a Structural and/or Resource Model for These Deposits. *Reviews in Economic Geology 15*, pp, 317-338.
and rutile. Contributions to Mineralogy and Petrology 151, pp. 413–433.

Antignano, A. and Manning, C.E., (2008). Rutile solubility in H_2O, H_2O-SiO_2, and H_2O-$NaAlSi_3O_8$ fluids at 0.7–2.0 GPa and 700–1000 °C: Implications for mobility of nominally insoluble elements. *Chemical Geology 255*, pp. 283-293.

Barley, M.E., Pickard, A.L., Hagemann, S.G., and Folkert, S.L., (1999). Hydrothermal origin of the 2 billion year old Mount Tom Pirce giant irohn ore deposit, Hamersley province, Western Australia. *Mineralium Deposita, v. 34*, pp. 784–789.

Barnes, H.L., (1997). Geochemistry of hydrothermal ore deposits (3rd ed.), *New York, Yohn Wiley and Sons*, pp. 972.

Barton, M.D. & Johnson, D.A. (1996). Evaporitic source model for igneous related Fe oxide-(REE-Cu-Au-U) mineralization. Geology 24, pp. 259-262.

Beukes, N. J., & Smit, C. A., (1987). New evidence for thrust faulting in Griqualand West, South Africa: Implications for stratigraphy and the age of red beds. *South African Journal of Geology 90*, pp. 378-394.

Beukes, N. J., (1983). Palaeoenvironmental setting of iron-formations in depositional basin of the Transvaal Supergroup, South Africa, in: Iron-formations: Facts and Problems, eds., A.F. Trendall and R.C. Morris. *Developments in Precambrian Geology 6*, pp. 131-198.

Beukes, N. J., (1984). Sedimentology of the Kuruman and Griquatown Iron-Formations, Transvaal Supergroup, Griqualand West, South Africa. *Precambrian Research 24*, pp. 47-84.

Beukes, N. J., (1987). Facies relations, depositional environments and diagenesis in a major early proterozoic stromatolitic carbonate platform to basinal sequence, Campbellrand Subgroup, Transvaal Supergroup, Southern Africa. *Sedimentary Geology 54*, pp. 1-46.

Beukes, N. J., Gutzmer, J., & Mukhopadhyay, J., (2003). The geology and genesis of high-grade hematite iron ore deposits. *Transactions of the Institute of Mining and Metallurgy B - Applied Earth Sciences 112*, B18-B25.

Beukes, N.J., and Gutzmer, J. (2008). Origin and Paleoenvironmental Significance of Major Iron Formations at the Archean-Paleoproterozoic Boundary. *Reviews in Economic Geology 15*, pp. 5-47.

Beukes, N.J., and Klein, C., (1990). Sedimentology and geochemistry of Early Proterozoic storm dominated deposits in a transition zone from microbanded Kuruman to granular Griquatown iron formation, Griqualand West: *Abstracts, Geocongress '90*, Geol. Soc. S. Afr., pp. 50-52.

Beyeme Z. J.C., (2009). Beneficiation potential of low-grade iron ore from a discard lumpy stockpile and fines tailings dam at Beeshoek-Mine, Northern Cape province, South Africa. (M.Sc. thesis): Johannesburg, Univ. of Johannesburg.

Blake R. L., Hessevick R. E., Zoltai T., and Finger L., (1966). Refinement of the hematite structure. *Amer. Mineral. 51*, pp. 123-129.

Blatt, H., (1982). Sedimentary Petrology: W. H. Freeman, San Francisco, CA.

Blockley, J.G., (1969). The stratigraphy of the Mount Tom Price ore body and its implication in the genesis of iron ore. *Geol. Surv. West. Aust. Ann. Rep. 1968*, pp. 46– 49.

Boggs, S., Jr., (2009). Petrology of Sedimentary Rocks. Cambridge University Press. London. 600 pp.

Brown, M.C., Oliver, N.H.S., and Dickens, G.R., (2004). Veins and hydrothermal fluid flow in the Mt. Whaleback Iron Ore District, eastern Hamersley Province, Western Australia. *Precambrian Research, v. 128*, pp. 441–474.

Busey, R. H., & Mesmer, R. E., (1977). Ionization equilibria of silicic acid and polysilicate formation in aqueous sodium chloride solutions to 300C. *Inorganic Chemistry 16*, pp. 2444 - 2450. *Canadian Mineralogist 18*, pp. 215-222.

Carney, M. D., & Mienie, P. J., (2003). A geological comparison of the Sishen and Sishen South (Welgevonden) iron ore deposits, Northern Cape Province, South Africa. *Transactions of the Institute of Mining and Metallurgy B - Applied Earth Sciences 112*, B81 - B88.

Cochrane, N., (2003). Phosphorus behavior during banded iron-formation enrichment. Unpublished BSc Thesis, Brisbane, Univerxity of Queensland, pp.86.

Cornell, R. M., Schwermann, U., (2003). The iron Oxides. Structure, properties, reactions, occurences and uses. Published by Wiley-VCH.

Cousins, D.P., (2016). A stratigraphic, petrographic and geochemical study of the Gamagara Formation at the Maremane Dome, Northen Cape province, South Africa. Unpublished Msc Thesis, Rhodes University, Grahamstown, South Africa.

Curtis, C.D. and Spears, D.A., (1968). The formation of sedimentary iron minerals. *Economic Geology,* 63**,** pp. 257–270.

Da Silva, R., (2011). Distribution and Geochronology of Unconformity-Bound Sequences in Paleoproterozoic Elim-Olifantshoek Red Beds: Implications for Timing of Formation of Sishen-Type Iron Ore and Heavy Carbonate Carbon Isotope Excursion. (M.S. thesis). Johannesburg, Univ. of Johannesburg, 103 pp.

Dalstra, H., & Rosiere, C. A. (2008). Structural controls on the high-grade iron ores hosted by banded iron formations: A global perspective. *Reviews in Economic Geology 15*, 73 -106.

Dalstra, H., Guedes, S.T., (2004). Giant hydrothermal hematite deposits with Mg–Fe metasomatism: a comparison of the Carajas, Hamersley, and other iron ores. *Econ. Geol. 99*, pp. 1793–1800.

Dalstra, H.J., (2006). Structural controls of bedded iron ore in the Hamersley Province, Western Australia: an example from the Paraburdoo Ranges. *Trans. Inst. Min. Metall. 115 (4),* pp. 139-145.

Damyanov, Z. and Vassileva M., (2001). Authigenic phyllosilicates in the middle Triassic Kremikovtsi sedimentary exhalative siderite iron formation, Western Balkan, Bulgaria. *Clays and Clay Minerals*, 49, 6, pp. 559–585.

Dill, H.G. (2001). The geology of aluminium phosphates and sulphates of the alunite group minerals: a review. *EarthSci. Rev. 53*, pp. 35-93.

Dorland, H., (1999). Paleoproterozoic laterite, red beds and ironstone of the Pretoria Group with reference to the history of atmospheric oxygen. MSc Thesis (unpublished), Rand Afrikaans University, Johannesburg.

Dukino, R.D., England, B.M., Kneeshaw, M., (2000). Phosphorus distribution in BIF-derived iron ores of Hamersley province, Western Australia. *Applied Earth Science, v 109*, pp. 168-176.

Edson, S. B., (1950). Interpretation of ore textures. Published by *the geological society of America.*

Evans, D. A., Gutzmer, J., Beukes, N. J., & Kirschvink, J. L., (2001). Paleomagnetic constraints on ages of mineralization in the Kalahari Manganese Field, South Africa. *Economic Geology 96*, pp. 621 - 631.

Evans, K. A., McCuaig, T. C., Leach, D., Angerer, T., & Hagemann, S. G. (2013). Banded iron formation to iron ore: A record of the evolution of Earth environments? *Geology 41*, pp. 99-102.

Ewers, W.E., Morris, R.C., (1981). Studies of the dales gorge member of the Brockman iron formation, Western Australia. *Econ. Geol. 76*, pp. 1929– 1953.

Fein, J.B., Hemley, J.J., D'Angelo, W.M., et al. (1992). Experimental study of iron-chloride complexing in hydrothermal fluids. *Geochim Cosmochim. Acta 56*, pp. 3179-1390.

Figueiredo e Silva R.C., Hagemann, S.C., Lobato, LM., Venemann, T., (2007b). Iron oxide paragenesis, quartz veins chronology and hydrothermal fluid evolution at the giant North Range Carajas iron deposits in Brazil. *Biennal Meeting of the Society for Geology Applied to Mineral Deposits, 9th, SGA, Dublin, Ireland, v. 2, Proccedings*, pp. 1223-1226.

Figueiredo e Silva R.C., Lobato L.M., Rosière C.A., Hagemann S., Zucchetti, M., Baars, F.J., Morais, R., and Andrade, I., (2008). A hydrothermal origin for the jaspilite-hosted, Giant Serra Norte Iron Ore Deposits in the Carajás Mineral Province, Pará State, Brazil. *Reviews in Economic Geology 15*, pp. 255-290.

Friese, A.E.W., and Alchin, D.J, (2007). New insights into the formation, structural development and preservation of iron ore deposits in the Northern Cape Province, South Africa. *The Australasian Institute of Mining and Metallurgy, Iron Ore 2005 Conference, Melbourne, Proccedings*, pp. 85-97.

Gallagher, V., (1988). Coupled substitutions in schorl-dravite tourmaline: new evidence from SE Ireland. *Mineralogical Magazine v. 52,* no.368, pp. 637-650.

Gandin, A., Wright, D. T., Melezhik, V., (2005). Vanished evaporites and carbonate formation in the Neoarchaean Kogelbeen and Gamohaan formations of the Campbellrand Subgroup, South Africa. *Journal of African Earth Sciences 41,* pp. 1–23.

Graham, J., (1973). Phosphorus in iron ore from the Hamersley iron formations. Aust. Inst. Min. Metall., Proc., 246, pp. 41-42.

Grant, J.A., (1986). The isocon diagram; a simple solution to Gresens' equation for metasomatic alteration. *Econ. Geol. 81*, pp 1976–1982.

Gresens, R. L., (1967). Composition-volume relationships of metasomatism. *Chemical Geology 2*, pp. 47 - 55.

Grobbelaar, W. S., Burger, M. A., Pretorius, A. I., Marais, W., & van Niekerk, I. J., (1995). Stratigraphic and structural setting of the Griqualand West and the Olifantshoek Sequences at Black Rock, Beeshoek and Rooinekke Mines, Griqualand West, South Africa. *Mineralium Deposita 30*, pp. 152-161.

Gross, G. A., (1980). A classification of iron formations based on depositional environments.
Gruner, J. W. (1930). Hydrothermal oxidation and leaching experiments, their bearing on the origin of Lake Superior hematite-limonite ores. *Economic Geology 25*, 697-719.

Gutzmer, J. and Beukes, N.J., (1996). Karst-hosted fresh-water Paleoproterozoic manganese deposits, Postmasburg, South Africa. Econ. Geoll. 91, pp. 1431-1454.

Gutzmer, J. and Beukes, N.J., (1998). Earliest laterites and possible evidence for terrestrial vegetation in the early Proterozoic. *Geology 26*, pp. 263-266.

Gutzmer, J., Chisonga, B. C., Beukes, N. J., & Mukhopadhyay, J., (2008). The Geochemistry of Banded Iron Formation-Hosted High-Grade Hematite-Martite Iron Ores. *Reviews in Economic Geology 15*, pp. 157-183.

Hagemann, S., Dalstra, H. I., Hodkiewicz, P., Flis, M., Thorne, W., & McCuaig, C., (2007). Recent Advances in BIF-related Iron Ore Models and Exploration Strategies. *In "Proceedings of Exploration 07: Fifth Decennial International Conference on Mineral Exploration"*, pp. 811-821.

Hagemann, S., Rosiere, C., Gutzmer, J., & Beukes, N. J., (2008). Introduction: Banded Iron Formation-Related High-Grade Iron Ore. *Reviews in Economic Geology 15*, pp. 1-4.

Hagemann, S.G., Barley, M.E., Folkert, S.L., Yardley, B.W., Banks, D.A., (1999). A hydrothermal origin for the giant Tom Price iron ore deposit. *Hughes FE (ed) Mineral* deposits, process to processing. *Balkema, Rotterdam*, pp. 41–44.

Halbich, E.W., Scheepers, R., Lamprecht, D., Van Deventer, J.L., De Kock, N.J., (1993). The Transvaal-Griqualand West banded iron-formation: geology, genesis, iron exploitation. *Journal of African Earth Sciences Vol 16, No 1/2*, pp. 63-120.

Harder, H., (1974). Illite mineral synthesis at surface temperatures. *Chemical Geology,* 14, pp. 241–253.

Harmsworth, R.A., Kneeshaw, M., Morris, R.C., Robinson, C.J., Shrivastava, P.K., (1990). BIF-derived iron ores of the Hamersley Province. Hughes, F.E. (Ed.), Geology of the Mineral Deposits of Australia and Papua New Guinea. *Aust. Inst. Min. Metall. Monogr.: Melbourne, vol. 14*, pp. 617– 642.

Heinrich C.A. and Seward T.M., (1990). A spectrophotometric study of aqueous iron (II) chloride complexing from 25 to 200°C. Geochim. Cosmochim. Acta 54, pp. 2207-2221.

Hem, J. D., (1960). Some chemical relationships among sulfur species and dissolved ferrous iron. *Geological Survey Water-supply Paper 1459-c.*

Henry, J.D. and Guidotti, C.V., (1985). Tourmaline as a petrogenetic indicator mineral: an example from the staurolite-grade metapelites of NW Maine. *American Mineralogist vol. 70,* pp. 1-15.

Hensler, A.S., Hagemann, S.G., Rosiere, C.A, Angerer, T., Gilbert, S., (2015). Hydrothermal and metamorphic fluid-rock interaction associated with hypogene "hard" iron ore mineralisation in the Quadril´atero Ferr´ıfero, Brazil: Implications from *in-situ* laser ablation ICP-MS iron oxide chemistry. *Ore Geology Reviews (2015),* doi:10.1016/j.oregeorev.2015.02.023.

Hikov, A., (2004). Aluminium-phosphate-suplhate minerals in advance argilic alteration zones in Petelovo and Pesovets deposits, Central Srednogorie. *Comptes rendus de l' Academis bulgare de Sciences, Tome 57, No 12.*

Holland, H.D, and Beukes, N.J. (1990). A paleoweathering profile from Griquland West, South Africa: Evidence for a dramatic rise in atmospheric oxygen between 2.2 and 1.9 by BP. *American Journal of Science 90, ser A*, pp. 1-34.

Holland, H.D., (1965). Some applications of thermochemical data to problems of ore depoists. II. Mineral assemblages and the composition of ore-forming fluids. *Econ. Geol. 60,* pp. 1101-1166.

Horstmann, U. E., & Halbich, I. W., (1995). Chemical composition of banded iron-formations of the Griqualand West Sequence, Northern Cape Province, South Africa, in comparison with other Precambrian iron formations. *Precambrian Research 72*, pp. 109-145.

James, H. L., (1954). Sedimentary facies of iron-formation. *Economic Geology 49*, pp. 235-293.

Kesler, S. E., Reich, M., & Jean, M., (2007). Geochemistry of fluid inclusion brines from Earth's oldest Mississippi Valley-type (MVT) deposits, Transvaal Supergroup, South Africa. *Chemical Geology 237*, pp. 274-288.

Klein, C. & Bricker, O.P., (1977). Some aspects of the sedimentary and diagenetic environment of Proterozoic banded iron-formation. *Econ. Geol., 72*, pp. 1457-1470.

Klein, C., (1974). Greenalite, stilpnomelane, minnesotaite, crocidolite and carbonates in a very low-grade metamorphic Precambrian iron formation. *Can. Mineral., 12*, pp. 475-498.

Klein, C., (2005). Some Precambrian banded iron-formations (BIFs) from around the world: Their age, geologic setting, mineralogy, metamorphism, geochemistry, and origin. A*merican Mineralogist 90*, pp. 1473-1499.

Klemm, D.D., (1979). A biogenetic model of the formation of the banded iron formation in the Transvaal Supergroup, South Africa. *Miner. Deposita*, 14: 381-385.

Knauth, L.P. and Lowe, D.R., (2003). High Archean climatic temperature inferred from oxygen isotope geochemistry of cherts in the 3.5 Ga Swaziland Supergroup, South Africa. *Geological Society of America Bulletin, vol 115, no 5*, pp. 566-580.

Konings, R.J.M., Boland, J.N., Vriend, S.P., Jansen, J.B.H., (1988). Chemistry of biotites and muscovites in the Abas granite, northern Portugal. *American Mineralogist vol. 73*, pp. 754-765.

Kullerud, G., Yund, R.A., Moh, G.H., (1969). Phase relations in the Cu-Fe-S, Cu-Ni-S and Fe-Ni-S and Fe-Ni-S systems. *Magmatic Ore Deposits, Econ. Geol. Publ. Co., Lancaster, PA*, pp. 323-343.

Land, J.S., (2013). Genesis of BIF-hosted hematite iron-ore mineralisation in the western margin of the Wolhaarkop Dome, Postmasburg, Northern Cape Province. Unpublished Msc Thesis, Rhodes University, Grahamstown, South Africa.

Land, J.S., Tsikos, H., Cousins, D.P., Luvizotto, T.Z., Beukes, N.J., (In review). Origin of paleosols and red beds in the Palaeoproterozoic Transvaal and Olifantshoek Supergroups of South Africa: provenance *versus* metasomatic controls. *Geological Journal, Wiley.*

Lebedev L.M., (1967). Metacolloids in endogenic deposits. Plenum press, New York.

Lobato, L. M., Silva, R. C. F., Rosière, C. A., Zucchetti, M., Baars, F. J., Pimentel, M., Rios, F. J., Seoane, J. C. S., Monteiro, A. M., (2005). Hydrothermal origin for the iron mineralization, Carajás Province, Pará State, Brazil, in *Iron Ore 2005*, pp. 99-110.

Lobato, L.M., Figueiredo e Silva, R.C., Hagemann, S.G., Thorne, W.S., Zuchetti, M., (2008). Hypogene alteration associated with high-grade banded iron formation-related iron ore. *In: Hagemann, S.G., Rosière, C.A., Gutzmer, J., Beukes, N.J. (Eds.), Rev Econ Geol,* pp. 107-128.

Lobato, L.M., Rosiere, C.A., Baars, F.J., Figueiredo e Silva R.C., Zucchetti, M., Rios, F.J., Seoane, J.C.S., Pimentel, M., Lindenmayer, Z.G., Mendes, G.E., Maceil, A.L., (2004). Timing of hydrothermal iron mineralization, Carajas province, PA. *Simposio Brasileiro Exploracao Mineral, 1st*, Ouro Preto, Brazil, Agencia papa o Desenvolvimento Technologico da Industria Mineral Brasileira (ADIMB).

Lowenstein, T.K., Hardie, L.A., Timoeeff, M.N., Demicco, R.V., (2003). Secular variation in seawater chemistry and the origin of calcium chlorite basinal brine. *Geology 31*, pp. 857-860.

Marinova, I., Ganev, V., Titorenkova, R., (2013). Colloidal origin of colloform-banded textures in the Paleogene low-sulfidation Khan Krum gold deposit, SE Bulgaria. *Miner. Deposita (2014)*. DOI 10.1007/s00126-013-0473-4.

Maynard, J.B., (1983). Geochemistry of Sedimentary Ore Deposits. *Springer-Verlag, New York*, 305 pp.

McClung, C. R., (2006). Basin analysis of the Mesoproterozoic Bushmanland Group of the Namaqua metamorphic province, South Africa. Ph.D. thesis (unpublished), University of Johannesburg, Auckland Park.

McLennan, S.M., Bock, B., Hemming, S.R., Hurowitz, J.A., Lev, S.M., & McDaniel, D.K., (2003). The roles of provenance and sedimentary processes in the geochemistry of sedimentary rocks, in Lentz, D.R., ed., Geochemistry of Sediments and Sedimentary Rocks: Evolutionary Considerations to Mineral Deposit-Forming Environments. *Geological Association of Canada, GeoText 4*, pp. 7 - 38.

Moore, J. M., Tsikos, H., & Polteau, S., (2001). Deconstructing the Transvaal Supergroup, South Africa: Implication for Palaeoproterozoic palaeoclimate models. *Journal of African Earth Sciences 33*, pp. 437-444.

Móricz F., Walder I., Mádai F., (2012). Pyrite oxidation under circumneutral pH condition. *Geosciences and Engineering, Miskolc, Miskolc University press, Vol.1, Num2.*, pp. 111-116, ISSN 2063-6997.

Morris, R.C. and Ewers, W.E., (1978). A simple strike-print technique for mapping mineral distributions in ores and other rocks. *Econ. Geol. 73*, pp. 562-566.

Morris, R.C., (1985). Genesis of iron ore in banded iron-formation by supergene and supergene-metamorphic processes - a conceptual model. In: *Wolf, K.H. (Ed.), Handbook of Strata-bound and Stratiform Ore Deposits. Elsevier, Amsterdam*, pp. 73–235.

Morris, R.C., Horwitz, R.C., (1983). The origin of the iron-formation-rich Hamersley Group of Western Australia-deposition on a platform. *Precambrian Res. 21*, pp. 273–297.

Morris, R.C., Thornber, M.R., and Ewers, W.E., (1980). Deep-seaterd iron ores from banded iron formation. *Nature, v. 288*, pp. 250–252.

Mukhopadhyay, J., Gutzmer, J., Beukes, N.J., and Bhattacharya, H.N., (2008). Geology and Genesis of the Major Banded Iron Formation-Hosted High-Grade Iron Ore Deposits of India. *Reviews in Economic Geology 15*, pp. 291-316.

Murowchick, J.B., Barnes, H.L., (1987). Effects of temperature and degree of supersaturation on pyrite morphology. *Americ. Min. 72*, pp. 1241-1250.

Newton R.C., Manning C.E., (2000b). Quartz solubility in concentrated aqueous NaCl solutions at deep crust–upper mantle metamorphic conditions: 2–15 kbar and 500–900 C°. Geochim. Cosmochim. Acta 64, pp. 2993–3005.

Norrish, K., & Hutton, J. T., (1969). An Accurate X-Ray Spectrographic Method for the Analysis of a Wide Range of Geological Samples. *Geochimica et Cosmochimica Acta 431*, 31p.

Ohmoto, H., (2003). Nonredox transformations of magnetite-hematite in hydrothermal systems. *Economic Geology 98*, pp. 157 - 161.

Oonk, P., (ongoing). Species-specific trace element and stable isotope geochemistry across the BIF stratigraphy of the Transvaal Supergroup in Griqualand West, South Africa and implications for the history of atmospheric oxygen. PhD. Thesis Ongoing. Rhodes University, Grahamstown, South Africa.

Passchier E.W. and Trouw R.A.J., (1996). Microtectonics Vol. 1., Rio De Janeiro, Springer Science & Business Media, pp. 366.

Pereira, A. C., Papini, R. M., (2015). Processes for phosphorus removal from iron ore - a review. *Rev. Esc. Minas vol.68 no.3***.**

Perry, E. C., & Ahmad, S. N., (1983). Oxygen isotope geochemistry of Proterozoic chemical sediments, in Medaris, L.G., Byers, C.W., Mickelson, D.M., and Shanks, W.C., eds., Proterozoic Geology: Selected papers from an international Proterozoic symposium. *Geological Society of America 161*, pp. 253 - 263.

Polteau, S., Moore, J. M., & Tsikos, H., (2006). The geology and geochemistry of the Paleoproterozoic Makganyene diamictite. *Precambrian Research 148*, pp. 257-274.

Powell, C.McA., Oliver, N.H.S., Li, Z.X., Martin, D.McB., Ronasziki, J., (1999). Synorogenic hydrothermal origin for giant Hamersley iron oxide ore bodies. *Geology 27*, pp. 175-178.

Purtov, V.K., Kotelnikova, A.L., (1993). Solubility of titanium in chloride and fluoride hydrothermal solutions. *Int. Geol. Rev. 35*, pp. 279–287.

Rafuza S., (2015). Carbonate Petrography and Geochemistry of BIF of the Transvaal Supergroup: evaluating the potential of Iron Carbonates as proxies for Palaeoproterozoic Ocean Chemistry. (MSc Thesis). Rhodes University, Grahamstown, South Africa.

Rapp, J.F., Klemme, S., Bulter, I.B., Harley, S.L., (2010). Extremely high solubility of rutile in chloride and fluoride-bearing metamorphic fluids: An experimental investigation. *Geology 38*, pp. 323-326.

Rasmussen, B., Fletcher, I.R., Muhling, J.R., Thorne, W.S., and Broadbent, G.C., (2007). Prolonged history of episodic fluid flow in giant hematite ore bodies: Evidence from in situ U-Pb geochronology of hydrothermal xenotime. *Earth and Planetary Science Letters, v. 258*, pp. 249-259.

Rivas-Sanchez, M. L., Alva-Valdivia, L.M., Arenas-Alatorre, J., UrrutiaFucugauchi, J., Ruiz-Sandoval, M., and Ramos-Molina, M.A., (2006). Berthierine and chamosite hydrothermal: genetic guides in the Pena Colorada ˜ magnetite-bearing ore deposit. *Mexico, Earth Planets Space, 58*, pp. 1389-1400.

Rosiere, C.A., Siemes, H., Quade, H., Brokmeier, H.G., Jansen, E.M., (2001). Microstructures, textures and deformation mechanisms in hematite. Journal of Structural Geology, v. 23, pp. 1429-1440.
Rusinova, O.V., Rusinov, V.L. and Troneva, N.V., (1986). Composition, some structural features, and formation conditions of wall-rock alteration and ore chlorites and berthierines. *Metasomatism, Mineralogy, and Genetic Questions of Volcanic-Hosted Gold and Silver Deposits*, pp. 5-40.

Saunders J.A., (1990). Colloidal transport of gold and silica in epithermal precious-metal systems: evidence from the Sleeper deposit, Nevada. *Geology 18*, pp. 757–760.

Sawkins, F.J., (1969). Chemical brecciation, an unrecognized mechanism for breccia formation?. *Econ. Geol. 64*, pp. 613–617.

Schalkwyk, G.A.C., (2005). Genesis and characteristics of the Wolhaarkop breccia and associated Manganore iron formation. (M.Sc. thesis): Johannesburg, Univ. of Johannesburg.
Secondary Enrichment of Metals in the Paleoproterozoic Hotazel Iron Formation, Kalahari Manganese Field, South Africa. *Economic Geology 98(7),* pp. 1449-1462.

Shelton, K.L., Bauer, R.M., Gregg, J.M., (1992). Fluid Inclusion studies of regionally extensive epigenetic dolomites, Bonneterre Dolomite (Cambrian), Southeast Missouri: evidence of multiple fluids during dolomitization and lead-zinc mineralisation. *Geol Soc Am Bull* 104, pp.675–683.

Simpson C.R.J., Mauk J.L., Arehart G.B., Mathews S.J., (1995). The formation of banded epithermal quartz veins at the Golden Cross Mine, Waihi, New Zeland. In: *Proceedings of the 1995 PACRIM Congress*, pp. 545–550.

Slack, J.F., Jiang, W. T., Peacor, D. R., Okita, P M., (1992). Hydrothermal and metamorphic berthierine from the Kidd Creek Volcanogenic Massive Suplhide deposit, Timmins, Ontario. Canadian Mineralogist, vol 30, pp. 1127-1142.

Strauss, C.A., (1964). The iron deposits of Sishen area, Cape Province, pp. 393-403. *In*: Haughton, S.H., Eds., *The Geology of Some Ore Deposits in Southern Africa, II. Geol. Soc. S. Afr., Johannesburg,* 793 pp.

Sumner, D.Y., Beukes, N.J., (2006). Sequence Stratigraphic Development of the Neoarchean Transvaal carbonate platform, Kaapvaal Craton, South Africa. *South African Journal of Geology*, 109, pp.11-22.

Takeno, N., (2005). *Atlas of Eh-pH diagrams: Intercomparison of thermodynamic databases.* Tokyo: National Institute of Advanced Industrial Science and Technology.

Taylor, D., Dalstra, H.J., Harding, A.E., Broadbent, G.C., Barley, M.E., (2001). Genesis of highgrade hematite orebodies of the Hamersley province, Western Australia. *Econ. Geol. Bull. Soc. Econ. Geol. 96*, pp. 837–873.

Taylor, R. (2009). Ore Textures. Recognition and Interpretation. Published by Springer. Doi: 10.1007/978-3-642-01783-4.

Taylor, S.R., and McLennan, S.M., (1985). The continental crust: Its composition and evolution. Oxford: Blackwell.

Thorne, W.S., Hagemann, S.G., Barley, M., (2004). Petrographic and geochemical evidence for hydrothermal evolution of the North Deposit, Mt Tom Price, Western Australia. *Mineral. Deposita 39*, pp. 766–783.

Toth, T.A. and Fritz, S.J., (1997). An Fe-berthierine from a Cretaceous laterite: Part I. Characterization. *Clays and Clay Minerals* 45, pp. 564–579.

Trendall, A. F., & Morris, R. C., (1983). *Iron-formation: Facts and Problems. In: Developments in Precambrian Geology 6.* Amsterdam: Elsevier Science Publishing.

Trendall, A.F., (1965a). Progress report of the Brockman Iron Formation in the Wittenoom-Yampire area. West. Aust., Geol. Surv., *Annu. Rep.*, 1964: pp.55-65.

Tsikos, H., Beukes, N. J., Moore, J. M., & Harris, C., (2003). Deposition, Diagenesis, and Secondary Enrichment of Metals in the Paleoproterozoic Hotazel Iron Formation, Kalahari Manganese Field, South Africa. *Economic Geology 98*, pp. 1449-1462.

Tsikos, H., Kalumbu, J., Shivute, F. and Moore, J.M. (2007). Anomalous high field strength elements (HFSE) enrichments in the Gamagar and Mapedi Formations: Implications regarding Fe- and Mn-ore genesis in the Transvaal Supergroup, South Africa. *Biennial SGA Metting 9th, Dublin, Proccedings v.2*, pp. 1011-1014.

Van Deventer, W.F., (2009). Textural and geochemical evidence for a supergene origin of the Paleoproterozoic high-grade BIF-hosted iron ores of the Maremane Dome, Northern Cape Province, South Africa. Unpublished M.Sc. (Geology). University of Johannesburg.

Van Schalkwyk, J. F. and Beukes, N.J., (1986). The Sishen iron ore deosit, Griqualand West, pp. 931 – 956, in *Mineral Deposits of Southern Africa, I.* Eds: CR Anhaeusser and S Maske. 1020 pp. Geological Society of South Africa: Johannesburg.

Van Schalkwyk, J.F. and Beukes, N.J., (1986). The Sishen Iron Ore deposit, Griqualand West. In: Anhaeusser, C. R., Maske, S. (eds.) *Mineral deposits of southern Africa.* Geol. Soc. S. Afr., Johannesburg, pp. 931-936.

Van Schalkwyk, J.F., (1984). Die Geologie van die Sishen-Ysterertsmyn. Unpublished M.Sc. (Geology). University of Johannesburg.

Van Wyk, J.P, (1980). Die geologie van die gebied Rooinekke-Matsap-Wolhaarkop in Noord Kaapland met spesiale verwysiging na die Koegas-Subgroep, Transvaal Supergroep. (Msc Thesis unpublished), Rand Afrikaans Univ., Johannesburg, pp. 159.

Van Wyk, J.P. and Beukes, N.J., (1982). The geology of the Sishen iron ore deposit. *GSSA, Mineral Deposits of Southern Africa, vol 1*, pp. 157-182.

Veena (2009). Understanding Geology. Published by Discovery Publishing House PVT.LTD.

Velde, B., (1985). Clay Minerals. A Physico-Chemical Explanation of their Occurrence. *Developments in Sedimentology, 40, Elsevier*, Amsterdam, pp. 427.

Vengosh, A., Starinsky, A., Kolodny, Y. and Chivas, A.R., (1991). Boron Isotope Geochemistry as a Tracer for the Evolution of Brines and Associated Hot-Springs from the Dead-Sea, Israel. *Geochimica Et Cosmochimica Acta, 55(6)*, pp. 1689-1695.

Walter, L.P., (2011). Economic Geology: Principles and Practice. Published by Wiley-Blackwell (2011), pp. 680.

Watson, E.B., Wark, D.A., Thomas, J.B., (2006). Crystallization thermometers for zircon and rutile. *Contributions to Mineralogy and Petrology 151*, pp. 413–433.

Webb, A.D., Dickens, G.R., Oliver, N.H.S., (2003). From banded iron formation to iron ore: geochemical and mineralogical constraints from across the Hamersley Province, Western Australia. *Chem. Geol. 197*, pp. 215-251.

Worden, R.H., Smalley, P.C., Fallick, A.E., (1997). Sulfur cycle in buried evaporites. *Geology 25*, pp. 643–646.

Yamaguchi, K. E., & Ohmoto, H., (2006). Geochemical and isotopic contraints on the origin of Paleoproterozoic red shales of the Gamagara/Mapedi Formation, Postmasburg Group, South Africa. *South African Journal of Geology 109*, pp. 123-138.

Zack, T., Kronz, A., Foley, S.F., Rivers, T., (2002). Trace element abundances in rutiles from eclogites and associated garnet mica schists. *Chemical Geology 184*, pp. 97–122.

Zack, T., Moraes, R., Kronz, A., (2004a). Temperature dependence of Zr in rutile: empirical calibration of a rutile thermometer. *Contributions to Mineralogy and Petrology 148*, pp. 471–488.

Appendix I

Borehole SLT207			
Sample Name	Depth (m)	Sample Name	Depth (m)
VLT1	153.1	VLT42	340.7
VLT2	161.3	VLT43	341.6
VLT3	171.2	VLT44	344.3
VLT4	168.4	VLT45	344.8
VLT5	179.9	VLT46	347.3
VLT6	182.7	VLT47	350.0
VLT7	201.6	VLT48	351.7
VLT8	205.0	VLT49	352.7
VLT9	227.4	VLT50	361.8
VLT10	234.3	VLT51	363.6
VLT11	236.7	VLT52	366.3
VLT12	246.1	VLT53	367.7
VLT13	252.0	VLT54	371.7
VLT14	255.3	VLT55	373.9
VLT15	260.5	VLT56	378.5
VLT16	264.2	VLT57	382.0
VLT17	268.5	VLT58	384.0
VLT18	270.7	VLT59	385.2
VLT19	273.2	VLT60	387.4
VLT20	274.4	VLT61	393.7
VLT21	278.9	VLT62	398.7
VLT22	282.3	VLT63	402.0
VLT23	282.8	VLT64	405.2
VLT24	287.7	VLT65	406.3
VLT25	291.6	VLT66	410.0
VLT26	294.2	VLT67	414.7
VLT27	294.5	VLT68	420.1
VLT28	298.8	VLT69	423.0
VLT29	299.6	VLT70	425.4
VLT30	301.3	VLT71	426.4
VLT31	306.5	VLT72	429.0
VLT32	307.3	VLT73	434.3
VLT33	308.8	VLT74	442.0
VLT34	314.9	VLT75	444.4
VLT35	315.3	VLT76	447.8
VLT36	317.5	VLT77	449.9
VLT37	318.4	VLT78	453.6
VLT38	321.6	VLT79	457.2
VLT39	328.2	VLT80	465.6
VLT40	330.5	VLT81	473.0
VLT41	336.3		

Borehole SA2491E	
Sample Name	Depth (m)
D1	339.1
D2	332.4
D3	332.1
D4	329.3
D5	328.4
D6	335.8
D7	327.2
D8	325.0
D9	323.1
D10	327.9
D11	319.1
D12	308.7
D13	306.6
D14	304.5
D15	304.0
D16	288.6
D17	283.5
D18	279.7
D19	278.5
D20	274.2
D21	260.8
D22	260.0
D23	243.2

Borehole SA2072	
Sample Name	Depth (m)
S1	204.0
S2	233.3
S3	230.1
S4	231.5
S5	232.5
S6	235.6

Sample names and stratigraphic depths

Appendix I

Borehole SLT284			
Sample Name	Depth (m)	Sample Name	Depth (m)
HLT1	172.8	HLT25	319.2
HLT2	187.1	HLT26	322.8
HLT3	200.1	HLT27	324.7
HLT4	201.5	HLT28	327.1
HLT5	223.0	HLT29	328.6
HLT6	239.0	HLT30	330.8
HLT7	242.0	HLT31	334.7
HLT8	246.1	HLT32	335.2
HLT9	265.4	HLT33	337.0
HLT10	269.7	HLT34	343.0
HLT11	272.8	HLT35	348.5
HLT12	274.3	HLT36	352.0
HLT13	276.5	HLT37	356.0
HLT14	277.7	HLT38	358.8
HLT15	281.8	HLT39	362.5
HLT16	282.8	HLT40	363.0
HLT17	286.2	HLT41	368.3
HLT18	286.8	HLT42	371.8
HLT19	292.0	HLT43	374.2
HLT20	302.0	HLT44	376.9
HLT21	305.2	HLT45	381.3
HLT22	307.7	HLT46	382.8
HLT23	311.7	HLT47	387.9
HLT24	314.6	HLT48	389.9

Sample names and stratigraphic depths

Appendix I

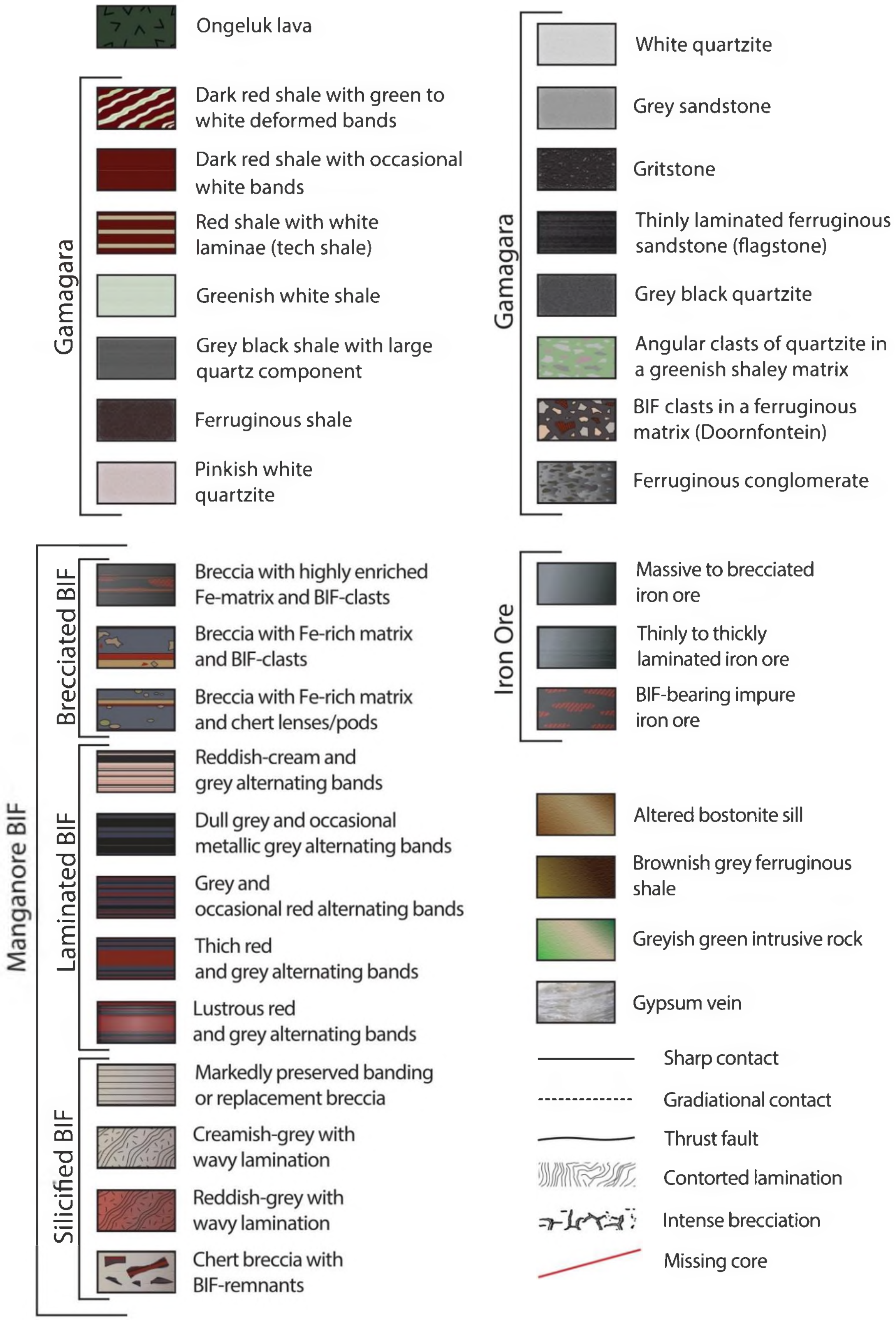

Detailed legend for stratigraphic logs

Appendix I

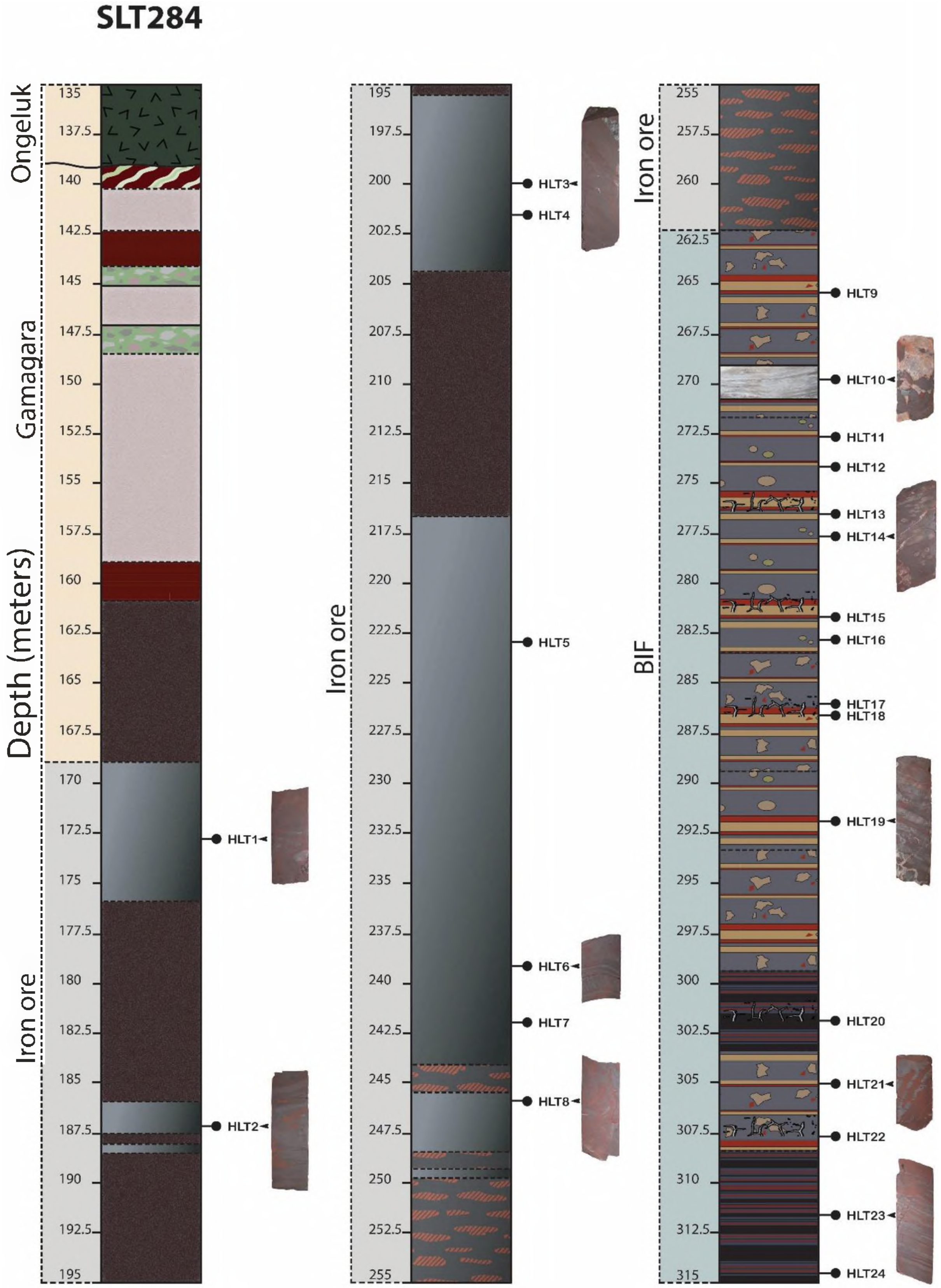

Stratigraphic log for drill core SLT284

Appendix I

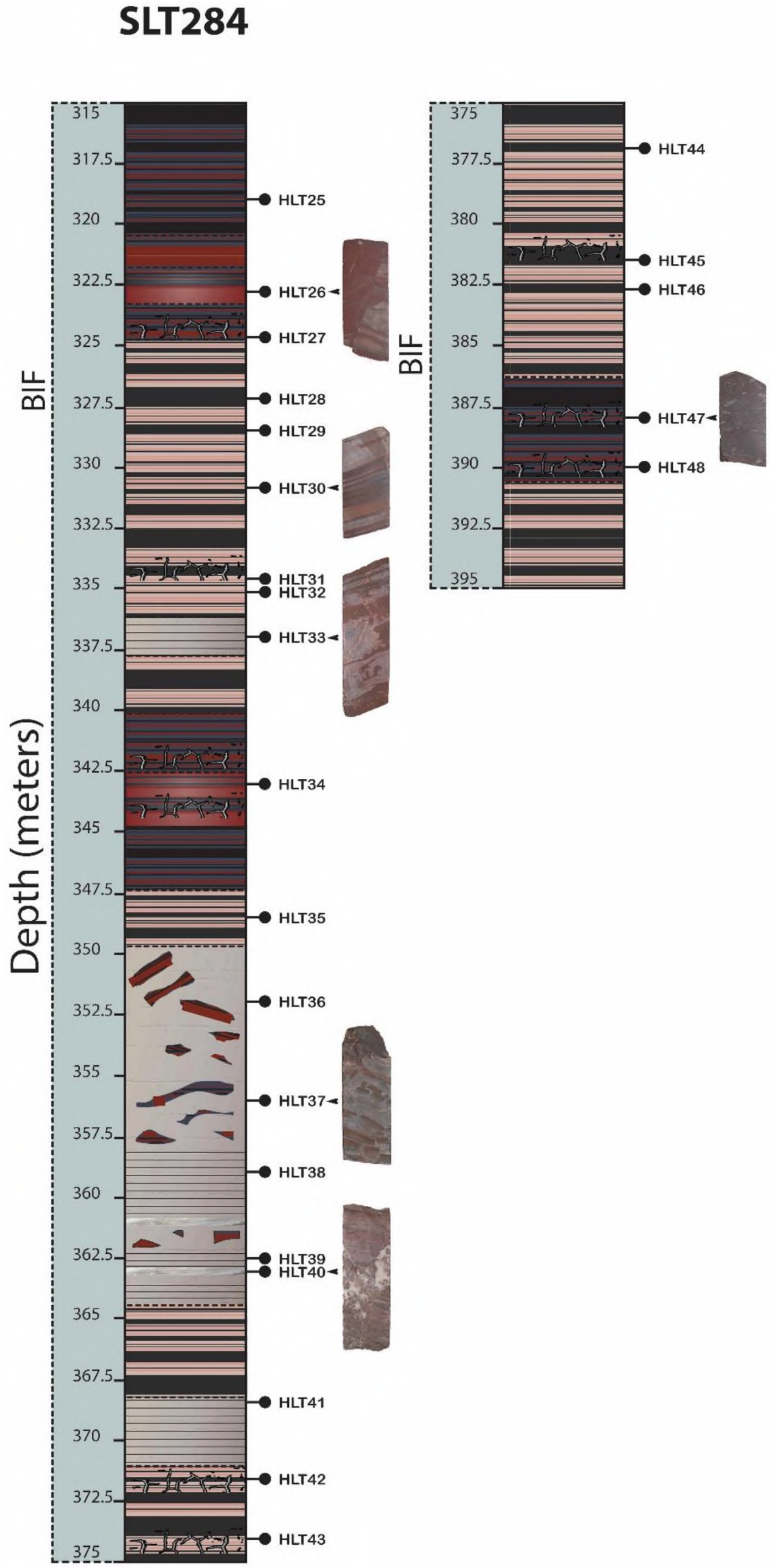

Stratigraphic log for drill core SLT284 (continued)

Appendix I

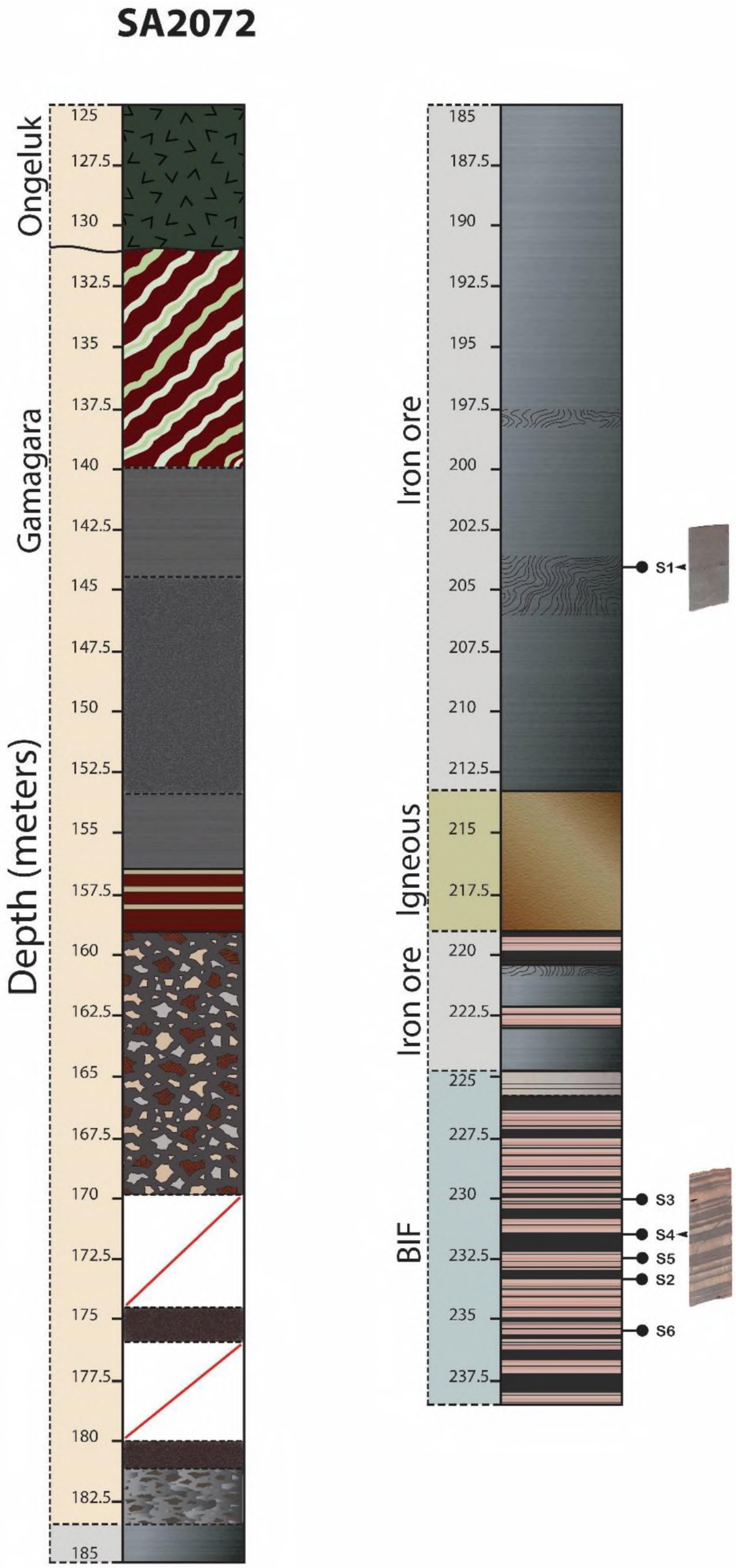

Stratigraphic log for drill core SA2072

Appendix II

X-ray diffraction analysis

Bulk-rock powder XRD patterns were acquired using a Bruker D8 Discover X-ray diffractometer, equipped with a Lynx Eye detector, housed in the Department of Chemistry at Rhodes University. Approximately 1 g of powder was packed onto a plastic, indented plate. The XRD instrument uses a Cu-Kα radiation (= 1.5405 Å, nickel filter) and is operated with power at 20mA and 40kV. The scanning was done from 5° to 65° (2θ) with scanning speeds of 1° per minute. X-ray diffraction data was treated using the computer software Crystal Sleuth and the database hosted by RRUF (Laetsch and Downs, 2006). A collation of the spectra obtained is available in Appendix II.

Electron Probe Microanalysis (EPMA)

EPMA analyses were conducted on 30 selected carbon-coated, polished thin sections after examination under the optical microscope. EPMA data acquisition was performed at the University of Cape Town, Department of Geological Sciences, on a JEOL JXA 8320 Superprobe, using 4 wave-dispersive spectrometres. Analytical conditions employed were: acceleration voltage 15kv, probe current 20nA, counting time 10sec on peak and 5 sec on background, and beam spot size less than 1 micron. Natural standards were used for measuring the characteristic X-rays. ZAF matrix correction method was employed for quantification. Additional qualitative data for mineral identification were obtained using a TESCAN Vega TS 5136LM SEM coupled with an Oxford Instruments EDS for spot analysis, housed in the department of Biology at Rhodes University. The obtained spectra were evaluated using the INCA software by Oxford Instruments.

Textural generations of hematite present in the MIF and Kuruman-Griquatown IF

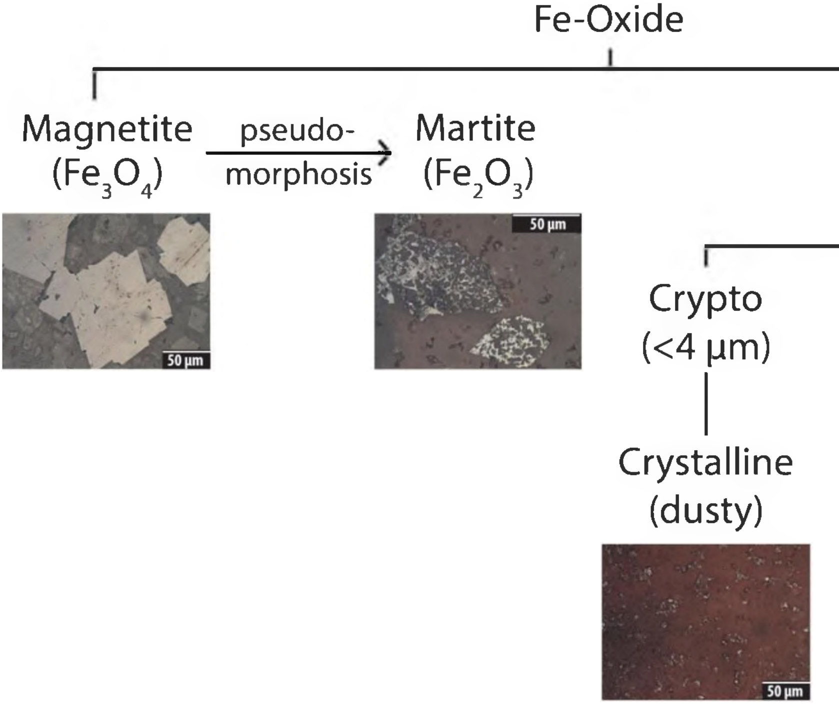

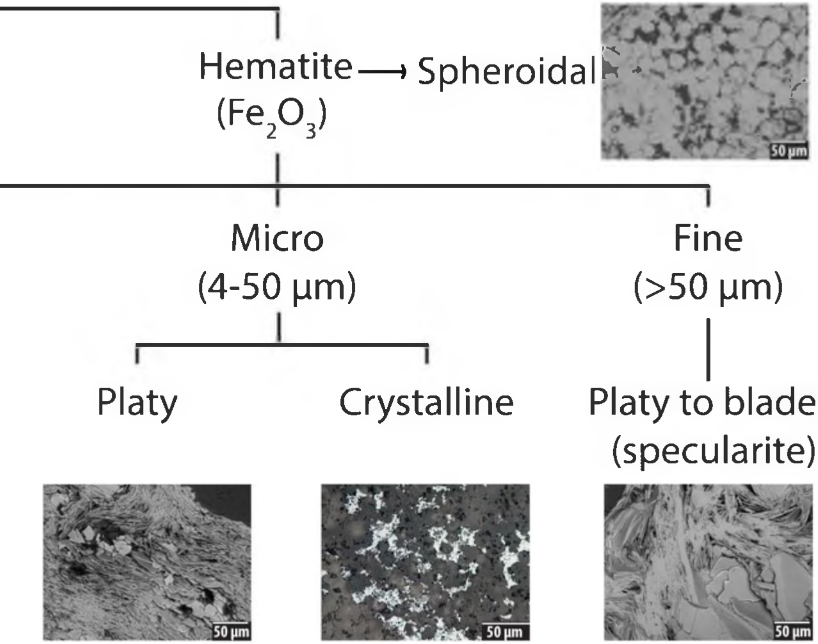
Hematite
(Fe_2O_3)
Spheroidal
50 µm
Micro
(4-50 µm)
Fine
(>50 µm)
Platy
Crystalline
Platy to bladed
(specularite)
50 µm
50 µm
50 µm

Appendix II

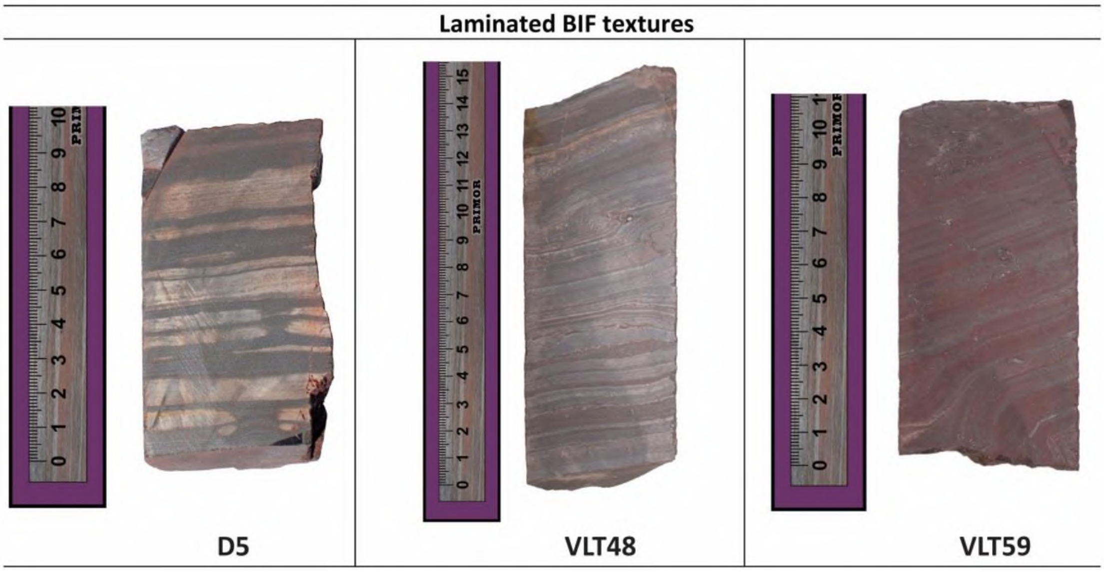

Figure. 2.1

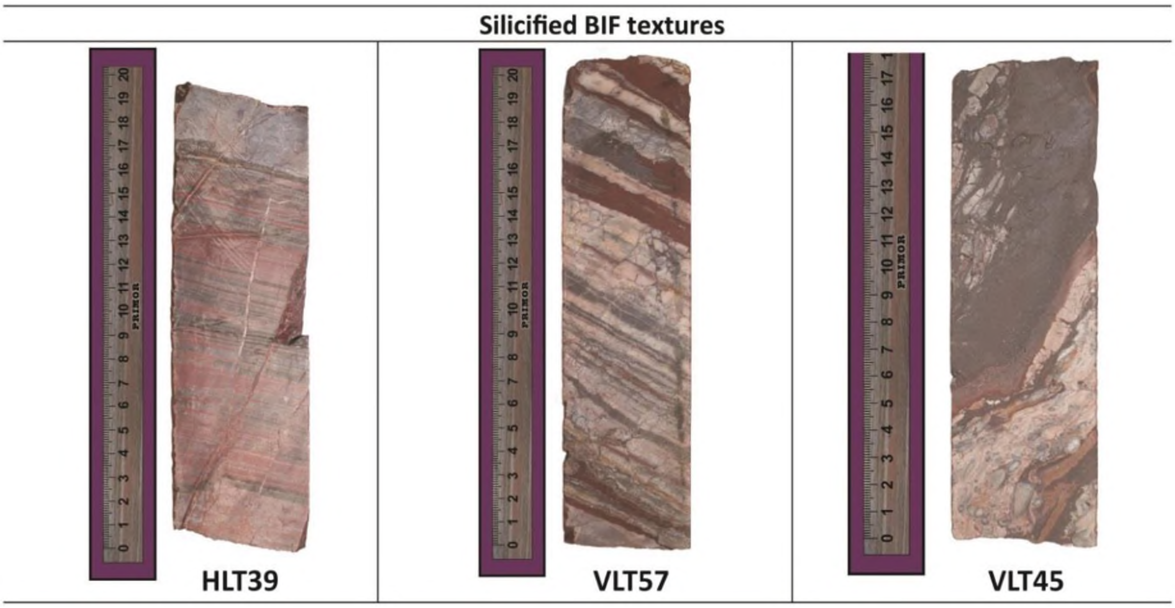

Figure. 2.2

Appendix II

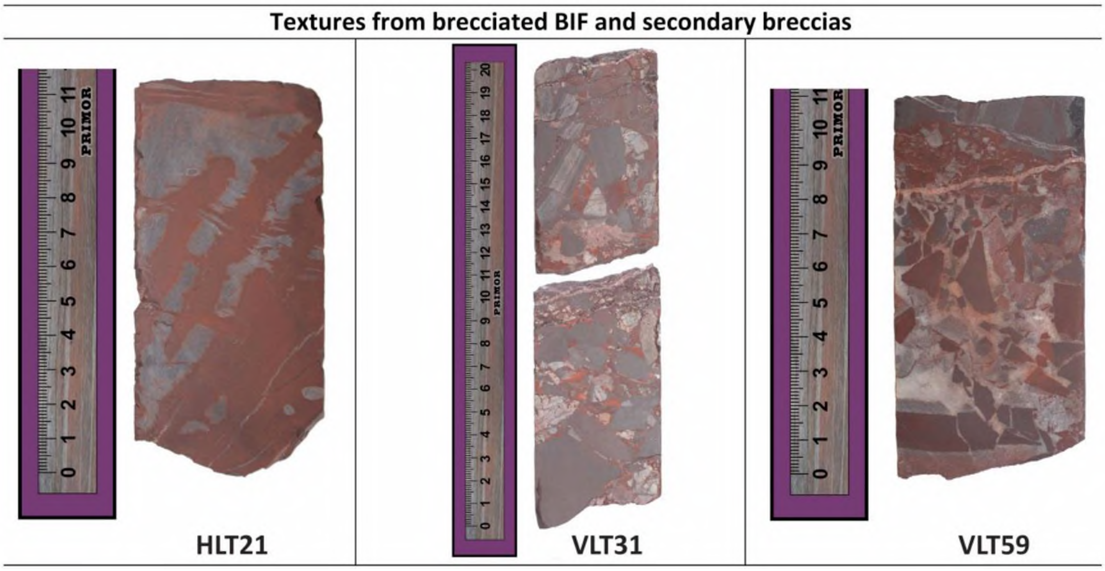

Figure. 2.3

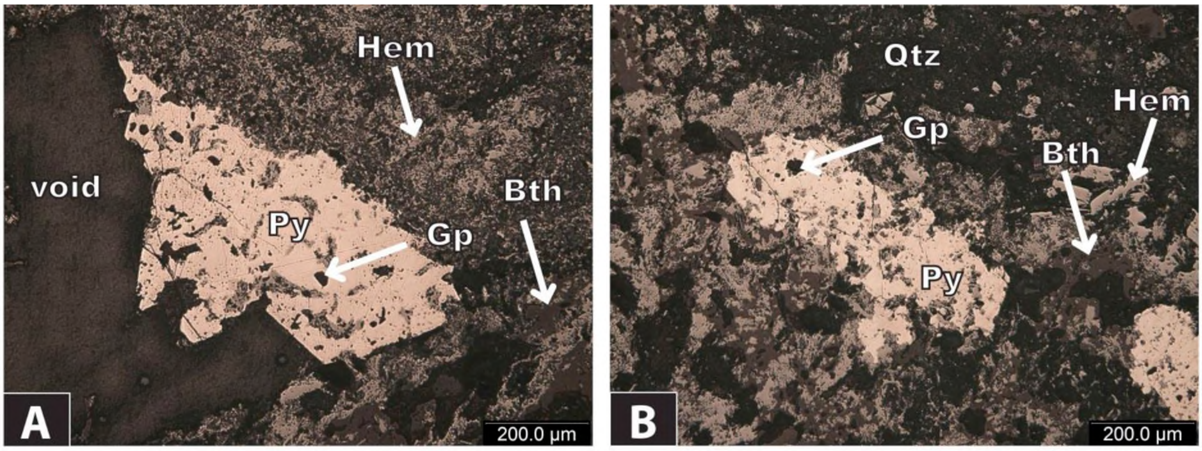

Figure. 2.4 - Pyrites from the iron ore

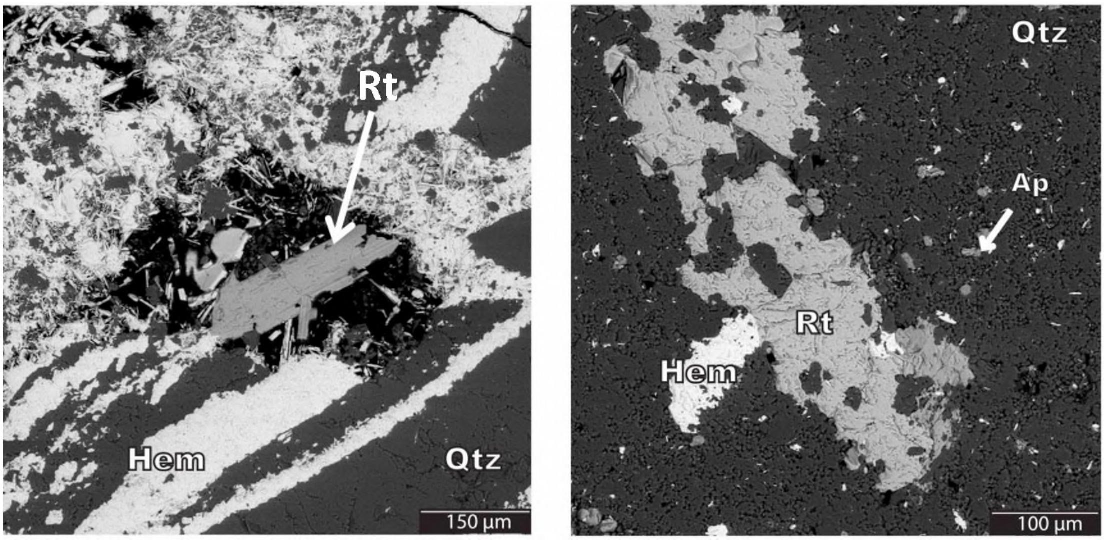

Figure. 2.5 - Rutile from the BIF

Appendix II

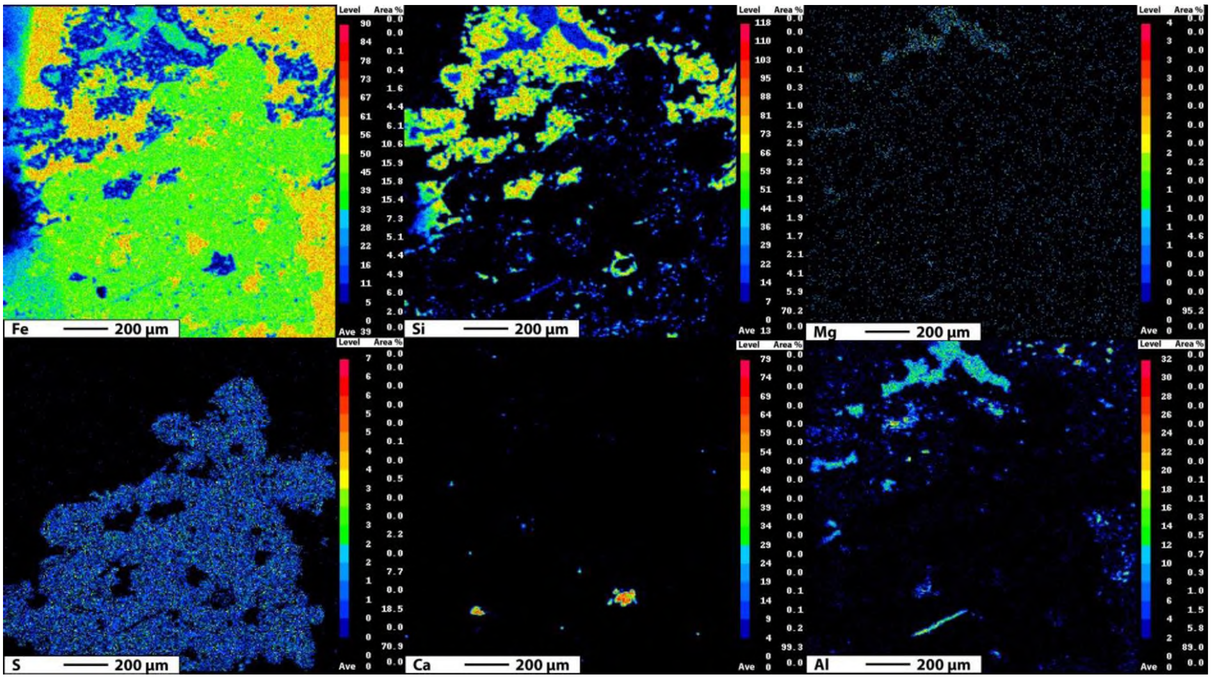

Figure. 2.6 - WDS elemental map-Pyrite+gypsum+berthierine

Selected XRD patterns

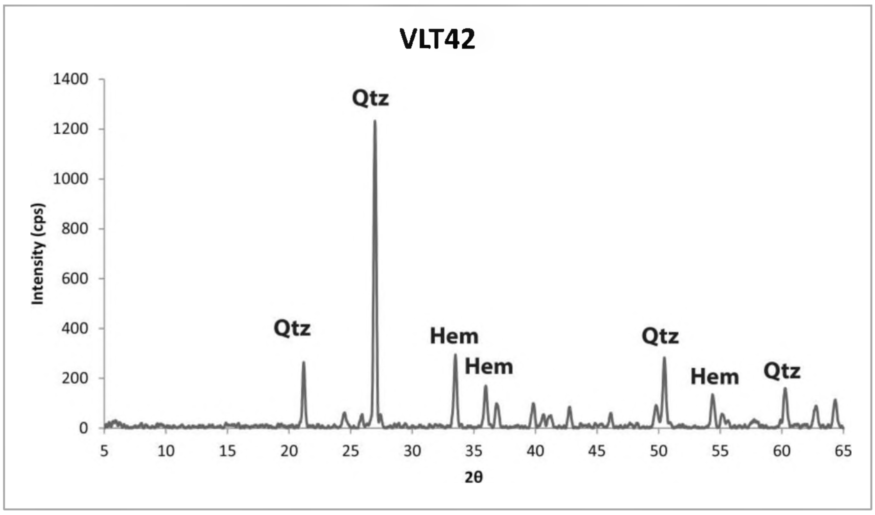

Appendix II

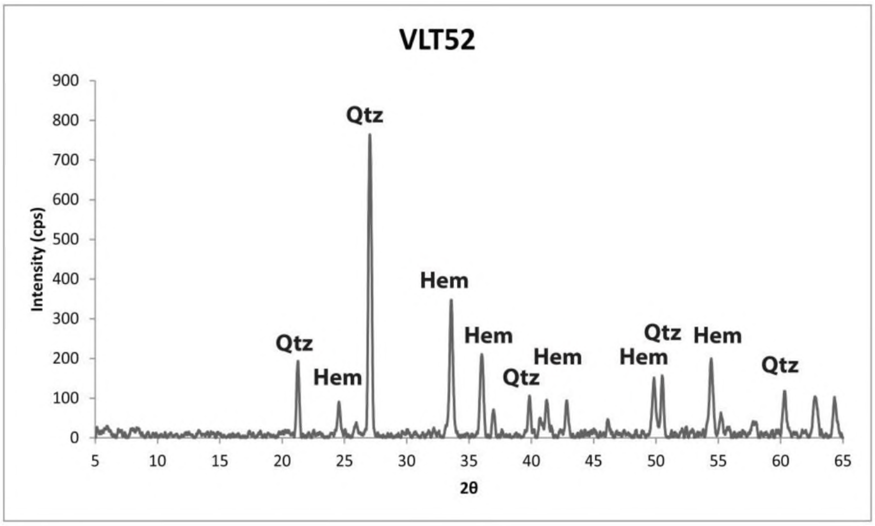
VLT52
Intensity (cps)
900
800
700
600
500
400
300
200
100
0
5
10
15
20
25
30
35
40
45
50
55
60
65
2θ
Qtz
Hem
Qtz
Hem
Hem
Qtz
Hem
Hem
Qtz
Hem
Qtz

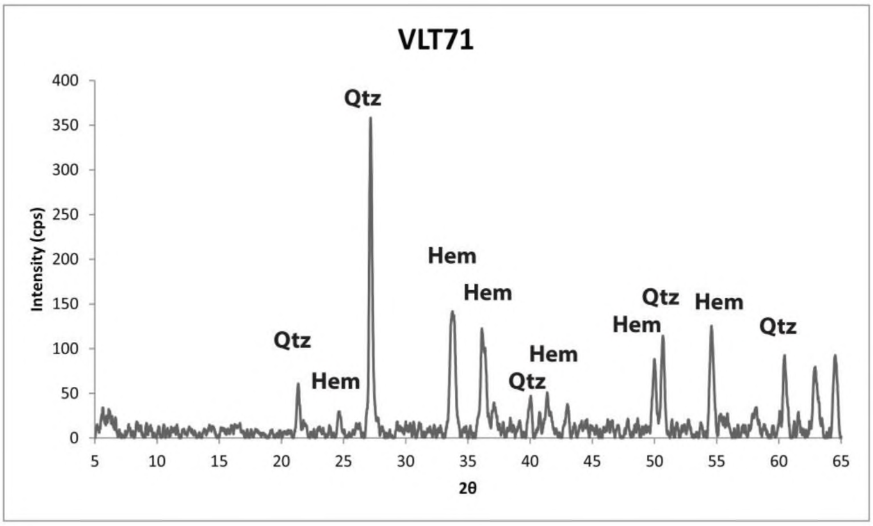
VLT71
Intensity (cps)
400
350
300
250
200
150
100
50
0
5
10
15
20
25
30
35
40
45
50
55
60
65
2θ
Qtz
Hem
Qtz
Hem
Hem
Qtz
Hem
Hem
Qtz
Hem
Qtz

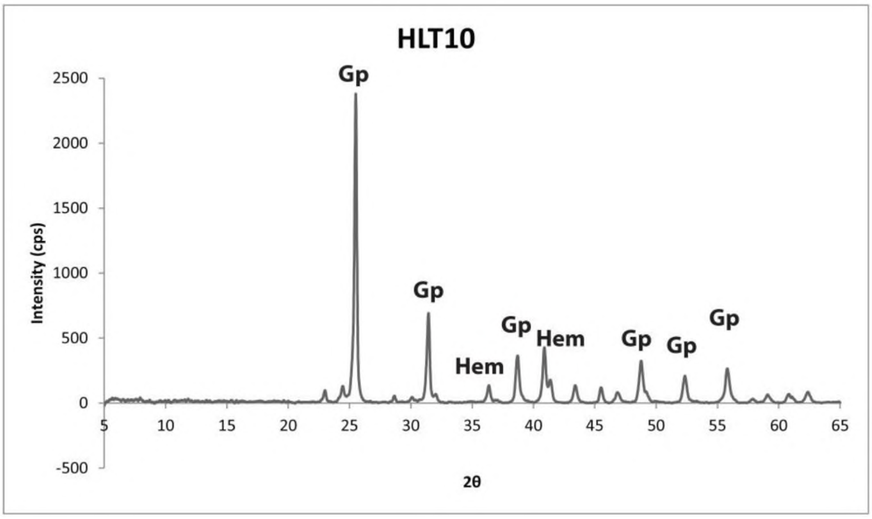
HLT10
Intensity (cps)
2500
2000
1500
1000
500
0
-500
5
10
15
20
25
30
35
40
45
50
55
60
65
2θ
Gp
Gp
Hem
Gp
Hem
Gp
Gp
Gp

Appendix II

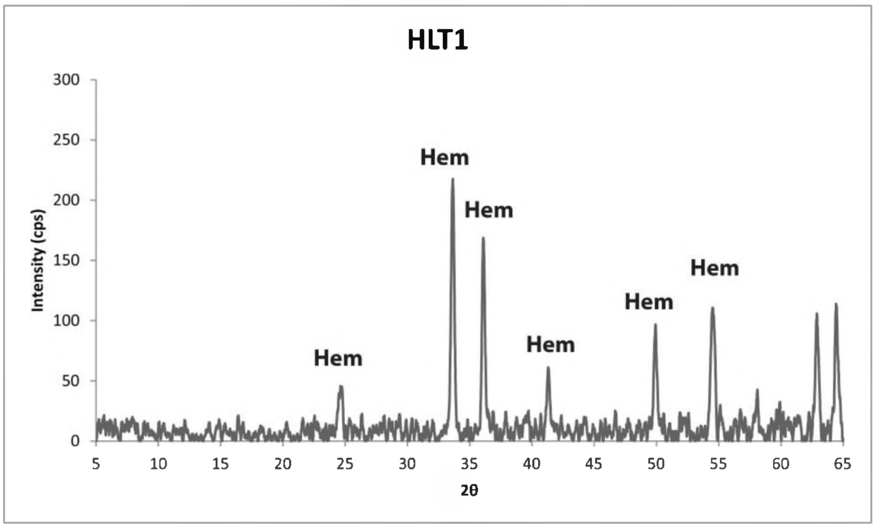
HLT1
Intensity (cps)
0
50
100
150
200
250
300
2θ
5
10
15
20
25
30
35
40
45
50
55
60
65
Hem
Hem
Hem
Hem
Hem
Hem

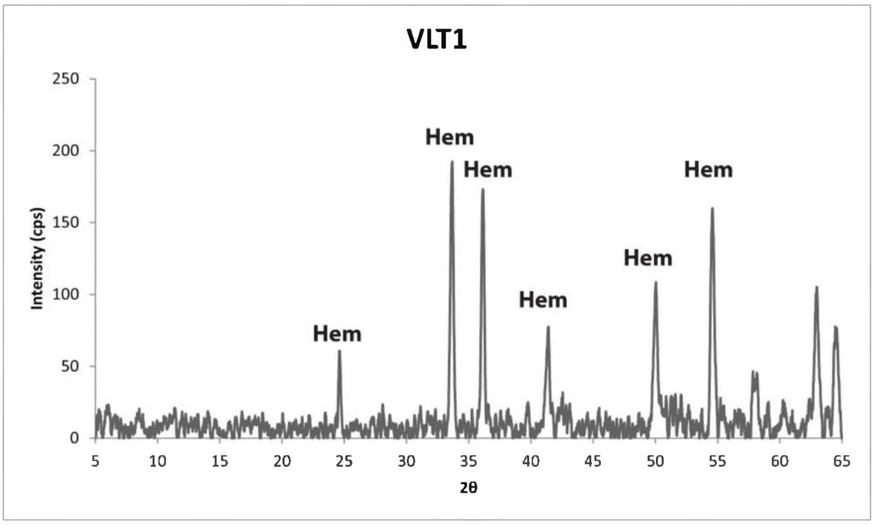
VLT1
Intensity (cps)
0
50
100
150
200
250
2θ
5
10
15
20
25
30
35
40
45
50
55
60
65
Hem
Hem
Hem
Hem
Hem
Hem

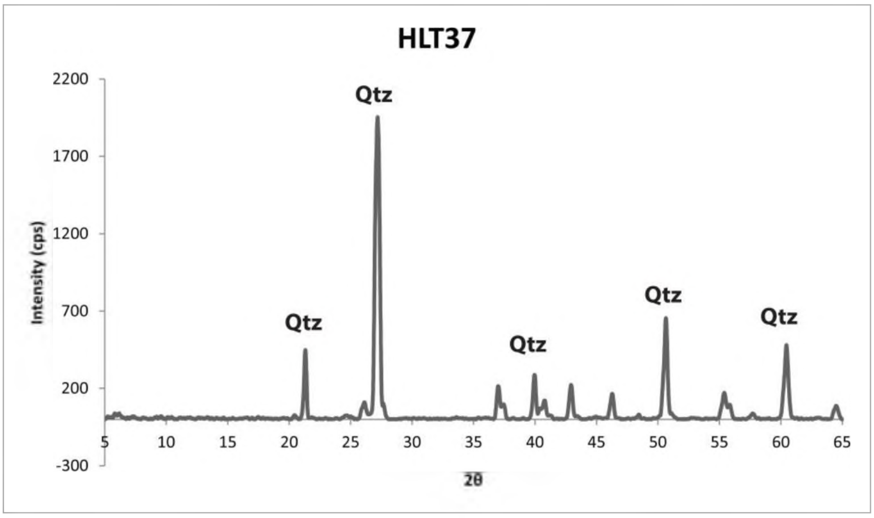
HLT37
Intensity (cps)
-300
200
700
1200
1700
2200
2θ
5
10
15
20
25
30
35
40
45
50
55
60
65
Qtz
Qtz
Qtz
Qtz
Qtz

Appendix II

Selected EDS spectra

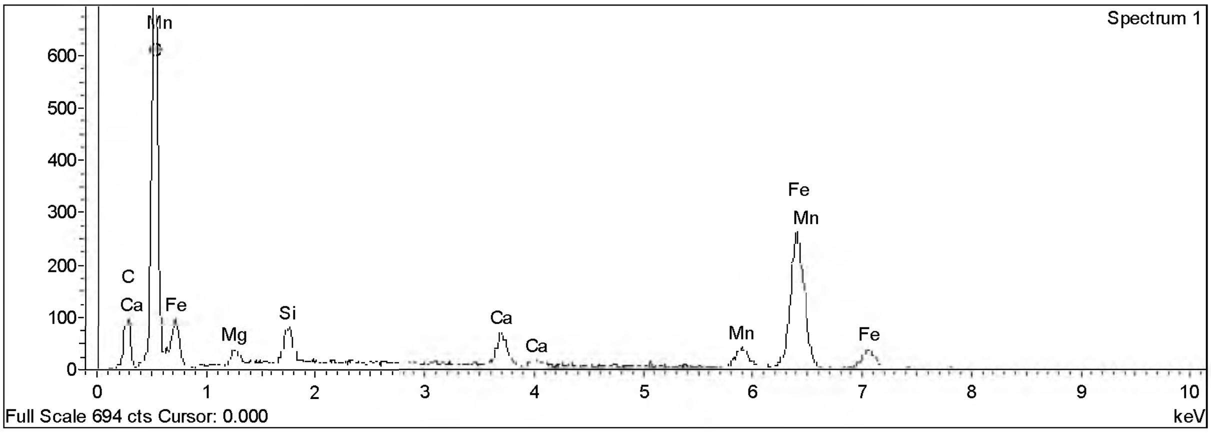

siderite

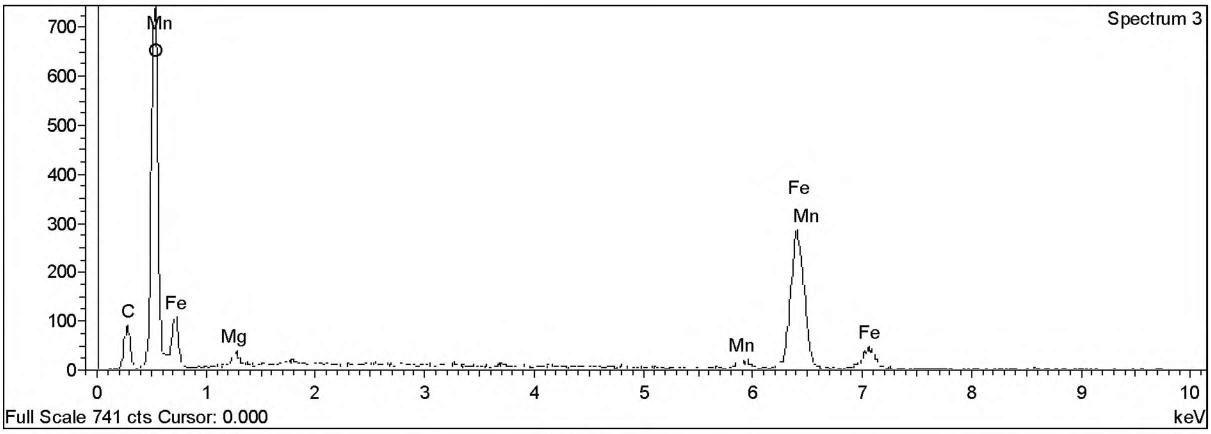

siderite 2

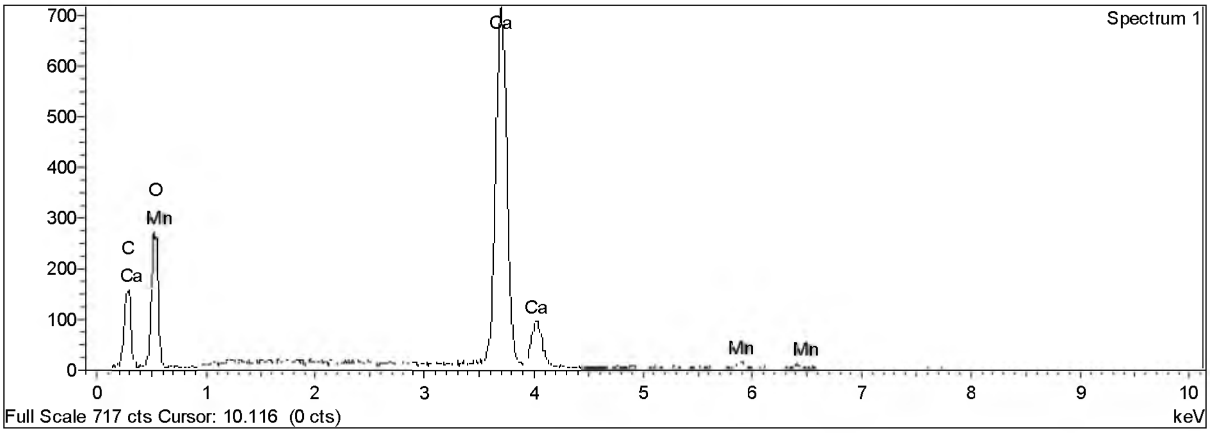

calcite

Appendix II

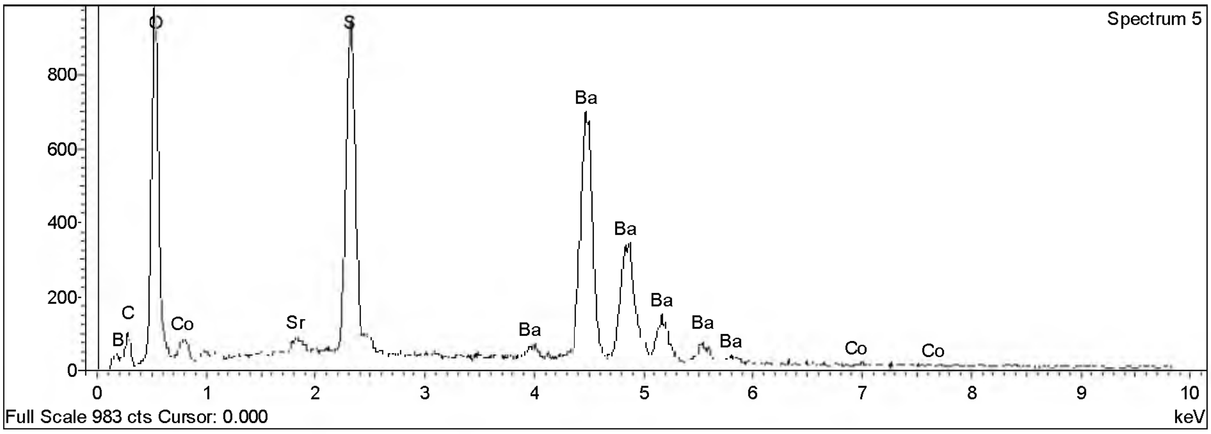

baryte

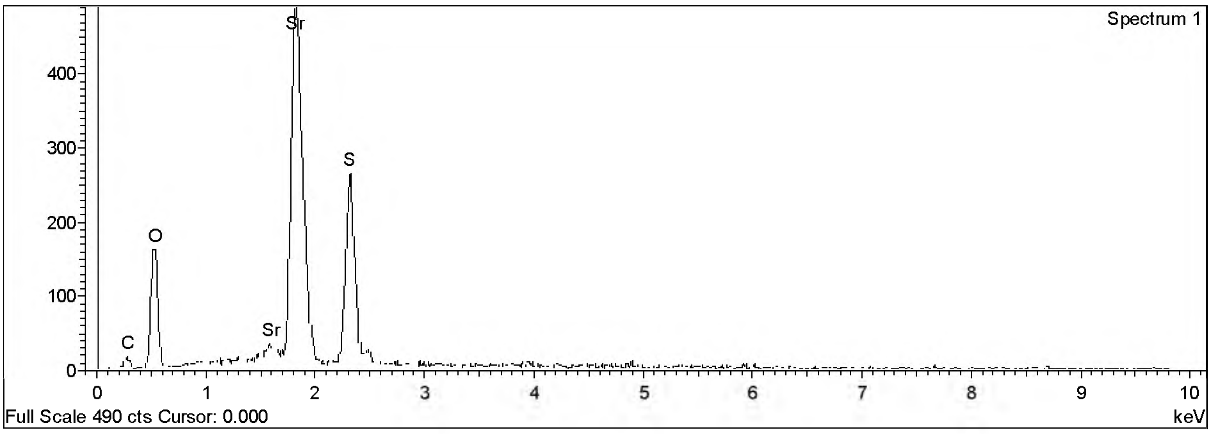

celestine

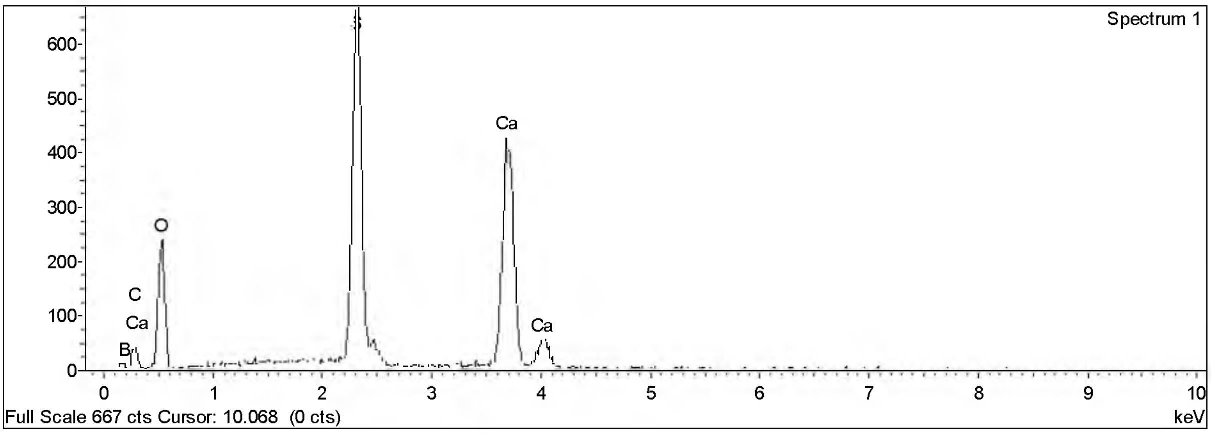

gypsum

Appendix II

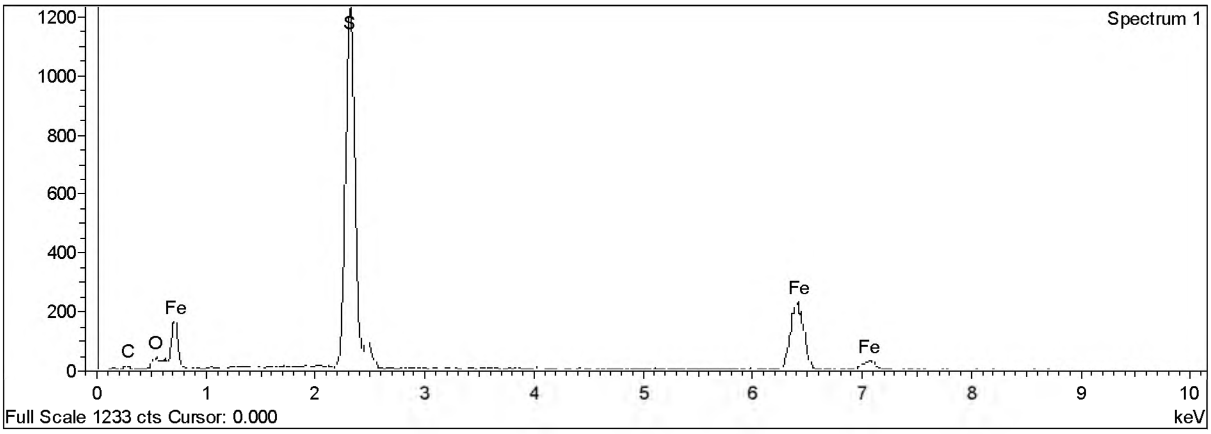

pyrite

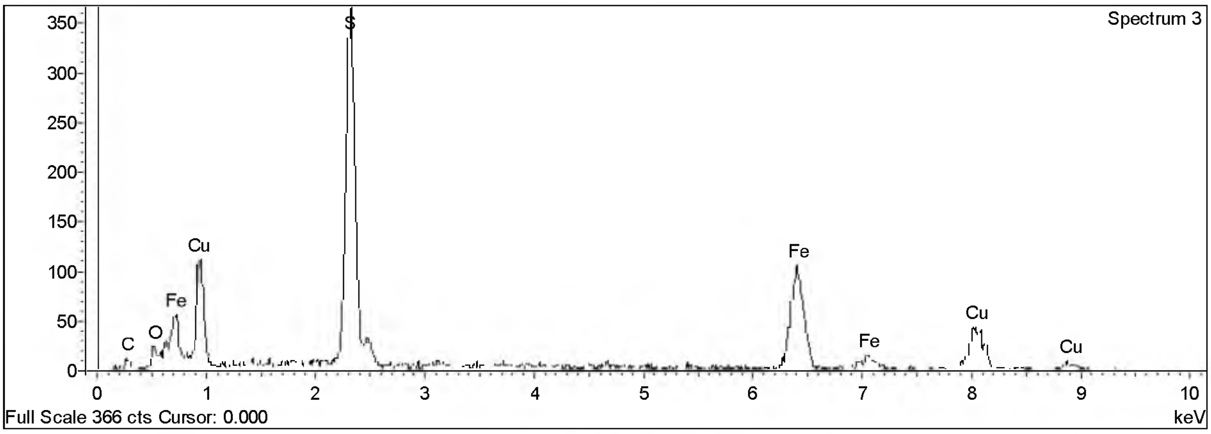

chalcopyrite

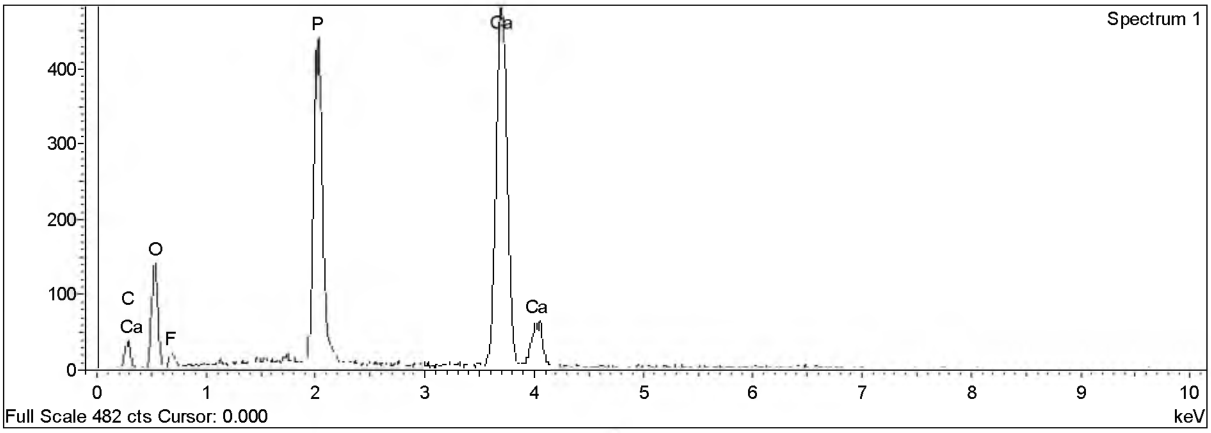

apatite

Appendix II

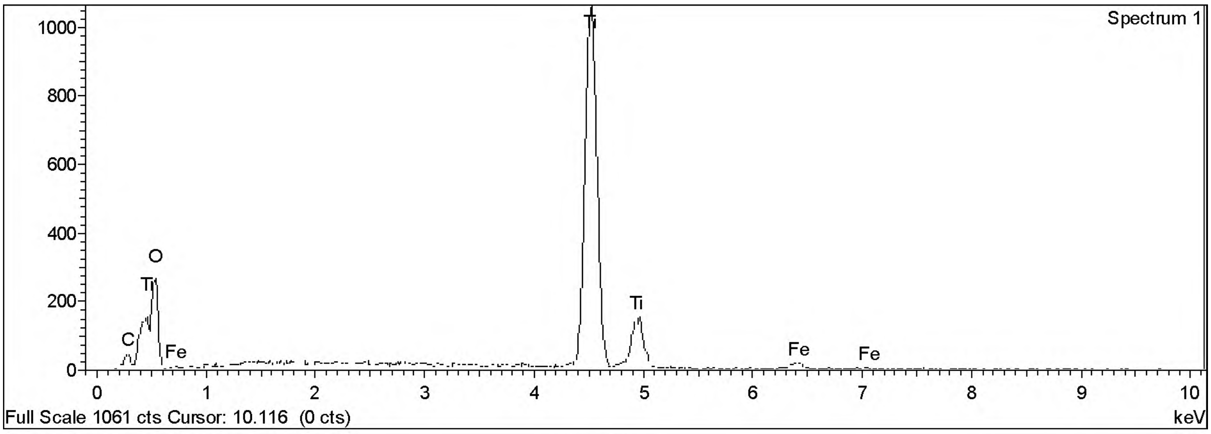

rutile

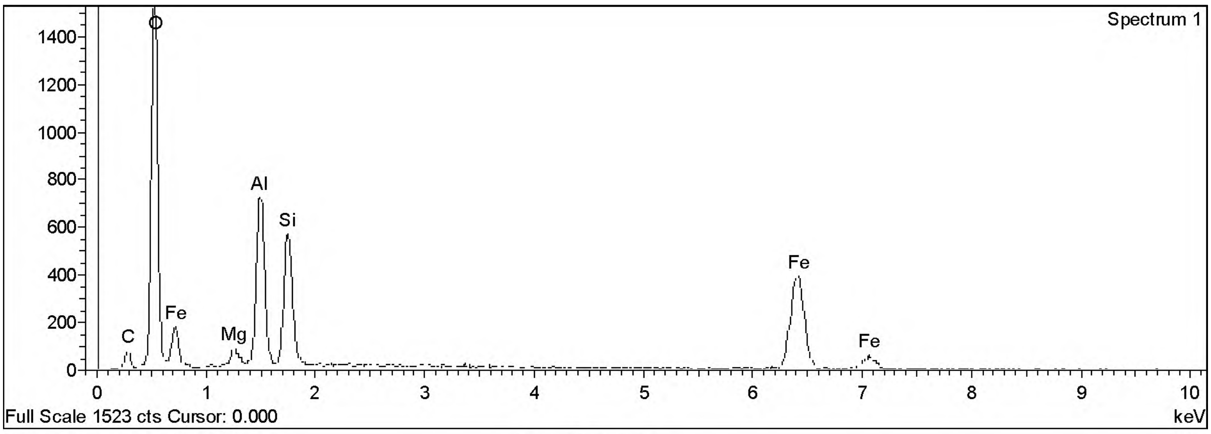

berthierine

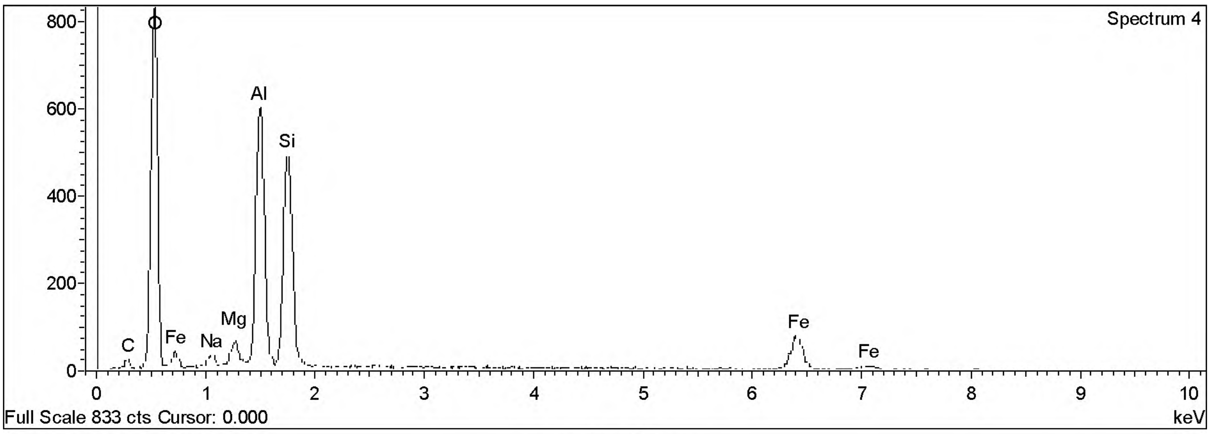

tourmaline

Appendix II

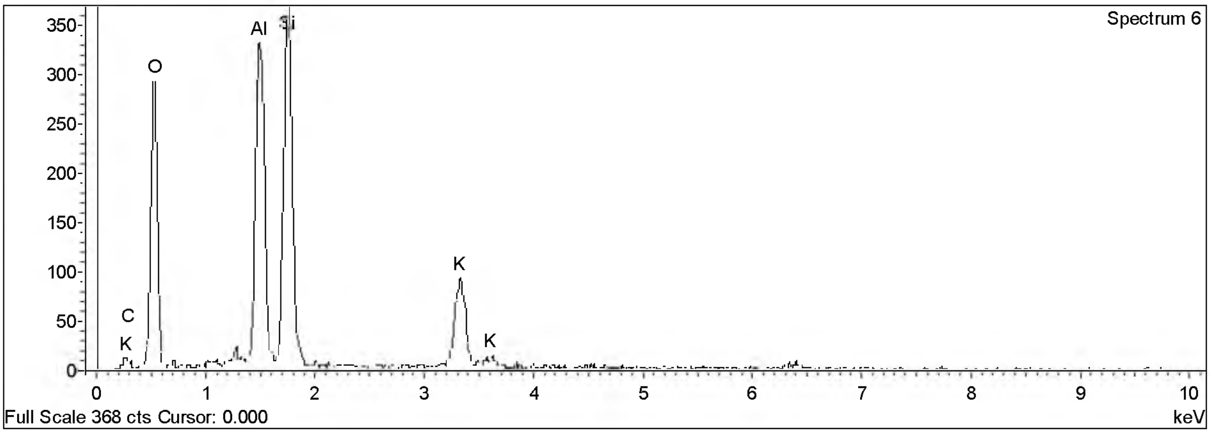

muscovite

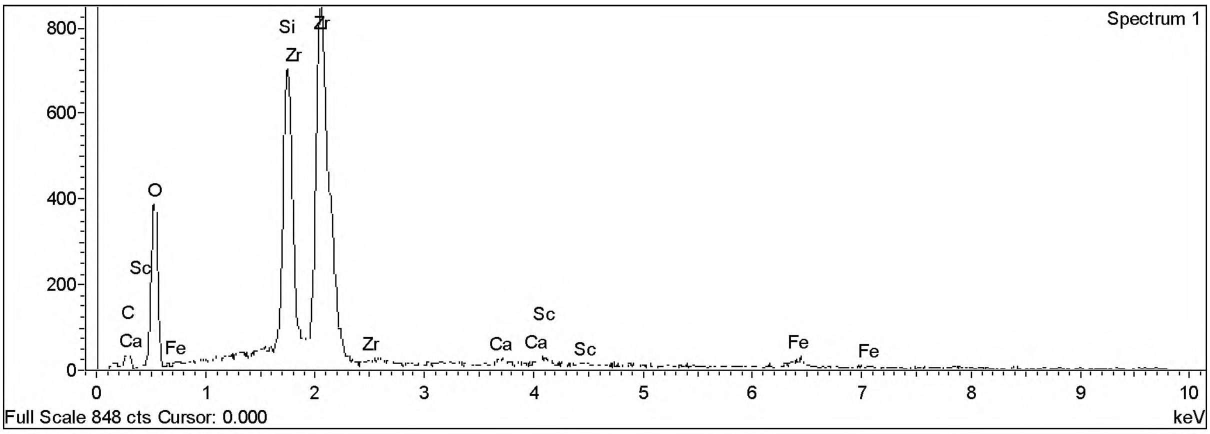

zircon-iron ore

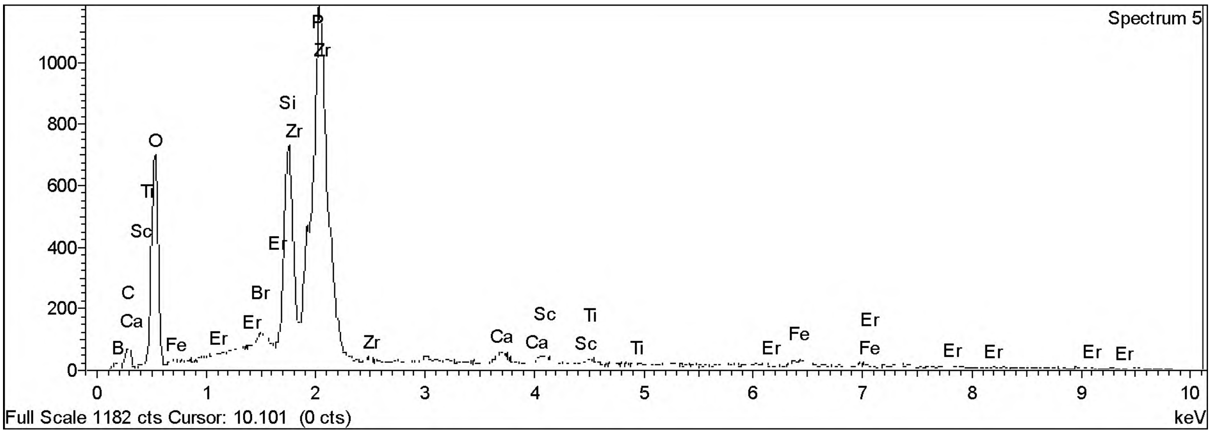

zircon-BIF

Appendix II

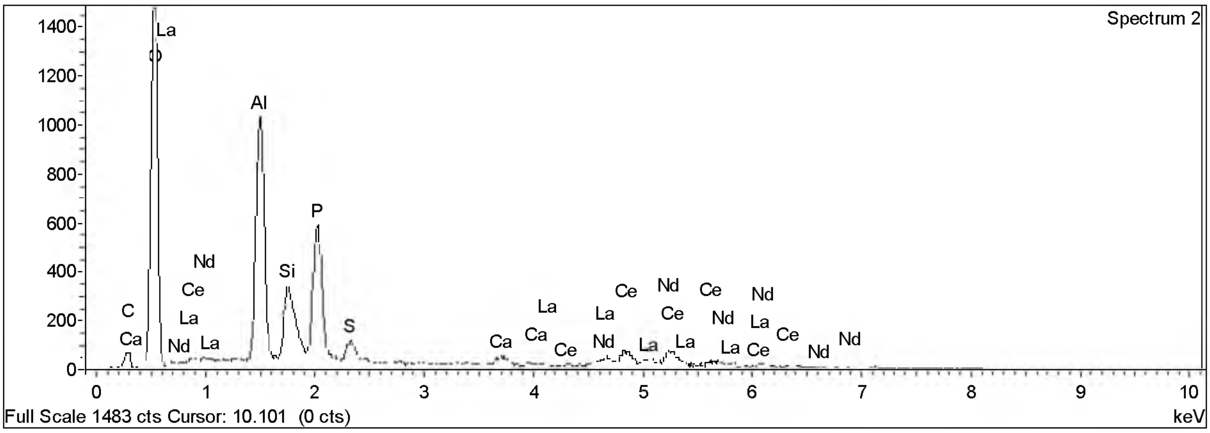

APS mineral (woodhouseite)

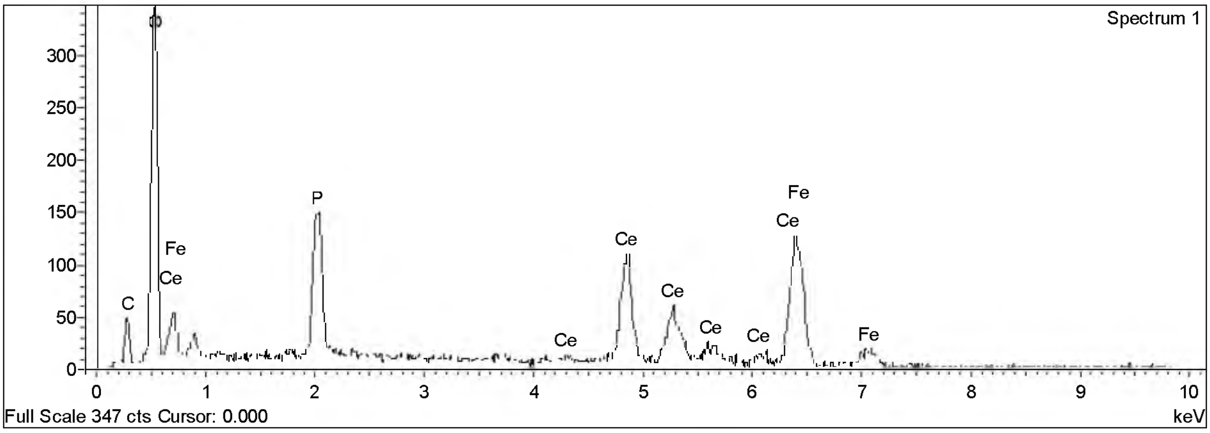

monazite in iron matrix

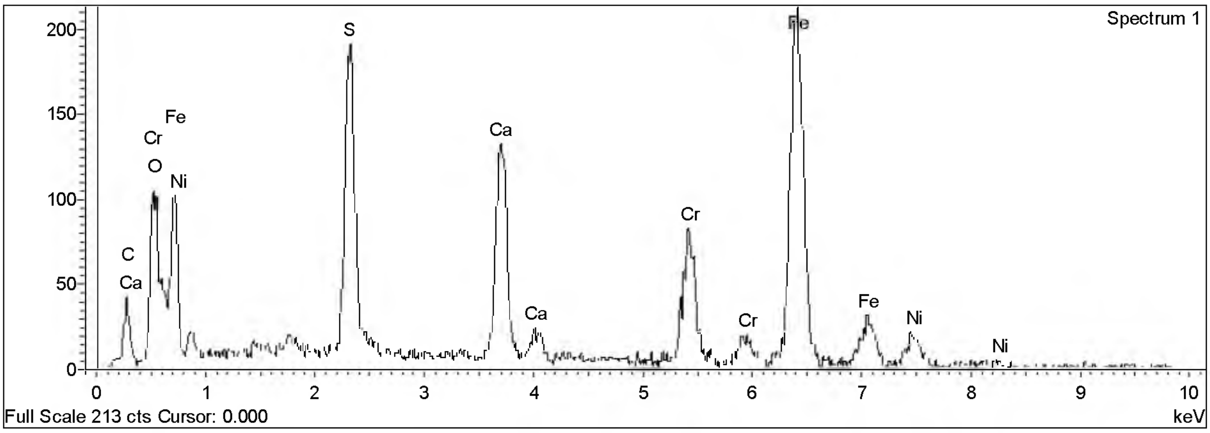

chromite in gypsum

Appendix II

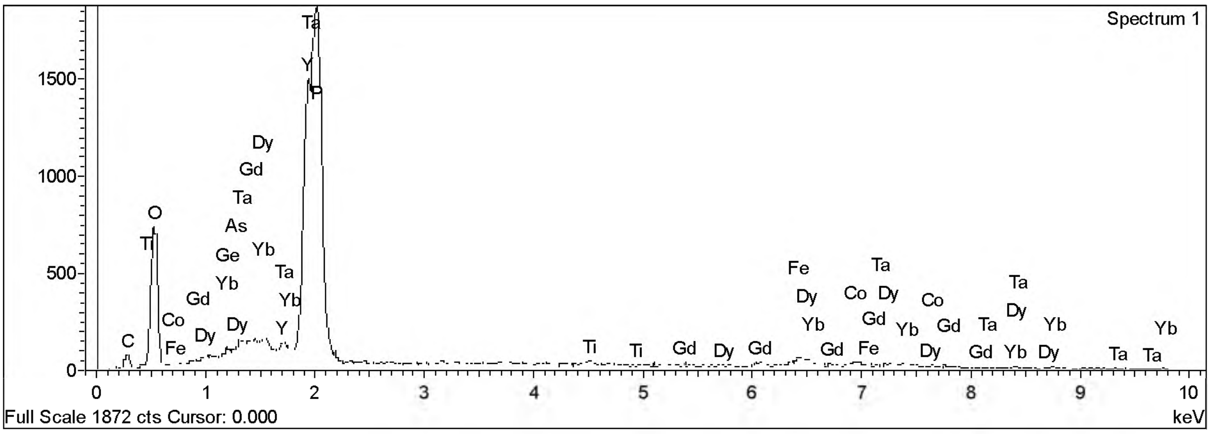

Xenotime in rutile+muscovite vein

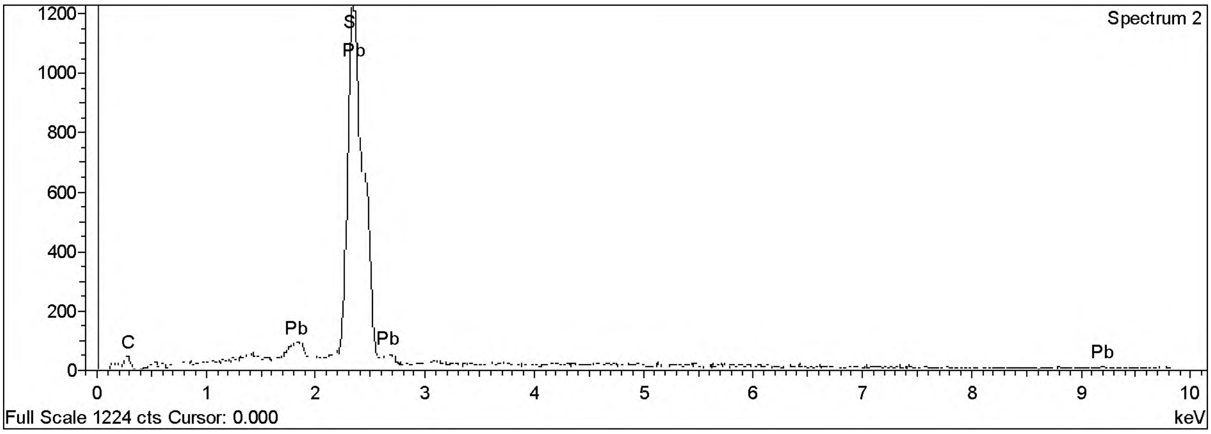

galena

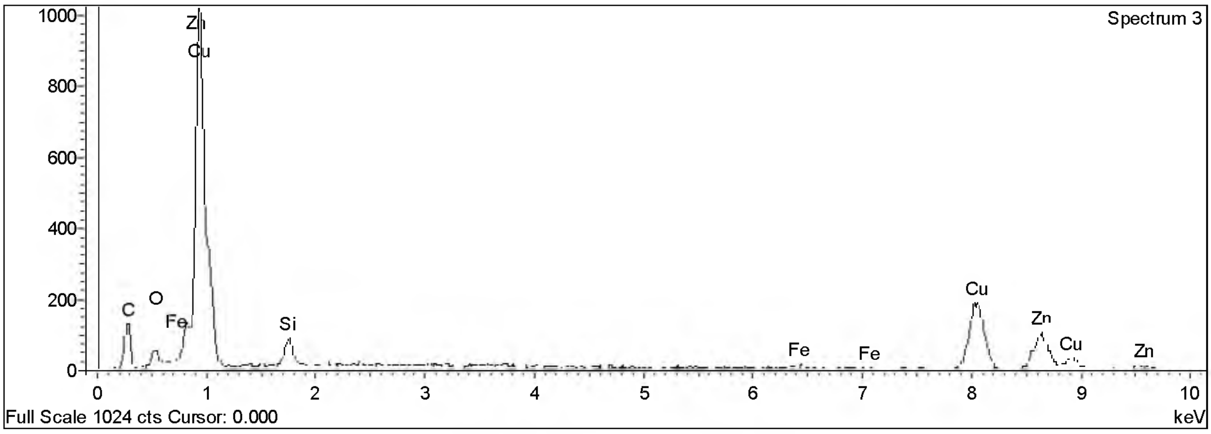

cuprite/brass

Mineral	SiO2	Na2O	TiO2	K2O	Al2O3
berthierine	21.99	0.0673	-	0.0183	16.09
berthierine	21.37	-	0.0232	0.0059	20.81
berthierine	22.53	0.0241	-	0.0355	14.69
berthierine	16.64	0.0775	0.0387	0.0243	13.25
berthierine	21.43	0.0507	0.0355	0.0377	15.15
berthierine	22.22	0.0506	0.0046	0.0284	16.05
berthierine	22.45	0.0338	0.0228	0.0144	24.8
berthierine	22.42	0.0297	-	-	25.13
berthierine	22.55	0.1189	-	0.0359	25.06
berthierine	21.67	0.0318	-	0.0304	25.9
berthierine	18.11	0.0912	0.0049	0.0372	17.88
berthierine	18.88	0.0231	0.0359	0.0238	18.39
berthierine	20.79	0.0553	0.0198	0.0162	20
berthierine	18.16	0.0187	0.0249	0.0276	17.76
berthierine	24.03	0.0078	-	0.0104	23.01
berthierine	22.49	0.0645	-	0.0019	26.38
berthierine	22.69	0.0393	0.0389	0.0065	23.24
berthierine	22.47	0.0143	-	-	23.89
berthierine	24.54	-	0.0041	0.0019	22.48
berthierine	22.58	0.068	0.019	0.0048	24.03
berthierine	23.36	0.0091	-	0.0162	24.5
berthierine	24.03	0.0031	0.0103	0.008	24.27
berthierine	23.24	-	-	-	24.49
berthierine	24.39	0.0242	-	0.0151	25.53
berthierine	23.48	0.0297	0.0508	0.018	23.82
berthierine	23.12	0.0271	0.0325	0.0109	24.78
berthierine	23.15	0.0104	0.0216	0.0245	24.72
berthierine	23.09	0.0104	-	0.0103	23.24
berthierine	24.04	0.0179	0.0245	0.0474	25.48

MgO	MnO	CaO	Cr2O3	FeO	Total	Sample
1.6579	0.1865	0.0128	0.0091	55.55	95.582	HLT2
1.2429	0.2393	0.0009	-	47.44	91.1323	HLT2
1.273	0.0928	0.0053	-	53.76	92.4107	HLT2
2.13	0.1323	0.0071	-	61.31	93.61	HLT2
1.69	0.1923	0.016	0.0112	50.5	89.1134	HLT2
1.6471	0.2603	0.0077	-	50.72	90.9888	HLT2
3.71	0.1518	-	0.009	41.88	93.0718	VLT10
3.2	0.1579	-	-	39.32	90.2577	VLT10
3.02	0.1656	0.0009	-	38.91	89.8614	VLT10
2.18	0.116	-	0.0456	42.54	92.5139	VLT10
2.44	0.1185	0.0262	0.0333	49.99	88.7313	VLT14
2.68	0.1339	0.0032	0.001	48.77	88.941	VLT14
2.76	0.2029	-	-	44.92	88.7643	VLT14
2.49	0.1372	0.0099	0.0393	51.46	90.1276	VLT14
2.77	0.0839	0.0796	0.0166	38.35	88.3584	VLT57B
2.43	0.0774	0.0426	0.0237	40.72	92.2302	VLT57B
2.94	0.1181	0.0667	0.0087	39.51	88.6583	VLT57B
2.42	0.1131	0.0083	0.0189	39.23	88.1646	VLT57B
3.48	0.108	0.0129	0.0122	39.85	90.4892	VLT57B
2.94	0.1225	0.0673	0.0453	42.13	92.007	VLT57B
3.78	0.1081	0.0191	0.0192	37.97	89.7818	VLT22
3.53	0.1793	-	0.0354	38.25	90.3162	VLT22
3.49	0.098	0.009	-	37.56	88.8871	VLT22
3.7	0.1283	0.0193	0.0047	35.23	89.0416	VLT22
3.38	0.0886	0.0361	0.0314	38	88.9347	VLT22
3.35	0.1344	0.013	0.0185	38.68	90.1665	VLT22
3.36	0.1449	-	-	38.37	89.8015	VLT22
2.11	0.262	0.0032	0.027	40.54	89.293	VLT22
2.21	0.2223	0.0001	0.0045	41.43	93.4768	VLT24

Mineral	SiO2	Na2O	TiO2	K2O	Al2O3
berthierine	22.7	0.0516	0.0019	0.0084	24.21
berthierine	23.63	0.0055	0.0319	0.0108	23.79
berthierine	22.42	0.0348	-	0.0073	24.94
berthierine	23.83	-	-	0.0051	23.54
berthierine	23.18	-	-	0.0086	24
berthierine	21.33	-	0.0141	-	26.58
berthierine	21.76	0.0006	0.0454	0.0054	25.49
berthierine	22.84	-	0.0042	0.0052	25.83
berthierine	22.3	-	0.0376	0.0016	25.86
berthierine	23.86	0.017	0.0148	0.0191	23.13
muscovite	50.35	0.1293	0.0156	9.66	35.05
muscovite	50.08	0.212	-	9.86	34.67
muscovite	50.1	0.155	0.0008	9.32	34.7
muscovite	50.41	0.2006	0.0073	9.69	34.63
muscovite	49.47	0.1193	0.0195	9.9	34.32
muscovite	47.12	0.211	0.0033	9.71	33.56
muscovite	50.21	0.1932	-	9.59	34.91
muscovite	49.96	0.2515	0.0484	9.87	34.84
tourmaline	35.75	1.9	0.0241	0.0074	34.24
tourmaline	36.58	2.69	-	0.0022	34.44
tourmaline	37	2.17	-	0.0058	33.68
tourmaline	37.35	2.49	0.0304	0.0039	34.35
tourmaline	38.01	2.16	0.091	0.0185	32.51
tourmaline	37.98	2.27	0.1025	0.0092	32.35

Mineral	S
baryte	25.51
baryte	26.36
baryte	24.84

MgO	MnO	CaO	Cr2O3	FeO	Total	Sample
3.41	0.1259	0.0032	0.018	38.6	89.1291	VLT24
2.53	0.1325	-	-	39.2	89.3308	VLT24
2.32	0.1339	0.0047	0.0172	39.6	89.478	VLT24
3.03	0.182	-	-	39.28	89.8671	VLT24
2.75	0.2331	-	0.0132	39.36	89.545	VLT24
2.2	0.1397	0.0149	0.0053	39.34	89.6241	VLT57A
2.26	0.1475	0.0153	0.0048	40.12	89.8491	VLT57A
2.42	0.0897	0.0058	0.0247	38.47	89.6896	VLT57A
2.39	0.1168	0.0168	-	38.55	89.2729	VLT57A
2.68	0.064	0.0099	0.1775	39.22	89.1924	VLT57A
0.4394	0.0093	0.1429	0.0596	1.63	97.4861	VLT57A
0.4919	0.0674	0.1053	0.0624	1.62	97.1691	VLT57A
0.4299	0.0019	0.1068	-	1.39	96.2045	VLT57A
0.4787	0.0544	0.1265	0.0732	1.4	97.0707	VLT57A
0.4574	0.0494	0.164	0.0411	2.15	96.6908	VLT57A
0.326	0.0281	0.4198	0.0927	1.61	93.0809	VLT57A
0.391	0.07	0.1597	-	1.65	97.174	VLT57A
0.3734	0.0847	0.4177	0.081	1.75	97.6768	VLT57A
4.59	0.0401	0.9433	-	10.56	88.074	VLT43
5.29	0.0588	0.0824	0.0195	10.7	89.8801	VLT43
4.79	0.1511	0.0193	-	12.6	90.4418	VLT43
4.56	0.0631	0.0643	-	11.64	90.5533	VLT43
3.99	0.04	0.028	0.0669	10.84	87.7544	VLT57A
3.29	0.0124	0.0196	0.1468	12.84	89.0205	VLT57A

Co	Ba	CaO	SrO	CuO	Total	Sample
-	54.45	-	1.93	-	81.8901	VLT14
-	54.4	-	1.9	-	82.6601	VLT14
0.0102	55.51	0.0075	1.58	0.0542	82.0203	VLT14

Mineral	S	Fe	Cu	Zn	Ni	Co	Total	Sample
pyrite	50.53	48.65	0.0035	-	0.0361	-	99.2197	HLT2
pyrite	48.85	46.39	-	0.0193	0.703	0.0112	95.9736	HLT2
pyrite	55.1	46.42	0.0222	0.0069	-	0.0063	101.555	VLT10
pyrite	53.12	46.32	0.0059	-	0.0186	0.0189	99.4835	VLT10
pyrite	55.43	46.49	0.0163	-	0.0109	-	101.947	VLT10

Mineral	MgO	CaO	FeO	MnO	P2O5	Total	Sample
apatite	-	54.33	0.0477	0.0407	39.62	94.0385	VLT14
apatite	0.0201	54.63	0.2363	0.016	39.44	94.3425	VLT14
apatite	0.0112	54.99	0.1531	0.0412	39.51	94.7056	VLT14
apatite	0.0277	55.4	0.1793	0.0465	41.49	97.1617	VLT14
apatite	0.0255	54.46	0.0187	0.0176	40.32	94.8419	VLT14
apatite	-	51.87	3.45	0.0342	38.34	94.2476	VLT14

Mineral	S	Co	Cr	Ba	CaO	SrO	NiO	CuO	Total	Sample
gypsum	40.2	-	-	0.0474	40.72	0.1257	-	-	81.0932	VLT43
gypsum	41.94	-	-	0.0435	39.27	0.1863	-	-	81.4398	VLT43
gypsum	41.28	-	-	0.0141	39.59	0.1643	-	-	81.0484	VLT43
gypsum	41.83	-	-	0.0124	39.24	0.0192	-	-	81.1017	VLT43
gypsum	42.12	-	-	0.0017	39.2	0.1309	-	-	81.4527	VLT43
gypsum	41.38	-	-	-	39.37	0.2139	-	-	80.964	VLT57B
gypsum	40.9	-	-	-	39.17	0.0685	-	-	80.1385	VLT57B
gypsum	41.06	-	-	0.0403	39.92	0.0964	-	-	81.1167	VLT57B
gypsum	47.01	0.0021	0.0131	-	38.86	0.0462	0.0132	-	85.9447	VLT47
gypsum	45.46	-	-	-	42.04	0.1962	-	0.0179	87.7382	VLT47
gypsum	32.46	0.0112	0.0048	0.0188	38.24	0.1577	0.0285	-	70.9211	VLT54
gypsum	30.81	0.0217	0.0632	0.052	41.51	-	0.0086	-	72.4655	VLT54
gypsum	33.12	-	0.0124	-	41.67	0.2007	-	0.024	75.0344	VLT54
gypsum	31.82	0.0021	-	0.0194	41.13	0.1428	0.0172	-	73.1315	VLT54

Raw probe data

Mineral	MgO	MnO	CaO
siderite	4.45	5.71	0.9243
siderite	4.41	3.09	0.3482
siderite	4.07	3.79	1.52
siderite	4.58	5.21	0.2768
siderite	4.62	2.23	0.1597
siderite	4.48	2.36	0.283
siderite	3.7	5.59	0.3166
siderite	4.32	2.39	0.7982
siderite	3.25	6.7	0.126
siderite	2.37	0.7808	1.1636
siderite	3.34	1.92	0.4412
siderite	2.71	0.6591	1.1476
siderite	2.7	0.6615	1.1733
siderite	3.06	1.81	0.2642
siderite	2.79	1.45	0.9704
siderite	4.14	1.71	0.0495
siderite	3.8	5.37	0.078
siderite	3.56	3.37	0.0637
siderite	3.77	3.93	0.1079
siderite	3.61	2.22	0.0455
siderite	3.66	3.23	0.0808
siderite	3.75	4.44	0.0666
siderite	4.21	1.58	0.0545
siderite	3.19	3.63	0.085

SiO2	FeO	SrO	Total	Sample
0.1038	44.57	-	55.7581	VLT46B
0.0421	51.71	-	59.7415	VLT46B
0.1339	49.02	-	58.5641	VLT46B
0.019	48.85	-	59.0077	VLT46B
0.0275	52.99	0.0411	60.0684	VLT43
0.0229	52.35	-	59.4959	VLT43
0.0017	49.28	0.0648	58.9531	VLT43
0.0181	51.86	0.0242	59.4105	VLT43
0.4751	42.68	-	53.2312	VLT22
0.0395	52.53	-	56.8839	VLT22
0.3075	52.5	0.0169	58.5256	VLT22
0.081	54.05	0.1015	58.7492	VLT22
0.0688	50.42	0.093	55.1166	VLT22
0.1381	52.41	0.0747	57.757	VLT22
0.027	54.36	0.0164	59.6138	VLT22
0.1559	53.1	0.0682	59.2236	VLT57A
-	50.1	0.0851	59.4331	VLT57A
0.0492	52.12	-	59.1629	VLT57A
0.8252	51.06	-	59.6931	VLT57A
0.0445	52.99	0.0768	58.9869	VLT57A
0.1449	51.53	0.017	58.6627	VLT57A
0.0689	51.22	0.094	59.6396	VLT57A
0.0435	52.87	-	58.758	VLT57A
0.1514	51.38	0.0594	58.4958	VLT57A

Appendix III

Determination of H_2O^- and loss on ignition (LOI)

The H_2O^- (wt. %) and LOI (wt. %) were determined at the Department of Geology, Rhodes University. Silica crucibles were used to hold the powdered samples. These crucibles were first cleaned with distilled water and left to dry in an oven at 110°C for 2 hours. They were then left to cool in a desiccator. The crucibles were then weighed to the fourth decimal place. Two grams of sample was placed in the crucibles and the mass of the sample and crucible were recorded to the fourth decimal. The sample was dried at 110°C for a minimum of 4 hours then placed in a desiccator to cool. The difference in mass between the sample and crucible before and after drying represents the H_2O^- of the sample. Following this, the same samples were ignited for a minimum of 8 hours at 1000°C in a blast furnace. The samples were then left in a desiccator to cool. Finally, each sample was reweighed in order to determine the mass of the material lost due to heating (LOI).

X-Ray Fluorescence (XRF)

Major and trace element oxides were obtained using XRF at two laboratories. The majority of the samples (n=66) were analyzed on a Philips PW 1480 XFR spectrometer housed in the Department of Geology, Rhodes University. Whole-rock analytical data for ten major element oxides and sixteen trace elements were determined using the methods outlined by Norrish and Hutton (1969). Major element (except Na_2O) analyses were obtained from fused lanthanum-bearing lithium borate glass disks whereas the trace element and Na_2O analyses were obtained from pressed powder pellets. The standards used during the analytical process include BCR-1, CAR-08, G-2, NIM-G, SCO-1, BHVO-1, G-2, BCR-1, GSN-005, JB-1, GSP-1, AGV-1, NIM-N, S-7, INS-79, INS-33, INS-79 as well as 3 in-house standards. Another n=48 samples were later analyzed on a Panalytical Axios XRF spectrometer housed in the Department of Geological Sciences at the University of Cape Town, South Africa. Routine analysis of Fe, Mn, Ti, Ca, K, S, P, Si, Al, Mg and Na were determined using fused disks prepared with lithium borate flux. Trace element concentrations were measured on pressed powder briquettes and intensity data were corrected for mass absorption/enhancement and spectral interferences with international rock standards used for calibration. The raw results obtained through XRF analysis can be found tabulated in Appendix III.

Raw whole-rock geochemical data

Sample No. wt. %	SiO_2	TiO_2	Al_2O_3	Fe_2O_3	MnO
HLT1	1.74	0.12	1.36	94.04	0.08
HLT2	2.79	0.06	1.12	95.06	0.01
HLT3	4.88	0.18	1.13	92.74	0.02
HLT5	2.42	0.17	1.22	93.27	0.06
HLT6	1.52	0.10	0.66	97.47	0.05
HLT7	1.10	0.07	0.70	97.49	0.01
HLT9	69.32	0.03	0.13	28.57	0.05
HLT12	47.20	0.05	0.10	50.26	0.06
HLT13	53.97	0.02	0.01	40.80	0.07
HLT15	57.47	0.03	0.13	40.71	0.06
HLT16	73.66	0.03	0.17	24.92	0.04
HLT21	59.46	0.09	0.65	39.00	0.04
HLT22	56.65	0.01	0.24	39.55	0.03
HLT23	57.41	bdl	0.05	41.39	0.02
HLT24	37.04	0.02	0.12	58.49	0.04
HLT25	45.25	0.02	0.16	52.74	0.04
HLT26A	73.15	0.02	0.08	25.99	0.05
HLT26B	25.32	bdl	0.12	68.79	0.02
HLT30	55.81	0.01	0.02	42.05	0.05
HLT32	56.01	0.01	bdl	42.76	0.04
HLT33	76.39	0.01	0.12	21.47	0.03
HLT34	68.45	0.01	bdl	30.77	0.05
HLT35	65.76	0.02	bdl	33.33	0.04
HLT36	96.50	bdl	0.09	2.69	0.03
HLT37	96.24	0.02	0.04	2.46	0.03
HLT38	96.54	0.01	0.05	2.40	0.03
HLT39	95.90	bdl	0.02	2.91	0.04
HLT41	65.71	0.01	0.18	33.23	0.06
HLT44	46.41	0.02	bdl	52.44	0.05
HLT45	55.87	0.03	0.45	42.22	0.05
HLT46	66.75	0.02	0.13	31.93	0.05
HLT47	46.97	0.02	bdl	51.33	0.05
HLT48	48.75	bdl	0.05	50.58	0.03

MgO	CaO	Na_2O	K_2O	P_2O_5	LOI	H_2O^-	Total
0.04	0.10	0.02	0.13	0.05	0.54	0.33	98.55
0.01	0.35	bdl	0.12	0.30	0.50	0.21	100.53
0.05	0.12	bdl	0.01	0.16	0.51	0.17	99.97
0.05	0.38	0.03	0.14	0.27	0.64	0.32	98.96
0.04	0.16	0.02	0.08	0.06	0.71	0.30	101.15
0.01	0.05	0.01	0.08	0.05	0.68	0.38	100.63
0.01	0.43	0.01	0.01	0.02	0.56	0.21	99.33
0.03	0.26	bdl	0.02	0.03	0.38	0.29	98.66
0.02	1.13	bdl	0.01	0.02	2.28	0.62	98.94
0.02	0.36	0.01	0.02	0.06	0.45	0.14	99.46
bdl	0.27	0.01	0.04	0.02	0.35	0.15	99.65
0.04	0.22	0.02	0.10	0.02	0.50	0.11	100.23
bdl	0.96	bdl	0.01	0.11	1.13	0.41	99.10
bdl	0.27	bdl	bdl	0.06	0.22	0.14	99.56
0.01	1.10	0.01	0.01	0.14	1.48	0.24	98.70
0.02	0.10	0.01	0.02	0.04	0.33	0.12	98.85
0.02	0.22	0.01	0.01	0.02	0.16	0.23	99.94
bdl	2.44	0.01	bdl	0.39	2.35	0.09	99.53
0.01	0.06	bdl	bdl	0.03	1.00	0.80	99.85
0.02	0.18	bdl	bdl	0.06	0.09	0.08	99.24
0.01	0.32	0.01	0.01	0.01	0.57	0.85	99.81
0.01	0.19	bdl	0.01	0.02	0.45	0.09	100.03
0.02	0.34	0.01	bdl	0.07	0.26	0.15	100.00
bdl	0.13	bdl	bdl	0.02	0.10	0.13	99.69
0.03	0.03	bdl	bdl	0.01	0.31	0.04	99.20
0.02	0.02	bdl	bdl	0.01	-0.18	0.14	99.05
bdl	0.33	0.01	bdl	bdl	0.46	0.24	99.91
0.03	0.14	0.01	0.02	0.04	0.33	0.13	99.88
0.03	0.20	bdl	0.01	0.02	0.14	0.06	99.38
0.01	0.21	0.01	0.09	0.03	0.42	0.01	99.40
0.01	0.07	bdl	0.02	0.01	-0.01	0.14	99.13
0.02	0.20	bdl	0.01	0.02	0.32	0.25	99.19
bdl	0.11	bdl	bdl	0.08	0.13	0.08	99.81

Raw whole-rock geochemical data

Sample No. wt. %	SiO_2	TiO_2	Al_2O_3	Fe_2O_3	MnO
VLT1	1.53	0.08	1.07	94.42	0.08
VLT4A	34.83	0.12	0.81	59.90	0.01
VLT4B	41.26	0.13	2.70	42.15	0.01
VLT3	47.62	0.08	0.59	50.02	0.05
VLT5	37.53	0.03	0.65	60.95	0.02
VLT6	6.52	0.05	0.91	91.75	0.03
VLT7	59.76	0.01	0.18	38.93	0.02
VLT10	10.69	0.12	1.35	86.67	0.05
VLT13	35.75	0.06	0.40	62.50	0.07
VLT15	34.80	0.04	0.22	63.54	0.02
VLT16A	39.84	0.04	0.23	59.09	0.02
VLT16B	94.05	0.01	0.06	6.14	0.04
VLT18	47.24	0.05	0.29	50.43	0.05
VLT19	55.89	0.03	0.11	41.51	0.04
VLT20	44.14	0.05	0.22	53.65	0.04
VLT22	89.05	0.01	0.08	9.82	0.06
VLT23	40.02	0.07	1.51	56.12	0.04
VLT24	64.68	0.02	0.59	34.17	0.04
VLT25	66.72	0.03	0.32	30.93	0.03
VLT26	22.51	0.06	0.55	74.74	0.07
VLT27	49.62	0.09	0.54	48.35	0.03
VLT29	39.65	0.08	0.29	57.97	0.04
VLT30	48.80	0.03	0.04	50.12	0.05
VLT34	65.49	0.03	0.07	32.42	0.05
VLT35	69.12	0.03	0.07	30.17	0.05
VLT36	36.49	0.03	0.05	61.34	0.04
VLT37	45.70	0.02	0.16	50.81	0.03
VLT38	66.65	0.03	0.04	33.23	0.06
VLT39	87.52	0.01	0.01	10.01	0.04
VLT40	64.98	0.01	0.03	31.71	0.04
VLT41	83.95	0.01	0.06	14.30	0.04
VLT42	67.16	0.01	0.05	29.38	0.08
VLT43	74.77	0.01	0.36	15.37	0.36
VLT44	84.77	0.01	0.02	13.72	0.03

MgO	CaO	Na_2O	K_2O	P_2O_5	LOI	H_2O^-	Total
0.05	0.41	0.01	0.15	0.23	0.96	0.20	99.18
0.01	0.07	bdl	0.12	0.03	1.60	0.27	97.77
0.08	0.17	0.05	0.66	0.09	2.71	0.55	90.57
0.03	0.13	bdl	0.09	0.06	0.44	0.26	99.36
0.02	0.04	bdl	0.05	0.03	0.21	0.18	99.71
0.02	0.06	bdl	0.12	0.05	0.37	0.17	100.04
bdl	0.06	bdl	bdl	0.02	0.26	0.15	99.39
0.08	0.11	0.01	0.10	0.08	0.44	0.11	99.81
0.05	0.09	0.01	0.04	0.04	0.19	0.11	99.31
0.01	0.04	0.01	0.02	0.03	0.70	0.11	99.54
bdl	0.02	bdl	0.03	0.03	0.34	0.24	99.88
0.03	0.03	bdl	0.01	0.02	-0.12	0.12	100.39
0.04	0.09	bdl	0.06	0.02	0.10	0.17	98.55
0.02	0.02	bdl	0.01	0.02	1.16	0.13	98.94
0.03	0.06	bdl	0.03	0.03	0.30	0.06	98.62
0.02	0.06	bdl	0.01	0.04	0.17	0.31	99.64
0.05	0.05	0.01	0.38	0.02	0.42	0.19	98.88
0.08	0.08	bdl	0.01	0.05	0.17	0.20	100.08
0.02	0.11	bdl	0.06	0.09	0.11	0.64	99.05
0.03	0.21	bdl	0.10	0.14	0.33	0.16	98.88
bdl	0.05	bdl	0.11	0.05	0.36	0.28	99.48
0.02	0.18	0.01	0.02	0.04	0.26	0.20	98.78
0.02	0.27	0.01	0.01	0.04	0.38	0.11	99.87
0.02	0.53	0.01	0.01	0.01	0.68	0.24	99.55
0.04	0.39	0.01	0.01	0.01	0.45	0.05	100.40
0.02	0.17	0.01	0.01	0.02	0.40	0.13	98.71
bdl	1.00	0.01	0.01	0.02	1.59	0.41	99.76
0.02	0.14	bdl	0.01	0.02	0.17	0.13	100.49
0.01	0.80	0.01	bdl	0.01	1.05	0.44	99.91
0.02	0.56	0.01	0.01	0.01	1.41	0.38	99.15
0.01	0.71	bdl	bdl	0.02	1.03	0.52	100.65
0.03	1.15	0.02	0.01	0.01	1.93	0.66	100.48
0.39	1.82	0.01	bdl	0.04	5.46	0.79	99.38
bdl	0.60	bdl	bdl	0.03	0.73	0.34	100.25

Raw whole-rock geochemical data

Sample No. wt. %	SiO_2	TiO_2	Al_2O_3	Fe_2O_3	MnO
VLT48	57.27	0.03	bdl	40.52	0.04
VLT49	68.11	0.01	0.01	31.12	0.04
VLT50	38.17	0.02	0.02	59.94	0.07
VLT51	23.87	0.03	bdl	72.78	0.05
VLT52	65.84	0.01	0.03	31.13	0.06
VLT55	53.08	0.01	bdl	41.62	0.05
VLT56	54.87	0.02	0.02	41.86	0.04
VLT59	34.48	0.02	bdl	62.88	0.05
VLT61	32.75	0.01	bdl	65.45	0.04
VLT62	33.29	0.01	0.11	64.92	0.01
VLT63	65.91	0.02	0.59	32.47	0.03
VLT64	74.53	bdl	0.04	23.19	0.04
VLT66	66.06	0.02	0.24	32.75	0.04
VLT68	60.69	0.01	0.02	36.52	0.06
VLT69	60.03	0.02	0.02	37.42	0.05
VLT70	57.52	0.01	bdl	40.58	0.05
VLT71	50.15	0.02	0.12	45.82	0.08
VLT73	39.68	0.02	bdl	57.47	0.06
VLT74	32.27	2.75	17.20	38.39	0.07
VLT76	51.20	0.02	bdl	45.84	0.05
VLT80	45.73	0.02	0.22	50.95	0.09

Sample No. wt. %	SiO_2	TiO_2	Al_2O_3	Fe_2O_3	MnO
D1	43.33	0.01	0.22	55.23	0.02
D2	56.71	bdl	0.02	42.41	0.02
D3	44.09	0.01	0.03	54.64	0.02
D4	47.32	0.01	0.12	51.62	0.03
D5	45.61	bdl	0.01	53.57	0.03
D6	46.80	0.01	0.14	52.07	0.03
D7	55.18	0.01	0.19	44.10	0.03
D8	38.49	0.01	0.24	60.41	0.03
D9	53.84	0.01	0.18	44.86	0.03
D10	49.24	bdl	0.01	50.07	0.02

MgO	CaO	Na_2O	K_2O	P_2O_5	LOI	H_2O^-	Total
0.01	0.64	0.01	0.01	0.02	0.94	0.29	99.76
0.01	0.15	bdl	0.01	0.02	0.25	0.13	99.85
0.04	0.30	bdl	0.01	0.08	0.27	0.11	99.02
0.03	0.72	bdl	0.01	0.08	1.26	0.25	99.07
0.02	1.06	0.01	0.01	0.01	1.33	0.22	99.71
0.03	1.71	0.01	0.01	0.05	2.32	0.11	98.98
0.01	1.17	0.01	0.01	0.08	1.57	0.19	99.84
0.02	0.64	bdl	0.01	0.02	1.00	0.15	99.26
0.03	0.09	bdl	0.01	0.07	0.26	0.11	98.82
bdl	0.48	bdl	bdl	0.07	0.74	0.16	99.79
0.64	0.43	bdl	0.01	0.05	0.29	0.32	100.76
bdl	0.79	bdl	bdl	0.03	1.11	0.35	100.08
0.03	0.29	bdl	0.01	0.02	0.36	0.11	99.91
0.04	0.60	0.02	0.01	0.04	0.94	0.12	99.06
0.03	0.88	0.01	0.02	0.02	1.15	0.10	99.74
0.04	0.23	bdl	bdl	0.01	0.31	0.11	98.87
0.05	1.61	0.01	0.01	0.04	0.95	0.20	99.05
0.06	0.41	0.01	0.01	0.06	0.66	0.13	98.55
0.19	0.12	0.41	4.02	0.08	3.29	0.61	99.40
0.03	0.60	bdl	0.01	0.04	0.74	0.16	98.68
0.04	1.13	0.01	0.05	0.05	1.52	0.16	99.97

MgO	CaO	Na_2O	K_2O	P_2O_5	LOI	H_2O^-	Total
0.02	0.04	bdl	0.01	0.05	0.41	0.07	99.41
bdl	0.02	0.01	bdl	0.03	0.15	0.03	99.40
0.03	0.14	0.01	bdl	0.05	0.17	0.04	99.23
0.01	0.03	0.02	0.01	0.04	0.22	0.08	99.51
0.01	0.02	bdl	bdl	0.04	0.13	0.07	99.49
bdl	0.13	bdl	0.01	0.12	0.18	0.08	99.57
bdl	0.04	0.02	0.02	0.05	0.07	0.07	99.78
0.01	0.07	0.01	0.01	0.08	0.01	0.17	99.54
bdl	0.03	bdl	0.01	0.04	0.74	0.24	99.98
bdl	0.01	bdl	bdl	0.03	-0.04	0.10	99.44

Raw whole-rock geochemical data

Sample No. wt. %	SiO_2	TiO_2	Al_2O_3	Fe_2O_3	MnO
D11	52.99	0.01	0.11	46.07	0.03
D12	52.26	bdl	0.03	46.83	0.05
D13A	56.15	0.01	0.07	43.40	0.02
D13B	36.40	bdl	0.03	63.18	0.02
D14	3.22	0.03	0.81	95.34	0.02
D15	22.13	0.04	1.28	74.80	0.03
D16	0.65	bdl	0.07	99.10	0.02
D17	50.78	bdl	0.02	47.94	0.02
D18	70.45	0.02	0.36	28.47	0.03
D19	46.14	0.01	0.21	52.83	0.02
D22	1.71	0.68	0.03	96.73	0.08

Sample No. wt. %	SiO_2	TiO_2	Al_2O_3	Fe_2O_3	MnO
S2	46.00	bdl	0.12	53.07	0.02
S3	54.69	bdl	0.05	43.80	0.03
S4	48.52	bdl	0.06	50.86	0.02
S5	61.62	bdl	0.14	36.89	0.02
S6	56.65	bdl	0.02	42.42	0.03

MgO	CaO	Na_2O	K_2O	P_2O_5	LOI	H_2O^-	Total
bdl	0.02	bdl	bdl	0.03	0.01	0.17	99.44
bdl	0.03	bdl	bdl	0.05	0.05	0.12	99.42
bdl	0.01	0.01	bdl	0.02	-0.02	0.13	99.80
bdl	0.03	bdl	bdl	0.04	-0.12	0.13	99.71
0.02	0.07	0.01	0.05	0.08	0.52	0.16	100.33
bdl	0.32	0.01	0.10	0.26	0.50	0.23	99.70
0.02	0.06	bdl	bdl	0.07	0.24	0.06	100.29
bdl	0.05	bdl	bdl	0.06	0.18	0.08	99.13
bdl	0.10	0.01	0.04	0.08	0.19	0.18	99.93
bdl	0.12	bdl	0.02	0.11	0.13	0.13	99.72
0.01	0.15	0.01	0.02	0.13	0.55	0.17	100.27

MgO	CaO	Na_2O	K_2O	P_2O_5	LOI	H_2O^-	Total
bdl	0.11	bdl	bdl	0.09	0.14	0.05	99.60
bdl	0.05	bdl	bdl	0.04	0.60	0.05	99.31
bdl	0.06	bdl	bdl	0.06	0.11	0.04	99.73
bdl	0.10	0.05	bdl	0.08	0.16	0.03	99.09
bdl	0.03	bdl	bdl	0.04	0.12	0.06	99.37

Raw whole-rock geochemical data

Sample No. ppm	Mo	Nb	Zr	Y	Sr
HLT1	7.1	3.0	20.9	14.9	117.4
HLT2	8.1	3.0	28.0	6.0	22.0
HLT3	bdl	4.0	38.7	11.2	148.7
HLT5	7.8	4.1	20.9	9.2	55.6
HLT6	5.1	6.0	42.0	15.0	137.0
HLT7	4.4	6.0	19.0	20.0	16.0
HLT9	3.4	1.7	3.8	bdl	7.1
HLT12	3.3	2.5	5.1	2.2	10.4
HLT13	5.1	bdl	2.3	bdl	25.4
HLT15	3.8	bdl	3.6	9.0	22.9
HLT16	2.4	1.3	5.6	1.5	14.9
HLT21	2.5	2.6	11.8	2.1	18.9
HLT22	5.0	4.0	14.0	2.0	30.0
HLT23	2.2	4.0	15.0	5.0	21.0
HLT24	4.6	3.2	1.9	2.8	36.1
HLT25	3.1	bdl	2.3	3.7	10.1
HLT26A	2.8	bdl	3.7	bdl	7.6
HLT26B	2.8	2.0	12.0	5.0	37.0
HLT30	2.4	bdl	1.9	6.9	5.3
HLT32	2.9	bdl	1.6	4.3	5.8
HLT33	3.0	1.2	2.2	4.2	12.7
HLT34	3.4	bdl	bdl	2.7	6.1
HLT35	2.7	1.5	bdl	2.0	17.1
HLT36	2.4	5.0	13.0	12.0	17.0
HLT37	3.1	bdl	2.3	11.7	3.7
HLT38	2.4	bdl	1.8	11.2	2.9
HLT39	3.1	4.0	13.0	1.0	19.0
HLT41	3.7	bdl	1.6	12.2	7.3
HLT44	4.2	2.0	3.0	6.5	3.3
HLT45	3.9	1.6	13.6	5.9	10.3
HLT46	3.2	bdl	9.0	8.0	8.1
HLT47	5.3	bdl	bdl	19.0	8.5
HLT48	4.4	5.0	12.0	3.0	14.0

Appendix III

U	Rb	Th	Pb	Zn	Cu	Ni	Cr	V
bdl	6.0	bdl	19.0	9.0	41.8	62.2	118.2	726.1
5.8	7.0	11.0	20.0	17.0	13.0	15.0	57.0	179.0
bdl	11.0	6.0	69.0	20.0	1901.0	1512.0	677.0	30.0
bdl	5.8	bdl	59.5	bdl	63.0	68.0	127.0	123.4
bdl	3.5	14.0	55.0	24.0	48.0	bdl	138.0	22.0
bdl	6.0	12.0	12.0	17.0	43.8	bdl	174.0	116.0
bdl	bdl	bdl	bdl	4.2	21.7	18.5	58.8	28.9
bdl	bdl	bdl	bdl	bdl	29.5	35.0	68.3	43.5
bdl	1.8	bdl	bdl	5.2	32.9	34.7	80.8	31.0
bdl	2.8	bdl	4.2	3.9	25.2	40.2	59.0	24.9
bdl	bdl	bdl	3.3	3.1	15.5	16.2	44.2	21.9
bdl	3.6	bdl	9.7	bdl	22.7	25.6	56.6	52.6
bdl	6.0	4.0	9.0	11.0	11.0	71.0	84.0	27.0
bdl	bdl	6.0	7.0	3.0	10.0	44.0	35.0	31.0
bdl	bdl	bdl	5.3	6.5	28.5	33.4	57.0	55.6
bdl	2.0	bdl	5.9	bdl	30.2	25.7	52.8	55.7
bdl	bdl	bdl	bdl	4.6	18.4	14.9	51.5	23.6
bdl	6.0	9.0	9.0	12.0	28.0	29.1	70.0	23.0
bdl	bdl	bdl	5.8	7.5	29.8	38.7	54.8	24.0
bdl	bdl	bdl	bdl	6.1	26.0	25.0	51.7	26.9
bdl	1.7	bdl	6.9	bdl	14.8	12.0	34.9	32.8
bdl	bdl	bdl	5.6	bdl	20.2	15.6	39.9	19.6
bdl	1.5	bdl	bdl	bdl	22.4	18.2	58.2	25.6
bdl	5.0	7.0	8.0	2.0	10.0	14.0	38.0	4.0
bdl	bdl	bdl	bdl	bdl	5.4	6.8	32.4	13.1
bdl	bdl	bdl	bdl	bdl	6.5	6.7	29.8	11.2
3.0	2.0	4.0	8.0	5.0	10.0	21.0	44.0	12.0
bdl	bdl	bdl	10.9	4.0	21.7	19.7	48.8	24.9
bdl	bdl	bdl	6.3	bdl	25.2	39.9	49.7	28.7
bdl	2.6	bdl	13.2	6.0	26.1	23.6	49.7	37.8
bdl	1.9	bdl	10.3	bdl	23.1	21.2	46.2	24.9
bdl	bdl	bdl	bdl	bdl	29.4	28.5	54.1	24.2
bdl	5.0	7.0	11.0	13.0	12.0	29.6	38.0	106.0

Raw whole-rock geochemical data

Sample No. ppm	Mo	Nb	Zr	Y	Sr
VLT1	4.7	bdl	16.4	8.5	14.7
VLT4A	3.0	5.0	26.3	7.4	189.0
VLT4B	bdl	6.0	34.3	6.0	1049.0
VLT3	4.1	2.7	14.3	3.6	55.6
VLT5	n.a.	6.0	17.0	bdl	16.0
VLT6	n.a.	4.0	21.0	7.0	27.0
VLT7	3.6	5.0	10.0	3.0	15.0
VLT10	3.1	5.0	22.0	6.0	23.0
VLT13	2.2	bdl	8.7	bdl	5.9
VLT15	2.2	5.0	19.0	1.0	13.0
VLT16A	2.4	5.0	15.0	1.0	13.0
VLT16B	3.8	bdl	bdl	bdl	2.1
VLT18	2.8	2.1	6.5	2.3	4.6
VLT19	3.1	bdl	3.0	bdl	10.5
VLT20	3.0	1.8	6.6	bdl	4.9
VLT22	4.5	bdl	bdl	bdl	1.6
VLT23	2.2	2.0	15.0	2.0	14.8
VLT24	3.3	1.9	3.0	bdl	4.4
VLT25	2.9	1.2	4.4	1.6	2.1
VLT26	3.3	bdl	9.7	4.0	5.6
VLT27	2.7	4.0	22.0	3.0	16.0
VLT29	3.7	3.1	10.8	2.3	5.6
VLT30	4.4	bdl	1.9	bdl	14.6
VLT34	4.2	1.4	4.1	bdl	13.2
VLT35	4.0	bdl	3.4	bdl	8.4
VLT36	4.5	bdl	2.4	bdl	5.5
VLT37	3.9	3.0	16.0	3.0	35.0
VLT38	3.6	1.9	3.1	bdl	4.3
VLT39	2.9	bdl	bdl	bdl	9.5
VLT40	2.8	bdl	2.4	bdl	12.2
VLT41	3.5	bdl	3.5	bdl	11.6
VLT42	3.7	bdl	1.3	bdl	66.3
VLT43	1.7	4.0	14.0	1.0	27.0
VLT44	3.3	4.0	17.0	2.0	23.0

U	Rb	Th	Pb	Zn	Cu	Ni	Cr	V
bdl	7.4	bdl	9.8	bdl	43.6	57.8	77.1	221.2
4.5	10.0	4.7	18.0	bdl	27.0	bdl	40.0	22.0
bdl	30.0	bdl	11.0	bdl	15.0	bdl	bdl	234.0
bdl	3.9	bdl	6.7	bdl	22.8	23.1	81.6	42.6
n.a	6.0	7.0	3.0	13.0	9.0	bdl	36.0	11.0
n.a	7.0	12.0	21.0	18.0	bdl	bdl	30.0	15.0
bdl	5.0	7.0	8.0	8.0	7.0	44.0	19.0	11.0
bdl	6.8	10.0	11.0	21.0	51.0	bdl	99.0	28.0
bdl	2.5	6.0	5.5	bdl	28.9	30.9	78.7	52.3
bdl	1.0	12.0	11.0	10.0	47.0	31.7	80.7	28.0
bdl	5.0	7.0	8.0	7.9	32.9	bdl	31.0	11.0
bdl	1.2	bdl	bdl	bdl	29.0	bdl	40.3	15.8
bdl	2.2	bdl	bdl	bdl	26.3	25.6	60.5	44.3
bdl	2.4	bdl	6.3	bdl	26.0	19.0	52.7	29.4
bdl	bdl	bdl	bdl	6.0	29.1	28.2	63.8	40.3
bdl	bdl	bdl	bdl	bdl	14.2	14.0	57.5	19.2
bdl	11.6	bdl	bdl	bdl	28.5	28.4	57.8	41.3
bdl	bdl	bdl	bdl	7.4	20.9	26.8	90.8	24.0
bdl	2.7	bdl	bdl	bdl	17.7	17.1	46.9	29.3
bdl	3.4	bdl	9.6	10.1	38.6	39.3	190.4	78.9
bdl	10.0	11.0	14.0	11.0	25.1	bdl	129.6	27.0
bdl	bdl	bdl	bdl	7.3	28.0	28.5	58.3	32.6
bdl	bdl	bdl	bdl	bdl	26.7	35.3	61.1	34.8
bdl	bdl	bdl	bdl	bdl	23.0	21.9	70.2	39.2
bdl	bdl	bdl	bdl	4.4	23.1	31.7	59.7	29.2
bdl	bdl	bdl	9.8	6.1	33.4	52.6	48.1	42.5
bdl	2.0	8.0	8.0	7.0	31.0	53.0	70.0	26.0
bdl	bdl	bdl	bdl	bdl	20.6	16.2	55.7	30.8
bdl	bdl	bdl	3.4	bdl	11.2	8.2	33.7	15.8
bdl	bdl	bdl	4.6	bdl	22.4	20.4	50.7	32.7
bdl	bdl	bdl	bdl	bdl	13.7	13.1	51.5	20.8
bdl	bdl	bdl	bdl	3.8	23.6	23.0	47.9	21.8
bdl	2.0	4.0	8.0	9.0	5.0	20.0	28.0	6.0
bdl	1.0	7.0	9.0	3.0	bdl	61.0	42.0	9.0

Raw whole-rock geochemical data

Sample No. ppm	Mo	Nb	Zr	Y	Sr	U
VLT48	2.9	bdl	1.9	bdl	15.9	2.7
VLT49	4.4	1.5	1.8	1.2	4.2	bdl
VLT50	4.6	2.6	4.2	bdl	4.1	bdl
VLT51	3.1	2.0	bdl	4.5	20.9	bdl
VLT52	6.2	1.5	1.4	5.7	28.3	bdl
VLT55	2.4	bdl	3.2	4.5	71.7	bdl
VLT56	2.8	bdl	2.2	12.6	36.1	bdl
VLT59	2.2	bdl	bdl	bdl	17.7	bdl
VLT61	2.8	bdl	2.0	7.8	8.4	bdl
VLT62	3.0	5.0	14.0	8.0	30.0	bdl
VLT63	2.0	bdl	1.7	5.7	11.5	bdl
VLT64	4.0	5.0	14.0	6.5	51.0	bdl
VLT66	3.4	bdl	bdl	13.1	7.5	bdl
VLT68	3.9	1.5	1.8	5.1	29.2	bdl
VLT69	4.5	bdl	3.3	6.0	42.3	bdl
VLT70	3.1	bdl	3.1	14.1	10.7	bdl
VLT71	4.1	bdl	1.9	3.0	53.8	3.5
VLT73	4.6	bdl	2.0	6.3	13.8	bdl
VLT74	bdl	27.7	280.3	30.3	152.3	bdl
VLT76	4.4	bdl	bdl	5.7	17.7	bdl
VLT80	3.4	2.3	4.6	4.0	58.0	bdl

Sample No. ppm	Mo	Nb	Zr	Y	Sr	U
D1	2.7	3.0	15.0	15.0	42.0	bdl
D2	2.3	3.0	11.0	6.0	14.0	bdl
D3	4.0	4.0	7.0	7.0	17.0	bdl
D4	4.0	2.0	14.0	6.0	14.0	bdl
D5	4.1	3.0	10.0	8.0	18.0	bdl
D6	4.3	4.0	16.0	27.0	17.0	bdl
D7	2.3	4.0	13.0	4.0	31.0	bdl
D8	3.2	6.0	17.0	5.0	40.7	bdl
D9	3.8	4.0	15.0	15.0	5.4	bdl
D10	3.5	4.0	bdl	7.0	19.0	bdl

Rb	Th	Pb	Zn	Cu	Ni	Cr	V
bdl	bdl	bdl	bdl	22.5	25.1	48.3	36.5
bdl	bdl	bdl	bdl	23.8	25.4	63.1	36.1
bdl	bdl	bdl	bdl	31.3	38.8	76.5	37.6
bdl	bdl	bdl	bdl	35.2	41.2	47.0	37.3
bdl	bdl	bdl	bdl	25.1	34.3	71.6	28.8
1.7	bdl	5.5	4.9	25.2	21.2	44.2	27.1
bdl	bdl	bdl	5.4	25.3	27.8	51.1	27.8
bdl	bdl	bdl	bdl	33.1	55.1	50.9	26.9
bdl	bdl	bdl	bdl	28.4	31.9	58.8	32.2
1.0	11.0	11.0	10.0	27.0	38.0	22.0	13.0
bdl	bdl	bdl	bdl	18.5	25.3	35.6	26.7
bdl	10.0	10.0	5.0	14.0	bdl	26.0	29.0
bdl	bdl	bdl	5.2	21.4	38.6	46.4	25.6
bdl	bdl	bdl	5.4	26.4	16.8	39.5	25.0
bdl	bdl	bdl	bdl	29.1	25.0	61.6	33.6
bdl	bdl	bdl	bdl	24.2	21.1	52.6	29.4
2.9	bdl	bdl	7.2	32.2	23.9	72.8	46.5
bdl	bdl	bdl	7.4	36.1	31.9	62.7	47.7
99.1	11.5	37.7	5.3	18.5	35.4	65.3	551.7
bdl	bdl	bdl	5.9	31.4	36.6	68.6	42.7
2.3	bdl	5.5	bdl	27.3	25.8	47.2	55.9

Rb	Th	Pb	Zn	Cu	Ni	Cr	V
bdl	3.0	4.0	10.0	23.0	bdl	47.0	30.0
2.0	5.0	9.0	9.0	1.0	97.0	21.0	5.0
2.0	7.0	7.0	14.0	71.0	2.0	21.0	12.0
4.0	3.0	13.0	10.0	33.0	62.0	41.0	28.0
9.0	7.0	11.0	9.0	bdl	121.0	49.0	182.0
6.0	6.0	5.0	9.0	50.0	bdl	28.0	26.0
4.0	10.0	6.0	9.0	46.0	2.0	32.0	21.0
4.0	11.0	10.0	14.0	10.0	bdl	52.0	135.0
3.0	8.0	9.0	14.0	17.0	26.0	25.0	18.0
bdl	7.0	9.0	6.0	10.0	17.0	33.0	16.0

Appendix III

Raw whole-rock geochemical data

Sample No. ppm	Mo	Nb	Zr	Y	Sr	U
D11	3.9	5.0	12.0	6.0	16.0	bdl
D12	3.2	3.0	11.0	3.0	14.0	bdl
D13A	3.9	4.0	11.0	4.0	13.0	bdl
D13B	5.0	3.0	12.0	6.0	14.0	bdl
D14	4.9	5.0	20.0	4.0	62.0	bdl
D15	2.4	5.0	28.0	19.0	48.0	bdl
D16	6.7	2.9	bdl	4.7	5.3	bdl
D17	2.8	3.0	1.0	5.0	17.0	bdl
D18	3.3	5.0	15.0	4.0	22.0	bdl
D19	2.7	3.0	12.0	6.0	30.0	bdl
D22	4.3	4.0	22.0	16.0	33.0	bdl

Sample No. ppm	Mo	Nb	Zr	Y	Sr	U
S2	2.6	3	14	8	12	bdl
S3	2.8	3	11	7	13	bdl
S4	3.2	4	12	2	14	bdl
S5	bdl	3	14	5	15	bdl
S6	4.2	4	3	7	15	bdl

Appendix III

Rb	Th	Pb	Zn	Cu	Ni	Cr	V
1.0	8.0	8.0	9.0	bdl	bdl	38.0	20.0
5.0	12.0	9.0	11.0	31.0	58.0	35.0	15.0
bdl	8.0	7.0	10.0	17.0	63.0	27.0	29.0
3.0	10.0	5.0	14.0	10.0	bdl	36.0	13.0
12.0	14.0	15.0	26.0	23.0	bdl	42.0	27.0
5.0	10.0	16.0	14.0	27.0	29.0	44.0	22.0
6.0	bdl	bdl	11.0	64.0	bdl	21.0	10.0
1.0	9.0	5.0	7.0	bdl	7.0	34.0	15.0
2.0	3.0	8.0	5.0	bdl	bdl	29.0	20.0
3.0	11.0	11.0	8.0	34.0	35.0	23.0	16.0
6.0	13.0	18.0	22.0	74.0	bdl	6.0	68.0

Rb	Th	Pb	Zn	Cu	Ni	Cr	V
3	4	11	8	26	bdl	30	15
2	7	7	6	3	bdl	21	15
bdl	10	12	13	10	bdl	29	21
4	8	5	9	11	bdl	19	11
4	7	9	12	10	18	38	20

Appendix III

Iron Ore			Ferruginous BIF								
sample	SiO_2	Fe_2O_3	sample	SiO_2	Fe_2O_3	sample	SiO_2	Fe_2O_3	sample	SiO_2	Fe_2O_3
HLT1	1.74	94.04	HLT12	47.20	50.26	VLT23	40.02	56.12	VLT80	45.73	50.95
HLT2	2.79	95.06	HLT24	37.04	58.49	VLT26	22.51	74.74	D1	43.33	55.23
HLT3	4.88	92.74	HLT25	45.25	52.74	VLT29	39.65	57.97	D3	44.09	54.64
HLT5	2.42	93.27	HLT44	46.41	52.44	VLT30	48.80	50.12	D4	47.32	51.62
HLT6	1.52	97.47	HLT47	46.97	51.33	VLT36	36.49	61.34	D5	45.61	53.57
HLT7	1.10	97.49	HLT48	48.75	50.58	VLT37	45.70	50.81	D6	46.80	52.07
VLT1	1.53	94.42	VLT3	47.62	50.02	VLT50	38.17	59.94	D8	38.49	60.41
VLT6	6.52	91.75	VLT5	37.53	60.95	VLT51	23.87	72.78	D10	49.24	50.07
VLT10	10.69	86.67	VLT13	35.75	62.50	VLT59	34.48	62.88	D13B	36.40	63.18
D14	3.22	95.34	VLT15	34.80	63.54	VLT61	32.75	65.45	D15	22.13	74.80
D16	0.65	99.10	VLT18	47.24	50.43	VLT62	33.29	64.92	D19	46.14	52.83
D22	1.71	96.73	VLT20	44.14	53.65	VLT73	39.68	57.47	S2	46.00	53.07
									S4	48.52	50.86

Altered BIF								
sample	SiO_2	Fe_2O_3	sample	SiO_2	Fe_2O_3	sample	SiO_2	Fe_2O_3
HLT13	53.97	40.80	VLT48	57.27	40.52	D11	52.99	46.07
HLT15	57.47	40.71	VLT52	65.84	31.13	D12	52.26	46.83
HLT21	59.46	39.00	VLT55	53.08	41.62	D13A	56.15	43.40
HLT22	56.65	39.55	VLT56	54.87	41.86	D17	50.78	47.94
HLT23	57.41	41.39	VLT68	60.69	36.52	S3	54.69	43.80
HLT30	55.81	42.05	VLT69	60.03	37.42	S5	61.62	36.89
HLT32	56.01	42.76	VLT70	57.52	40.58	S6	56.65	42.42
HLT35	65.76	33.33	VLT71	50.15	45.82			
HLT45	55.87	42.22	VLT76	51.20	45.84			
HLT46	66.75	31.93	D2	56.71	42.41			
VLT19	55.89	41.51	D7	55.18	44.10			
VLT27	49.62	48.35	D9	53.84	44.86			

Silicified BIF					
sample	SiO_2	Fe_2O_3	sample	SiO_2	Fe_2O_3
HLT9	69.32	28.57	VLT39	87.52	10.01
HLT16	73.66	24.92	VLT40	64.98	31.71
HLT33	76.39	21.47	VLT41	83.95	14.30
HLT36	96.50	2.69	VLT42	67.16	29.38
HLT37	96.24	2.46	VLT43	74.77	15.37
HLT38	96.54	2.40	VLT44	84.77	13.72
HLT39	95.90	2.91	VLT49	68.11	31.12
HLT41	65.71	33.23	VLT63	65.91	32.47
VLT25	66.72	30.93	VLT64	74.53	23.19
VLT34	65.49	32.42	VLT66	66.06	32.75
VLT35	69.12	30.17	D18	70.45	28.47
VLT38	66.65	33.23			

SiO_2 and Fe_2O_3 values of all samples used to define the 4 geochemical groups

Appendix III

Iron Ore

Sample	Co	Ba	S	La	Ce	Nd	Ga
HLT2	41	98	74	16	bdl	10	bdl
HLT6	17	12	16930	bdl	bdl	bdl	bdl
HLT7	bdl	975	19	55	92	33	bdl
VLT6	13	12	bdl	1	bdl	15	bdl
VLT10	12	94	66	bdl	bdl	bdl	bdl
D14	8	21	7857	bdl	bdl	bdl	bdl
D16	bdl	66	58	bdl	bdl	9	n.a
D22	13	6906	2346	bdl	bdl	5	5

Siliceous BIF

Sample	Co	Ba	S	La	Ce	Nd	Ga
HLT36	bdl	22	933	12	11	5	bdl
HLT39	bdl	15	2557	10	bdl	bdl	bdl
VLT43	2	22	21132	bdl	bdl	7	bdl
VLT44	bdl	2	4699	14	5	8	2
VLT64	14	2	bdl	bdl	bdl	4	bdl
D18	24	26	bdl	bdl	bdl	bdl	1

Ferruginous BIF

Sample	Co	Ba	S	La	Ce	Nd	Ga
HLT26B	17	25	16930	bdl	bdl	bdl	1
HLT48	12	11	74	bdl	bdl	10	2
VLT4A	24	41	bdl	1	bdl	bdl	4
VLT5	3	9	6243	11	bdl	bdl	2
VLT6	13	12	bdl	1	bdl	15	bdl
VLT15	bdl	736	bdl	42	54	24	bdl
VLT16A	4	273	bdl	bdl	bdl	1	bdl
VLT37	bdl	12	bdl	2	bdl	bdl	2
VLT62	22	6	5608	bdl	bdl	11	2
D1	7	10	7840	bdl	bdl	9	bdl
D3	4	91	58	bdl	1	15	2
D4	13	bdl	bdl	bdl	bdl	bdl	bdl
D5	39	97	bdl	2	3	9	bdl
D6	16	27	bdl	bdl	9	3	2
D8	16	46	bdl	bdl	17	2	bdl
D10	4	374	bdl	bdl	bdl	bdl	bdl
D13B	13	7	bdl	bdl	bdl	3	bdl
D15	bdl	6	bdl	bdl	bdl	4	1
D19	9	87	bdl	bdl	bdl	bdl	bdl
S2	13	12	bdl	1	bdl	15	4
S4	12	20	bdl	1	bdl	bdl	5

Altered BIF

Sample	Co	Ba	S	La	Ce	Nd	Ga
HLT22	7	23	7857	bdl	bdl	7	bdl
HLT23	40	5	2827	bdl	bdl	5	bdl
VLT4B	bdl	47795	15739	bdl	bdl	53	bdl
VLT27	7	23	13	bdl	bdl	1	bdl
D2	8	31	bdl	bdl	bdl	bdl	bdl
D7	1	32	bdl	bdl	bdl	3	bdl
D9	12	4	bdl	2	5	11	1
D11	9	244	bdl	3	bdl	2	bdl
D12	13	26	bdl	bdl	bdl	bdl	bdl
D13A	8	37	bdl	7	27	14	bdl
D17	bdl	35	bdl	bdl	bdl	8	bdl
S3	5	6	bdl	bdl	bdl	1	bdl
S5	8	8	bdl	4	bdl	bdl	5
S6	9	244	bdl	3	bdl	2	bdl

Ba, S, Co and REE concentrations of analyzed samples

Appendix III

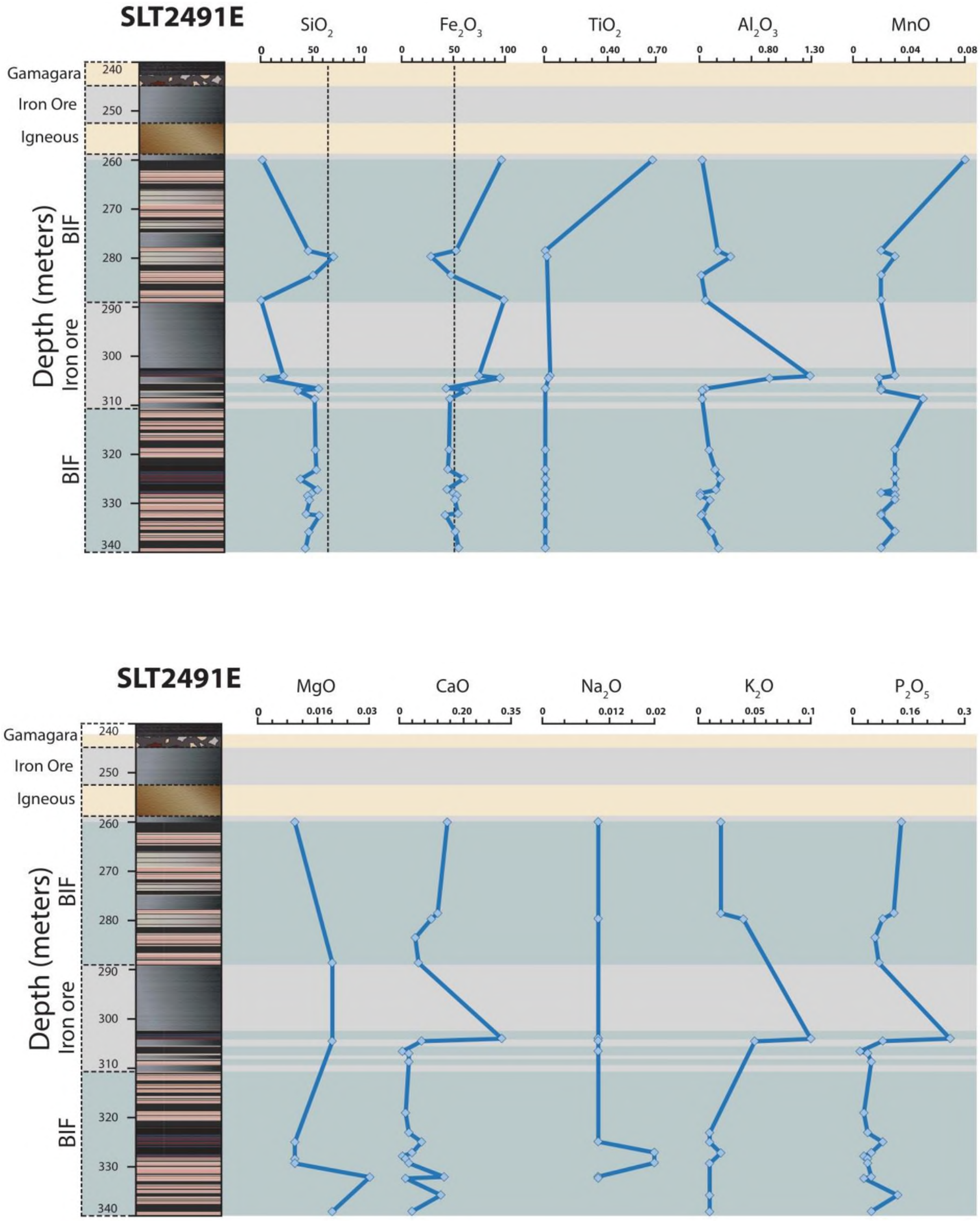

Chemostratigraphic plots for drill core SLT2491E

Appendix III

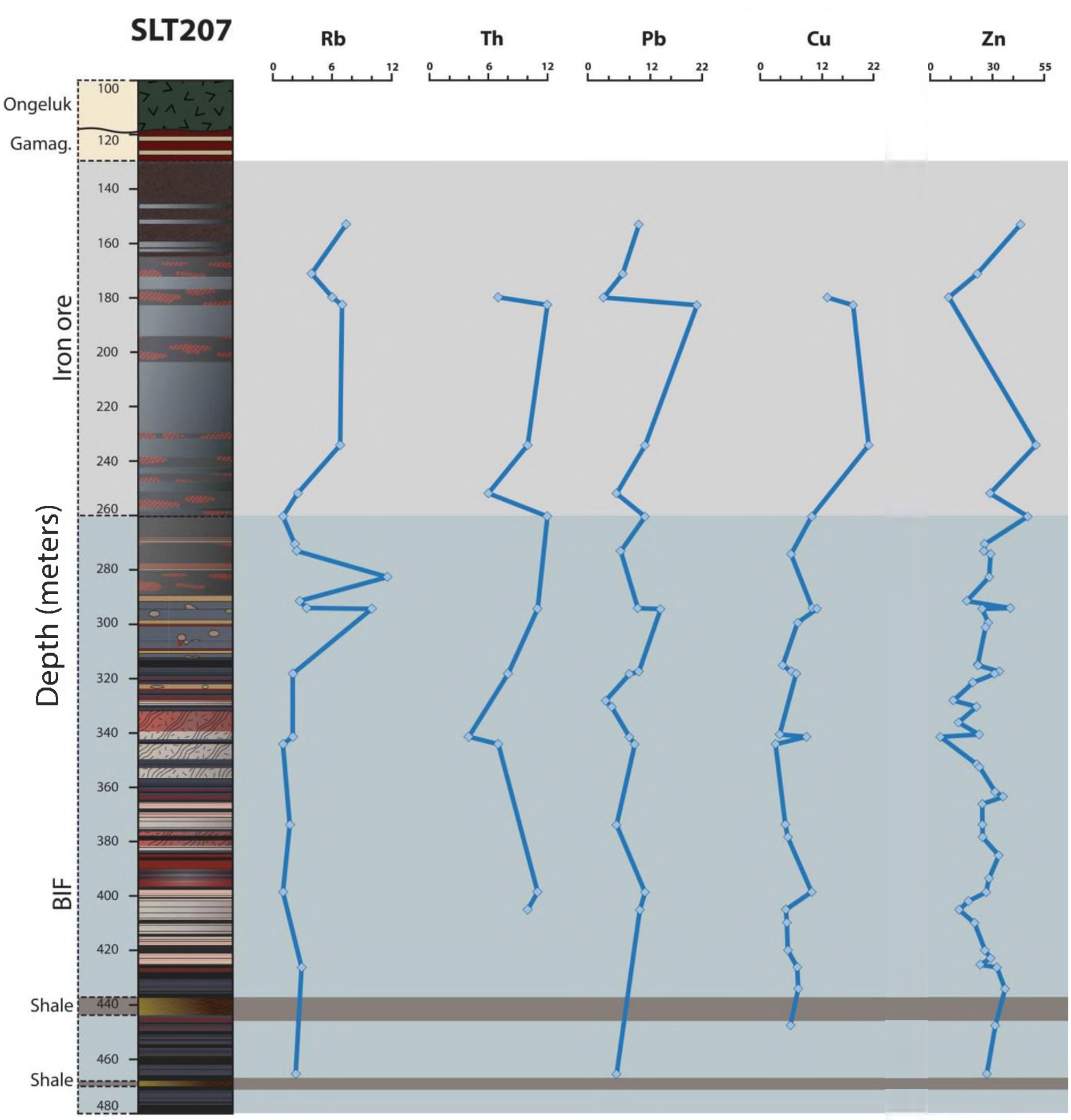

Chemostratigraphic plots for drill core SLT207

Appendix III

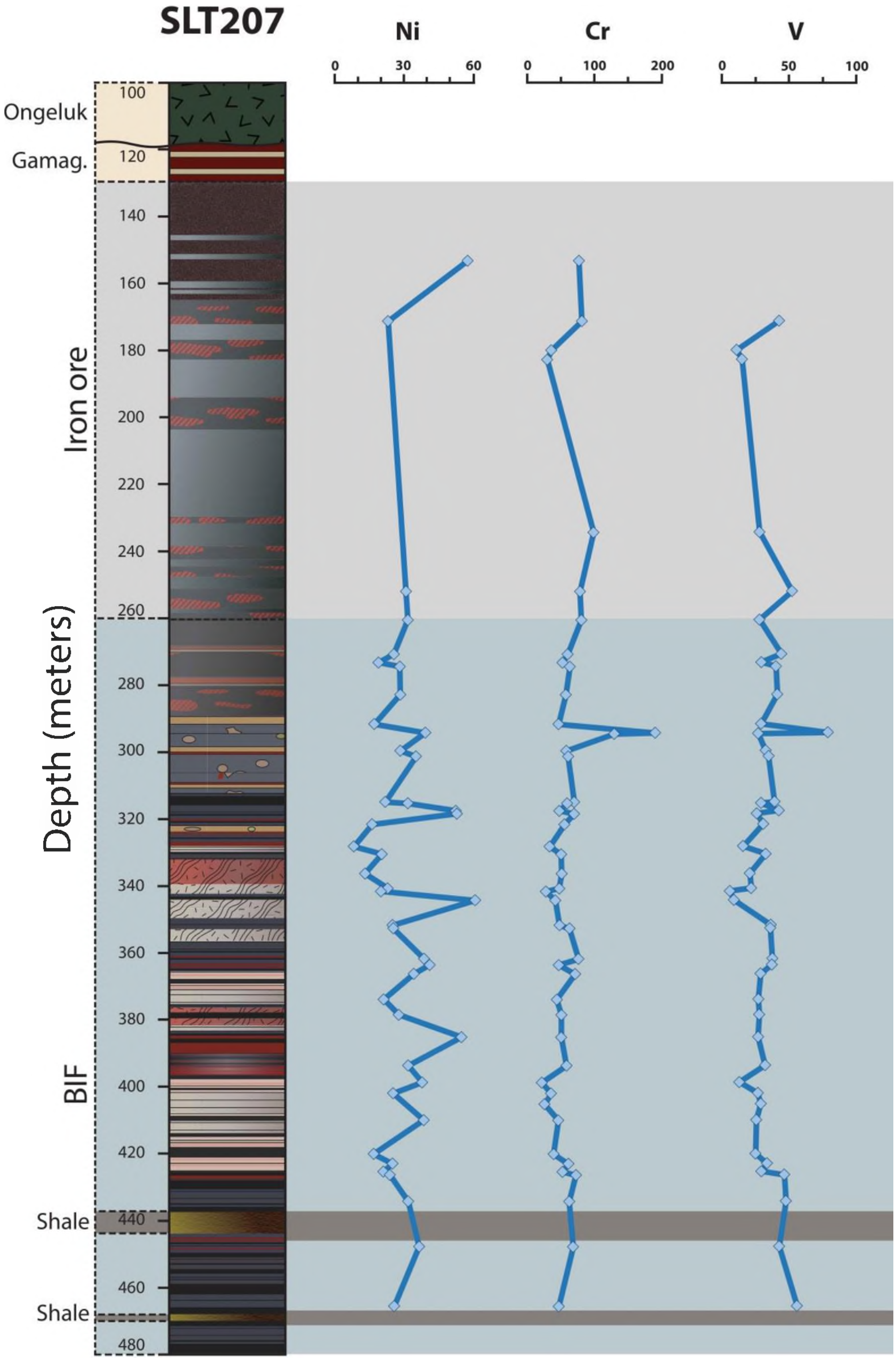

Chemostratigraphic plots for drill core SLT207

Appendix III

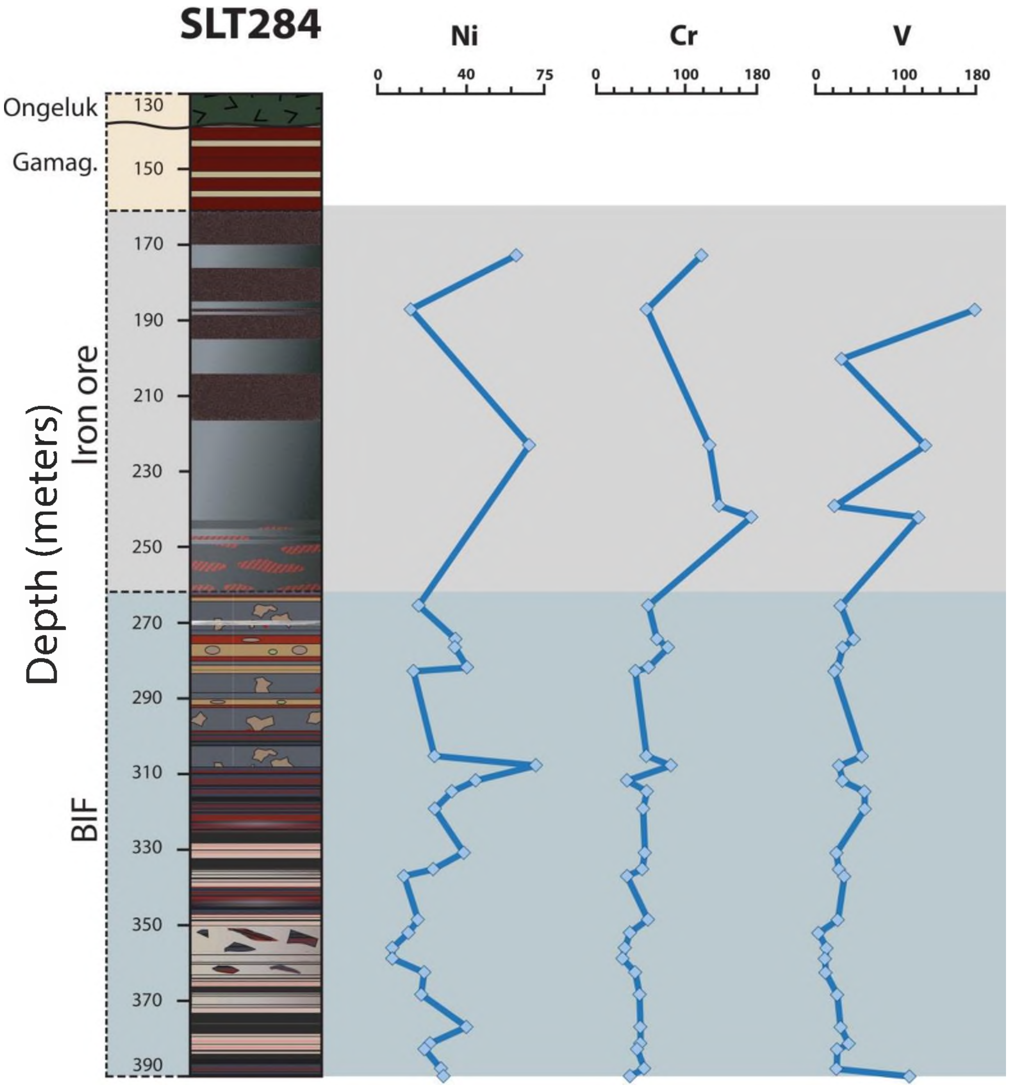

Chemostratigraphic plots for drill core SLT284

Appendix III

Geochemical Group	Iron Ore (n=12) Average	STD	%RSD	Ferruginous BIF (n=37) Average	STD	%RSD	Altered BIF (n=31) Average	STD	%RSD	Siliceous BIF (n=23) Average	STD	%RSD
SiO_2 (wt%)	3.23	2.89	89.35	40.92	7.42	18.13	56.52	4.32	7.64	75.93	11.49	15.13
TiO_2	0.15	0.18	121.22	0.03	0.02	72.82	0.02	0.02	108.93	0.01	0.01	86.27
Al_2O_3	0.87	0.45	51.27	0.22	0.35	157.13	0.11	0.17	154.19	0.13	0.15	114.28
Fe_2O_3	94.51	3.28	3.47	57.16	7.06	12.35	41.41	4.27	10.32	13.73	11.44	83.31
MnO	0.04	0.03	69.98	0.04	0.02	45.36	0.04	0.01	37.03	0.06	0.07	113.63
MgO	0.03	0.02	71.24	0.02	0.01	60.04	0.01	0.01	118.17	0.06	0.17	285.44
CaO	0.17	0.13	78.24	0.25	0.30	119.59	0.41	0.50	120.86	0.44	0.42	94.49
Na_2O	0.01	0.01	88.16	0.01	0.00	40.79	0.01	0.01	115.43	0.01	0.00	31.57
K_2O	0.09	0.05	52.89	0.03	0.07	238.17	0.02	0.03	169.35	0.01	0.02	164.29
P_2O_5	0.13	0.09	69.99	0.06	0.05	78.61	0.04	0.02	58.97	0.02	0.02	109.68

Geochemical Group	Iron Ore (n=12) Average	STD	%RSD	Ferruginous BIF (n=37) Average	STD	%RSD	Altered BIF (n=31) Average	STD	%RSD	Siliceous BIF (n=23) Average	STD	%RSD
Mo (ppm)	5.11	1.7	32.9	3.52	0.87	24.68	3.32	0.97	29.28	3.18	0.69	21.80
Nb	3.92	1.1	28.4	3.37	1.24	36.79	3.15	1.07	33.97	2.86	1.63	56.95
Zr	22.58	8.3	36.7	9.08	6.26	68.93	7.05	5.89	83.57	5.61	5.46	97.35
Y	10.21	5.2	50.6	5.46	5.90	108.13	5.38	5.89	109.50	5.93	4.78	80.69
Sr	55.14	50.8	92.2	18.98	14.65	77.19	20.98	14.48	69.02	15.58	15.32	98.30
Rb	6.14	2.3	37.7	3.90	2.59	66.44	3.16	2.08	65.75	2.34	1.28	54.50
Th	11.50	2.6	22.8	7.78	2.80	35.97	7.90	2.25	28.52	5.83	2.64	45.27
Pb	25.78	21.8	84.5	8.50	3.24	38.14	8.00	2.61	32.65	7.28	2.53	34.68
Cu	40.12	559.4	1394.4	25.82	12.01	46.50	21.22	9.59	45.18	14.94	6.37	42.60
Zn	15.40	5.4	34.8	9.80	2.88	29.40	7.80	2.83	36.30	4.50	1.73	38.36
Ni	343.00	653.8	190.6	29.61	19.74	66.65	27.87	20.30	72.83	18.99	12.04	63.40
Cr	86.83	179.1	206.2	54.19	28.28	52.18	50.28	22.67	45.08	44.23	12.15	27.47
V	152.57	199.8	131.0	42.02	34.53	82.19	26.73	9.99	37.36	22.64	9.83	43.44

Calculated standard deviations and relative standard deviations

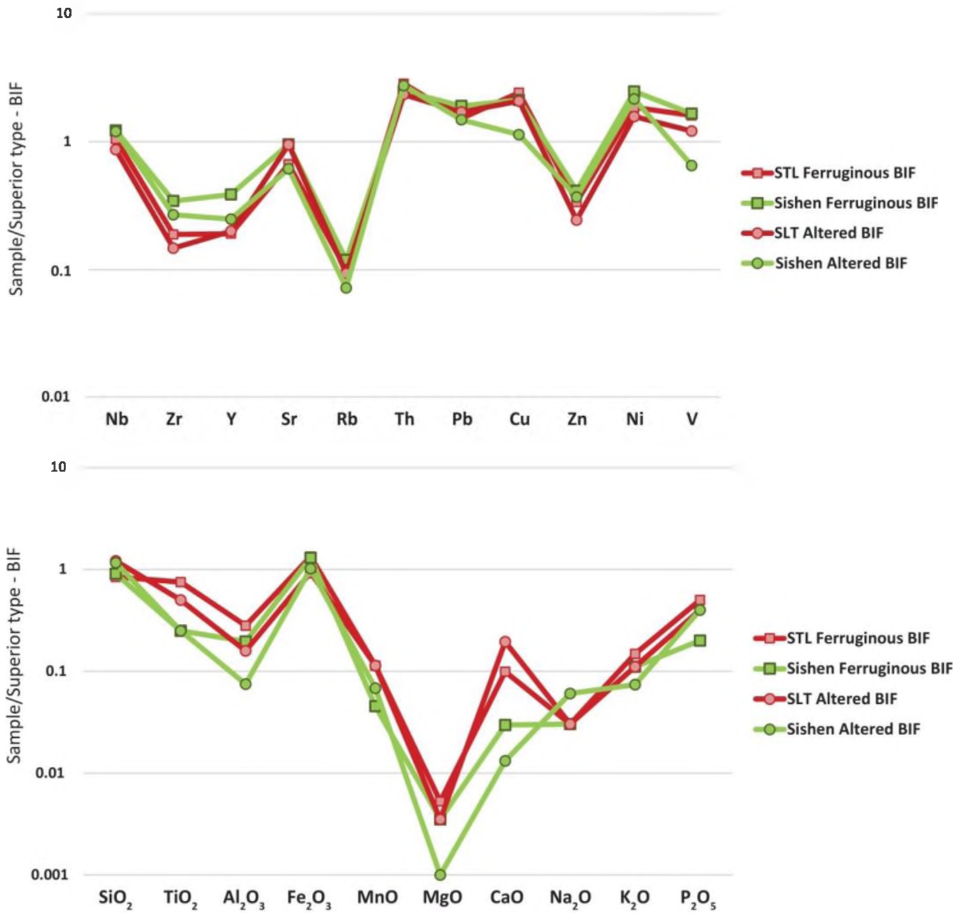

Spidergraphs comparing BIF between Sishen and SLT cores